5-2016

A Biologically Informed Structure to Accuracy in Osteometric Reassociation

Kyle Mccormick
The University of Tennessee at Knoxville, kmccorm7@vols.utk.edu

To the Graduate Council:

I am submitting herewith a dissertation written by Kyle Mccormick entitled "A Biologically Informed Structure to Accuracy in Osteometric Reassociation." I have examined the final electronic copy of this dissertation for form and content and recommend that it be accepted in partial fulfillment of the requirements for the degree of Doctor of Philosophy, with a major in Anthropology.

Dawnie Steadman, Major Professor

We have read this dissertation and recommend its acceptance:

Amy Mundorff, Benjamin Auerbach, James Fordyce

Accepted for the Council:
Dixie L. Thompson

Vice Provost and Dean of the Graduate School

(Original signatures are on file with official student records.)

A Biologically Informed Structure to Accuracy in Osteometric Reassociation

A Dissertation Presented for the

Doctor of Philosophy

Degree

The University of Tennessee, Knoxville

Kyle McCormick

May 2016

ACKNOWLEDGEMENTS

If I thanked everyone that made this dissertation possible, I would have to double the length of this document. First and foremost, my parents, Michael and Suzan McCormick. Few have a chance to be raised in such a loving and nurturing environment. Ma, you are the most selfless and caring person I have met. Dad, you passed before you could truly see me succeed, but you are part of me. You live on through my actions and accomplishments. Every day I will try to make what I do worthy of you. My brothers, Aidan and Colin McCormick. I could not ask for two better guys to grow up with. Although, given what I put both of you through, I doubt either of you would say the same.

David Mackres, my first professor in physical anthropology at Washtenaw Community College. Your class made me decide to switch majors from computer science to anthropology. That was a decision I have cursed many times, but I am now very thankful for it. Drs. Norm Sauer, Todd Fenton for the life-shaping summer learning forensic anthropology in London and then for trying to talk me out of going into the field shortly after. Dr. Mary Megyesi you were my teaching assistant in London and thank you for giving me partial credit on my first biological profile exam when I called the skull of a very old woman that of a baby. Dr. P. Willey for never allowing any thing I did to be good enough. I need that push to become a better anthropologist and to realize

what it takes to succeed in this field. Dr. Eric Bartelink for being the ying to P.'s yang and for giving me my first taste of statistics.

A special thanks to my committee: Drs. Dawnie Steadman, Amy Mundorff, Ben Auerbach, and James Fordyce. Dawnie, no one has been as influential on shaping me as an anthropologist as you were. You are truly a force to be reckoned with and I could not be more proud to be your academic progeny. Amy, you are an amazing person, a heck of an anthropologist, and a hero. Ben, thank you for opening my eyes to a whole new arena of literature and showing me how to become a better scientist. Jim, you are a friend and a mentor. There are few things I will miss more than our talks over a few root beers. We once loudly discussed the serious flaws of the species and race concepts for fifty-five minutes (we were timed). Also, Drs. Lee Meadows-Jantz and Joanne Devlin, I truly enjoyed work for and with you. I look forward to seeing you both at our annual AAFS get together. Dr. Richard Jantz, you are awe-inspiring. The simple and calm ways that you can explain complex subjects will never cease to amaze me. Your willingness to help and collaborate are admirable.

I will miss my friends in Knoxville more than words can properly express. Katie, you have been there with me and for me since that fateful day in Binghamton. Little did we know what a strange and wonderful friendship would come from that day. Even though we are apart, you will always have a piece of my heart. Dr. Michael Kenyhercz, I owe Bean a few hugs for introducing us as FSA's. There is no better scientists, anthropologists, or friend. You are destined for great things and I hope I can be part of

some of them. Alex Craib, Christina Fojas, Adam Burnett, Zach Marion, Stephanie Hacker, Chris Hartnett, Alana Brooks, and countless others. You made some tough years much better, allowing me to laugh and keep focused on what matters.

Thank you to everyone at the Defense POW/MIA Accounting Command. Especially, Dr. John Byrd for your excellent science and research on osteometric reassociation; Dr. Robert Mann for your sage advice; and Dr. Thomas Holland for inspiring such respect and admiration. Finally, thank you to everyone at the lab that made me feel at home during my time as an FSA. I am back and now I can truly make it my home.

ABSTRACT

Commingled assemblages present a common situation in osteological analysis where discrete sets of remains are not readily apparent, thereby hindering biological profile construction and the identification process. Of the methods available for resolving commingling, osteometric reassociation is considered a reliable and relatively objective technique. Traditional osteometric sorting methodologies is a decision-making, error-mitigation approach, where possible matches are eliminated if the calculated *p*-value exceeds an analyst-defined threshold. This approach implicitly assumes that all bone comparisons are equally accurate as long as the threshold is attained. This assumption, however, is not based in biological reality. This study tests a hypothetical structure of accuracy in osteometric reassociation to accomplish two goals: First, provide a biological logic to osteometric reassociation, centered on the developmental and mechanical relationships influencing limb bone morphology. This logic is assessed by comparing accuracy, or how often the predicted match is the correct match, in reassociating commingled limb elements by four types of comparisons: homologous, serially homologous, within-limb, and between-limb. Second, improve models for osteometric reassociation by incorporating Bayesian statistics and novel information on bone shape and size through geometric morphometric landmark data.

Landmark data were collected from the limb bones (excluding the fibula) of 208 adult males (n=103) and females (n=105) from the William M. Bass donated skeletal collection. From these data, limb bones were commonly represented as log-centroid size and partial least squares components of Procrustes coordinates. Then, 10 individuals were randomly removed from the total sample, acting as a small-scale, closed-population commingled assemblage. Bayesian regression via Hamiltonian MCMC was used as the osteometric reassociation model to predict the best match for commingled limb bones. This process was repeated 1000 times for each bone comparison. Accuracy was defined as the number of times the best match was the correct match divided by 1000. Accuracy was structured from highest to lowest: homologous, within-limb, between-limb, serially homologous. Research design, functional canalization of joints, and developmental modularity are possible factors influencing the observed structure of osteometric reassociation accuracy.

TABLE OF CONTENTS

Chapter 1 Introduction 1
1. Biological theory 3
1.1. Quantifying limb bone morphology 5
1.2. Bayesian statistics and the osteometric reassociation model 6
2. Research objectives 7
2.1. Hypothesis 7
2.2. Significance of research 8
3. Chapter organization 9
Chapter 2 Analysis of Commingled Remains 11
2. Factors influencing resolution of commingling 12
2.1. Why assemblages become commingled 14
3. Methods for resolving commingling 15
3.1. Estimating the number of individuals 16
3.2. Methods for reassociating commingled remains 18
3.3. Examples of commingling resolution 18
3.4. Osteometric reassociation 20
4. Summary 34
Chapter 3 Limb Ontogeny 36
1. Embryonic development of the mammalian limb 36
2. Limb bone ossification 41
3. Limb bone ossification: Timing and morphological change 47
3.1. Humerus 47
3.2. Radius 50
3.3. Ulna 51
3.4. Femur 52
3.5. Tibia 56
4. Summary 58
Chapter 4 Bone Biomechanics and Functional Adaptation 60
1. Bone loading regime 61
1.1. Bone sensing and communication of mechanical loading: The osteocyte 63
2. Macroscopic osseous response to mechanical loading: Modeling 64
2.1. Modeling 65
2.1.1. The upper limb 65
2.1.2. The lower limb 68
2.1.4. Modeling and osteometric reassociation 70
2.2. Limb bone response to loading by region: Linear measurements 70
2.3. Epiphyseal response to loading 72
2.3.1. Epiphyseal response and osteometric reassociation 73
3. Summary and functional adaptation and osteometric reassociation accuracy 74

Chapter 5 Limb Integration and Modularity 76
1. Integration and modularity 76
2. Limb integration and modularity 77
3.1. Limb integration and modularity and osteometric reassociation accuracy 78
4. Limb variation 78
4.1. Limb variation and osteometric reassociation accuracy 79
5. A biologically informed hierarchical structure of osteometric reassociation accuracy 80
Chapter 6 Materials and Methods 83
1. Materials 83
1.1. Geometric morphometric landmark data collection 83
2. Methods 91
2.1. Data Analysis 93
2.1.1. Generalized Procrustes Analysis (GPA) 93
2.1.2. Partial least squares (PLS) 95
2.1.3 Simulated Commingling 98
2.1.4 Bayesian regression 99
2.1.5. Markov Chain Monte Carlo (MCMC) 100
2.1.6. Model diagnostics 103
2.1.7. Kernel density estimation 104
2.1.8. Estimating best matches 104
2.1.9. Accuracy 108
2.1.10. Typicality 109
2.2. Summary of data analysis 109
3. Discussion 110
4. Summary 112
Chapter 7 Results 113
1. Intraobserver error 113
2. Accuracy 115
3. Comparisons details 119
3.1. Homologous comparisons 120
3.2. Serially homologous comparisons 122
3.3. Within-limb comparisons 123
3.4. Between-limb comparisons 125
6. Summary 125
Chapter 8 Discussion 130
1. The experimentally determined structure of accuracy in osteometric reassociation 130
2. Classification example 136
2.1. Diagnostic criteria 137
2.2. Centroid size 137
2.3. First PLS component 140

2.4. Second PLS component 140
2.5. Third PLS component 140
2.6. Fourth PLS component 145
2.7. Fifth PLS component 145
2.8. Sixth PLS component 146
2.9. Seventh PLS component 146
2.10. Eighth PLS component 146
2.11. Model discussion 146
3. Summary 160
Chapter 9 Conclusion 161
1. Future implications and broader impact 161
1.1 Comparative biology 161
1.2 Applications in biological anthropology 163
List of References 166
Appendix 180
A.1 Homologous comparisons 181
A.1.1. Correct match ranks 181
A.1.2. Descriptive statistics 189
A.2. Serially homologous comparisons 192
A.2.1. Correct match rank 192
A.3. Within-limb comparisons 198
A.3.1. Correct match rank 198
A.3.2. Descriptive statistics 206
A.4. Between-limb 209
A.4.1. Correct match rank 209
A.4.2. Descriptive statistics 227
Vita 233

LIST OF TABLES

Table 2.1. A comparison of cranial measurements of an unknown skull to the mean values of four reference samples in FORDISC 3. Differences between the unknown skull and group means are highlighted by the red box and are represented by '+' and '-', where the measurement is large r or smaller than the group means, respectively. Measurements that deviate one to two standard deviations away from the group mean are shown by '++' or '--'. Adapted from Jantz and Ousley (2005), FORDISC Help File version 1.35. 28
Table 3.1. The appearance and fusion times for the secondary ossification centers of the humerus. All timings from Scheuer and Black, 2004. 49
Table 3.2. The appearance and fusion times for the secondary ossification centers of the radius. All timings from Scheuer and Black, 2004. 51
Table 3.3. The appearance and fusion times for the secondary ossification centers of the ulna. All timings from Scheuer and Black, 2004. 52
Table 3.4. The appearance and fusion times for the secondary ossification centers of the femur. All timings from Scheuer and Black, 2004. 55
Table 3.5. The appearance and fusion times for the secondary ossification centers of the tibia. All timings from Scheuer and Black, 2004. 58
Table 6.1. Number of Landmarks by Bone. 84
Table 6.2. Landmark Descriptions. 84
Table 6.3. Number of Individuals by Sex. 88
Table 6.4. Number of Individuals by Ancestry. 88
Table 7.1. Descriptive statistics for error in landmark placement (methodological error) and stylus placement (personal error) between repeats of the same individual (n = 10) as measured by Procrustes distance. These errors are compared to shape variability in the reference sample. 114
Table 7.2. The accuracy and number of comparisons for each comparison type. 115
Table 7.3. The accuracy of different calculations of predictive probability by comparison type. Equal variable weights provide the best accuracy for all comparison types and is in bold. 116
Table 7.4. Accuracy of homologous comparisons by predictive probability type. The '~' denotes prediction and is read as y~x, where the bone on the right side of '~' predicts the bone to the left of '~'. 116
Table 7.5. Accuracy of serially homologous elements by predictive probability type. The '~' denotes prediction and is read as y~x, where the bone on the right side of '~' predicts the bone to the left of '~'. 117
Table 7.6. Accuracy of within-lower limb comparisons by predictive probability type. The '~' denotes prediction and is read as y~x, where the bone on the right side of '~' predicts the bone to the left of '~'. 117

Table 7.7. Accuracy of within-upper limb comparisons by predictive probability type. The '~' denotes prediction and is read as y~x, where the bone on the right side of '~' predicts the bone to the left of '~'. 117
Table 7.8. Accuracy of between-lower limb comparisons by predictive probability type. The '~' denotes prediction and is read as y~x, where the bone on the right side of '~' predicts the bone to the left of '~'. 118
Table 7.9. Accuracy of between-upper limb comparisons by predictive probability type. The '~' denotes prediction and is read as y~x, where the bone on the right side of '~' predicts the bone to the left of '~'. 118
Table 7.10. Between upper limb and lower limb comparisons by predictive probability type. The '~' denotes prediction and is read as y~x, where the bone on the right side of '~' predicts the bone to the left of '~'. 118
Table 7.11. Correct match predictive probability rank for homologous comparisons (n = 10000). 121
Table 7.12. Descriptive statistics for predictive probability and typicality values for correctly and incorrectly classified homologous comparisons. 122
Table 7.13. Correct match predictive probability rank for serially homologous comparisons (n = 4000). 124
Table 7.14. Descriptive statistics for predictive probability and typicality values for correctly and incorrectly classified serially homologous comparisons. 125
Table 7.15. Correct match predictive probability rank for within-limb comparisons (n = 8000). 126
Table 7.16. Descriptive statistics for predictive probability and typicality values for correctly and incorrectly classified within-limb comparisons. 127
Table 7.17. Correct match predictive probability rank for between-limb comparisons (n = 18000). 128
Table 7.18. Descriptive statistics for predictive probability and typicality values for correctly and incorrectly classified between limb comparisons. 129
Table 8.1. Correlation of proximal-distal nutrient foramen placement between left and right sides. 132
Table 8.2. A comparison of accuracy for proximal and distal elements by comparison type. 135
Table 8.3. Simulated commingled assemblage. 136
Table 8.4. Summary statistics for centroid size regression model. 138
Table 8.5. Summary statistics for PLS component 1 regression model. 141
Table 8.6. Summary statistics for PLS component 2 regression model. 143
Table 8.7. Cumulative predictive probabilities. The correct match and best match, 33-08D, is highlighted in bold. 145
Table 8.8. Summary statistics for PLS component 3 regression model. 147
Table 8.9. Summary statistics for PLS component 4 regression model. 149
Table 8.10. Summary statistics for PLS component 5 regression model. 151
Table 8.11. Summary statistics for PLS component 6 regression model. 153

Table 8.12. Summary statistics for PLS component 7 regression model. 155
Table 8.13. Summary statistics for PLS component 8 regression model. 157
Table 8.14. The number of times an individual could be rejected as a possible match using the 5% and 95% quantiles as thresholds. 159
Table 8.15. Density weighted predictive probabilities for the classification example. . 159
Table 9.1. Correct match predictive probability ranks for right femur predicting left femur. 181
Table 9.2. Correct match predictive probability ranks for left femur predicting right femur. 182
Table 9.3. Correct match predictive probability ranks for left radius predicting right radius. 183
Table 9.4. Correct match predictive probability ranks for right radius predicting left radius. 184
Table 9.5. Correct match predictive probability ranks for left tibia predicting right tibia. 185
Table 9.6. Correct match predictive probability ranks for right tibia predicting left tibia. 186
Table 9.7. Correct match predictive probability ranks for left ulna predicting right ulna. 187
Table 9.8. Correct match predictive probability ranks for right ulna predicting left ulna. 188
Table 9.9. Predictive probability and typicality descriptive statistics for correct and incorrect left femur predicting right femur. 189
Table 9.10. Predictive probability and typicality descriptive statistics for correct and incorrect right femur predicting left femur. 189
Table 9.11. Predictive probability and typicality descriptive statistics for correct and incorrect left radius predicting right radius. 190
Table 9.12. Predictive probability and typicality descriptive statistics for correct and incorrect right radius predicting left radius. 190
Table 9.13. Predictive probability and typicality descriptive statistics for correct and incorrect left tibia predicting right tibia. 190
Table 9.14. Predictive probability and typicality descriptive statistics for correct and incorrect right tibia predicting left tibia. 191
Table 9.15. Predictive probability and typicality descriptive statistics for correct and incorrect left ulna predicting right ulna. 191
Table 9.16.Predictive probability and typicality descriptive statistics for correct and incorrect right ulna predicting left ulna. 191
Table 9.17. Correct match predictive probability ranks for right ulna predicting right tibia. 192
Table 9.18. Correct match predictive probability ranks for right tibia predicting right ulna. 193

Table 9.19. Correct match predictive probability ranks for right femur predicting right humerus. 194
Table 9.20. Correct match predictive probability ranks for right humerus predicting right femur. 195
Table 9.21. Predictive probability and typicality descriptive statistics for correct and incorrect right ulna predicting right tibia. 196
Table 9.22. Predictive probability and typicality descriptive statistics for correct and incorrect right tibia predicting right ulna. 196
Table 9.23. Predictive probability and typicality descriptive statistics for correct and incorrect right femur predicting right humerus. 196
Table 9.24. Predictive probability and typicality descriptive statistics for correct and incorrect right humerus predicting right femur. 197
Table 9.25. Correct match predictive probability ranks for right ulna predicting right radius. 198
Table 9.26. Correct match predictive probability ranks for right ulna predicting right humerus. 199
Table 9.27. Correct match predictive probability ranks for right tibia predicting right femur. 200
Table 9.28. Correct match predictive probability ranks for right radius predicting right ulna. 201
Table 9.29. Correct match predictive probability ranks for right radius predicting right humerus. 202
Table 9.30. Correct match predictive probability ranks for right humerus predicting right ulna. 203
Table 9.31. Correct match predictive probability ranks for right femur predicting right tibia. 204
Table 9.32. Correct match predictive probability ranks for right humerus predicting right radius. 205
Table 9.33. Predictive probability and typicality descriptive statistics for correct and incorrect right ulna predicting right radius. 206
Table 9.34. Predictive probability and typicality descriptive statistics for correct and incorrect right ulna predicting right humerus. 206
Table 9.35. Predictive probability and typicality descriptive statistics for correct and incorrect right tibia predicting right femur. 206
Table 9.36. Predictive probability and typicality descriptive statistics for correct and incorrect right radius predicting right ulna. 207
Table 9.37. Predictive probability and typicality descriptive statistics for correct and incorrect right radius predicting right humerus. 207
Table 9.38. Predictive probability and typicality descriptive statistics for correct and incorrect right humerus predicting right ulna. 207
Table 9.39. Predictive probability and typicality descriptive statistics for correct and incorrect right humerus predicting right radius. 208

Table 9.40. Predictive probability and typicality descriptive statistics for correct and incorrect right femur predicting right tibia. 208
Table 9.41. Correct match predictive probability ranks for right humerus predicting left ulna. 209
Table 9.42. Correct match predictive probability ranks for right humerus predicting left radius. 210
Table 9.43. Correct match predictive probability ranks for right femur predicting right ulna. 211
Table 9.44. Correct match predictive probability ranks for right femur predicting right radius. 212
Table 9.45. Correct match predictive probability ranks for right femur predicting left tibia. 213
Table 9.46. Correct match predictive probability ranks for left ulna predicting right radius. 214
Table 9.47. Correct match predictive probability ranks for left radius predicting right ulna. 215
Table 9.48. Correct match predictive probability ranks for left humerus predicting right ulna. 216
Table 9.49. Correct match predictive probability ranks for left humerus predicting right radius. 217
Table 9.50. Correct match predictive probability ranks for left femur predicting right tibia. 218
Table 9.51. Correct match predictive probability ranks for right ulna predicting right femur. 219
Table 9.52. Correct match predictive probability ranks for right ulna predicting left radius. 220
Table 9.53. Correct match predictive probability ranks for right tibia predicting right radius. 221
Table 9.54. Correct match predictive probability ranks for right tibia predicting right humerus. 222
Table 9.55. Correct match predictive probability ranks for right radius predicting right tibia. 223
Table 9.56. Correct match predictive probability ranks for right radius predicting right femur. 224
Table 9.57. Correct match predictive probability ranks for right radius predicting left ulna. 225
Table 9.58. Correct match predictive probability ranks for right humerus predicting right tibia. 226
Table 9.59. Predictive probability and typicality descriptive statistics for correct and incorrect right femur predicting right radius. 227
Table 9.60. Predictive probability and typicality descriptive statistics for correct and incorrect right femur predicting left tibia. 227

Table 9.61. Predictive probability and typicality descriptive statistics for correct and incorrect left ulna predicting right radius. 227
Table 9.62. Predictive probability and typicality descriptive statistics for correct and incorrect left radius predicting right ulna. 228
Table 9.63. Predictive probability and typicality descriptive statistics for correct and incorrect left humerus predicting right ulna. 228
Table 9.64. Predictive probability and typicality descriptive statistics for correct and incorrect left humerus predicting right radius. 228
Table 9.65. Predictive probability and typicality descriptive statistics for correct and incorrect left femur predicting right tibia. 229
Table 9.66. Predictive probability and typicality descriptive statistics for correct and incorrect right humerus predicting right tibia. 229
Table 9.67. Predictive probability and typicality descriptive statistics for correct and incorrect right humerus predicting left ulna. 229
Table 9.68. Predictive probability and typicality descriptive statistics for correct and incorrect right ulna predicting right femur. 230
Table 9.69. Predictive probability and typicality descriptive statistics for correct and incorrect right ulna predicting left radius. 230
Table 9.70. Predictive probability and typicality descriptive statistics for correct and incorrect right tibia predicting right radius. 230
Table 9.71. Predictive probability and typicality descriptive statistics for correct and incorrect right tibia predicting right humerus. 231
Table 9.72. Predictive probability and typicality descriptive statistics for correct and incorrect right radius predicting right tibia. 231
Table 9.73. Predictive probability and typicality descriptive statistics for correct and incorrect right radius predicting right femur. 231
Table 9.74. Predictive probability and typicality descriptive statistics for correct and incorrect right radius predicting left ulna. 232

LIST OF FIGURES

Figure 3.1.The Limb Bud. A. The location of the Apical Ectodermal Ridge (AER, in blue) and Zone of Polarizing Activity (ZPA, yellow). B. The expression location of major genes in limb development. Modified from Zeller et al. 2009, Figure 3..... 39
Figure 3.2. The osteoclast (a) and osteoblast (b) lineage. From Robling et al. (2006) Figure 3. 44
Figure 3.3. Diagram of the formation of a Haversian system (osteon) via bone turnover from the BMU. From Curry 2002 Figure 1.2. 44
Figure 4.1. Four typical bone loading regimes: A. Axial compression, B. Bending, C. Twisting, D. Shear. Thick arrows represent direction of force and thin arrows show the resulting strain. From Pearson and Lieberman 2004, Figure 2. 61
Figure 4.2. Stress/strain curve depicting how an object reacts to an applied load. From Curry 2002, Figure 2.7. 62
Figure 4.3. Example of an osteon. Modified from Gray (1918) by Bduttabaruah. https://commons.wikimedia.org/wiki/File:Transverse_Section_Of_Bone.png..... 63
Figure 4.4. Left is a cross section of a new born tibia from a normal mechanical environment. Right, a new born tibia lacking mechanical loading due to spina bifida. From Robling and Turner 2009 Figure 2. Reprinted from Ralis et al. 1976. 65
Figure 4.5. Asymmetry in humeral diaphyseal cross sectional shape from hypervigorous activity favoring the dominate limb. Player A and Player B were each professional tennis players in their mid-twenties with 18 years playing experience. From Jones et al., 1977. 69
Figure 4.6. The tibial cross-sectional shape. From Shaw and Stock 2009a, Figure 3. ... 71
Figure 5.1. The proposed hypothetical structure of accuracy in osteometric reassociation. 82
Figure 6.1. Age at Death Distribution of the Sample (n = 208)..... 88
Figure 6.2. Graphical representation of size and shape and their relation to form and proportion. 89
Figure 6.3. The Microscribe G2X Digitizer used in the current study. 91
Figure 6.4. Schematic representation of Generalized Procrustes analysis. From Mitteroecker et al. (2013), Figure 2. 94
Figure 6.5. Relationship between predictive ability of a variable and the distribution of simulated y-values, or the standard error around the mean estimate. Each sample is 100,000 random draws from a normal distribution with a mean of 0 and different standard d eviations. The blue sample (low) has a standard deviation of 1 and the pink sample (high) has a standard deviation of 3. 106
Figure 6.6. The density distributions of the samples in Figure 19. A high standard error in the estimation of y results in low density estimates, especially for the mean

predicted y-value. Conversely, a low standard error results in high density estimates for values around the mean. 107
Figure 8.1. Histogram and kernel density estimate of y-values and match probabilities for centroid size. Red lines represent the 5% and 95% quantiles, respectively. 138
Figure 8.2. Summary and diagnostic visuals for centroid size regression model parameters. The density plot visualizes the posterior distribution of a parameter. The autocorrelation bar graph represents the correlation or dependency of MCMC draws. The chain mixture or trace plot measures how well the sampler is exploring parameter space. 139
Figure 8.3. Histogram and kernel density estimate of y-values and match probabilities for PLS component 1. Red lines represent the 5% and 95% quantiles, respectively. . 141
Figure 8.4. Summary and diagnostic visuals for PLS component 1 regression model parameters. The density plot visualizes the posterior distribution of a parameter. The autocorrelation bar graph represents the correlation or dependency of MCMC draws. The chain mixture or trace plot measures how well the sampler is exploring parameter space. 142
Figure 8.5. Histogram and kernel density estimate of y-values and match probabilities for PLS component 2. Red lines represent the 5% and 95% quantiles, respectively. . 143
Figure 8.6. Summary and diagnostic visuals for PLS component 2 regression model parameters. The density plot visualizes the posterior distribution of a parameter. The autocorrelation bar graph represents the correlation or dependency of MCMC draws. The chain mixture or trace plot measures how well the sampler is exploring parameter space. 144
Figure 8.7. Histogram and kernel density estimate of y-values and match probabilities for PLS component 3. Red lines represent the 5% and 95% quantiles, respectively. . 147
Figure 8.8. Summary and diagnostic visuals for PLS component 3 regression model parameters. The density plot visualizes the posterior distribution of a parameter. The autocorrelation bar graph represents the correlation or dependency of MCMC draws. The chain mixture or trace plot measures how well the sampler is exploring parameter space. 148
Figure 8.9. Histogram and kernel density estimate of y-values and match probabilities for PLS component 4. Red lines represent the 5% and 95% quantiles, respectively. . 149
Figure 8.10. Summary and diagnostic visuals for PLS component 4 regression model parameters. The density plot visualizes the posterior distribution of a parameter. The autocorrelation bar graph represents the correlation or dependency of MCMC draws. The chain mixture or trace plot measures how well the sampler is exploring parameter space. 150
Figure 8.11. Histogram and kernel density estimate of y-values and match probabilities for PLS component 5. Red lines represent the 5% and 95% quantiles, respectively. 151
Figure 8.12. Summary and diagnostic visuals for PLS component 5 regression model parameters. The density plot visualizes the posterior distribution of a parameter.

The autocorrelation bar graph represents the correlation or dependency of MCMC draws. The chain mixture or trace plot measures how well the sampler is exploring parameter space..... 152
Figure 8.13. Histogram and kernel density estimate of y-values and match probabilities for PLS component 6. Red lines represent the 5% and 95% quantiles, respectively. 153
Figure 8.14. Summary and diagnostic visuals for PLS component 6 regression model parameters. The density plot visualizes the posterior distribution of a parameter. The autocorrelation bar graph represents the correlation or dependency of MCMC draws. The chain mixture or trace plot measures how well the sampler is exploring parameter space..... 154
Figure 8.15. Histogram and kernel density estimate of y-values and match probabilities for PLS component 7. Red lines represent the 5% and 95% quantiles, respectively. 155
Figure 8.16. Summary and diagnostic visuals for PLS component 7 regression model parameters. The density plot visualizes the posterior distribution of a parameter. The autocorrelation bar graph represents the correlation or dependency of MCMC draws. The chain mixture or trace plot measures how well the sampler is exploring parameter space..... 156
Figure 8.17. Histogram and kernel density estimate of y-values and match probabilities for PLS component 8. Red lines represent the 5% and 95% quantiles, respectively. 157
Figure 8.18. Summary and diagnostic visuals for PLS component 8 regression model parameters. The density plot visualizes the posterior distribution of a parameter. The autocorrelation bar graph represents the correlation or dependency of MCMC draws. The chain mixture or trace plot measures how well the sampler is exploring parameter space..... 158

Chapter 1

Introduction

The mass grave designated BA05 (Batajnica 05) was the largest of a series of mass graves excavated during 2002 around Batajnica, Serbia. Some victims were likely killed on site and tossed into the grave, while others were moved from other areas. Some bodies were deposited as tidily packaged bundles and others dumped out of the back of trucks as a jumble of soil, remains and other effects. In an attempt to conceal the crime, those responsible further distorted the remains with fire. In total, 378 cases composed of 289 bodies, 89 body parts, and 594 single disarticulated bones and bone fragments were recovered from 12 different deposits of human remains (Tuller et al., 2008). This complex set of circumstances led to commingling of victim remains. In such situations discrete individuals are not readily apparent. Incomplete, commingled remains preclude full assessment of the biological profile, which may greatly impede identification, illustrating the need for methods that can accurately and reliably reassociate commingled assemblages into discrete individuals.

Methods for reassociating commingled remains are varied, including visual pair-matching (Adams and Kongisberg, 2004), articulation fit (Adams and Byrd, 2006), taphonomic comparisons (Adams and Byrd, 2006), osteometrics (Byrd and LeGarde, 2014; Byrd, 2008; Byrd and Adams, 2003; Rosing and Pischtschan, 1995), age indicators (Schaefer, 2008), and DNA sampling (Hines et al., 2014; Mundorff et al., 2014). Multiple techniques should be used in conjunction to resolve commingling (SWGANTH, 2013). Increased confidence is placed those techniques that are objective and reliable, such as osteometric reassociation, which statistically

evaluates bone dimensions (SWGANTH, 2013).

While an osteometric approach to reassociation is considered objective and statistically superior to visual methods, there are limitations to its current usage in skeletal biology. First, the current approach is based on frequentist inference and does not provide a cohesive way to compare multiple possible matches. Instead, a possible match is assessed independently of other possibilities via a null hypothesis test (Byrd and LeGarde, 2014; Byrd, 2008). Second, osteometric reassociation models rely solely on standard osteological measurements (SOM) for quantifying long bone morphology. Important information concerning limb bone morphology, especially shape, is lost with SOM (Ousley and McKeown, 2001). Shape is useful for investigating relationships in biological structures (Bookstein, 1999), making it a valuable source of information for osteometric reassociation. Third, outside of one exception investigating asymmetry (LeGarde, 2012), the biological basis underlying osteometric reassociation is undeveloped. Incorporating an understanding of long bone development and function into statistical models may enhance the predictive strength of osteometric methods. Predictive strength in this study is assessed through the accuracy of reassociating commingled limb bones. Accuracy is defined as the number of times the predicted match is the correct match divided by the number of comparisons.

Osteometric reassociation comparisons can be divided into four types based on limb bone element(s): homologous (femur/femur), serially homologous (femur/humerus), within-limb and between-limb (Young and Hallgrimsson, 2005). Currently, osteometric reassociation studies have not used developmental and mechanical relationships in limb segments to construct models

to anticipate the structure of limb covariation, and as such, accuracy in reassociation (Byrd and LeGarde, 2014; Byrd, 2008; Adams and Byrd, 2006; Byrd and Adams, 2003). Instead, accuracy in osteometric sorting is tied to the alpha-level chosen by the researcher (Byrd and LeGarde, 2014; Byrd, 2008), leading to the implicit assumption that comparison types are equally accurate. However, this assumption requires explicit testing. Biological theory can be used to inform a hypothesis concerning the accuracy of osteometric reassociation comparison types.

1. Biological theory

This dissertation argues for a biologically informed structure of osteometric reassociation. The deep evolutionary history of the ontogeny of paired appendages and the highly conserved nature of these developmental processes show that limb elements have high levels of covariance (Young et al., 2010). Embryonic limb development, however, does show some degree of independence, both within-and between-limbs, suggesting that this covariance is structured (Capdevila and Belmonete, 2001). Limb elements develop and function together, showing the interplay between development and function in form and providing another influence on the covariation structure of limb morphology. These factors logically lead to the hypothesis that some types of osteometric comparisons should be more accurate than others.

As a living tissue, bone is capable of adapting to its loading environment (Ruff et al., 2006; Lieberman et al., 2004; Frost, 2003, 1996; Curry, 2002; McGowan, 1999). Of these processes of mechanical adaptation, modeling and functional constraint of articulating bone portions should have the most obvious effects on osteometric reassociation accuracy. Modeling serves to change diaphyseal morphology to accommodate loading (Robling and Turner, 2009;

Robling et al., 2006; Frost, 2003; Curry, 2002). Functional cohesiveness of joints keeps gross dimensions of articulating portions canalized against biomechanical loading, instead allowing trabecular architecture to adapt to loading (Lanzenby et al., 2008).

Developmental processes and functional adaptation are used by evolutionary biologists to understand limb covariation structure. The observed patterns of vertebrate limb covariation are understood using the concepts of modularity and integration. Modularity and integration are closely related concepts that seek to explain the processes that lead the observed structure of variance and covariance. Size is the most important overall integrating factor. Standardizing for body size gives a baseline level of covariation. Covariation beyond this baseline are generally structured between homologous elements, within-limbs, serially homologous elements, and between-limbs (Young and Hallgrimsson, 2005). Higher covariation between elements should lead to better predictability and correct decisions regarding osteometric reassociation. Thus, comparison types that have higher covariation between elements should be more accurate.

Humans show differential amounts of functional limb integration during use, with upper limbs being relatively independent compared to lower limb loading during use. Integration and asymmetric use should structure accuracy in osteometric reassociation, with homologous elements (femur/femur) showing the highest levels, followed by within-limb, then serially homologous elements (humerus/femur), with the lowest levels of covariation between-limbs (Hallgrimsson et al., 2002). These biological factors suggest that our ability to resolve commingling through osteometric models is dependent on the type of comparison being made. This ability, however, has not been formally tested.

Within these comparison types, other patterns may emerge. Elements within a limb show differing degrees of developmental modularity (Zeller et al., 2009). The autonomy of within-limb length measurements further supports modularity of bones of the same limb (Auerbach and Sylvester, 2010). Given the trends in development and function, for all comparison types lower limb comparisons should show the highest levels of accuracy, followed by upper limb comparisons. Between-upper limb and-lower limb comparisons should have the lowest levels of accuracy.

1.1. Quantifying limb bone morphology

Landmark-based coordinate data maintain spatial relationships and are a useful approach to characterize shape (Bookstein, 1991). Shape, in this context, is defined as the geometric properties of an element that are invariant to effects of translation, scaling, and rotation (Monteiro et al., 2000). Although allometric shape differences due to size are maintained in size-standardization of landmark data, this form of analysis is bereft of isometric size information. Geometric morphometric analysis (isometrically) size-standardizes data to make changes in landmark positions—or shape changes—comparable. Landmark data are size-standardized by subjecting data to a Generalized Procrustes Analysis (Adams et al., 2013). This analysis superimposes each specimen's configuration of landmarks onto a common coordinate system and derives shape variables known as Procrustes coordinates and a composite size variable, centroid size (Bookstein, 1991). Thus, Generalized Procrustes Analysis simultaneously extracts information on size and shape from landmark data. This form of data has yet to be applied to osteometric reassociation models.

1.2. Bayesian statistics and the osteometric reassociation model

This dissertation seeks to further improve current osteometric reassociation models by using Bayesian statistics to model novel data on long bone morphology. Current methods for osteometric reassociation use frequentist inference. Frequentist inference, however, cannot directly address the primary question of interest: do the elements in question derive from one individual? Bayesian inference can address this question by assigning a probability of correct reassociation. Bayesian inference is based on the theorem proposed by Thomas Bayes (Bayes, 1764) and is generally written as:

$$\text{Posterior Probability} = \text{Likelihood} \times \text{Prior Probability}$$

The prior probability is the chance of an event before considering information from data. Data are incorporated by calculating the likelihood of an event given the data. The likelihood measures the relative strength of the data for a given hypothesis, or in the case of commingling resolution, a correct match. The product of these numbers is the posterior probability, which can be interpreted as the probability of a correct match given the prior probability and the data. When no prior information is available the assumed prior probability is a uniform prior, where all matches are equally as probable.

Beyond inference, this dissertation uses Bayesian modeling, where prior probability distributions are assigned to model parameters. Bayesian regression is used to estimate a distribution of possible match values for a given comparison. Possible matches can be fit against this distribution to arrive at relative match probabilities. This dissertation assesses osteometric reassociation accuracy by simulating a large number (n=1000) of small-scale (n=10) commingled assemblages to see how often the predicted best match is the correct match.

2. Research objectives

In applying biological theory and a Bayesian framework to osteometric reassociation, this dissertation addresses two research objectives:

Provide a biological foundation to osteometric reassociation, centered on the developmental and mechanical relationships influencing limb bone morphology.

Limb covariation structure is the result of the factors above (Young and Hallgrimsson, 2005). The accuracy of osteometric reassociations should closely approximate this structure. A biological foundation will improve our understanding of different types of osteometric comparisons and should help drive decisions in practical applications commingling resolution.

Improve models for osteometric reassociation by incorporating Bayesian statistics and novel information on bone shape and size through geometric morphometric landmark data.

Current osteometric reassociation methodology uses SOM to eliminate possible matches using frequentist inference (Byrd and LeGarde, 2014). While useful, this methodology lacks a means for directly comparing possible matches or incorporating information on bone shape. This dissertation addresses those limitations through Bayesian regression and geometric morphometric landmark data.

2.1. Hypothesis

These research objectives are addressed by testing the following hypothesis:

Accuracy in osteometric reassociation is structured by developmental pathways and functional integration.

Accuracy in element comparison type is arranged in the following order from high to low:

1. Homologous elements

2. Within-limb

    2a. Lower limb comparisons

    2b. Upper limb comparisons

3. Serially homologous elements

4. Between-limb comparisons

    4a. Lower limb comparisons

    4b. Upper limb comparisons

    4c. Upper limb and lower limb comparisons

2.2. Significance of research

Osteometric reassociation, like most practical applications of forensic anthropology, is an inductive process, where specific observations are used to make broader statements concerning an assemblage or case (Boyd and Boyd, 2011; Byrd, 2008). Statistical theory is also inductive, using a sample to make general statements about the characteristics of a larger population. In light of this commonality, it is not surprising that a majority of osteometric reassociation research concerns statistical applications. The scientific method, on the other hand, is deductive, where general processes (theory) inform hypotheses that are tested using samples. In practice, scientific research typically uses both induction and deduction in a self-reinforcing framework of knowledge building (Feyeraben, 1981). This study is deductive, by using biological theory to construct hypotheses concerning the structure of osteometric reassociation accuracy and testing these hypotheses using a sample of discrete individuals. The results of these tests are then applied inductively to make general statements about osteometric reassociation in practice. In

this regard, this study is novel and significant in its use of deduction to incorporate biological theory into our understanding of osteometric reassociation.

Beyond theoretical additions, this study introduces a novel methodology for quantifying long bone morphology through the use of geometric morphometric landmark data. As discussed above, these data provide information on both aspects of limb morphology—shape and size. Geometric morphometric landmark data are a higher fidelity representation of limb morphology compared to SOM, which should improve the performance of osteometric reassociation models.

Lastly, this study introduces Bayesian modeling into osteometric reassociation. This form of modeling has become practical due to the wide-spread availability of Markov Chain Monte Carlo simulation, which explores parameter space to estimate the posterior distribution of a parameter. This process explicitly models uncertainty in variable estimation, allowing for multiple possible matches to be evaluated relative to each other.

3. Chapter organization

Chapter 2 provides a general overview of commingled remains in biological anthropology, discusses factors influencing its analysis and previous research on osteometric reassociation, with a focus on the statistical theory underpinning this research. This chapter further frames the issues introduced in this chapter. Chapters 3 to 5 provide the biological theory used in this study by discussing previous research concerning limb bone ontogeny and ossification, functional adaptation, as well as limb integration and modularity. Chapter 3 starts with a description of long bone growth and ossification, followed by a discussion of the current knowledge of embryonic limb development. This chapter discusses the developmental processes

that link long bone ontogeny and provides the pattern and timing of ossification and gross morphological changes to these bones. Chapter 4 shows how past research has used the concepts of integration and modularity to progress our understanding of phenotypic variation of the limb. Chapter 5 describes the material properties of bone and how bone responds to its loading environment.

Chapter 6 presents the materials and methods utilized in this study. This chapter presents relevant geometric morphometric concepts and provides the justification for the mathematical techniques used to manipulate raw coordinate data into a useable format. Following this presentation is a discussion of Bayesian modeling through Hamiltonian Markov Chain Monte Carlo and Bayesian statistics and how this form of modeling and inference are incorporated into the research design through simulating commingled assemblages. Chapter 7 details the results of reassociating elements from simulated commingled assemblages and provides a step by step example of this method. Chapter 8 discusses the results with regards to the proposed hypothetical structure to accuracy in osteometric reassociation. Chapter 9 gives some concluding remarks and possible future research and application.

Chapter 2

Analysis of Commingled Remains

Commingled assemblages present a situation in osteological analysis where discrete sets of remains are not readily apparent. Commingled assemblages, such as ossuaries, are a fairly common situation in bioarchaeology (Curtin, 2008; Herrmann and Devlin, 2008; Ubelaker and Rife, 2008; Willey and Emerson, 1993; Willey, 1990). With the increasing utilization of forensic anthropologists in arenas such as mass disaster (Mundorff, 2012, 2008; Blau and Briggs, 2011; Sledzik and Rodriguez, 2002; Hinkes, 1989), cremation litigation (Steadman et al., 2008), and human rights investigations (Varas and Leiva, 2012; Primorac et al., 1996), resolution of commingling is becoming commonplace in forensic anthropological analysis (Adams and Byrd, 2014, 2008). The goals of these two subfields in terms of analyzing commingled remains, however, are different. Bioarchaeological analysis typically focuses on population-level inference. The resolution of commingling in bioarchaeological contexts is often limited to reconstructing mortuary practices (Curtin, 2008; Ubelaker and Rife, 2008), or estimating the number of individuals represented for demographic estimates and other inferences of past population lifeways (Willey, 1990; Owsley et al., 1977; Ubelaker, 1974). Forensic analysis of commingled remains, on the other hand, focuses on the individual, where the goal is victim identification and reassociating remains into discrete individuals (Adams and Byrd, 2014, 2008, 2006; Byrd and Adams, 2009, 2003). This focus on victim identification and reassociating individuals has led to an increase in research on methodology for resolving commingling (Adams and Byrd, 2014, 2008).

This study continues this tradition of research by testing a biologically informed structure of osteometric reassociation. To accomplish this aim, this study makes three assumptions. First, the number of commingled individuals is known. Second, all long bones for each individual are represented in the commingled assemblage. Third, all long bones are complete, without fragmentation. These assumptions are rarely, if ever, encountered in practice. This chapter contextualizes the current study by addressing the methodological and analytical considerations for resolving commingling in a forensic context, focusing on osteometric reassociation. Factors affecting the composition of commingled assemblages are first introduced. Then, the process of analyzing commingled assemblages and methods for reassociating elements are provided. The relationship between these two topics is illustrated through two examples. These examples are followed by an in-depth discussion of osteometric reassociation, focusing on limitations of current approaches and highlighting the need for the current study.

2. Factors influencing resolution of commingling

The commingled assemblage simulated in this study represents an optimal situation, in which a small number of known and complete individuals (n=10) comprise the assemblage. This sort of commingled assemblage, where the individuals are known, is referred to as a closed population (Mundorff, 2008). There are several instances of closed population commingled assemblages from forensic contexts, including aircraft crashes with known manifests (Vidoli and Mundorff, 2012; Mundorff, 2008; Adams and Byrd, 2006) and small-scale mass graves (Varas and Leiva, 2012).

Conversely, an open population is when the number and identity of the commingled individuals are unknown. Commingling contexts involving open populations include the South East Asian Tsunami or the Stanton Island ferry crash (Mundorff, 2008). Other commingled assemblages have characteristics of both open and closed populations, such as the September 11th World Trade Center attack (Mundorff, 2008). The airplane passengers and a list of other probable victims were known, however, given the sheer magnitude of the attack, the actual number and identities of the victims in the tower and surrounding area was unknown (Mundorff, 2008). In some cases, such as mass graves from war crimes, circumstantial evidence, such as eye witness testimony, can give the anthropologist an idea of the general demographics and number of individuals represented by the commingled assemblage. Although some information is available concerning the commingled assemblage in these contexts, these commingled assemblages should be considered an open population, because other circumstances including secondary deposition introduces uncertainty into analysis.

Additionally, this study's simulated commingled assemblage represents complete sets of remains with no element fragmentation or missing bones. In authentic commingling situations, the recovery probability for the commingled assemblage is less than 100% (Konigsberg and Adams, 2014). The recovery probability of any assemblage is influenced by taphonomic processes, which result in element fragmentation and loss (Konigsberg and Adams, 2014). Taphonomic processes influencing remains recovery can be either intrinsic or extrinsic. Intrinsic factors are particular to the individual or skeletal element. Factors of this type include overall skeletal and element size, element location (either proximal or distal), bone density, and the

distribution of spongy and cortical bone within an element (Willey et al., 1997). Extrinsic factors derive from outside forces acting on the body. Factors of this type include depositional context, environment (especially soil chemistry), as well as human and other animal activity.

2.1. Why assemblages become commingled

Every commingled assemblage is the result of unique sets of circumstances (Mundorff, 2008). The characteristics of these circumstances influence the degree of commingling and nature of the recovered assemblage. For example, the crash of American Airlines (AA) flight 587 lead to fragmented and distorted human remains scattered across an area approximately 90 by 152m (Vidoli and Mundorff, 2012). Despite the high amount of distortion to the victim's remains, the degree of disaster-induced (Type 2) commingling was low and recovery-induced (Type 1) commingling was moderate (Mundorff, 2008). Additionally, because the flight manifest and victims on the ground were known, the victims of AA flight 587 were considered a closed-population.

As shown through the example of BA05 in Chapter 1, mass graves represent another set of processes where remains become commingled in a forensically relevant situation (Tuller et al., 2008). The remains of this commingled assemblage were considerably more complete than the highly fragmented remains resulting from the AA flight 587 crash, despite some distortion and fragmentation from deposition processes and burning. Unlike the closed-population of AA flight 587, the victims recovered from BA05 ended up in the grave through a nearly impossible to track set of events. Because of this uncertainty, BA05 was considered an open-population.

The complex set of processes leading to the recovered commingled assemblage of BA05 demonstrates the importance of a careful and scientific recovery. A total station and data logger were used to take body points on remains in situ (Tuller et al., 2008). Spatial points were taken on bodies (>=50% present) and body parts (<=50% present) (Tuller et al., 2008). A formula was created that calculated the distance between two points in a 3-D space to produce a list of potential matches, in ranked order. DNA was used to establish matches and compared to the rank order established by spatial analysis. Of 32 DNA reassociated body parts, 88% (28) were first rank (closest together), 6% were second rank, and 3% each for third and fourth ranked (Tuller et al., 2008). Matching body parts were typically much less than one meter apart.

These examples highlight the need for a varied set of methods to resolve commingling. The highly fragmented remains from AA flight 587 limited the utility of many available anatomical methods. Remains recovered from BA05, on the other hand, were relatively complete with recorded spatial relationships between elements. Using the logic of reassociation used in this study and described in Chapter 6, independent information, such as spatial relationships can be combined with anatomical relationships to provide a more comprehensive estimate of reassociation.

3. Methods for resolving commingling

Resolving commingling is a multistage process involving a number of methods. The use and effectiveness of these methods depend on the nature of the recovered assemblage, which is largely the result of factors discussed above. Resolution starts with an inventory of all remains with a focus on keeping provenience information intact (SWGANTH, 2013). After remains are

inventoried, fractured elements are reassociated with each other. Sorting then begins with a hierarchical process of segregating elements by type, side, age, and size (SWGANTH, 2013; Snow, 1948).

3.1. Estimating the number of individuals

In cases of open populations, estimations of the number of individuals represented by the commingled assemblage are required (Konigsberg and Adams, 2014; Adams and Konigsberg, 2008, 2004). Estimation methods have a long history in zooarchaeology as the Minimum Number of Individuals (MNI) and Lincoln Index (LI) (Orchard, 2005; Ringrose, 1993; Allen and Guy, 1984; Grayson, 1981, 1978). The highest number of repeated elements is the MNI. As the name implies, MNI typically provides underestimates of the actual number of individuals and grossly underestimates the number of individuals when recovery probabilities are low (Adams and Konigsberg, 2008, 2004). The LI provides more realistic estimates and is based on capture/recapture method used in living animal populations to estimate size (Adams and Konigsberg, 2008, 2004). First, an initial group of animals is tagged then released. Sometime later another group of animals is caught and the percentage of those animals with tags is assumed to be the percentage in the total population with tags. Since the number of originally tagged animals is known, an estimate of the total population can be easy calculated. This concept can be applied to estimate the number of individuals in a commingled assemblage using paired long bones. Bones from one side of the skeleton are analogous to the initial capture stage. The bones from the other side of the skeleton are analogous to the recapture stage. Left and right sides are then paired (the tagged animals in the recapture). The LI is then calculated as:

$$N = L*R/P \qquad (2.1)$$

where N is the estimated number of individuals, L is the number of left bones of an element, R is the right bones of an element, and P is the number of pairs of that element (Konigsberg and Adams, 2014).

The conceptual basis of the LI has been used to develop methods for estimating the number of individuals represented in human commingled assemblages. These methods include the Grand Minimum Total (GMT) and the Most Likely Number of Individuals (MLNI) (Konigsberg and Adams, 2014; Adams and Konigsberg, 2008, 2004). The GMT is a variation of the MNI and is calculated as:

$$N = L*R-P \qquad (2.2)$$

where the annotation is the same as (2.1). The GMT typically gives higher estimates than the MNI and is more akin to the LI. The LI, however, is sensitive to sample bias from taphonomic processes or recovery practices (Konigsberg and Adams, 2014; Adams and Konigsberg, 2008, 2004). The MLNI accounts for this sensitivity and is calculated as:

$$MLNI = \frac{(L+1)(R+1)}{(P+1)} - 1 \qquad (2.3)$$

where MLNI is the most likely number of individuals and the rest of the annotation is the same as (2.1 and 2.2). Another benefit of the MLNI is the ability to understand uncertainty around this estimate through highest density regions (Konigsberg and Adams, 2014; Adams and Konigsberg, 2008). Highest density regions are conceptually similar to confidence intervals, where the actual number of individuals represented is expect to fall within this region with a particular level of certainty. As an estimation method, MLNI is far superior to MNI or GMT by providing a better

point estimate while expressing uncertainty around this estimate. However, MLNI assumes that the anthropologist is able to reliably identify matching pairs (Adams and Konigsberg, 2004). Thus, MLNI is affected by the condition of remains and the ability of the anthropologist.

3.2. Methods for reassociating commingled remains

After the commingled assemblage is inventoried and sorted and the number of individuals represented is known or estimated, the process of reassociating elements begins. Methods for reassociating elements include visual pair-matching, articulation fit, taphonomic comparisons, osteometrics, and DNA sampling (SWGANTH, 2013). Multiple methods should be used in conjunction to reassociate elements, with an emphasis placed on methods that are objective (Byrd and Adams, 2003).

The importance of accuracy and objectivity in resolving commingling is paramount (Byrd, 2008). Many techniques for sorting commingled remains, however, are subjective and based on the experience of the observer, or do not lend themselves to quantifying the accuracy or confidence of results (Byrd, 2008). Osteometric reassociation is an objective and quantifiable way to reassociate elements by using which uses statistical models to compare bone dimensions (Byrd and LeGarde, 2014; Konigsberg and Frankenberg, 2013; O'Brien and Storlie, 2011; Byrd, 2008; Adams and Byrd, 2006; Byrd and Adams, 2003; Rosing and Pischtschan, 1995; Buikstra and Gordon, 1984; Snow and Folk, 1970).

3.3. Examples of commingling resolution

As mentioned above, every commingled assemblage is unique and the process for resolving commingling is idiosyncratic to the situation. The utility and power of methods for

reassociating commingled remains is dependent on these idiosyncrasies. As the number of individuals and the degree of information loss increases, the complexity and limitations on analysis rapidly rises. This complexity and limits on analysis are shown through two examples.

Adams and Byrd (2006) describe a case of commingling from a military helicopter crash in Vietnam. Two individuals were on board the helicopter when it crashed and the recovered remains were largely complete. This situation is optimal for reassociating remains for several reasons. First, this type of commingled assemblage is considered a closed population. Second, the number of commingled individuals is small and the elements are relatively whole, increasing the power of anthropological techniques. Third, when the number of commingled individuals is two, methodological results that suggest segregation have the same conclusions as those suggesting similarity. Furthermore, in this situation a rust stain from a zipper crossed multiple elements, showing that the remains were articulated at the time of the incident. In most situations, however, taphonomy is regarded as supplemental evidence (Adams and Byrd, 2006).

The commingled assemblage presented by Adams and Byrd (2006) was a case where analysis was straightforward and osteological methods of reassociation were powerful. The World Trade Center disaster, however, was at the opposite end of the logistical spectrum. The disaster claimed 2749 lives (Mundorff, 2008). As of 2006, 20,730 fragments of human remains had been recovered (Mundorff, 2008). Remains were buried under the rubble of seven buildings spread across sixteen acres, with excavations in some areas totaling one hundred and forty vertical feet (Mundorff, 2008). Because of this extreme complexity, methods available for reassociating elements were limited to articulation, anatomic matching, and DNA (Mundorff,

2012). Emphasis was placed on the triage process by creating the correct number of cases (sets of remains) through identifying commingling, sorting remains, and identifying remains that have a high probative value (Mundorff, 2012; Kontanis and Sledzik, 2008). Ultimately, DNA proved to be the best method for resolving commingling and identifying victims (Mundorff, 2008). However, because of the focus on triage, some sets of remains were reassociated using osteological methods, like rearticulating fractured bone portions, allowing for a more complete set of remains and identification using methods like fingerprint analysis (Mundorff, 2008).

These two examples show the extreme variability encountered during commingling resolution, highlighting the need for a diverse set of flexible and reliable methods available to the analyst. Osteological methods for reassociating commingled remains are powerful in situations where the commingled assemblage is a closed population of a few individuals represented by complete elements. This study focuses on osteometric reassociation, an objective and quantifiable method for reassociating commingled remains.

3.4. Osteometric reassociation

Studies on osteometric reassociation test the null hypothesis that the dimensions of two bones are similar enough to have derived from the same individual (Byrd and LeGarde, 2014; Konigsberg and Frankenberg, 2013; Byrd, 2008; Adams and Byrd, 2006; Byrd and Adams, 2003; Rosing and Pischtschan, 1995; Buikstra and Gordon, 1984; Snow and Folk, 1970). These studies exclusively use standard osteological measurements (SOM) to quantify bone morphology and focus on statistical methods for reassociating elements. Rosing and Pischtschan (1995) showed a high incidence of false positives (four of five comparisons) when reassociating foreupper limb

elements by regressing ulna length on radius length. Combinations of radii and ulnae from different individuals plotted closer to the regression line more often than radii and ulnae from the same individual, despite the high correlation ($r = 0.963$) between the two length measurements (Rosing and Pischtschan, 1995). The authors attributed the high degree of error, in part, to the "harsh reduction of the available information" when quantifying bone dimensions using SOM, concluding that osteometric reassociation methods are not useful for re-associating commingled elements (Rosing and Pischtschan, 1995:40). The authors went on to state that three-dimensional bone dimensions should have much more information than SOM in regards to osteometric reassociation. This addition to osteometric reassociation models, however, has not been attempted.

Other studies have been less critical of osteometric reassociation as a method for sorting commingled remains into discrete individuals (Byrd and LeGarde, 2014; O'Brien and Storlie, 2011; Byrd, 2008; Byrd and Adams, 2003; Buikstra et al., 1984). Most of these studies utilize SOM as a means of eliminating possible matches (Byrd and LeGarde, 2014; Byrd, 2008; Byrd and Adams, 2003; Buikstra et al., 1984). An early example of using SOM to test incongruences between bones is by Buikstra et al. (1984). To address whether two vertebrae are from the same individual, Buikstra et al. (1984) use a *t*-test to evaluate the difference between articulating vertebral body measurements. The authors show that the dimensions of the vertebrae are too different to be from the same individual and likely represent two different individuals (Buikstra et al., 1984). While osteometric comparisons did not change the conclusions of subjective methods, including visual articulation comparisons, it provides a quantitative means for

supporting results (Buikstra et al., 1984).

The utility of osteometrics as a means for segregating commingling remains is taken further by Byrd and LeGarde (2014); Byrd (2008); Adams and Byrd (2006); and Byrd and Adams (2003). Through the use of case studies and simulation, these studies demonstrate that commingled limb elements can be reliably segregated when there is considerable size variation between individuals (Byrd and LeGarde, 2014; Byrd, 2008; Adams and Byrd, 2006; Byrd and Adams, 2003). This methodology implies that, because of the broad variation in intra-individual bone size, reassociation of commingled elements is achievable when the assemblage represents a closed population of a few, different-sized individuals (Byrd and LeGarde, 2014; Byrd, 2008; Byrd and Adams, 2003).

The logic of reassociation through elimination was first introduced by Byrd and Adams (2003). This approach starts with adding available SOM for each element and taking the natural logarithm of these sums (Byrd and Adams, 2003). Next, a regression model is estimated from reference data. One element is considered the dependent variable and is regressed on the other element, which is the independent variable.

The decision considering what element is regressed on the other depends on context (Byrd and Adams, 2003). For example, if a commingled assemblage is composed of two left humeri and two left femora, but each humerus is associated with a torso, the researcher is interested in reassociating the femora with the larger collection of elements. Thus, the femora are the dependent variables and the humeri are the independent variables. Such situations are analogous to regressing stature on long bone measurements, because the researcher is interested

in estimating stature from long bone measurements (Byrd and Adams, 2003).

Byrd and Adams (2003) use the 90% prediction interval of the regression equation to test the null hypothesis that the sizes of each bone are consistent with belonging to the same individual. If the actual size of the predicted bone falls outside of this interval, the null hypothesis is rejected. The researcher then concludes the two elements are too different in size to come from the same individual and the bones are segregated. However, if this test fails to reject the null hypothesis, it is not accepted. Rather, if the actual bone size falls within the 90% prediction interval, this result is viewed as evidence against segregation, not as a decision criterion for reassociation (Byrd and Adams, 2003).

The form of decision making used by Byrd and Adams (2003) follows an interpretation of the Neyman-Pearson approach to hypothesis testing, where decisions concerning the null hypothesis are strictly based on whether a test statistic passes an *a priori* threshold value. Buikstra et al. (1984) use this approach, in the form of a *t*-test, to show the lack of congruence between vertebrae. In that case, a *t*-statistic is calculated from the difference between articulating vertebral measurements. This value is compared against a *t*-distribution with the appropriate degrees of freedom, to attain a *p*-value.

The alpha-level (α) is the threshold that the *p*-value must minimally attain to be considered "significant" enough to reject the null hypotheses. Alpha-levels are chosen by the researcher; and as such, they are subjective. An alpha-level is understood by researchers working within the Neyman-Pearson paradigm as their tolerance to be wrong in deciding whether to reject the null hypothesis.

Under the Neyman-Pearson paradigm, the actual *p*-value is irrelevant, only that this value equals or exceeds the alpha-level is relevant (Royall, 2000). The researcher is making a dichotomous decision whether to reject or accept the null hypothesis. Conceptually, under this paradigm, there is no degree of belief in the null hypothesis—the null hypothesis is either rejected or it is accepted (Royall, 2000). The explicit decision-making rational and ease of interpretation of this approach to science has obvious strengths, especially with regard to osteometric reassociation. The elements in question either derive from the same individual or they do not—there are only two possible outcomes (Byrd, 2008).

The Neyman-Pearson approach, however, does have some drawbacks (Byrd and LeGarde, 2014, Byrd, 2008). As stated above, if the actual bone-size measure fell outside of the 90% prediction interval (analogous to $\alpha = 0.10$), it was rejected as a possible match (Byrd and Adams 2003). No attempt was made to interpret how far the actual bone-size measure deviated from the predicted value (Byrd and LeGarde, 2014; Byrd, 2008; Byrd and Adams, 2003). This approach is perfectly suited for reassociating remains from one particular commingled assemblage: a closed-population, composed of two individuals, where one possible match can be eliminated at the chosen alpha-level. If the commingled assemblage represents more than two individuals, however, each possible match must be rejected before elements can be reassociated. Each rejection decision requires an additional statistical test, which increases the chance of Type 1 error, or erroneously rejecting the null hypothesis. These limitations are addressed and models for osteometric reassociation greatly expanded upon by Byrd (2008).

Byrd (2008) provides a more nuanced statistical framework and presents specific

osteometric reassociation models for paired elements, articulating bones, and other element comparisons. Similar to Byrd and Adams (2003), these osteometric models are used to eliminate possible matches. Again, possible matches are evaluated by comparing a *p*-value to an alpha-level (ranging from $\alpha = 0.05$ to $\alpha = 0.10$, depending on the type of comparison) to eliminate possible matches. Byrd (2008) also provides a means for aggregating multiple test results in commingling situations beyond two individual assemblages or when more than two elements are compared.

Paired elements are compared by summing the difference between homologous measurements from the right and left side to arrive at a *D*-value, representing the deviation of left and right side measurements from each other (Byrd, 2008).

$$D = \sum(a_i - b_i) \quad (2.4)$$

where *a* is the right side bone measurement *i*, and *b* is the left side bone measurement *i* for each included measurement (Byrd, 2008). The deviation of this number from zero is divided by the standard deviation of the reference sample and evaluated against the *t*-distribution with two tails to obtain a *p*-value (Byrd, 2008). The null hypothesis assumes no difference between left and right side measurements if both elements belong to the same individual (Byrd, 2008). As the following chapters demonstrate, this assumption is not based on biological reality. Upper limb elements should show directional asymmetry favoring the dominant side due to differential use. Unlike the upper limb, lower limb elements are relatively more integrated and stereotypic during use, eliminating or dramatically reducing asymmetry in left and right measurements.

LeGarde (2012) examined the influence asymmetry on osteometric reassociation,

representing the first systematic use of biological theory on the subject. LeGarde (2012) used SOM and a novel measurement, maximum diameter of the humerus at the deltoid tuberosity, to examine levels of asymmetry in the humerus, radius, and femur. Using a biologically informed research design, LeGarde (2012) tested the assertion that levels of asymmetry should be greater in the humerus and radius when compared to the femur. Asymmetry was defined as a significant difference ($\alpha = 0.10$) in left and right side *D*-values. LeGarde (2012:33), however, reversed left (*a*) and right bone (*b*) measurements in her calculation of *D* when compared to Byrd (2008), without explanation. Reversing left and right measurements leads to mirror-image distributions of *D*-values compared to those expected from Byrd (2008). A negative mean for *D*-values suggests a left-side bias for Byrd (2008) and a right-side bias for LeGarde (2012).

Overall, the results of LeGarde (2012) followed expectations from biomechanical theory. Roughly 50% of the test sample (75 of 151 individuals with known handedness) showed some significant form of bilateral asymmetry (LeGarde, 2012). Of the total sample (239 individuals) 49 individuals had significant asymmetry of the humerus, with 37 showing only humeral asymmetry (LeGarde, 2012). Thirty-eight individuals showed radial asymmetry, with 23 individuals exhibiting only radial asymmetry (LeGarde, 2012). These results suggest that proximal elements have a more asymmetric response to loading than distal elements. Interestingly, only nine individuals exhibited both humeral and radial asymmetry, suggesting a decoupling of osteogenic response between the humerus and radius (LeGarde, 2012). As expected, the femur showed the lowest amount of asymmetry and only 8 of 152 individuals were significantly asymmetric (LeGarde, 2012).

The distribution of *D*-values for the humerus (four measurements, n = 147) was a mean of -1.5427 and a standard deviation of 3.61595, and for the radius (three measurements, n = 221), a mean of -.3078 and standard deviation of 1.26604, and a mean of 1.0789 with a standard deviation of 3.9084 for the femur (maximum length only, n = 152) (LeGarde, 2012). These distributional properties of *D*-values suggest that expecting no difference between paired elements, as tested by the null hypothesis, is a flawed expectation and not supported by biology or empirical results. This criticism, however, may have little practical consequence. When LeGarde's (2012) sample was applied to the paired element osteometric reassociation model of Byrd (2008), the Type 1 error rates ($\alpha = 0.10$) were almost exactly as expected, with mean errors of 10% for the humerus models, 11.25% for radius models, and 6.3% for femur models, with 9.2% overall error (Byrd and LeGarde, 2014).

Despite paired element models preforming close to expectations, the results of LeGarde (2012) suggest there is room for improvement. For example, Byrd and LeGarde (2014:170) state: "Models for comparison of right- and left-paired bones were developed that emphasize shape." Shape, in this context, is not defined and it is unclear how these models emphasize shape information available in SOM. Shape information available in SOM is made clear by Jantz and Ousley (2005). Shape differences between bones expressed by SOM are represented by a combination of smaller and larger values for homologous measurements, shown by the '+' and '-' in Table 2.1 (Jantz and Ousley, 2005).

Table 2.1. A comparison of cranial measurements of an unknown skull to the mean values of four reference samples in FORDISC 3. Differences between the unknown skull and group means are highlighted by the red box and are represented by '+' and '-', where the measurement is large r or smaller than the group means, respectively. Measurements that deviate one to two standard deviations away from the group mean are shown by '++' or '--'. Adapted from Jantz and Ousley (2005), FORDISC Help File version 1.35.

			Group Means			
			BF	BM	WF	WM
Example 2		Chk	67	99	173	286
AUB	126	+	115.6	120.6	116.8	123.2
BBH	138		131.5	137.7	134.2	141.7
BNL	94	--	98.6	104.5	99.2	106.2
BPL	96		99.0	104.3	92.2	98.2
DKB	20	-	22.5	23.6	19.9	21.2
FRC	108	-	108.1	112.9	109.2	114.7
GOL	168	--	178.3	186.9	177.5	188.1
MAB	67	+	62.7	66.2	58.1	61.5
MAL	53		56.0	58.0	51.1	54.4
MDH	25	-	28.1	32.5	27.6	32.4
NLB	26		25.0	26.2	22.5	23.8
NLH	54	+	48.2	52.5	48.9	52.9
OCC	94	-	97.3	98.4	97.7	100.9
PAC	114		112.6	117.3	112.6	118.3
UFHT	71		66.9	72.6	66.8	71.8
WFB	94		93.2	96.1	93.9	96.9
XCB	144	+	133.0	135.5	135.6	140.2
ZYB	138	++	121.9	130.5	120.7	129.7

The formula for calculating the *D*-value for paired elements subtracts left side measurements from the right side and sums these differences (see equation 2.4). Shape differences between paired elements, where some measurements are higher and some lower, will at least partially cancel each other out, leading to deflated *D*-values and two bones appearing more similar than they are. Thus, shape differences, as expressed by SOM, add noise to and possibly inflate Type 2 error rates of paired element models. This issue could be eliminated by summing the absolute value of the difference between left and right side measurements. The absolute difference between measurements would also eliminate the effect of handedness, where left-handed individuals should have negative and right-handed positive *D*-values.

Articulating bones are compared using a similar logic as paired elements (Byrd and LeGarde 2014, Byrd 2008). This model follows the approach of Buikstra et al. (1984), where articular breadth measurements are subtracted from each other and this value is divided by the standard deviation of the reference sample and evaluated against the two-tail *t*-distribution to obtain a *p*-value.

$$D = c_i - d_j \qquad (2.5)$$

where measurement *i* of bone *c* is subtracted from measurement *j* of bone *d* (Byrd, 2008). The deviation of this number from the reference sample mean is divided by the reference sample standard deviation to arrive at a *t*-statistic, which is evaluated against the *t*-distribution with two-tails to obtain a *p*-value (Byrd, 2008). Unlike paired element comparisons, a more conservative alpha-level of 0.05 is suggested for articulating elements (Byrd, 2008).

Other elements comparisons follow the regression method described by Byrd (2008).

Unlike Byrd (2008), which used the 90% prediction interval as the criterion for evaluating the null hypothesis, a *t*-value is derived from the deviation of the actual bone-size value from the predicted value using an equation modified from the confidence interval model provided by Giles and Klepinger (1988) (Byrd, 2008). Similar to other comparisons, this *t*-value is evaluated against a two-tail *t*-distribution to obtain a *p*-value.

As mentioned above, reassociating elements through eliminating other possibilities becomes more difficult and subject to Type 1 error as the number of individuals represented in the commingled assemblage increases. In such circumstances, a course of action—the final decision on reassociation—requires many decisions based on independent statistical tests. To circumvent this limitation, Byrd and LeGarde (2014) and Byrd (2008) advocate the use of an omnibus statistic, which sums the negative logarithm of each p-value in the domain of a course of action, with sign reversed.

$$O = \sum - \ln(pi) \qquad (2.6)$$

where *p* is the *p*-value of the *i*th test (Byrd, 2008). The *p*-value associated with the omibus statistic is an aggregate of all tests within a course of action (Byrd, 2008). A course of action is chosen if it is the only one that cannot be eliminated as a possible course (Byrd, 2008).

Further building a statistical framework for osteometric reassociation, Byrd (2008) introduces the severity principle. Severity, as a concept, focuses on identifying and mitigating error in decision making (Mayo and Spanos, 2009). The researcher makes a decision concerning the null hypothesis based on observing the output of a statistical test. A researcher feels confident in his or her decision concerning a hypothesis if the test used has a high chance of

detecting the falsity of the hypothesis (Mayo and Spanos, 2010). Tests of the hypothesis are based on statistical models. Statistical models are mathematical representations of experimental data, generalized from probability distributions. Thus, the concept of severity encompasses the hypothesis, the test used to assess the hypothesis, and the data used to generate the model on which the test is based (Mayo and Spanos, 2010). Severity is formalized as 1-*p*, where *p* is the *p*-value for a particular test (Byrd, 2008). Formalized severity offers nothing novel to analysis; it is simply a clever work-around for interpreting a *p*-value as a measure of belief in a course of action.

The introduction of the omnibus statistic and the severity principle into the statistical framework of osteometric reassociation by Byrd and LeGarde (2014) and Byrd (2008) represents a significant change in interpretation from Byrd and Adams (2003).

> "Byrd and Adams (2003) originally proposed the use of the prediction interval of a regression model as a basis for the test, where all case values falling outside the prediction interval were rejected. This Neyman-Pearson-type approach to hypothesis testing requires one to choose the prediction interval value (90% or 95%) in advance and then react only to whether the case values fell within or outside the interval. This approach has some notable limitations. First, it ignores important information, such as how far outside the interval a set of case specimens fall. If their test value was within the prediction interval, was it close to the boundary or near the value expected under the statistical model? Second, the original approach provides no objective method of assessing the family of result that are obtained when more than two bones are included in a test or when results of multiple tests must be evaluated. The method of hypothesis testing is redirected here to a form more in line with Fisher's (1958, 1959) significance testing (Byrd, 2008:208)."

This interpretative shift blends two distinct forms of testing statistical hypotheses—Neyman-

Pearson hypothesis testing and Fisherian significance testing (Lew, 2013; Royall, 1997). These approaches have two different purposes: the former sets an *a priori* criterion (alpha-level) for decided between two competing hypotheses, the latter attempts to interpret the strength of evidence against the null hypothesis. In short, a hypothesis test is not a significance test (Lew, 2013; Royall, 1997). A significance test results in a *p*-value, where a hypothesis test results in a decision. Most contemporary frequentists, however, blend these two forms of hypothesis testing into a third formulation called rejection trials (Royall, 1997). Rejection trials use an *a priori* alpha-level as a decision making criterion, similar to the Neyman-Pearson approach. The *p*-value, however, is subjectively interpreted by the researcher as a measure of the strength of evidence against the null hypothesis (Royall, 1997).

While this shift towards including additional information into the decision making process increases subjectivity, it also increases rationality. As stated above, the decision to reassociate a set of remains should be based on multiple lines of evidence, of which osteometric reassociation is just one. Incorporating multiple lines of evidence into a decision is a subjective process, based, in part, on the experience of the researcher. Thus, to a researcher tasked with making a decision to reassociate remains, it matters if a *p*-value from an osteometric reassociation test is 0.049 or 0.000001—the latter is much stronger evidence against the null hypothesis than the former. A *p*-value, however, is just one metric for quantifying evidence from osteometric reassociation models.

Konigsberg and Frankenberg (2013) criticize the use of *p*-values and the frequentist approach in general, because it violates the likelihood principle. The likelihood principle asserts

that inferences from an experiment should be based on the actual observations; other possible outcomes are irrelevant. In the commingling context, the researcher makes decisions based on observed bone relationships. Hypothetical, more extreme versions of bone relationships do not matter. Because a *p*-value represents the frequency of computing a test statistic as extreme or *more extreme* given that the bones are from the same individual, it is inappropriate for the assessment of commingled remains from closed-population contexts (Konigsberg and Frankenberg, 2013. Konigsberg and Frankenberg (2013) suggest a Bayesian framework for osteometric reassociation, which compares competing hypotheses (possible matches) directly to one another.

One way to operationalize the Bayesian approach is to assign relative probabilities to competing hypotheses, based on either prior information or assigning each hypothesis an equal probability (Byrd and LeGarde, 2014; Konigsberg and Frankenberg, 2013). Prior probabilities are multiplied by the likelihood based on the data to obtain a posterior probability (Byrd and LeGarde, 2014; Konigsberg and Frankenberg, 2013). This approach has the advantage of comparing all possibilities in one model, unlike a frequentist approach that requires a test for each hypothesis and another test to compute an overall *p*-value. A major limitation to a Bayesian approach is the inappropriate or subjective use of prior information to inform prior probabilities of possible matches.

Beyond possible matches, prior probability distributions can also be assigned to the parameters used in estimating the model, such as the slope and y-intercept in linear regression. Using a Bayesian approach outlined in Chapter 6, these prior distributions are used along with

the likelihood function based on the data to explore parameter space to arrive at a posterior distribution for each model parameter (Kery, 2010; Lynch, 2007). This approach explicitly treats model parameters as distributions, instead of point values. This treatment is a major difference between frequentist and Bayesian modeling.

Models are required to make sense of scientific observations or systems of processes. Statistical models are written in the language of mathematics and they are independent from the mode of inference used to analyze them (Kery, 2010). For example, the form of modeling used in this study, linear regression, is neither inherently Bayesian nor frequentist. These paradigms differ mainly on their definition of probability, or understanding uncertainty, and learning about parameters in stochastic systems (Kery, 2010; Mayo and Spanos, 2009; Lynch, 2007).

Common to both paradigms, data are understood as the observed manifestation of stochastic systems (Lynch, 2007). These paradigms differ on how they view parameters—the quantities used to describe these random processes. Frequentists view parameters as fixed and unknown measures (Kery, 2010; Mayo and Spanos, 2010). Bayesians, on the other hand, view parameters as unobserved realizations of random processes, or in other words, distributions (Kery, 2010).

4. Summary

Commingled assemblages in a forensic context vary widely in terms of size and composition of element completeness and representation. A diverse, flexible, objective, and reliable set of methods, used in conjunction, is needed for resolving various commingling

situation. Of these methods, osteometric reassociation is generally accepted as both objective and reliable (SWGANTH, 2013).

Studies concerning osteometric reassociation have largely focused on the statistical interpretation of osteometric reassociation models based on SOM. Outside of one notable exception (LeGarde, 2012), this focus has left the biological foundation of the accuracy in osteometric reassociation largely unexamined. Additionally, the exclusive use of SOM as a means for quantifying limb bone morphology has left other avenues for quantifying long bone morphology unexamined.

Chapter 3

Limb Ontogeny

This chapter focuses on how developmental pathways of limb bones structure morphological relationships. This discussion begins with the embryonic development of the vertebrate limb. Various interrelated genes and molecular signals determine this development, with some limb elements sharing more developmental commonalities than others (Zeller et al., 2009). Next, a general description of long bone ossification is given, with particular focus on morphological change though out ontogeny. The ontogenetic relationships between limb elements and surrounding tissues are important to understand how limb bones covary. Muscle mechanics, for example, influence limb bone development during all stages of ontogeny, showing the interplay between development and function in form (Cowgill, 2007).

1. Embryonic development of the mammalian limb

The general body plan of a vertebrate embryo is defined early in development, around 13 days of prenatal life in humans with the development of the primitive streak, a structure that establishes bilateral symmetry (Klingenberg, 2008; Scheuer and Black, 2004; Karensty, 2003; Mariani and Martin, 2003; Capdevila and Belmonte, 2001; Shubin et al., 1997). The embryo subdivides into secondary fields through a multistep process where cells in a region are defined. Then, signaling centers provide positional cues that are transcribed on a cellular basis, forming a primordium, or the earliest recognizable stage of organ and tissue development (Johnson and Tabin, 1997). Limb primordium is a consolidation of embryonic cells that bud out from the lateral plate mesoderm and interact with mesenchymal cells enveloped in an ectodermal jacket

(Capdevila and Belmonte, 2001; Rabinowitz and Vokes, 2012). The limb is organized by contributions of the lateral plate, which form bone, cartilage and tendons, and somatic mesoderm, which form muscles, nerves and vessels, to create the limb bud (Johnson and Tabin, 1997).

Pattern formation and the anatomical regions involved are highly conserved in most vertebrates, including mammals, and are controlled through signaling and patterning genes (Rabinowitz and Vokes, 2012; Capdevila and Belmonte, 2001; Johnson and Tabin, 1997). The conservative nature of embryonic development is why such a wide array of mammals (and vertebrates in general) have a similar overall body plan (Karensty, 2003). The large amount of phenotypic diversity in mature limb form is due to differential expression and molecular interactions mediated by realizator genes (Capdevila and Belmonte, 2001; Johnson and Tabin, 1997). Homologous elements have the exact same developmental programs expressed on opposing side of the embryo (Karensty, 2003; Capdevila and Belmonte, 2001), with early morphological difference between these elements the result of mechanical interactions (Cowgill, 2007). Thus, homologous elements should have the highest accuracy in osteometric reassociation. Upper limb and lower limb developmental programs are nearly identical, separated by location, timing, and the expression of certain HOX and T-box genes (Karensty, 2003; Capdevila and Belmonte, 2001). The similarity in the developmental programs of serially homologous elements is second only to homologous elements, which may lead to a similar structure in accuracy in osteometric sorting. Limb development, however, is complex. The next sections highlight some of these important complexities for understanding accuracy in

osteometric sorting.

1.1. Limb bud development

Limb development is characterized by the initiation of limb development, establishment of developmental axes and outgrowth and patterning along these axes (Rabinowitz and Vokes, 2012). Two anatomically distinct structures of the limb bud drive these processes: the apical ectodermal ridge (AER) and zone of polarizing activity (ZPA) (Figure 3.1). These structures are associated with two major axes of outgrowth: the proximal/distal (P/D) and anterior/posterior (A/P), for the AER and ZPA, respectively (Karsenty, 2003; Capdevila and Belmonte, 2001; Johnson and Tabin, 1997).

Beginning around the fourth week of development, mesenchymal cells proliferate from the lateral plate mesoderm at positions along the embryonic axis coordinated by Hox gene expression (Zeller et al., 2009). In humans this process begins for the upper limb at stage 12, or 30 days of prenatal life, adjacent to the seventh to twelfth somites (Scheuer and Black, 2004). The lower limb begins a few days later during stage 13, or 32 days of prenatal life, adjacent to the 25^{th}-29^{th} somites (Scheuer and Black, 2004). These cellular proliferations create a bulge underneath the surrounding ectodermal cells, forming an ectodermal pocket that is the limb bud (Zeller et al., 2009; Johnson and Tabin, 1997). Differences between the upper limb and lower limb are evident at this beginning stage of limb bud development, where molecular and genetic factors affecting the upper limb are absent in the lower limb (Tzchori et al., 2009).

The AER, formed by ectodermal cells, is located at the distal tip of the limb bud (Figure 2). The AER is a major signaling center, producing many molecules important to limb

development and is the primary signaling center for P/D axis outgrowth (Rabinowitz and Vokes, 2012; Zeller et al., 2009). The FGF gene family, produced mainly by the AER, encodes crucial signals during early development in the epithelial mesenchyme and progenitor pool specification (Zeller et al., 2009). The element identity of these progenitor pools are specified by the AER in a P/D fashion. The opposing activities of P/D axis specification of retinoic acid in the proximal limb and AER-derived FGFs in the distal limb is known as the two-signal model (Mercader et al., 2000). These differing signaling factors suggest a degree of autonomy between proximal and more distal elements within a limb. Given that these factors are identical across limbs, this finding suggests that development factors may lead to higher reliability in osteometric sorting between homologous and serially homologous elements when compared to elements within a limb.

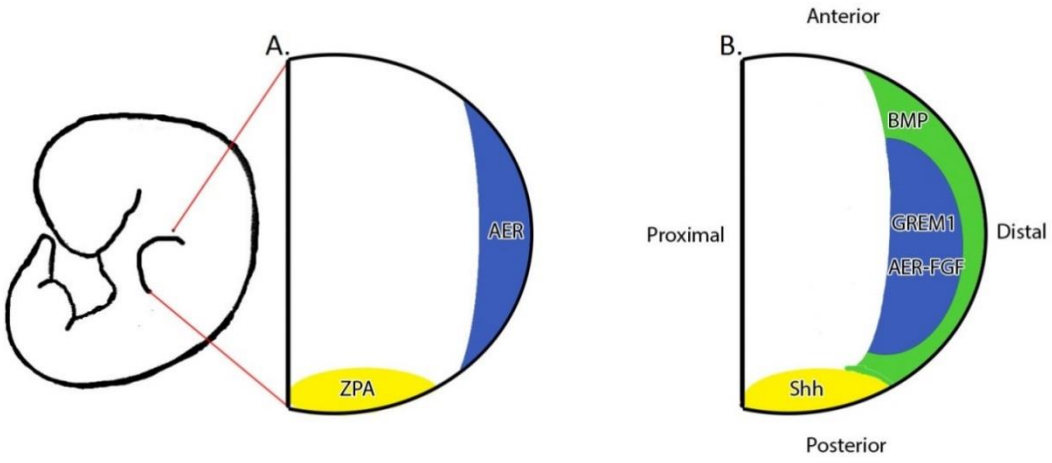

Figure 3.1.The Limb Bud. A. The location of the Apical Ectodermal Ridge (AER, in blue) and Zone of Polarizing Activity (ZPA, yellow). B. The expression location of major genes in limb development. Modified from Zeller et al. 2009, Figure 3.

The ZPA is a collection of mesenchymal cells located on the posterior portion of the limb bud that is responsible for establishing the A/P axis (Rabinowitz and Vokes, 2012; Zeller et al., 2009). The ZPA secretes the SHH morphogen, which diffuses across the posterior limb bud to establish a spatial and temporal gradient of SHH signaling (Rabinowitz and Vokes, 2012). The formation of the A/P axis suggests a different patterning to a developmentally-driven structure of osteometric sorting reliability when compared to the P/D axis. Unlike factors affecting P/D axis formation, which in part segregates elements into proximal and more distal domains, A/P factors differentially affect the ulna and tibia, with similar factors influencing the humerus and femur as well as the radius and fibula. It is worth noting, however, that the cell identities are not determined during this stage. Cellular identities are determined during the next stage of limb development: the expansion, determination and differentiation phase.

During the expansion, determination and differentiation phase of limb bud development, mesenchymal cells in the center of the limb bud condenses into a preskeletal blastema, consisting of cartilage precursors surrounded by precursor cells for muscles and tendons (Al-Qattan et al., 2009). The center of the blastema differentiates into either chondrocytes or osteoblasts (Al-Qattan et al., 2009). The type of differentiation depends on the form of ossification that the limb element ultimately will undergo. A large majority of the limb is formed thorough endochondral ossification, which begins with blastema differentiation into chondrocytes, forming the cartilage template. Only the blastema that form the distal phalanges differentiate into osteoblasts via intramembranous ossification (Al-Qattan et al., 2009). The process of chondrification begins in

the upper limb at 36-38 days of prenatal growth and slightly later in the lower limb at 41-44 days of prenatal growth (Al-Qattan et al., 2009; Scheuer and Black, 2004).

2. Limb bone ossification

The embryonic development of the limb produces a largely avascular cartilage template. The ossification process of this cartilaginous template is known as endochondral ossification. This form of ossification is distinguished from intramembranous ossification, where bone forms from direct transformation of a highly vascular membrane (Scheuer and Black, 2004). Limb bone ossification results in an element composed of two types of structurally distinct bone: trabecular and cortical bone. Trabecular bone is found in the metaphyses and epiphyses of long bones and has a large surface area. Trabecular bone is highly vascular and plays a major role in metabolic activity. In youth, trabecular bone begins as primary spongiosa, which are simple, randomly oriented cylindrical struts, roughly 0.1mm in diameter and 1 mm in length. During growth, primary spongiosa are replaced by secondary spongiosa. Secondary spongiosa are typically thicker than their primary counterparts, often connected by sheets of bone, and have differing orientations depending on the location within the bone (Curry, 2002). Randomly oriented cylindrical struts are found toward the diaphysis, away from loading surfaces. The number of sheet-connections and the organization of the struts increase the closer the spongiosa are to the joint surface. These spongiosa appear more organized in joints where the loading regime is relatively constant. Trabecular bone is more pliable than compact bone and gives bone its toughness, allowing joint surfaces to absorb compressive force and transfer it towards the diaphysis (Curry, 2002).

Cortical bone forms the outer surface of joints and nearly the entire diaphysis. Cortical bone is solid with only space for blood vessels and channels connecting mature bone cells. Cortical bone gives bone its strength, or ability to resist deformation during loading. In humans, cortical bone is arranged in concentric lamellae that alternate in thickness, typically between 2-6 μm thick (Curry, 2002).

Long bone ossification starts through perichondral ossification where osteoprogenitor cells differentiate into bone-forming cells, called osteoblasts, which surround the center of the diaphysis. Osteoblasts are bone-forming cells and can have two different fates. Some osteoblasts flatten and become bone-lining cells. Bone-lining cells cover the four bone envelopes: periosteal, endosteal, haversian, and trabecular (Frost, 2003; Curry, 2002). Bone-lining cells also line the blood channels in bone that control the movement of ions between the body and bone (Curry, 2002). Osteoblasts that do not become bone-lining cells deposit osteoid. Some osteoblasts work together with osteoclasts, which are bone destroying cells, in a collection of cells called the basic multicellular unit (BMU) to turnover bone, creating harversian systems, or osteons (Figure 3.1 and 3.2). Osteoblasts secrete osteoid, which is then mineralized into bone. The process of osteoid deposition and mineralization leads to osteoblasts becoming entombed in spaces called lacunae, becoming osteocytes. The roll that osteocytes play in sensing and transmitting biomechanical information is discussed in Chapter 4.

While the cartilage template is avascular in the early stages of perichondral ossification, the perichondrium is not. Osteoblasts surround this vascular network and begin to secrete osteoid, forming the periosteal bone collar (Scheuer and Black, 2004). Bone collar formation is

coupled with chondrocyte hypertrophy and matrix vesicle formation in the template underneath the bone collar. These matrix vesicles release calcium hydroxyapatite crystals, leading to the initial calcification of the template. Vascular invasion continues through the bony collar, providing blood supply to the cartilage template as well as leading to osteogenic invasion and the formation of the marrow cavity (Scheuer and Black, 2004). At this stage, intramembranous and endochondral ossification has begun at the bone collar.

After the primary center of ossification begins to develop, the cells at the ends of the template begin to hypertrophy and matrix vesicles form. This hypertrophy is followed by vascular and osteogenic mesenchyme invasion (Scheuer and Black, 2004). Bone formation at the epiphyses is true endochondral ossification, where bone is laid down directly on the cartilaginous template.

After the formation of the primary center of ossification and the hypertrophy of the epiphyseal chondrocytes, the metaphysis, or growth plate, forms between these two regions (Scheuer and Black, 2004). The metaphysis is primarily responsible for longitudinal growth but also has a role in appositional growth. The metaphysis has four zones of cellular development: the germinal zone, proliferation zone, zone of cartilage transformation, and zone of ossification (Scheuer and Black, 2004). While the metaphysis is positioned between the epiphysis and diaphysis, cellular hypertrophy and metamorphosis occurs towards the diaphysis. In the germinal zone, which is positioned closest to the epiphysis, chondrocytes are small and randomly distributed, receiving vascular supply from the epiphyseal vessels that penetrate the region between the epiphysis and metaphysis called the terminal plate (Scheuer and Black, 2004). In

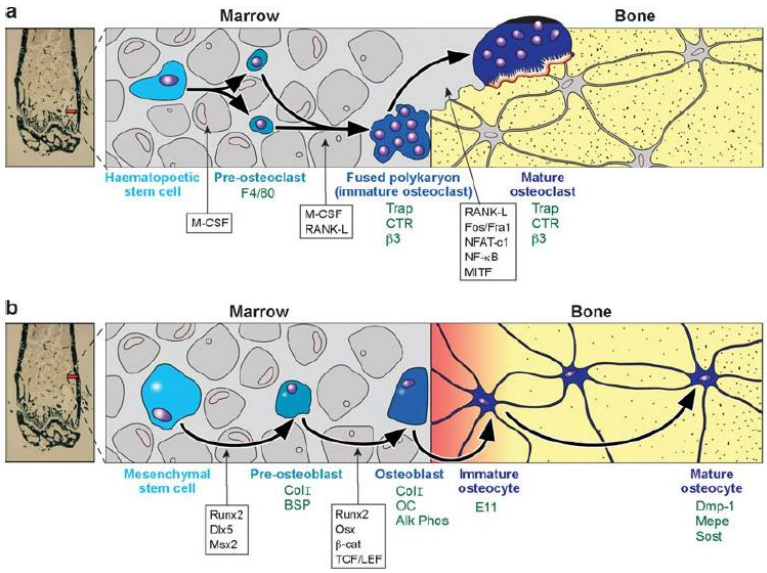

Figure 3.2. The osteoclast (a) and osteoblast (b) lineage. From Robling et al. (2006) Figure 3.

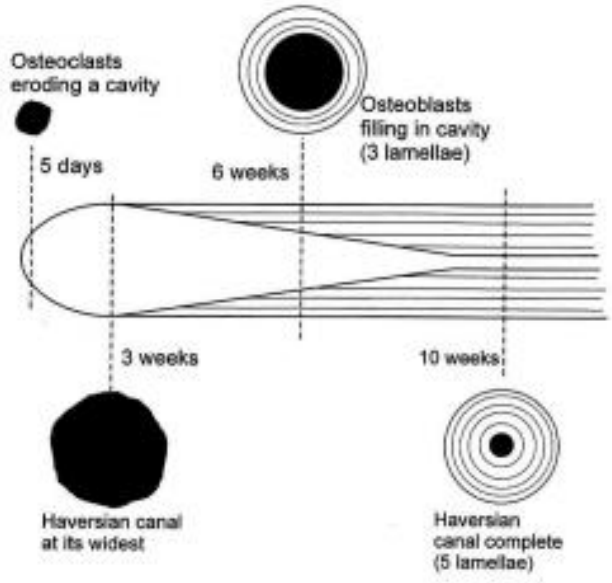

Figure 3.3. Diagram of the formation of a Haversian system (osteon) via bone turnover from the BMU. From Curry 2002 Figure 1.2.

the proliferative zone, adjacent to the germinal zone, chondrocytes hypertrophy then mitotically divide and develop into wedge-shapes and align along their narrow edges in columns (Scheuer and Black, 2004). Chondrocytes continue to hypertrophy as they progress towards the zone of cartilage transformation. This phase of continued hypertrophy that began in the proliferative zone may be considered a separate zone, known as the zone of hypertrophy (Junqueira and Carneiro, 2005). In the zone of cartilage transformation, matrix vesicles begin to deposit hydroxyapatite as chondrocytes begin to degenerate and the metaphyseal sinusoidal loop advances vascular invasion (Scheuer and Black, 2004). In the zone of ossification, osteoblasts differentiate from stromal cells and begin to lay down bone on the mineralized cartilage formed in the zone of cartilage. A similar set of cellular processes observed in the metaphysis also occur in the epiphysis. At the epiphyses, trabecular bone is formed through chondrocyte hypertrophy, multiplication, organization, and ossification starting with the germinal zone towards the perichondrium and ending with primary spongiosa formation towards the center of the epiphysis (Scheuer and Black, 2004).

While general bone form is under genetic control, bone obtains its shape, size, and integrity through biomechanical influence (Frost, 1996; Lee and Frost, 1992). Primary spongiosa are remodeled into thicker and more organized secondary spongiosa through microdamage triggers (Frost, 1996). Biomechanical influences are also responsible for the shape differences between the epiphysis and diaphysis. The epiphysis of long bones is wider than the diaphysis for two reasons: to help disperse the large biomechanical loads encountered at the joint and to accommodate joint cartilage. Cartilage is inferior to trabecular bone in terms of loading

potential. The same load requires roughly four times the amount of cartilage in relation to bone (Frost, 1996).

Towards the diaphysis, loads are focused on the cortical bone. This focus is accomplished through trabecular bone remodeling and inwaisting from modeling, where bone is removed from the periosteal surface and deposited on the endosteal surface, giving the diaphysis its shape (Frost, 1996). Inwaisting and appositional growth appear to be opposing mechanisms because each occurs from osteoblastic and osteoclastic activity on the endosteal and periosteal surfaces, but in opposing patterns. These mechanisms serve different roles. Inwaisting focuses biomechanical loads from the epiphysis to the diaphysis; giving long bones there shape. Appositional growth serves to maintain bone integrity (resist buckling) during longitudinal growth.

The process of long bone ossifications demonstrates interactions between development, surrounding tissue, and mechanical influence in shaping long bone morphology. The genetically-controlled general morphology is molded by its mechanical environment and the necessity to accommodate other tissue, such as cartilage and muscles. These processes are necessary to maintain functional integrity of long bones, suggesting a feedback mechanism between mechanical regime and ontogeny in the shaping long bones (Ruff, 2000). Thus, while the initial process of limb development shows various levels of autonomy between elements within a limb, the interplay of growth and mechanical regime influencing form and function suggests that within-limb covariation should increase during ontogeny as a result of these factors.

3. Limb bone ossification: Timing and morphological change

This section describes the ossification process of the limb elements included in this study, extending beyond embryonic development and covering post-natal ontogeny. Included in this section is the timing of primary and secondary centers of ossification, location of nutrient foramina, and shape changes during ontogeny. This discussion informs accuracy in osteometric reassociation by giving specific context to changes and relationships between elements that should be relevant to accuracy in osteometric sorting. For example, some of the landmarks used in this study assess diaphyseal shape at the nutrient foramen (see Chapter 6). If the placement of the nutrient foramen on the diaphysis between paired elements is highly variable, this will reduce accuracy in osteometric reassociation for homologous elements.

Generally speaking, females mature skeletally faster than males. If possible, sex-specific times for fusion and ossification are given. When general age ranges are given, males tend to be towards the upper end and females the lower-end of the age range. Unless otherwise noted, all information is from Scheuer and Black (2004).

3.1. Humerus

The humerus is first identifiable as a mesenchymal consolidation at 38 prenatal days. Chondrification begins around 38-41 days and most of the major features of the bone are identifiable by 53 days. The primary center of ossification appears histologically at seven weeks. Roughly 88% of fetuses have an anteriorly placed primary nutrient foramen at midshaft, with accessory foramina usually placed posteriorly (Skawina and Wyczolkowski, 1987). The positioning of the nutrient foramen appears to be dynamic, as the primary nutrient foramen is often anteromedial, slightly below midshaft at birth. There is also marked humeral torsion

around birth, but this torsion is restricted to the junction of the diaphysis and proximal epiphysis. Torsion decreases throughout ontogeny, reaching adult levels around 18 years old (Cowgill, 2007). Adult torsion, however, is population specific, likely due to differences in activity patterns, further showing how mechanical influences during ontogeny shape limb bone morphology (Cowgill, 2007).

At around three years of age, the proximal metaphyseal surface begins to change to accommodate the shape of the proximal epiphysis. These metaphyseal changes continue into puberty with the development of a process on the posterolateral diaphyseal boarder that articulates with the posterior notch of the compound proximal epiphysis. Around one year, the radial fossa develops, followed by the development of the deltoid tuberosity around four to six years.

Table 3.1 provides the timings for the appearance and fusion of the secondary centers of ossification of the humerus. By birth, roughly 80% of the humerus is ossified, with small main proximal and distal secondary epiphyses. The ossification of the humeral head, however, is highly variable and may not begin to ossify until six months. Similar to the appearance of the humeral head, the ossification of the greater tubercle is also variable, ranging from three months to three years after birth. However, the most common time frame for the appearance of the greater tubercle is one to two years. Additionally, there is debate whether the proximal epiphysis ossifies from two or three centers. A separate ossification center for the lesser tubercle may be a product of convention, as many anatomy texts mention three separate centers, but most radiological studies show only two distinct centers. If the lesser tubercle does appear as a

separate center, it fuses quickly with the humeral head and the proximal epiphysis is a single compound epiphysis by five to seven years of age. Because the proximal epiphysis is the growing end of the bone, accounting for 80% of longitudinal growth, fusion corresponds to the end of growth.

The distal epiphysis forms from four separate centers of ossification. The capitulum is the first to appear between six months and two years. The medial epicondyle is next to appear, by the fourth year, followed by the trochlea by year eight. The lateral epicondyle is the last to begin ossification at 10 years old. Soon after the appearance of the lateral epicondyle, the capitulum, trochlea, and lateral epicondyle form a single compound epiphysis at around 10 years in females and 12 years in males. Unlike the proximal epiphysis, this compound epiphysis quickly fuses to the distal diaphysis. The medial epicondyle is the last to fuse to shaft and the timing of this fusion is variable from 11-15 years in females and 12-17 in males.

Table 3.1. The appearance and fusion times for the secondary ossification centers of the humerus. All timings from Scheuer and Black, 2004.

Ossification Center	Appearance		Fusion	
	Female	**Male**	**Female**	**Male**
Proximal Epiphysis			13-17 years	16-20 years
Head	Birth-6 months	Birth-6 months		
Greater Tubercle	1-2 years	1-2 years		
Lesser Tubercle?	4-5 years	4-5 years		
Distal Epiphysis				
Capitulum	1-2 years		11-15 years	12-17 years
Trochlea	8-9 years		11-15 years	12-17 years
Lateral Epipcondyle	10-12 years		11-15 years	12-17 years
Medial Epipcondyle	4-6 years		13-15 years	12-17 years

3.2. Radius

The mesenchymal radius is apparent by 38 days of prenatal life. Chondrification begins shortly after at 41 days, with the primary center of ossification beginning at around 51 days of prenatal life. Ossification reaches the neck of the radius by 18-28 weeks of prenatal life. At birth the radial tuberosity is only partially ossified and remains mostly cartilaginous. A single nutrient foramen, located on the anterior surface of the proximal third of the diaphysis, is present in 95% of individuals (Skawina and Wyczolkowski, 1987). During the first year of life a pronounced lateral diaphyseal curvature develops and the medial surface of the diaphysis/metaphysis junction flattens as the ulnar notch develops.

Table 3.2 presents the appearance and fusion times for the secondary ossification centers of the radius. The proximal epiphysis appears around five years of age. This epiphysis is formed from a single, flat, disc-like ossification center, although rarely two adjacent ossification centers may form this epiphysis. The wedge-shaped joint space is wider laterally because the metaphyseal surface is offset from the articular surface of the capitulum, leading to a lateral projection of the radial head/neck after ossification. The fovea for the capitulum articulation is apparent around 10-11 years and deepens as the epiphysis develops. The fusion of this epiphysis is between 11.5-14 years in females and 13.5-16 years in males.

The distal epiphysis is the growing end of the bone, responsible for 75-80% of the longitudinal growth. This epiphysis appears as a single center between one to three years of age. Fusion of this epiphysis occurs in females between 15-16 years and males between 17-18 years.

Table 3.2. The appearance and fusion times for the secondary ossification centers of the radius. All timings from Scheuer and Black, 2004.

Ossification Center	Appearance		Fusion	
	Female	**Male**	**Female**	**Male**
Proximal Epiphysis	4.5-6 years	4.5-6 years	11.5-14 years	13.5-16 years
Distal Epiphysis	1-3 years	1-3 years	14-17 years	16-20 years
Radial Tuberosity	Puberty	Puberty	Puberty	Puberty

3.3. Ulna

By 38 days of prenatal life the mesenchymal ulna is present. Chondrification begins soon after at 41-44 days, with the proximal epiphysis appearing just prior to the distal epiphysis at 46 and 49 days, respectively. The primary center of ossification begins soon after the appearance of the distal epiphysis at 51 days. Over 90% of fetuses have a single nutrient foramen located at midshaft (Skawina and Wyczolkowski, 1987). Between 18 and 28 weeks of prenatal life ossification has reached the distal aspect of the coronoid process and radial notch. At birth, the ulna is ossified to the midpoint of the trochlear notch proximally, and to the junction of the distal epiphysis distally. The diaphysis is straighter than the adult form and proximally is flattened mediolaterally and more triangular shaped distally, with distinct posterior and interosseous crest boarders. A faint groove for the extensor carpi ulnaris is also present at birth.

One of the first changes to the ulna after birth is the development of the supinator crest during the first year of life, followed by the diaphysis taking the adult sigmoid curvature. Until the age of 8-10 the trochlear notch is wide to accommodate the proximal epiphysis. The coronoid process and ulnar tuberosity remain under-developed until later childhood.

The ulna has at least two proximal and one distal secondary centers of ossification (Table 3.3). The proximal epiphysis forms the olecranon process portion of the trochlear notch. The

coronoid process and the distal two-thirds of the trochlear notch are formed by the proximal extension of the primary center of ossification. This epiphysis appears in females at 8 years and males at 10 years as a collection of at least two ossific nodules. This epiphysis fuses between 12-14 years in females and 13-16 years in males.

Because it is the growing end of the ulna, the distal epiphysis appears few years earlier and fuses a few year later than the proximal end. The distal epiphysis appears between five and a half and seven years of age. In females, this epiphysis fuses between 15-17 years. In males, this epiphysis fuses between 17-20 years.

Table 3.3. The appearance and fusion times for the secondary ossification centers of the ulna. All timings from Scheuer and Black, 2004.

Ossification Center	Appearance		Fusion	
	Female	**Male**	**Female**	**Male**
Proximal Epiphysis	8-10 years	8-10 years	12-14 years	13-16 years
Distal Epiphysis	5.5-7 years	5.5-7 years	15-17 years	17-20 years

3.4. Femur

The mesenchymal femur appears around 41 days of prenatal life and chondrification begins almost immediately at 41-44 days. Proximally, the head is visible by 48 days, with the neck and trochanters five days later. Distally, the condyles also appear at 53 days of prenatal life. Around the same time, between 49-56 days, ossification begins with the development of the boney collar at midshaft, with endochondral ossification beginning a week later. Diaphyseal ossification has reached the neck proximally and the epiphysis distally by 12-13 weeks. A primitive nutrient foramen appears around 10 weeks, but in many cases gives way to one to two nutrient foramina located on the upper two-thirds of the diaphysis near the linea aspera by 13-28

weeks (Skawina and Wyczolkowski, 1987). By term, there may be an additional nutrient foramen on the anterior surface of the diaphysis just below the neck.

Due to muscle mechanics, the femur undergoes significant shape changes during natal development. The linea aspera and gluteal tuberosity appear as thickened portions of periosteal bone by 12-13 weeks. However, these muscle attachment sites, including the spiral line, do not become well-developed until adolescence. By the second trimester, remodeling processes begin at the extremities of the diaphysis, leading to an increase in length and width of the diaphysis. During the seventh prenatal month, the proximal metaphysis remodels from a convex dome to two planes lying parallel to the cartilaginous head and greater trochanter, respectively. A month later, the distal metaphysis flattens out and develops a central depression to accommodate the appearance of the distal epiphysis.

Around this time femoral torsion becomes apparent. Unlike humeral torsion at this phase, which is relower limbated to the proximal end, the torsion of the femur is throughout the entire diaphysis; starting at -10-0 degrees during early development and reaching levels of 30-40 degrees by birth (Watanabe, 1974). Levels of femoral torsion decrease during growth, reaching adult the adult average of around 15 degrees by the late teens (Schacher et al., 2009). While this change is gradual, there are two spikes in torsion development. The first is between one and two years, as the child learns to walk, and another during the onset of puberty when pelvic changes lead to walking style changes (Fabry et al., 1973). There is, however, considerable variation in the degree of adult femoral torsion. This variation has been attributed to population differences (Schacher et al., 2009) and osteoarthritic changes with increased age (Tonnis et al., 1999).

Again, like the humerus, the ontogeny of femoral torsion is directly linked to biomechanical influences and the need to accommodate bone form to function.

Other morphological features of the femur also undergo considerable change during childhood. At birth the femoral neck is vertically oriented. This angle is decreased in response to hip abductor development as the child learns to walk (Morgan and Summerville, 1960). This decrease in angle, coupled with angular remodeling to increase apposition on the medial surface, changes the loading axis of the femur and draws the distal end of the femur in medially. This medial shift increases the bicondylar angle, which helps with the adoption of efficient walking achieved in childhood (Tardieu, 1998; Tardieu and Trinkaus, 1994). Along with external morphological changes during adolescence, the trabecular architecture of the femur changes in response to load-bearing as a child's gait develops. By two years old, primary trabeculae begin to remodel and by five years of age secondary trabeculae are obvious, aligning along the principle loading axis (Osborne and Effmann, 1981).

Anterior curvature is another morphological change during ontogeny. At birth, infant femora are relatively straight. Slight anterior bowing begins to develop around the onset of walking, around 18 months. Between the ages of 7-13 years, the femora develop the adult degree of anterior curvature.

The femur has three proximal and one distal secondary centers of ossification (Table 3.4). The distal epiphysis is the largest and fastest growing long bone epiphysis. It is the first long bone epiphysis to form at 36-40 weeks prenatal life and appears as single ossific nodule. This epiphysis expands rapidly to the condylar areas by one to three years of age, and becomes

Table 3.4. The appearance and fusion times for the secondary ossification centers of the femur. All timings from Scheuer and Black, 2004.

Ossification Center	Appearance		Fusion	
	Female	**Male**	**Female**	**Male**
Proximal Epiphysis				
Head	0.5-1 year	0.5-1 year	12-16 years	14-19 years
Greater Trochanter	2-5 years	2-5 years	14-16 years	16-18 years
Lesser Trochanter	7-11 years	7-11 years	16-17 years	16-17 years
Distal Epiphysis				
Femoral Condyles	36-40 weeks (in utero)		14-18 years	16-20 years

recognizable. By seven years and nine years in females and males, respectively, the epiphysis is as wide as the metaphysis and the condyles have taken on their distinctive shapes. The distal end is the growing end of the femur and is responsible for 70% of longitudinal growth. This epiphysis is one of the last to fuse between 14-18 years in females and 16-20 years in males. Fusion of this epiphysis coincides with the end of growth in height.

Unlike the humerus, where the proximal epiphyses form a compound epiphysis prior to fusion, the proximal femoral epiphyses fuse to the diaphysis independently. At birth, however, there is only one metaphyseal surface, divided into medial and lateral portions for the head and trochanters, respectively. By two years old this single metaphyseal surface divides into separate regions for each secondary center.

The head is the first of the secondary centers to begin ossification. Rarely is this center visible at birth, but is almost always apparent by the age of one, with a median age of around six months. The greater trochanter is the next proximal epiphysis to begin ossification between two to five years of age. Ossification begins in females almost two years earlier than in males, with the median age of the former at 2 years 10 months and the latter at 4 years. Like its counterpart

on the humerus, the lesser trochanter is the last proximal epiphysis to begin ossification, with ossification times between 7-11 years old. The pattern of fusion for the proximal epiphyses follows the same pattern as their appearance. The head typically fuses first, although this timing is variable, with fusion occurring in females between 12-16 years of age and 14-19 years in males. The greater trochanter is next, with females fusing between 14-16 years and males between 16-18 years. The lesser trochanter is typically last, although this epiphysis may fuse concurrently with the greater trochanter in males. Fusion times in females range from 16-17 years and 16-17 years in males.

3.5. Tibia

The appearance and chondrification of the tibia is very similar to the femur. The mesenchymal consolidation is identifiable at 41 days of natal life, with chondrification beginning roughly 3 days later. By week eight of natal development, most of the major features of the tibia are apparent, including the condyles and major ligaments. This is also the time when ossification begins with the appearance of the boney collar at midshaft. All proximal and distal morphological structures are identifiable by the 20^{th} week. At birth, 80% of the bone is represented by an ossified shaft, with a very large nutrient foramen on the posterior surface of the proximal third of the diaphysis in the region of the popliteal surface and soleal line (Skawina and Wyczolkowski, 1987).

Similar to the femur, the tibia undergoes several morphological changes early in life. However, in contrast to the femur, few of these changes have been directly attributed to the biomechanical influence of walking. For example, the angle formed by the tibial plateau and the

diaphysis, known as the angle of retroversion, changes rapidly from a high angle at birth to a lower angle by two years old. High angles have been observed in adult populations that spend a large amount of time in a squatting position, suggesting that biomechanics may have some influence on the angle of retroversion later in life (Kate and Robert, 1965).

Tibial torsion is another morphological feature that changes rapidly in infants. At birth, most infants have slightly medially rotated tibia. By 2 years of age, this torsion typically changes to an average of 25 degree lateral rotation (Ritter et al., 1976). Despite independent walking by most toddlers at two years old, no correlation was found between tibial torsion and independent walking, nor was any correlation found for sex or ancestry (Ritter et al., 1976). The ontogeny and subsequent adult form of tibial torsion, however, is quite variable. Roughly a third of two year olds maintain a medial rotation of the tibia, with this percentage decreasing to 8-10% by seven years old (Hutter and Scott, 1949). There appears to be no correction of medial tibial torsion after the age of seven, as this is the level of medial torsion observed in adults.

The tibia is represented by two proximal and one distal secondary centers of ossification (Table 3.5). The proximal epiphysis is present in about 80% of newborns and is almost always present by three months of age. By six to seven years the condyles have developed into their adult form. The tibial tuberosity develops as an outgrowth of the proximal epiphysis. This outgrowth begins at four months in utero, but does not begin to ossify until much later. The tibial tuberosity begins to fuse slightly later than the condyles at 14 years in females and 16.5 years in males.

The distal epiphysis appears soon after birth and begins ossifying within the first year (Table 5). The malleolus begins ossifying between 8-10 years of age. It is not uncommon for the malleolus to ossify as a separate center of ossification from the rest of the epiphysis. This epiphysis begins fusion at 12-13 years in females and 14-15 years in males.

4. Summary

The hypothetical structure of reassociation accuracy presented in Chapter 1 from highest to lowest is: homologous comparisons, followed by within-limb, between-limb, and lastly, serially homologous comparisons. However, homologous and serially homologous elements have the most and second most developmental commonalities, respectively. Developmental processes should also affect accuracy of specific within limb comparisons. The overall

Table 3.5. The appearance and fusion times for the secondary ossification centers of the tibia. All timings from Scheuer and Black, 2004.

Ossification Center	Appearance		Fusion	
	Female	**Male**	**Female**	**Male**
Proximal Epiphysis				
Condyles	eeks (prenatal)-2 months (postr		12-16 years	14-19 years
Tuberosity	8-12 years	9-14 years	14 years	16.5 years
Distal Epiphysis	3-10 months	3-10 months	14-18 years	16-20 years

architecture and general process is the same for each developing limb, however certain factors differentially affect limbs and elements within a limb. These developmental pathways suggest that accuracy in osteometric reassociation should follow the relatedness of factors affecting limb element development. During P/D axis growth, distal elements (radius/ulna and tibia) develop through the same factors, with certain factors only affecting the proximal elements

(humerus/femur). During A/P axis growth, a different pattern emerges, with the proximal (humerus/femur) and lateral-distal elements (radius) sharing a pathway and the medial-distal element (ulna/tibia) developing through another. Considering both axes, the lateral-distal limb element shares a common pathway with both the proximal element and medial-distal element, with the proximal and medial-distal elements developing through different pathways along both axes. Given this pattern of axes development, the radius may have higher within-limb accuracy than other within-limb comparisons. Additionally, accuracy of within-lower limb comparisons may be low because the femur and tibia show developmental autonomy across both axes.

As discussed throughout the chapter, function influences form. Long bone morphology adapts to accommodate its loading environment throughout ontogeny. This accommodation is most obvious through changes in humeral and femoral torsion throughout ontogeny. Thus, functional similarities may obscure or augment developmental relationships. If functional similarities obscure developmental relationships, accuracy in sorting functionally cohesive elements, such as the femur and tibia, may be higher than the developmental differences would suggest. In a similar vein, developmentally related elements that are not functionally related, such as the femur and humerus may have lower accuracy than developmental similarities would suggest.

Chapter 4

Bone Biomechanics and Functional Adaptation

Chapter 3 suggests that based on ontogenetic factors, the hypothetical accuracy of osteometric reassociation from highest to lowest are: homologous elements, serially homologous elements, within-limb, and between-limbs. Homologous elements have identical developmental programs. Serially homologous elements have similar programs with some factors distinguishing them, such as location, timing, molecular expression, or certain genes. Within-limb elements develop from the same limb bud, but axes patterning shows some degree of autonomy between these elements. The developmental program of between-limbs elements that are not homologous or serially homologous have the least in common.

The previous chapter also described the timing and patterning of limb bone ossification. This description includes some morphological changes to bone occurring during ontogeny as a result of mechanical interactions. Functional adaptation is the conceptual framework used to understand how the mechanical environment influences limb bone morphology (Ruff et al., 2006; Pearson and Lieberman, 2004; Curry, 2002). As a living tissue, bone has a myriad of ways to accommodate its mechanical environment. Many of these important adaptations are not macroscopically evident (Curry, 2002). Thus, these adaptations are not relevant to this study because reassociating commingled bones uses gross morphological relationships. Instead, this chapter focuses on functional adaption theory and research resulting in gross morphological change. Variation in this response is influenced by an individual's genetic repertory, hormonal changes experienced during puberty, nutrition and health, as well as activity pattern (Frost, 2003;

Curry, 2002; Martin et al., 1998). These interrelated variables influence the morphology of the adult skeleton and are the basis for how functional adaptation structures accuracy in osteometric reassociation. First, a few important concepts for understanding bone functional adaptation must be understood.

1. Bone loading regime

The loading regime of bone is a dynamic process, derived from either muscle force acting on an origin or insertion point or from external forces acting across a joint surface (Pearson and Lieberman, 2004). Four general forms of loading are responsible for bone loading: axial compression, bending, twisting, and shear (Figure 4.1). Bone loading leads to two important concepts for understanding bony response to loading: stress and strain.

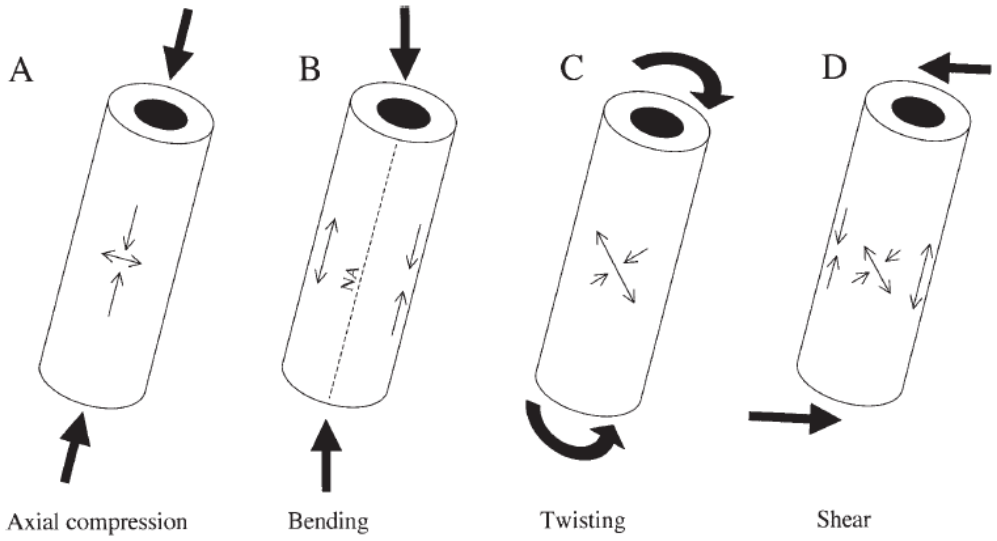

Figure 4.1. Four typical bone loading regimes: A. Axial compression, B. Bending, C. Twisting, D. Shear. Thick arrows represent direction of force and thin arrows show the resulting strain. From Pearson and Lieberman 2004, Figure 2.

Stress is defined as the intensity of a force across a plane. Strain is how a material deforms in response to an applied load (Curry, 2002). The relationship between stress and strain is visualized using a stress/strain or a load-deformation curve (Figure 4.2). When a stress is applied to a material, the initial strain is the elastic phase. If the stress is removed when a material is in the elastic phase, the material will return to its original shape (McGowan, 1999). The yield point is the transition from the elastic to the plastic phase. Once a material enters the plastic phase, it remains deformed after the stress is removed. If stress increases past the plastic phase, the material fails and fractures (McGowan, 1999). Limb bones adapt to their loading environments by differentially adding and removing bone in areas of high stress to reduce strain (Curry, 2002). The osteocyte is the cellular mechanism by which bones sense this strain and communicate this information to elicit an osseous response.

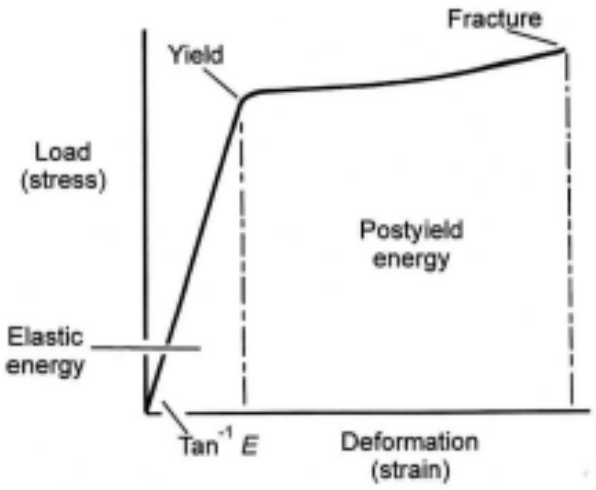

Figure 4.2. Stress/strain curve depicting how an object reacts to an applied load. From Curry 2002, Figure 2.7.

1.1. Bone sensing and communication of mechanical loading: The osteocyte

Osteocytes are connected to each other and transmit signals via cytoplasmic extensions that travel through bone channels, or canaliculi (Figure 4.3). The network of osteocytes is responsible for maintaining mature bone. Osteocytes have proteins, such as sclerostin, that help in mineral metabolism and phosphate regulation (Bonewald, 2011).

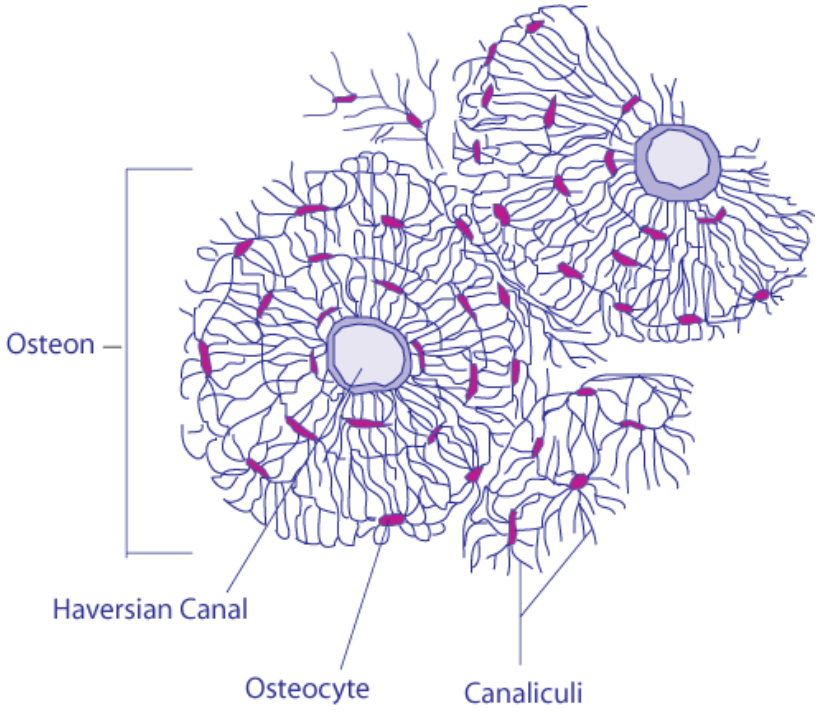

Figure 4.3. Example of an osteon. Modified from Gray (1918) by Bduttabaruah. https://commons.wikimedia.org/wiki/File:Transverse_Section_Of_Bone.png

The osteocyte has long been thought to be the cell that senses and communicates loading information to other bone cells (Robling and Turner, 2009; Robling et al., 2006; Frost, 2003; Frost, 1996; Turner and Forwood, 1995). Despite a lack of initial evidence, this cell was considered a good candidate for bony response to loading because of the fluid-filled network of

canaliculi that connected osteocytes to bone envelopes and each other (Turner and Forwood, 1995). While early research on the role of the osteocyte network showed that these cells did respond to mechanical loading by fluid flow through the network, evidence suggested little, if any, communication of osteocytes to surrounding tissue, including the mesnchymal cells of the periosteal and endosteal surfaces (Turner and Forwood, 1995).

More recent research, however, provides strong evidence that the osteocyte is indeed the cell responsible for sensing and transmitting mechanical load information to cells involved in boney response (Robling and Turner, 2009; Robling et al., 2006). Mechanical loading of bone leads to stress, which in turn causes strain, or bone deformation. Osteocytes sense strain, and along with bone-lining cells, work together in a network to transmit signals to osteoblasts and osteoclasts (Robling and Turner, 2009). Intracellular calcium signals are passed by bone-lining cells through canaliculi. Extracellular information is passed by paracrines, like adenosine triphosphate, to the mesenchymal cells lining the periosteal and endosteal bone surfaces. These mesenchymal cells differentiate into osteoblasts and send RANK-L signals to recruit osteoclasts (Robling and Turner, 2009; Robling et al., 2006).

2. Macroscopic osseous response to mechanical loading: Modeling

Modeling is the action of osteoblasts and osteoclasts working on different bone surfaces in concert (Frost, 2003). As a bone grows in length, it needs to increase girth to order to maintain structural integrity. The increase in girth is known as appositional growth. Modeling changes a bone's shape to accommodate its loading regime and maintain relative proportionality during appositional growth (Robling and Turner, 2009; Robling et al., 2006; Frost, 2003; Curry,

2002). After appositional growth is complete, the modeling response of bone is dramatically decreased (Pearson and Lieberman, 2004). Bone shape, however, is still affected by mechanical loading into adulthood, albeit to a much lesser degree than during ontogeny (Ruff et al., 2006).

Bones are a compromise between metabolic efficiency and strength (Curry, 2002; McGowan, 1999). Optimal bone morphology should limit peak strains with the minimum amount of structural tissue (Frost, 2003). For example, if the mechanical environment is compromised during gestation, limb bones attain only 30-50% of normal bone mass and do not develop their characteristic shape (Figure 4.4).

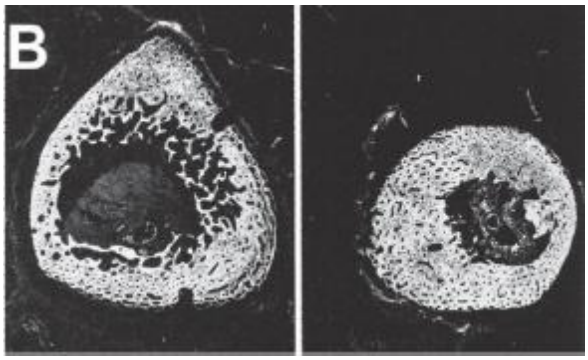

Figure 4.4. Left is a cross section of a new born tibia from a normal mechanical environment. Right, a new born tibia lacking mechanical loading due to spina bifida. From Robling and Turner 2009 Figure 2. Reprinted from Ralis et al. 1976.

2.1. Modeling

2.1.1. The upper limb

Hypervigorous mechanical usage tends to increase longitudinal bone growth slightly (Frost, 2003). This trend is shown through asymmetry of long bone length with the dominant limb being slightly longer than its counterpart (Auerbach and Ruff, 2006). The slight increase in

length is coupled with a dramatic increase in diaphyseal appositional growth over the non-dominant limb (Jones et al., 1977). In a survey of 84 professional tennis players, Jones et al. (1977) found that humeral cortical bone thickness was 34.9% and 28.4% greater in the dominant upper limb of males and females, respectively.

These results show that generally, modeling reacts to loading in a predictable way—increased loads lead to increased bone apposition (Frost, 2003; Curry, 2002). This increased apposition, however, was not uniform. Males were more responsive to loading when compared to females (Jones et al., 1977). Apposition tended to favor the periosteal over endosteal surface. Yet, this only held true for the professional tennis players along the transverse plane; along the sagittal plane, endosteal apposition was greater than periosteal apposition. The difference in surface apposition between the transverse and sagittal planes led to changes in bone shape over the non-dominant upper limb. The dominant upper limb became oblong compared to its counterpart, showing that the repetitive stress of tennis resulted in added cortical bone and changed cross-sectional shape to reduce humeral strain. The results of Jones et al. (1977) show that asymmetry in overall use and type of motion can lead to asymmetric changes in diaphyseal size and shape. These differences should decrease accuracy for between-upper limb comparisons.

Shaw and Stock (2009b) also looked at the effect of loading regime on modeling response on the upper limb using humeral and ulnar cross-sectional geometry of 50 college swimmers, cricket players, and non-athletes. Cross-sectional geometry was used to assess strength and shape differences between groups. The shape measurement used was the maximum

and minimum second moments of area (I_{max}/I_{min}). This measure is a geometric property of a diaphyseal cross section that describes how cortical bone is distributed with regard to an axis (Lieberman et al., 2004). The strength measurements included cortical area and total subperiosteal area, which measure resistance to axial compression, and the polar second moment of area, which is the sum of two perpendicular second moments of area, which measures resistance to torsion (Shaw and Stock, 2009a).

The swimmers, who began training around 11 years old, experienced stereotypic bilateral loading on their upper limbs (Shaw and Stock, 2009b). The cricketers, who began training at a similar age as the swimmers, experienced unilateral loading through repeated throwing. Non-athletes, none of whom undertook strenuous exercise, served as a control.

There were no significant differences ($\alpha = 0.05$) in cross-sectional measurements of upper limb strength between the dominant upper limbs of swimmers and cricketers. Similarly, the non-dominant upper limbs of cricketers and non-athletes showed no significant differences in cross-sectional measurements of upper limb strength. The swimmers, however, typically had significantly stronger non-dominant upper limbs compared to the other two groups. Overall, the upper limb showed less difference in strength measurements between groups. Shape differences in the upper limbs among groups were less obvious than those observed by Shaw and Stock (2009a). No significant differences were found in either upper limb among groups. The dominant upper limb of cricketers was significantly more circular than non-athletes, but not swimmers.

The results of Jones et al. (1977) and Shaw and Stock (2009b) show, on average, that bone responds to hypervigorous activity by increasing cortical area and changing diaphyseal shape. As Figure 4.5 illustrates, however, modeling response is idiosyncratic to the individual. Despite similar starting ages, years of experience, and loading regimes, Player A and Player B showed different patterns of bone apposition. Player A shows a relatively even apposition of bone on the periosteal and endosteal surfaces. Player B, in contrast, showed a dramatic increase periosteal apposition and slight endosteal resorption, especially in the transverse plane.

2.1.2. The lower limb

By examining the tibial midshaft cross-sectional geometry of 50 male college students from three different cohorts: long-distance runners, field hockey players, and non-athletes, Shaw and Stock 2009a provide insight on how loading regime affect lower limb elements. The long-distance runners, who began training at around 13 years old, typically experienced lower impact, long-term, stereotypic loading on their tibiae (Shaw and Stock, 2009a). In contrast, the field hockey players, who began training around 10 years old, experienced high impact, short-term, multidirectional movement (Shaw and Stock, 2009a). Again, non-athletes served as a control.

As expected, long distance runners and field hockey players were significantly stronger ($\alpha = 0.05$) in most measurements of tibial strength, compared to non-athletes. While long distance runners tended to have the highest values of tibial strength measurements, only cortical area was significantly different when compared to field hockey players. One other cross-sectional property differed significantly between long distance runners and field hockey players, diaphyseal shape (Figure 4.6). Higher values, as seen in long distance runners (mean = 2.604),

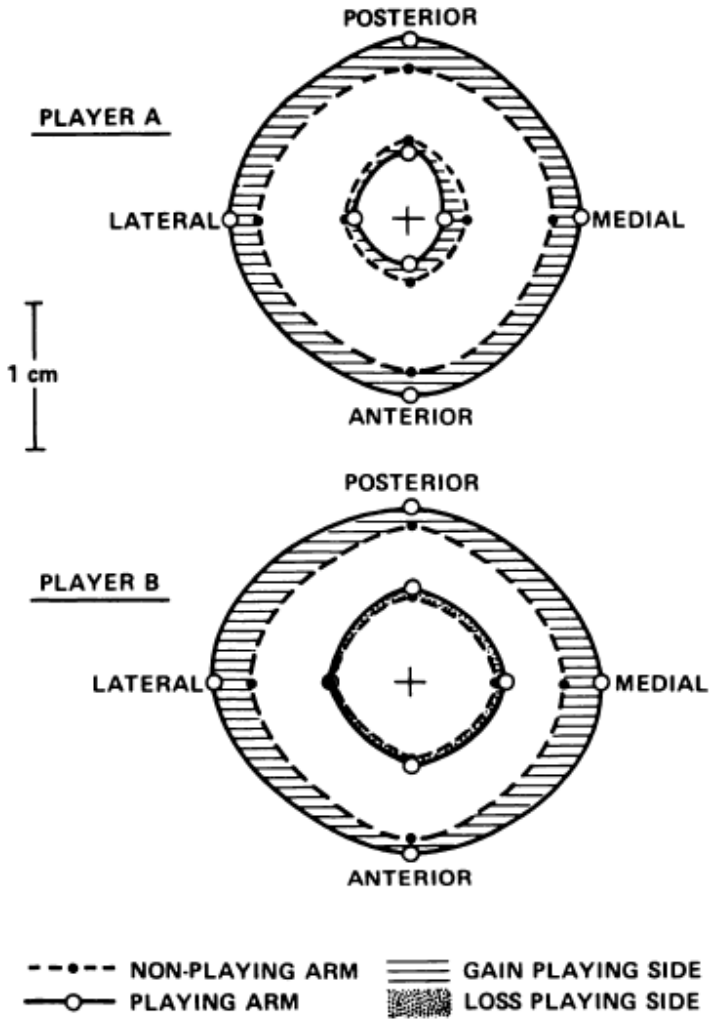

Figure 4.5. Asymmetry in humeral diaphyseal cross sectional shape from hypervigorous activity favoring the dominate limb. Player A and Player B were each professional tennis players in their mid-twenties with 18 years playing experience. From Jones et al., 1977.

represent an anterior/posterior elongated tibial cross-section. Lower values, as seen in field hockey players (mean = 2.220), represent tibial cross-sections that roughly approximate an equilateral triangle. The non-athletes had cross-sectional shapes that fell in between these two extremes. Again, this study shows that long bone shape and size responds predictably to the level and type of mechanical loading. Unlike the upper limb, however, modeling response in the lower limb is closer to uniform between left and right sides (Shaw and Stock, 2009a), suggesting that mechanical loading should serve to increase accuracy in lower limb comparisons.

2.1.4. Modeling and osteometric reassociation

As the above studies illustrate, modeling response to biomechanical loading leads to predictable and obvious changes to limb bone morphology. As such, modeling should be a major factor in structuring accuracy in osteometric reassociation. The patterning of modeling response should serve to help differentiate limb bones between people and individualize elements through common function and loading regime. Repetitive, stereotypic function should lead to high within-limb accuracy, with coordinated function leading to high between-limb accuracy. All of the above studies focused on long bone diaphyseal morphology, as this portion of the bone shows the most obvious response to loading (Lieberman et al., 2004; Lieberman et al., 2001). Other aspects of limb bones also response to loading, although in a different manner than diaphyses.

2.2. Limb bone response to loading by region: Linear measurements

As the studies in the modeling section show, differential limb use leads to an increased osseous response in the dominant limb, leading to asymmetry (Shaw and Stock, 2009b; Bass et

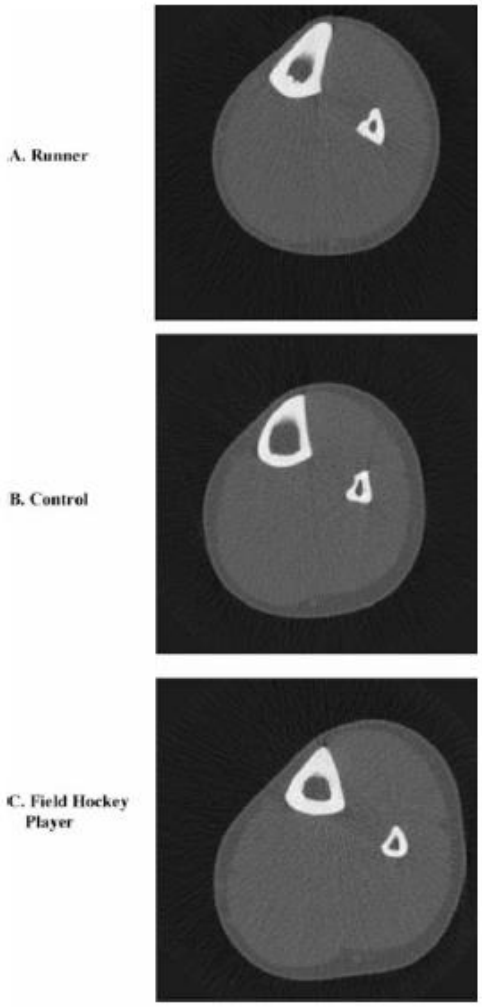

Figure 4.6. The tibial cross-sectional shape. From Shaw and Stock 2009a, Figure 3.

al., 2002; Jones et al., 1977). These studies focused on modeling response through diaphyseal cross-sectional measurements. Asymmetry in limbs has also been addressed using long bone measurements (Auerbach and Ruff, 2006). As expected, regardless of limb, diaphyseal girth measurements showed the highest level of asymmetry and variability (Lazenby et al., 2008; Auerbach and Ruff, 2006; Plochocki, 2004). Differences in diaphyseal dimensions were most pronounced in the upper limb, favoring the right side (Auerbach and Ruff, 2006; Plochocki, 2004). The lower limb showed a much lower degree of asymmetry (Auerbach and Ruff, 2006; Plochicki, 2004). This finding was expected, given the coordinated and stereotypical use of the lower limbs, further supporting higher accuracy in osteometric reassociation for lower limb comparisons. In contrast to diaphyseal measurements, articular and length measurements showed the lowest amount of asymmetry, with differences typically not reaching statistical significance ($\alpha = 0.05$) (Lazenby et al., 2008; Auerbach and Ruff, 2006).

2.3. Epiphyseal response to loading

At first glance, the lack of asymmetry in articular dimensions is interesting and unexpected because joint surfaces experience a high level of stress during mechanical loading (Curry, 2002; McGowan, 1999). Yet, despite the high level of stress, articular dimensions show a low level of asymmetry compared to diaphyseal measurements, suggesting minimal osseous response to loading. However, epiphyses are mainly trabecular bone, which is tough, deforming in response to stress (Curry 2002; McGowan 1999). Gross articular dimensions do not measure trabecular bone response to loading.

Lazenby et al. (2008) examined osseous response to loading by measuring midshaft cross-sectional geometry as well as distal epiphyseal trabecular bone density, connectivity, and thickness of 29 paired second metacarpals. The authors found a similar degree of bilateral asymmetry in the connectivity and thickness of epiphyseal trabecular bone, showing that epiphyses respond in a similar magnitude to loading as diaphyses, but through different mechanisms. Joints are constrained to maintain functional cohesiveness between articulations. Functional cohesiveness and adaptation to mechanical loading is maintained through keeping articular dimensions canalized and trabecular connectivity and thickness plastic in response to loading (Lazenby et al., 2008).

2.3.1. Epiphyseal response and osteometric reassociation

Epiphyseal response to loading occurs below the bone surface through increasing trabecular connectivity and thickness, suggesting that it is not relevant for understanding accuracy in osteometric reassociation. However, the trabecular response of epiphyses to loading serves to maintain functional cohesiveness and relationships. If articular dimensions changed in response to loading throughout ontogeny, function may become compromised. Gross dimension canalization compensated for by trabecular response to loading seen in epiphyses strongly suggests that articulating elements should have high levels of accuracy in osteometric reassociation. Joint surfaces not only transmit loads, but determine limb stability and range of motion (Ruff, 2002). It is reasonable to assume that bones with a limited range of motion and a large amount of articulating surface area should have high accuracy in osteometric reassociation. If this assumption holds, then within-lower limb comparisons should have higher levels of

accuracy compared to the upper limb due to the limited range of motion and large articulating surface of the knee compared to the elbow. The elbow, however, is a complex hinge joint, with a larger more stable articulating surface between the ulna and humerus compared to the radius and humerus. Because of these differences, humerus and ulna comparisons may have higher accuracy compared to humerus and radius comparisons.

3. Summary and functional adaptation and osteometric reassociation accuracy

As a living material, bone adapts to its loading regime. Mechanisms by which bone adapts to its mechanical environment through gross morphological changes should influence accuracy in osteometric reassociation. Modeling is a major adaptive process occurring mainly during ontogeny that changes bone size and shape by adding and removing bone from the peri- and endosteal surfaces. Modeling is mediated by several factors including hormonal changes experienced during puberty, nutrition and health. These processes and mediating factors lead to limb bone morphology that are unique to the individual, allowing for limb bones to be accurately reassociated. Elements that share a similar loading environment should have a similar modeling response, thus increasing covariation and accuracy in osteometric reassociation. Humans are bipeds that are typically one-upper limb dominant. These characteristics lead to several nuances to the relationship of form and function and osteometric reassociation accuracy. First, besides being functionally constrained at the knee, lower limb bones are intimately linked during locomotion. The functional relationship of the lower limbs should lead to high levels of accuracy for between-and within-lower limb comparisons as well as homologous lower limb comparisons. Upper limbs, on the other hand, have a larger range of motion and since they are

not directly used for locomotion, are able to function more or less independently of the opposing upper limb. This patterning of human limb function should lead to lower accuracy for within- and between-upper limb comparisons and homologous comparisons.

This overlap between development and function is most obvious in the canalization of gross dimensions of articulating portions. Instead, articulating portions respond to mechanical loading by changing the underlying trabecular structure of the epiphyses. This loading response highlights the importance of maintaining functional cohesiveness between articulating portions. Diaphyses, in contrast, show plasticity in gross dimension, suggesting that model's effect on osteometric reassociation accuracy should be most obvious in those dimensions.

Chapter 5

Limb Integration and Modularity

Chapters 3 and 4 provide the experimental framework for understanding the processes contributing to limb development and functional adaptation, respectively. These two bodies of research have been applied to understand limb covariation structure (Young et al., 2010; Young and Hallgrimsson, 2005; Hallgrimsson et al., 2002; Capdevila and Belmonete, 2001). Integration and modularity are two theoretical concepts used, along with the above research, to explain the hierarchical structure of the vertebrate body. These concepts are useful for understanding how the body works together as a functional unit (Wagner et al., 2007). As such, integration and modularity build a portion of the theoretical foundation used in this study and provide a blueprint for developing a hypothetical structure of accuracy in osteometric reassociation.

1. Integration and modularity

Different aspects of an organism are more integrated than others. More integrated portions an organism are considered modules. Modularity and integration are abstract concepts that capture various types, levels, and structures of variation (Wagner et al., 2007). Modules are many times hierarchically structured. For example, cell types are packaged together in organs, groups of organs work together to perform particular bodily functions, and all of these bodily functions work together in the organism. Integration focuses on causal factors responsible for trait covariation (Wagner, 2007). Within an organism there are two major kinds of integration: functional and developmental. Physical elements that interact with each other to perform an

action are functionally integrated (Cheverud, 1996). Aspects of the body that covary during ontogeny are developmentally integrated (Cheverud, 1996).

Like integration, modularity focuses on factors causing trait covariation. However, modules are typically juxtaposed against other trait sets to describe relationships between trait sets (Mitteroecker and Bookstein, 2008). Features that vary together more than they vary with other features of the same kind are a variational module. Aspects of an organism that work together to perform a physiological function that is relatively separate from other aspects of that organism is a functional module (Wagner et al., 2007). For example, human upper limbs and lower limbs can be considered separate functional modules since they function more or less independently. Portions of the embryo that form through an autonomous signaling cascade or are quasi-autonomous from other portions in regards to pattern formation and differentiation are developmental modules (Wagner et al., 2007). As shown in Chapter 3, differences in gene expression along developmental axes of the limb lead to some modularity between elements.

2. Limb integration and modularity

Young et al. (2010) and Young and Hallgrimsson (2005) used linear limb bone measurements to understand the effect of integration and modularity on limb covariance structure. The species in these studies represent a range of functional locomotor types, limb divergence, and phylogenetic relatedness. The results suggest an overall structural similarity in the covariance across broad phylogenetic and functional morphologies, showing a common underlying structure to limb integration. Specifically, the highest correlations are between homologous elements, followed by within-limb elements, proximal serially homologous

elements, distal serially homologous elements, with hand and feet elements showing the lowest correlations (Young and Hallgrimsson, 2005). In species with coordinated upper and lower limb locomotion, many times the correlations between serially homologous elements exceed within-limb correlations (Young et al., 2010; Young and Hallgrimsson, 2005). In species with disassociated upper and lower limb function, such as humans, integration is highest within and between functionally related limbs and lower overall levels of integration (Young et al., 2010; Young and Hallgrimsson, 2005).

3.1. Limb integration and modularity and osteometric reassociation accuracy

The common underlying structure to limb integration identifying by Young et al. (2010) and Young and Hallgrimsson (2005) provide the basis for the hypothetical structure of osteometric reassociation accuracy. Homologous elements share a common developmental program and varying degrees of functional similarity, which manifests in high integration of these elements. Thus, homologous elements should have the highest accuracy in reassociation. Within-limb elements should have the next highest levels of accuracy, followed by serially homologous comparisons. Lastly, between-limb comparisons should have the lowest reassociation accuracy. The functionally divergent limb use seen in humans should lower accuracy of comparisons between upper and lower limbs as well as serially homologous and between-upper limb comparisons.

4. Limb variation

Studies on the relative variation in human limb bone length measurements provide two important insights for accuracy in osteometric reassociation: modularity between proximal and

distal elements and higher variation in distal elements compared to proximal (Auerbach and Sylvester, 2011; Holliday and Ruff, 2001; Jantz and Jantz, 1999). For males, Auerbach and Sylvester (2011) give correlation coefficients of 0.82 for the femur and tibia and 0.70 for humerus and radius maximum lengths. Females have correlation coefficients of 0.77 and 0.65 for the femur and tibia and humerus and radius, respectively (Auerbach and Sylvester, 2011). Rosing and Pischtschan (1995) provide a correlation coefficient of 0.96 for ulna and radius maximum length from a pooled sample of males and females. The difference in correlation coefficients between these elements highlights the modularity of proximal elements from distal ones. Allometric trends in proximal and distal elements also points to modularity between these elements.

Auerbach and Sylvester (2011) show that proximal elements tend to be near isometric, while distal elements have positive allometric coefficients, a trend also seen in secular height increase (Jantz and Jantz, 1999). These allometric and secular trends in limb proportions support the findings of Holliday and Ruff (2001), who show that distal elements, especially the tibia, have more variation than proximal ones.

4.1. Limb variation and osteometric reassociation accuracy

Studies of limb variation support a degree of modularity between proximal and distal elements suggested by developmental processes. Interestingly, the tibia and femur have a degree of modularity across both developmental axes and the tibia shows more variability than the radius. The correlations between the maximum lengths of the femur and tibia, however, are higher than those of the humerus and radius (Auerbach and Sylvester, 2011). Regardless, the

higher correlations for the radius and ulna compared to the proximal and distal limb element correlations, suggest lower accuracy of proximal and distal limb comparisons compared to distal limb comparisons.

It seems reasonable that high variation in distal element measurements would lead to lower levels of accuracy in reassociating these bones. This assertion may be true for non-(serially) homologous comparisons involving distal elements. The reverse association may be true for distal homologous and serially homologous comparisons. Accuracy in osteometric reassociation depends not only on high covariance between an individual's limb bones, but high variation between individuals. Stated another way, limb measurements with high covariation may have minimal usefulness in osteometric reassociation if the range of possible values for those measurements is tightly constrained around the mean, because many possible elements may be good matches. Conversely, measures with low covariation may be useful if the range of possible values of those measurements is spread out around the mean, because possible matches are likely to be poor matches.

5. A biologically informed hierarchical structure of osteometric reassociation accuracy

Chapter 2 discusses commingled remains resolution and highlighted a gap in current osteometric reassociation methodology from a lack of a biological foundation. The body of research presented in Chapters 3-5 addresses this limitation by presenting relevant concepts and research in limb ontogeny, functional adaptation, and integration and modularity.

Chapter 3 shows that embryonic limb development does show some degree of modularity, both within-limb and between upper and lower limbs. As limb bones develop, they

are also influenced by mechanical loading by muscles, showing the interplay between development and function in form. These factors logically lead to the proposal that some types of osteometric comparisons should be more accurate than others.

Chapter 4 further delves into the relationship between ontogeny, function and form by examining bone functional adaptation to mechanical loading. Of the processes of bone mechanical adaptation, modeling and functional constraint should have the most obvious effects on reassociation accuracy. Modeling serves to mainly change diaphyseal morphology to accommodate loading. Functional constraint keeps gross dimensions of articulating portions canalized against biomechanical loading, instead allowing trabecular architecture to adapt to loading. The alternate form of functional adaptation in epiphyses highlights the importance of cohesiveness in articulating portions of bones, suggesting that elements forming a joint should have high reassociation accuracy. This assertion may be especially true for elements that articulate across a large surface area and are restricted in movement to a single or a few planes of motion (Ruff, 2002).

This chapter contextualizes the previous two by showing how developmental and mechanical influences are used to understand limb covariation structure. The observed patterns of vertebrate limb covariation are explained using the concepts of modularity and integration. Development and function structure limb covariance (Young et al., 2010; Young and Hallgrimsson, 2005; Hallgrimsson et al., 2002). Thus, there is a common underlying structure of limb integration across a broad sampling of species due to shared developmental processes, with functional differences leading, in part, to species-specific integration structure.

From this research, a structure to accuracy in osteometric reassociation was hypothesized (Figure 5.1). Homologous elements will have the highest accuracy of all comparison types. Within homologous elements, lower limb comparisons should have higher accuracy than upper limb comparisons. Next, within-limb comparisons will follow homologous comparisons. Again, lower limb comparisons will have higher accuracy than upper limb comparisons. Serially homologous comparisons will follow within-limb comparisons. Lastly, between-limb comparisons will have the lowest accuracy. However, between-lower limb comparisons should have accuracy near those of serially homologous comparisons, because of functional integration during locomotion. Comparisons between upper limbs and lower limbs will have the lowest accuracy of all comparisons because of comparatively low functional and developmental integration.

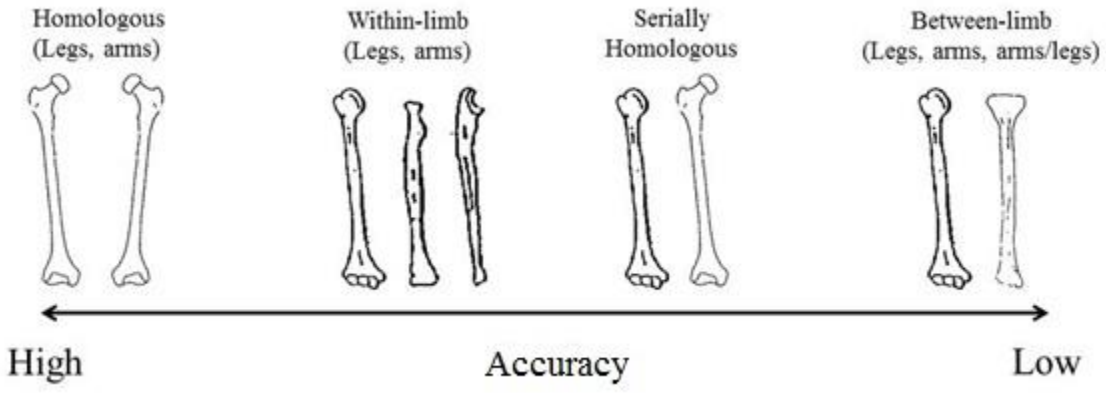

Figure 5.1. The proposed hypothetical structure of accuracy in osteometric reassociation.

Chapter 6

Materials and Methods

1. Materials

As discussed in Chapters 1 and 5, osteometric reassociation models lack a biological foundation and have relied solely on SOM's to quantify limb bone morphology. This study addresses those limitations through assessing a biologically-informed structure of accuracy in osteometric reassociation by applying Bayesian regression to geometric morphometric landmark data. These data consist of landmark coordinates collected on five paired long bones (humerus, radius, ulna, femur, tibia) from 208 individuals curated at the William M. Bass Donated Skeletal Collection at the University of Tennessee, Knoxville (Table 6.1 and 6.2). All individuals are adults, ranging in age from 19 to 62 years at death (Figure 6.1). Individuals in this study were chosen based on completeness of elements (i.e. no-to-slight damage to limb bones) and ease of landmark assessment (i.e. individuals with surgical limb bone intervention or moderate-to-extreme osteoarthritis were excluded). Information on the sex and ancestry composition of the sample is provided in Tables 6.3 and 6.4, respectively.

1.1. Geometric morphometric landmark data collection

Before discussing the benefits of three-dimensional coordinate data over traditional SOM, it is useful to discuss four concepts for understanding the geometric properties of bone structure: shape, size, form, and proportion (Figure 6.2). Size is a relative comparison of objects across a measurement, such as maximum length. When shapes are the same, size is

Table 6.1. Number of Landmarks by Bone.

Bone	Landmarks
Humerus	25
Ulna	25
Radius	17
Femur	29
Tibia	21
Total	117

Table 6.2. Landmark Descriptions.

Number	Bone	Landmark Description
1	Humerus	Superior-most point humeral head
2	Humerus	Superior point greater tubercle
3	Humerus	Anterior point of lesser tubercle
4	Humerus	Anterior point of head/neck intersection
5	Humerus	Medial point of head/neck intersection
6	Humerus	Posterior point of head/neck intersection
7	Humerus	Lateral point of head/neck intersection
8	Humerus	Anterior midshaft
9	Humerus	Medial midshaft
10	Humerus	Posterior midshaft
11	Humerus	Lateral midshaft
12	Humerus	Anterior nutrient foramen
13	Humerus	Medial nutrient foramen
14	Humerus	Posterior nutrient foramen
15	Humerus	Lateral nutrient foramen
16	Humerus	Medial point of medial epicondyle
17	Humerus	Lateral point of lateral epicondyle
18	Humerus	Superior point of olecranon fossa
19	Humerus	Medial point of olecranon fossa
20	Humerus	Lateral point of olecranon fossa
21	Humerus	Anterior point of the capitulum
22	Humerus	Inferior point of capitulum
23	Humerus	Distal-lateral point of trochlea
24	Humerus	Apex of trochlear groove

Table 6.2. Continued.

Number	Bone	Landmark Description
25	Humerus	Distal-medial point of trochlea
26	Ulna	Anterior point of olecranon process
27	Ulna	Superior point of olecranon process
28	Ulna	Posterior point of olecranon process
29	Ulna	Medial point of olecranon process
30	Ulna	Lateral point of olecranon process
31	Ulna	Medial point of midtrochlear notch
32	Ulna	Lateral point of midtrochlear notch
33	Ulna	Medial point of coronoid process
34	Ulna	Anterior-medial point of coronoid process
35	Ulna	Anterior point of coronoid process
36	Ulna	Medial intersection of coronoid and radial notch
37	Ulna	Inferior point of radial notch
38	Ulna	Lateral point of radial notch
39	Ulna	Anterior midshaft
40	Ulna	Medial midshaft
41	Ulna	Posterior midshaft
42	Ulna	Lateral midshaft
43	Ulna	Anterior nutrient foramen
44	Ulna	Medial nutrient foramen
45	Ulna	Posterior nutrient foramen
46	Ulna	Lateral nutrient foramen
47	Ulna	Anterior point of ulnar head
48	Ulna	Inferior point of styloid process
49	Ulna	Posterior point of ulnar head
50	Ulna	Lateral point of ulnar head
51	Radius	Superior point of radial head above radial tuberosity
52	Radius	Inferior point of radial head above rad tuberosity
53	Radius	Superior point of lateral radial head
54	Radius	Center of radial tuberosity
55	Radius	Anterior midshaft
56	Radius	Medial midshaft
57	Radius	Posterior midshaft

Table 6.2. Continued.

Number	Bone	Landmark Description
58	Radius	Lateral midshaft
59	Radius	Anterior nutrient foramen
60	Radius	Medial nutrient foramen
61	Radius	Posterior nutrient foramen
62	Radius	Lateral nutrient foramen
63	Radius	Superior point of ulnar notch
64	Radius	Inferior-anterior point of ulnar notch
65	Radius	Inferior-posterior point of ulnar notch
66	Radius	Posterior point of dorsal tubercle
67	Radius	Inferior point of styloid process
68	Femur	Superior most point of femoral head
69	Femur	Anterior point of head/neck intersection
70	Femur	Medial point of head/neck intersection
71	Femur	Posterior point of head/neck intersection
72	Femur	Lateral point of head/neck intersection
73	Femur	Apex of greater trochanter above trochanteric fossa
74	Femur	Lateral point of greater trochanter
75	Femur	Posterior-proximal point of lesser trochanter
76	Femur	Anterior midshaft
77	Femur	Medial midshaft
78	Femur	Posterior midshaft
79	Femur	Lateral midshaft
80	Femur	Anterior nutrient foramen
81	Femur	Medial nutrient foramen
82	Femur	Posterior nutrient foramen
83	Femur	Lateral nutrient foramen
84	Femur	Center of adductor tubercle
85	Femur	Medial intersection of anterior patella surface/shaft
86	Femur	Lateral intersection of anterior patella surface/shaft
87	Femur	Lateral point of lateral epicondyle
88	Femur	Lateral point of lateral femoral condyle
89	Femur	Posterior point of lateral femoral condyle
90	Femur	Medial point of lateral femoral condyle

Table 6.2. Continued.

Number	Bone	Landmark Description
91	Femur	Inferior point of lateral femoral condyle
92	Femur	Central/deepest point of intercondylar fossa
93	Femur	Medial point of medial femoral condyle
94	Femur	Posterior point of medial femoral condyle
95	Femur	Lateral point of medial femoral condyle
96	Femur	Inferior point of medial femoral condyle
97	Tibia	Medial intercondylar tubercle
98	Tibia	Anterior point of medial condyle
99	Tibia	Medial point of medial condyle
100	Tibia	Posterior point of medial condyle
101	Tibia	Lateral intercondylar tubercle
102	Tibia	Anterior point of lateral condyle
103	Tibia	Lateral point of lateral condyle
104	Tibia	Posterior point of lateral condyle
105	Tibia	Anterior point of tibial tuberosity
106	Tibia	Anterior midshaft
107	Tibia	Medial midshaft
108	Tibia	Posterior midshaft
109	Tibia	Lateral midshaft
110	Tibia	Anterior nutrient foramen
111	Tibia	Medial nutrient foramen
112	Tibia	Posterior nutrient foramen
113	Tibia	Lateral nutrient foramen
114	Tibia	Inferior-anterior point of fibular notch
115	Tibia	Inferior-posterior point of fibular notch
116	Tibia	Inferior point of anterior colliculus
117	Tibia	Inferior point of posterior colliculus

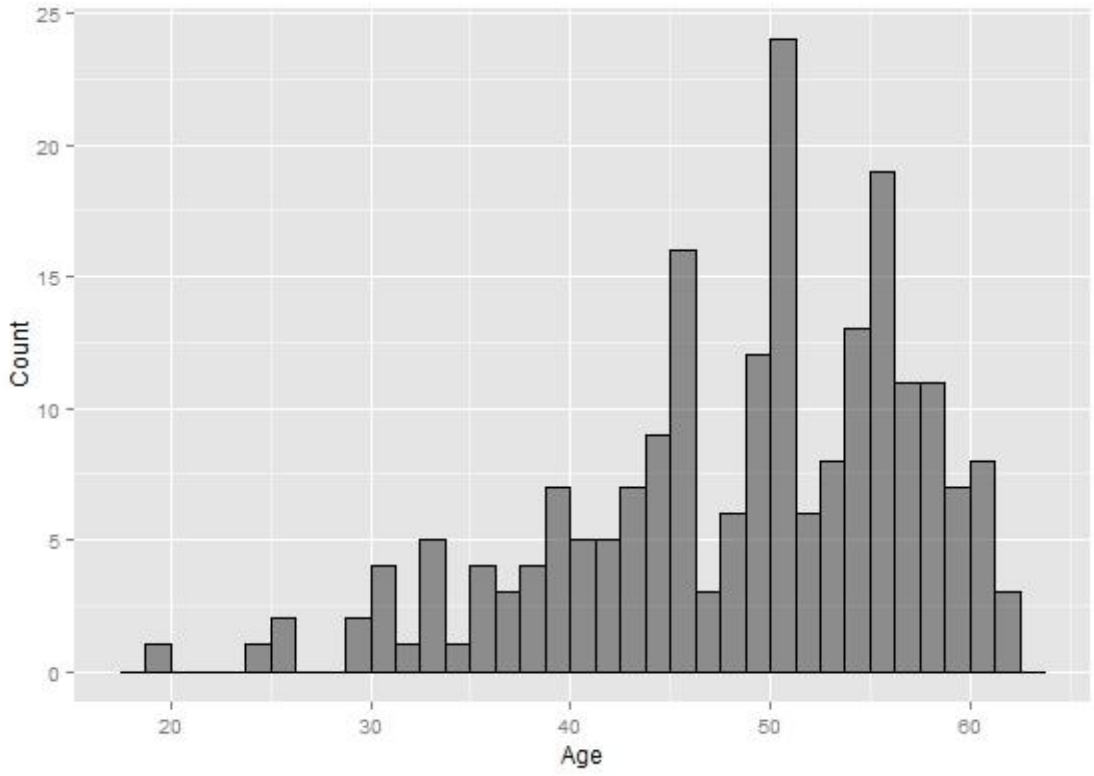

Figure 6.1. Age at Death Distribution of the Sample (n = 208).

Table 6.3. Number of Individuals by Sex.

Sex	# of Individuals
Female	105
Male	103
Total	208

Table 6.4. Number of Individuals by Ancestry.

Ancestry	# of Individuals
White	195
Black	10
Hispanic	3
Total	208

differ, size is an ambiguous concept without a unique quantification (Mitteroecker et al., 2013). Unlike size, shape has a unique definition. Shape is the geometric properties of an object that are invariant to translation, rotation, and scaling (Mitteroecker et al., 2013). Form is the geometric properties of an object that are invariant to only translation and rotation (Mitteroecker et al., 2013). Thus, two objects have the same form if they are both the same shape and size. Proportion is the comparison of size measures of an object without (or minimal) reference to the spatial relationship between the measures, such as the ratio of maximum length and width (Figure 6.2b).

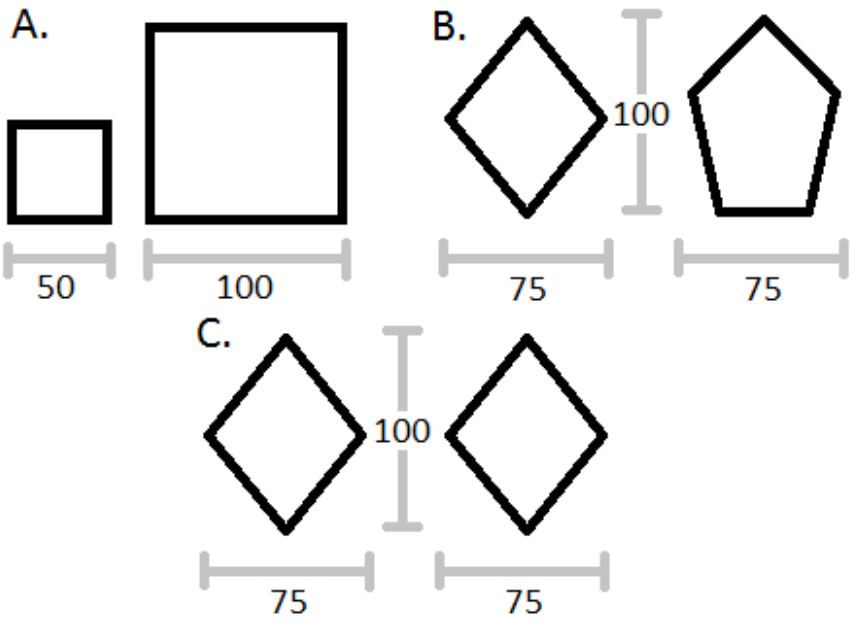

Figure 6.2. Graphical representation of size and shape and their relation to form and proportion.

Because the spatial context of landmarks is not maintained through data collection, SOM rarely have relationships with other dimensions (Ousley and McKeown, 2001). As such, these measurements mainly inform on size relationships, while providing only general information on shape through the use of proportions or comparisons of homologous measurements with generally similar spatial contexts, such as maximum breadth at midshaft. This type of shape information, however, can be misleading. As Figure 6.2b shows, these different shapes have the same maximum length and width measurements, but different shapes. The object forms presented in Figure 6.2c are identical to the diamond in Figure 6.2b, but using the information provided by SOM, these objects are indistinguishable from the pentagram in Figure 6.2b. This limitation is an example of the "harsh reduction of available information" available from SOM (Rosing and Pischtschan 1995:40). Geometric morphometric landmark data provide a way of addressing this limitation in information loss by retaining the relative geometric properties of bone form.

Landmark data were collected using a Microscribe G2X Digitizer (Year of manufacture: 2002, Manufacturers: Solution Technologies, Oella, Maryland) (Figure 6.3). This model of digitizer consists of base that rests on a fixed space, an upper limb with multiple joints terminating into a stylus, which designates the point in space to be collected, to a positional accuracy of 0.23 mm (Immersion, 2002). The instrument is connected to a foot pedal or a hand-held button and to a computer via a USB port. When the stylus is positioned on the appropriate landmark, the foot pedal or button is pressed and the position of the landmark is communicated

to the computer and stored in an Advantage Data Architect database via a custom version of 3Skull (Ousley, 2004).

Figure 6.3. The Microscribe G2X Digitizer used in the current study.

2. Methods

Prior to digitizing, each landmark is assessed and marked with an erasable pencil. These landmarks fall into one of three broadly defined categories (Bookstein, 1991):

Type 1: intersection of biological structures. e.g., medial intersection of coronoid and radial notch;

Type 2: maximum or minimum curvatures or projections, e.g., anterior point of coronoid process;

Type 3: composite landmarks based on estimates, e.g., anterior diaphysis at nutrient foramen.

A majority of the landmarks in this study are Type 2, and to a lesser extent, Type 3. Type 1 landmarks are typically discrete points in space are highly repeatable and regarded as providing the strongest evidence for homology between specimens (Bookstein, 1991). Type 2, and especially Type 3 landmarks, are subject to assessment error and homology is supported by geometric, not histological evidence (Bookstein, 1991). Because the current study examines one species, only error in landmark assessment is relevant.

Uncertainty in landmark placement represents methodological error in morphometric data (Arnqvist and Martensson, 1998). Methodological error is minimized in this study by standardizing element placement and observer viewpoint during landmark assessment and the use of calipers to determine the position of composite measurements. To maintain the same relational space during data collection, both the base of the digitizer, which acts as the datum, and the specimen being digitized must remain stationary—only the digitizer upper limb and stylus can move. This requirement leads to another form of error in morphometric data, personal error, or uncertainty in the placement of the stylus on the landmark (Arnqvist and Martensson, 1998). Instrument error is the last form of error in morphometric data. As stated above, the digitizer used in this study has a positional accuracy of 0.23 mm, making the effect of instrument error minimal (Immersion, 2002).

2.1. Data Analysis

2.1.1. Generalized Procrustes Analysis (GPA)

Raw landmark data are subjected to a GPA using the program MorphoJ (Klingenberg, 2011) to extract Procrustes coordinates and centroid size. This analysis superimposes landmarks in a sample by translating, scaling, and rotating coordinates to a common shape space (Figure 6.4). This superimposition starts by calculating the centroid for each specimen. The centroid is the average of all landmarks (Mitteroecker et al., 2013). A specimen's centroid acts as a "gravitational center", allowing for its configuration of landmarks to be represented by a single point (Mitteroecker and Gunz, 2009; Zelditch et al., 2004; Rosas and Bastir, 2002). Centroid size is a composite measurement of size that is equal to the summed squared distances between all landmarks and their centroid (Mitteroecker et al., 2013). Compared to SOM, centroid size is a better representation of size because it incorporates information from all coordinates, instead of only along an axis, such as maximum length (Mitteroecker et al., 2013). As such, centroid size is less affected by shape differences when compared to other size measures, making comparisons of size between different shaped objects relatable (Mitteroecker et al., 2013).

To remove the effect of isometric size, each specimen is translated according to their centroid position and scaled to the mean centroid size (Mitteroecker and Gunz, 2009). For mathematical simplicity, mean centroid size is scaled to 1 and its position is centered on the origin, so each centroid is a single point on the surface of a unit sphere (Mitteroecker and Gunz, 2009; Zelditch et al., 2004).

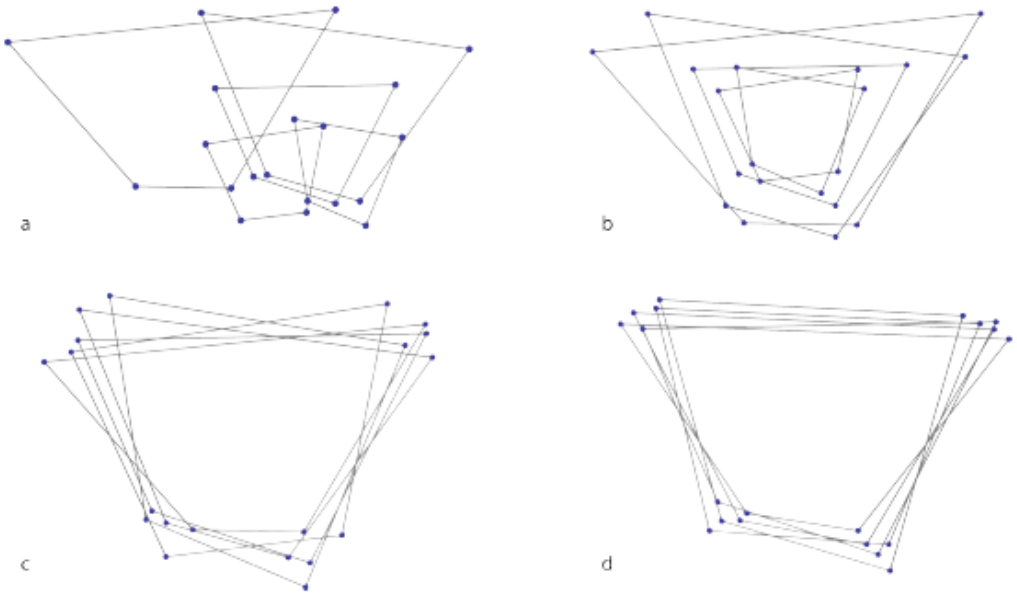

Figure 6.4. Schematic representation of Generalized Procrustes analysis. From Mitteroecker et al. (2013), Figure 2.

After isometric size is removed, each specimen is iteratively rotated on its centroid to minimize the overall distance of the specimen's landmarks to other specimens (Rohlf, 1999). This overall distance is known as the Procrustes distance, which is the square root of the sum of squared differences between a specimen's landmarks and the average position of those landmarks (Rohlf, 1999). Thus, an element's Procrustes distance is a measure of its overall shape difference from the mean shape of the reference sample (Rohlf, 1999; Bookstein, 1991). Through scaling, translation and rotation, the result of GPA is a common space, known as Kendall's shape space (Mitteroecker et al., 2013). Shape space is non-Euclidean (non-linear) in nature; taking the form of the surface of a sphere (Rohlf, 1999). This space is reflected along its equator (Mitteroecker and Gunz, 2009). Thus, only the northern hemisphere of this space, where

the centroids are translated to its pole (origin), is relevant (Mitteroecker and Gunz, 2009). The position of landmarks in this space are Procrustes shape coordinates, which are directly comparable aspects of shape across elements of the same configuration. Shape space can be extended into form space by incorporating the natural logarithm of centroid size as a variable (Mitteroecker et al., 2013). Form space relates the overall form of objects while maintaining the isotropic properties of shape space (Mitteroecker et al., 2013). Because of this relational property, the natural log of centroid size is used as the size metric during analysis. All subsequent analyses were performed in R (R Core Team, 2015).

2.1.2. Partial least squares (PLS)

Because of the large number of coordinates and non-homologous landmarks between different elements, partial least squares analysis is applied to the Procrustes shape coordinates. This process allows selection of a small number of relevant composite variables and direct comparability between different elements. Partial least squares analysis is a class of techniques for data reduction and latent variable analysis (Chen and Hoo, 2011; Boulestiex and Strimmer, 2006; Rosipal and Kramer, 2005; Haenlein and Kaplan, 2004; Wegelin, 2000). This class of techniques shares a common method of extracting components—via ordinary least squares regression. Partial least squares is similar to Principal Components Analysis (PCA) and Canonical Correlation Analysis (CCA), which extract orthogonal score vectors that are weighted composites of the original dataset (Rosipal and Kramer, 2006). Typically, the goal with any type of predictive data reduction analysis is two-fold: 1) to find linear combinations that well-represent the original variables; and 2) to find highly correlated linear combinations. Because

PCA captures a maximum amount of variation from the original variables, it is an optimal solution to the first goal. In a predictive framework, where one block of variables is used to predict another block, PCA fails to achieve the second goal. This failure is due to the fact that PCA components between blocks of variables are not related to each other. On the other hand, CCA optimally achieves the second goal by creating linear combinations of each block that are maximally correlated with one another. However, CCA fails at the first goal because these linear combinations are not designed to capture information or variance within a block and are based on the correlation matrix of raw variables, obscuring the biological meaning of components and making the interpretation of components difficult (Wegelin, 2000; Bookstein, 1996). Furthermore, CCA components are unstable in instances of multicollinearity and solutions are not uniquely defined when the number of variables is large compared the sample size (Wegelin, 2000). While not optimal, PLS achieves both goals of predictive data reduction by finding linear combinations of variables through the covariance of raw variables that both capture variability and are highly correlated (Wegelin, 2000; Bookstein, 1996). Components of the X-block (T, see equation 7 below) are orthogonal, good representations of X, and are good at explaining Y. Components of the Y-block (U, see equation 7 below) are orthogonal, good representations of Y, and are highly correlated with T. Stated another way, PLS models create components that predict a set, or sets, of dependent variables from a set of independent variables that have the best predictive power on the dependent variables (Chen and Hoo, 2011). Partial least squares components are constructed from the following procedure (Maitra and Yan, 2008; Wegelin, 2000):

Let X and Y be two blocks of variables, where X is a n*p matrix and Y is a n*q matrix. Find a linear decomposition of X and Y such that $X = TP^T+E$ and $Y = UQ^T+F$, where

X-scores = Tn*r; Y-scores = Un*r

X-loadings = Pp*r; Y-loadings = Q 1*r

X-residuals = E n*p; Y-residuals = F n*1 (6.1)

Components are extracted iteratively and the number of components (r) depends on the rank of X and Y (Maitra and Yan, 2008). Decomposition is finalized when the covariance of T and U is maximized and convergence is reached (Chen and Hoo, 2011).

Solution of first eigenvector $= X^t YY^t X; Y^t XX^t Y$ (6.2)

Once the first components have been extracted, the original values of X and Y are deflated as (Maitra and Yan, 2008),

$X_1 = X - tt^TX$ and $Y_1 = Y - tt^TY$ (6.3)

The process is repeated until all possible components T and U are extracted, when X is reduced to a null matrix (Chen and Hoo, 2011). Decisions on the number of components to retain for further analysis are typically done through cross-validation resampling procedures (Sanchez, 2015; Garthwaite, 1994). The cross-validation procedure used in this analysis is a form of jackknife resampling (Sanchez, 2015):

1. The dataset is divided into 10 groups of approximately equal size.
2. One segment is the test set and the other nine are used to estimate the model and predict the observations in the test set.

The formula for assessing component acceptance is:

$Q^2_h = 1- (PRESS_h / RSS_{h-1})$, where

h = component

PRESS = Predicted Error Sum of Squares

RSS = Residual Sum of Squares (6.4)

3. This process is repeated using all 10 groups as a test set.

Component T_h is considered to be significant and is included in the analysis if Q^2_h is greater than or equal to 0.0975 (Sanchez, 2015). The package "plsdepot" (Sanchez, 2015) was used in R to extract significant PLS components.

2.1.3 Simulated Commingling

After the limb bone morphology of each individual is represented as a log centroid size and PLS components, 10 individuals are randomly removed from the total data set. These 10 individuals act as a simulated commingled population. One element is chosen as the independent (x) variable, with the 10 possible matching elements acting as the dependent (y) variable. For example, if we are interested in reassociating a left femur with 10 possible right femora, then the left femur is predicting the right femur. In this situation, the left femur is the independent variable and the right femur is the dependent variable. A left femur is selected from the commingled assemblage and compared to the 10 possible right femur matches. These comparisons are made using the osteometric reassociation model described below, with the remaining sample (total sample excluding the commingled individuals) acting as training data.

2.1.4 Bayesian regression

Because PLS components are orthogonal (Rosipal and Kramer, 2006) and log centroid size is uncorrelated with shape (Mitteroecker et al., 2013), each predictive variable can be treated as an independent line of evidence for reassociation. The model used for assessing each predictive variable is simple linear regression, which takes the form of:

$$y_i = \alpha + \beta x_i + \varepsilon_i \quad (6.5)$$

Where y_i and x_i are the *i*th case of the dependent and independent variables, respectively. The y-intercept is represented by α; and β represents the the slope, or coefficient by which the independent variable changes in relation to the dependent variable. The error term is ε_i and represents the stochastic part of the model that accounts for all other factors that influence the value of the dependent variable. The y-intercept and slope are the deterministic portions of the model.

Typically, the regression line is fit by finding the line that minimizes the squared vertical distance between all data points. While point estimates for the y-intercept and slope are calculated, uncertainty is not incorporated into those estimates. Confidence intervals attempt to deal with this limitation by defining a range of possible values for these parameters within an estimated level of certainty. Linear regression of this type is associated with frequentist inference and does not provide an intuitive or easily interpretable way for comparing multiple possible values of y_i. Bayesians specify regression models in terms of probability distributions, eliminating these inferential limitations. Bayes theorem is used to specify probability distributions, taking the form of:

$$\rho(\theta|y,x) \propto \rho(y|\theta,x)\rho(\theta,x) \quad (6.6)$$

In this unnormalized form, the posterior probability $\rho(\theta|y,x)$ of parameters θ given data y and constants x is proportional (for fixed y and x) to the product of the likelihood function $\rho(y|\theta,x)$ and prior $\rho(\theta,x)$(Stan Development Team, 2015).

The Bayesian regression model used in this study assigns a normal distribution to the y-variable, with improper prior distributions for regression parameters. Prior distributions for the regression parameters are improper in the sense that they are modeled as random draws from a uniform distribution. Unbounded (-∞ to +∞) uniform priors are assigned to the alpha and beta regression parameters, with a positive uniform (0< to +∞) assigned to sigma. This model is needed because of its flexibility. Variable values will change based on the type of comparison and to a lesser degree, the variable values of the individuals in the training set. Thus, an abstracted regression model is needed to help ensure predictions are realistic for all variables. These uniform priors are essentially non-informative, leading the posterior distribution of the regression parameters to be driven by the likelihood of the training data.

2.1.5. Markov Chain Monte Carlo (MCMC)

Bayesians view parameters as observed realizations of random variables drawn from a probability distribution. As such, parameters are modeled as distributions, not point estimates with uncertainty around that estimate, which is the case in frequentist modeling. Markov Chain Monte Carlo methods provide a means for exploring the parameter space utilizing equation 6.6. Given a model, a likelihood, and data, MCMC simulate draws from the posterior distribution using quasi-dependent sequences of random variables (Kery, 2010; Lynch, 2007). This process

is repeated a large number of times to approximate the parameter's posterior distribution, or parameter space.

There are many algorithms available for searching this parameter space. All of these algorithms require an initial burn-in or wupper limb-up period (Stan Development Team, 2015; Kery, 2010; Lynch, 2007). This period is the initial sequence of random draws that are strongly influenced by initial starting values and are not representative of the posterior distribution of the parameter (Lynch, 2007). The Markov Chain is considered representative of the posterior parameter space once the chain has converged to equilibrium (Stan Development Team, 2015).

The effectiveness of a MCMC algorithm is measured by its ability to quickly reach convergence and exhaustively explore the parameter space. Many algorithms are inefficient in these respects because they can rely heavily on initial starting values and incoherently search parameter space (Stan Development Team, 2015). Hamiltonian Monte Carlo sampling, however, is both coherent and efficient (Stan Development Team, 2015). This method is based on modeling the behavior of particles using the properties of physical system (Hamiltonian) dynamics (Stan Development Team, 2015; Neal, 2011). This system state consists of the position of the particle, q, and the momentum of the particle, p (Neal, 2011). The position and momentum of the particle are described by its potential and kinetic energy, respectively (Neal, 2011). These energy forms are inversely related. As this particle moves across a surface, its potential and kinetic energy change with the slope of the surface.

Hamiltonian dynamics are extended to searching parameter space by interpreting the parameter θ as the position of a fictional particle at a point in time, with a potential energy

defined by the negative log of the probability density of θ and a stochastic momentum variable (Stan Development Team, 2015; Neal, 2011). Several properties of Hamiltonian dynamics make it ideal for searching parameter space (Neal, 2011). The first property is *reversibility*, allowing for reversals of the Markov chain, which promotes thorough exploration of parameter space. Second, is *conservation*, which along with reversibility, helps insure the target distribution is approximately invariant (Neal, 2011). The last property is *volume preservation* of the parameter space. This property simplifies the calculation of the acceptance probability for Metropolis updates (Neal, 2011).

Stated simply, Hamiltonian MCMC is an efficient and effective way of exploring parameter space. This method allows for the explicit modeling of uncertainty in parameter estimates, including the dependent variable. Thus, instead of a point estimate for the expected bone value, Hamiltonian MCMC provides a range of values for estimated bone value. These values are weighted by their relative simulated frequency.

The Hamiltonian MCMC sampler STAN implemented with the package "rstan" (Stan Development Team, 2015) in R was used to simulate y-values. Specifically, each variable was modeled using 1000 iterations across four chains with three simulated y-values per iteration. The package "shinyStan" (Stan Development Team, 2015) was used in R to periodically assess model diagnostics to confirm proper mixing and Markov chain convergence. The default in STAN is to treat the first half of iterations as the wupper limb up period (Stan Development Team, 2015). Thus, for each commingled assemblage 6000 y-values were simulated for each

predictive variable. Further treatment is required to transform these values into a probability density function to assess the relative probabilities of each possible match.

2.1.6. Model diagnostics

Convergence of the MCMC simulations is required for the simulated y-values to be a good predictive representation (Stan Development Team, 2015). Visual inspection of autocorrelation and chain mixture and metrics, including r-hat and effective sample size values, are methods for assessing model convergence. Autocorrelation plots should look like an inverse exponential curve in histogram form, where autocorrelation is high initially and drops off quickly. Chain mixture plots should show no discernable pattern, where each chain moves around parameter space without getting "stuck" in a particular area. An r-hat value is an estimate of convergence based on mean and standard deviation estimated from each chain (Stan Development Team, 2015). Chains have properly converged with r-hat values between 1.0-1.2; the closer to 1.0, the better the convergence. Effective sample size (effective n) is an estimate of the information available from each simulation; the closer the effective sample size is to the number of simulations, the better the chain convergence.

Given the number of commingled assemblages simulated in this study (n=40,000) and at least six variables for each simulation, assessment of model diagnostics for each variable in each simulation would be impractical. Instead, model diagnostics are assessed periodically and over all accuracy is used as a means for identifying unwieldly models. The example presented in the Chapter 7 provides a step-by-step analysis of a commingled simulation, including all model diagnostics.

2.1.7. Kernel density estimation

Kernel density estimation is a means of estimating a probability density function based on the frequency of sample values (Duong, 2007; Simonoff, 1996). This family of techniques fits a continuous line to the shape of the data with a kernel and bandwidth (Simonoff, 1996). The kernel is a non-negative function centered on zero that integrates to one (Duong, 2007). The bandwidth is a free parameter that determines the width of the data range on which the kernel function is fit (Park and Marron, 1990). A small bandwidth for the data results in an under-smoothed density estimate, containing spurious data artifacts and is essentially "connecting the dots" between data points. An overly wide bandwidth results in an over-smoothed density and obscures the underlying structure of these data. The function density( ) in the package "stats" (R Core Team, 2015) was used in R to fit a kernel density to the simulated y-values. The bandwidth used in this study is approaches an optimal solution for the density estimate by selecting a bandwidth that is the standard deviation of the kernel function (R Core Team, 2015).

2.1.8. Estimating best matches

The result of this analysis is a probability density function of y-values for a given x-value for each predictive variable on which the values for the 10 possible matches can be evaluated. The function approx( ) in the package "stats" (R Core Team, 2015) was used in R to evaluate densities for each possible match. These densities are used in four different ways to estimate the best match for each commingled assemblage; two overall best match estimates, one only considering size information, and one only considering shape information. In the first overall best match estimate, each possibility is weighted by its density estimate for each variable. This calculation takes the form of:

$$Pr_i = \frac{\Sigma(di_{1\ldots n})}{\Sigma(dtot_{1\ldots n})} \qquad (6.7)$$

where Pr_i is the match probability for the i^{th} possible match, di_n is the density estimate of the i^{th} possible match for the n^{th} predictive variable and $dtot_n$ is the density estimate of all possible matches for the n^{th} predictive variable. Calculating match probability in this way does not weigh each predictive variable equally. Predictive variables that have high correlations between x-and y-values will result in tightly dispersed simulated y-values, because uncertainty in its prediction is low (Figure 6.5). Conversely, predictive variable that have low correlations also have high uncertainty in y-value predictions, leading to widely dispersed y-values (Figure 6.5). This relationship between predictive ability of a variable and the standard error of simulated y-values affects the resulting density estimates (Figure 6.6). With this calculation of match probability, predictive variables with higher correlations will lead to higher density estimates and larger relative contributions to the overall match probability. However, these larger relative contributions may swamp the contribution of other, lower correlated variables, leading to spurious classifications if the best match from predictive variables with high correlations is not the correct match.

The second calculation of overall match probability weights all predictive variables equally. This calculation takes the form of:

$$Pr_i = (\frac{di_1}{dtot_1} + \frac{di_2}{dtot_2} + \cdots \frac{di_n}{dtot_n})/n \qquad (6.8)$$

where the notation is the same as formula 13. Here, densities are normalized into probabilities

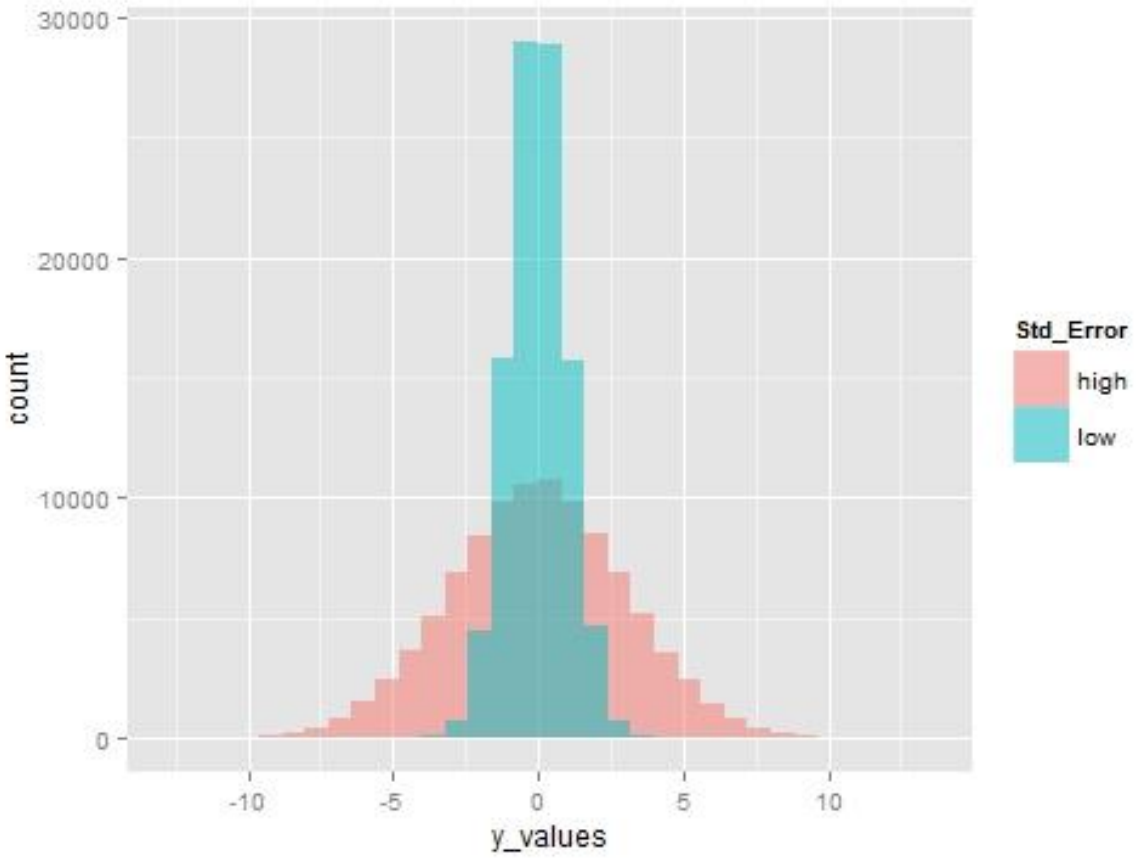

Figure 6.5. Relationship between predictive ability of a variable and the distribution of simulated y-values, or the standard error around the mean estimate. Each sample is 100,000 random draws from a normal distribution with a mean of 0 and different standard d eviations. The blue sample (low) has a standard deviation of 1 and the pink sample (high) has a standard deviation of 3.

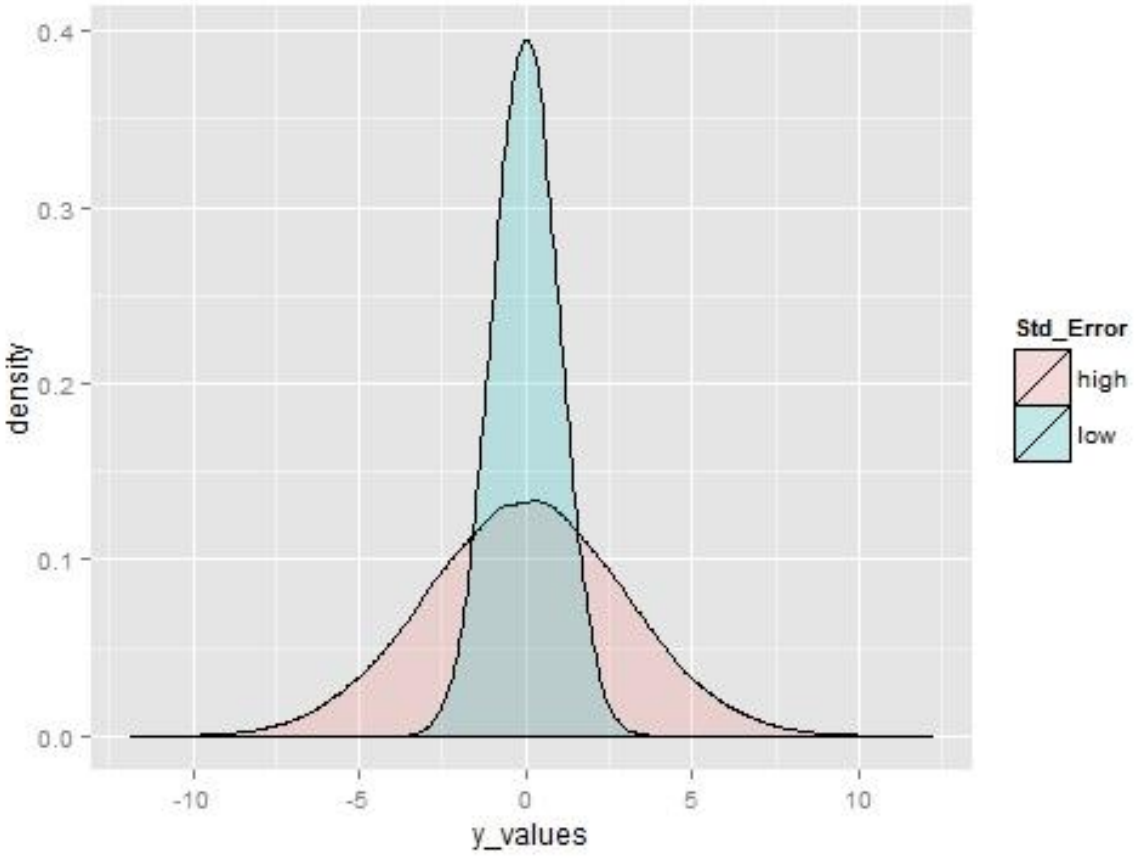

Figure 6.6. The density distributions of the samples in Figure 19. A high standard error in the estimation of y results in low density estimates, especially for the mean predicted y-value. Conversely, a low standard error results in high density estimates for values around the mean.

for each variable. The overall match probability is the sum of these probabilities divided by the number of variables.

The match probability considering size information is based on centroid size. This size match probability takes the form of:

$$Pr_i = \frac{di_{size}}{dtot_{size}} \qquad (6.9)$$

where Pr_i is the size match probability for the i^{th} possible match, di_{size} is the density estimate of the i^{th} possible match for centroid size and $dtot_{size}$ is the density estimate of all possible matches for centroid size.

The match probability considering shape information is based on the PLS components. This shape match probability takes the form of:

$$Pr_i = \frac{(\frac{di_{pls.1}}{dtot_{pls.1}} + \frac{di_{pls.2}}{dtot_{pls.2}} + \cdots \frac{di_{pls.n}}{dtot_{pls.n}})}{pls.n} \qquad (6.10)$$

where Pr_i is the shape match probability for the i^{th} possible match, $di_{pls.n}$ is the density estimate of the i^{th} possible match for the n^{th} PLS component and $dtot_{pls.n}$ is the density estimate of all possible matches for the n^{th} PLS component.

2.1.9. Accuracy

Accuracy is defined as the number of times the best match is the correct match divided by the number of simulations. For each comparison, commingled assemblages are simulated and the best match is predicted 1000 times. This number of simulations should adequately account for sampling error in assessing osteometric reassociation accuracy.

2.1.10. Typicality

Typicality is a measure of how typical a possible match is to the mean expected value (Ousley and Jantz, 2004). Predictive probabilities measure the strength of evidence for a match in relationship to other matches. Predictive probabilities cannot identify cases where no individual is a good match. This study calculates typicality values for possible matches to assess its ability to detect model error, or when the best match is not the correct match. Typicality is defined as the mean expected value density divided by the possible match density.

2.2. Summary of data analysis

Raw landmark data are subjected to a GPA to extract log centroid size and Procrustes coordinates. Log centroid size represents the size component for the osteometric reassociation model. Procrustes coordinates are reduced into PLS components, representing the shape component for the osteometric reassociation model. After the limb bone morphology of each individual is represented as a log centroid size and PLS components, 10 individuals are randomly removed from the total data set. These 10 individuals act as the simulated commingled assemblage. One element is chosen as the independent variable and is compared to 10 possible matching elements, which are the dependent variables. The remaining individuals in the total data set are the training set for the osteometric reassociation model.

The osteometric reassociation model is Bayesian regression via Hamiltonian MCMC. Log centroid size and PLS components are assessed individually using this model. For each variable, 6,000 dependent variable values are simulated for the dependent variable value. This sample of dependent variable values is smoothed into a probability density function using kernel density estimation. Values for the 10 possible matches are then evaluated against this probability

density to arrive at density values for each possible match. This process is repeated across all relevant predictive variables. Density values are then normalized in to match probabilities for each possible match. The best match is considered the possible match with the highest probability. This process is repeated 1000 times for each comparison. The accuracy of a comparison is the number of times the best match is the correct match divided by 1000.

3. Discussion

Geometric morphometric landmark data are used to test the hierarchical structure of osteometric reassociation as developed from biomechanical and developmental theory. The novelty of this approach is two-fold: first, it is only the second study to incorporate biomechanical theory into the methodology of osteometric reassociation and is the first to apply both biomechanical and developmental theory. Second, this study is the first to use landmark data to quantify long bone morphology for osteometric reassociation. These data are superior to SOM by providing a better metric of size through log centroid size and explicitly quantifies shape through Procrustes coordinates. The use of geometric morphometric landmark data greatly alleviates the issue of a "harsh reduction of available information" provided by SOM (Rosing and Pischtschan 1995:40).

While the nature of centroid size makes it a comparable variable across different elements, Procrustes coordinates are not. It is necessary to subject the Procrustes coordinates to PLS analysis to provide composite variables that explain the covariation of shape between elements. These PLS components are orthogonal and these shape components are size-

independent. Because of these properties, each variable is an independent line of evidence and can be examined individually.

Bayesian statistics is employed in this study in two ways: for modeling and for inference. Regression modeling through a Bayesian paradigm makes assumptions explicit by assigning distributions to parameters and simulating random draws from those distributions and evaluating those draws with the likelihood given the data. This process explicitly models uncertainty in parameter estimates by representing them as distributions instead of point estimates. These distributions are evaluated through a constant value for the independent variable to estimate a distribution of possible values for the dependent variable. The independent variable represents the bone, of which the 10 possible matches, or dependent variable, are being compared. These comparisons come in the form of a probability of a correct match relative to the other possibilities.

Given that the simulated commingled assemblages are closed-populations with no element loss, overall posterior probabilities are an appropriate metric for reassociation. In real-world situations, commingled assemblages meeting these conditions are rare. Posterior probabilities offer no information on closed-population and element loss assumptions. For the method used in this study to have real-world applicability, posterior probabilities should be coupled with a measure of typicality. In this regard, the predictive distribution is also useful. The predictive distribution can be used to assess how typical an element is compared to the predicted value of that bone. A typicality probability can be understood as similar to a *p* value,

where low values (< 0.05) indicate a questionable match no matter how large the predictive probability (Jantz and Ousley 2005).

4. Summary

Geometric morphometric landmark data is a reliable and repeatable way of capturing information on long bone morphology. These data are subjected to a GPA to convert data into a comparable shape space in the form of Procrustes coordinates. These coordinates are then transformed into PLS components that explain the covariation of shape between elements. Commingled assemblages are then simulated by randomly sampling 10 individuals from the total dataset. The PLS components and centroid size are used to assess the relative probability of a correct match through the use of Bayesian regression. The best match is considered the bone with the largest overall posterior probability. Accuracy is assessed through the rate that the best match is not the correct match. These error rates are compared across comparison types to test the hierarchical structure to accuracy in osteometric reassociation.

Chapter 7

Results

This chapter provides the results of reassociating elements from simulated commingled assemblages with regards to the hypothetical structure of accuracy in osteometric reassociation. First, intraobserver error results are presented. Next, overall accuracy and accuracy by comparison type are given. After accuracy results, comparison types are considered in more detail. Details include the predictive probability rank for correct matches and descriptive statistics for predictive probabilities and typicality values. Lastly, a step-by-step example of this methodology is provided. This consideration gives a nuanced understanding of the methodology used for resolving commingling and guidelines for interpreting outputs of this method in practical applications that will be discussed in Chapter 8.

1. Intraobserver error

As discussed in Chapter 6, there are three types of error associated with geometric morphometric data: instrument, methodological, and personal error (Arnqvist and Martensson, 1998). Instrument error is reported in Chapter 6. Methodological and personal errors represent intraobserver error. To assess intraobserver error, the landmarks of the left-side elements of one individual (101-10D) were marked with an erasable pencil and collected 10 separate times over the course of several months and the left-side elements of 101-10D were marked with an erasable pencil once and collected 10 times, which assess methodological error and personal error, respectively. These data were standardized separately using Generalized Procrustes Analysis, in order to compare Procrustes distances between trials. These Procrustes distances are

an overall measure of the absolute magnitude of shape deviation for each trial from the mean shape of the sample (Klingenberg and Monteiro, 2005). The variability in shape difference from methodological and personal error is compared to shape variability in the reference sample (Table 7.1).

Table 7.1. Descriptive statistics for error in landmark placement (methodological error) and stylus placement (personal error) between repeats of the same individual (n = 10) as measured by Procrustes distance. These errors are compared to shape variability in the reference sample.

	Methodological Error			**Personal Error**			**Reference Sample**		
Bone	Mean	Max.	Min.	Mean	Max.	Min.	Mean	Max.	Min.
Humerus	0.0167	0.0183	0.0153	0.0067	0.0084	0.0049	0.0614	0.1790	0.0197
Ulna	0.0091	0.0216	0.0060	0.0059	0.0080	0.0045	0.0613	0.3653	0.0234
Radius	0.0087	0.0182	0.0054	0.0067	0.0113	0.0054	0.0603	0.1810	0.0199
Femur	0.0151	0.0400	0.0069	0.0045	0.0062	0.0035	0.0684	0.2206	0.0188
Tibia	0.0080	0.0110	0.0064	0.0044	0.0053	0.0032	0.0426	0.2180	0.0180
Total	**0.0115**			**0.0056**			**0.0588**		

Error in data acquisition is minimal. The mean Procrustes distance between repeated measures (n = 10) of methodological error is 0.0115, which is over five times smaller than the mean Procrustes distance of the reference sample (0.0588). The mean and range of methodological error is comparable between elements, especially when this error is compared to the shape variability in the reference sample. The magnitude of difference between shape variability in the reference sample and methodological error ranges from almost 4 times greater for the humerus to almost 7 times greater for the radius and ulna. Additionally, methodological error is only twice as large as personal error, suggesting that the identification of landmarks on an element is highly repeatable and an appreciable amount of methodological error may be

accounted for by error in stylus placement. These results compare favorably with those of Holliday and Friedl (2013), who used a similar suite of landmarks to examine hominoid humeral morphology. These authors reported an average difference over 4 times between mean Procrustes distance of human humeri (n = 74, mean distance = 0.04) compared to repeated trials of the same specimen (n = 20, mean distance = 0.0095) (Holliday and Friedl 2013).

2. Accuracy

Forty different element comparisons were analyzed, resulting in 40,000 simulated commingled assemblages and an overall accuracy of 0.514, or 20,572 correct classifications (Table 7.2). For every comparison type, equal variable weight provided the best correct classification rates (Table 7.3). Because of this consistent performance, general accuracy refers to correct equal weight classifications, unless otherwise noted.

Table 7.2. The accuracy and number of comparisons for each comparison type.

Comparison Type	Comparisons	Accuracy
Homologous	10	0.787
Serially Homologous	4	0.409
Within Limb	8	0.499
Between Limbs	18	0.415
Total	40	0.514

Homologous elements have the highest accuracy (Table 7.4), followed by within limb (Tables 7.6-7.7), between limbs (Tables 7.8-7.10), and lastly, serially homologous elements (Table 7.5). However, homologous comparisons have very high accuracy and all other comparison types are within 4% of each other. For within-and between-limb comparisons,

Table 7.3. The accuracy of different calculations of predictive probability by comparison type. Equal variable weights provide the best accuracy for all comparison types and is in bold.

Comparison Type	Density	**Equal**	Size	Shape
Homologous	0.568	**0.787**	0.517	0.609
Serially Homologous	0.294	**0.409**	0.278	0.259
Within Limb	0.346	**0.449**	0.334	0.232
Between Limbs	0.315	**0.415**	0.300	0.230
Total	0.377	**0.514**	0.355	0.318

differences between upper limb and lower limbs is minimal, especially for between-limb comparisons (between-lower limb accuracy = 0.455 and between-upper limb accuracy = 0.450). Between upper limb and lower limb comparisons have the lowest overall levels of accuracy and are lower than serially homologous comparisons.

Table 7.4. Accuracy of homologous comparisons by predictive probability type. The '~' denotes prediction and is read as y~x, where the bone on the right side of '~' predicts the bone to the left of '~'.

Comparison Type	Density	Equal	Size	Shape
Right Femur~Left Femur	0.535	0.782	0.488	0.615
Left Femur~Right Femur	0.550	0.722	0.487	0.577
Right Tibia~Left Tibia	0.669	0.884	0.633	0.711
Left Tibia~Right Tibia	0.694	0.900	0.652	0.726
Right Humerus~Left Humerus	0.493	0.792	0.468	0.573
Left Humerus~Right Humerus	0.503	0.836	0.477	0.636
Right Radius~Left Radius	0.452	0.668	0.412	0.480
Left Radius~Right Radius	0.478	0.704	0.453	0.552
Right Ulna~Left Ulna	0.650	0.818	0.553	0.633
Left Ulna~Right Ulna	0.662	0.812	0.559	0.654
Average	**0.569**	**0.787**	**0.518**	**0.616**

Table 7.5. Accuracy of serially homologous elements by predictive probability type. The '~' denotes prediction and is read as y~x, where the bone on the right side of '~' predicts the bone to the left of '~'.

Comparison Type	Density	Equal	Size	Shape
Right Femur~Right Humerus	0.288	0.356	0.286	0.193
Right Humerus~Right Femur	0.279	0.366	0.269	0.232
Right Tibia~Right Ulna	0.309	0.451	0.292	0.271
Right Ulna~Right Tibia	0.310	0.451	0.283	0.299
Average	**0.297**	**0.406**	**0.283**	**0.249**

Table 7.6. Accuracy of within-lower limb comparisons by predictive probability type. The '~' denotes prediction and is read as y~x, where the bone on the right side of '~' predicts the bone to the left of '~'.

Comparison Type	Density	Equal	Size	Shape
Right Femur~Right Tibia	0.363	0.492	0.353	0.282
Right Tibia~Right Femur	0.368	0.492	0.357	0.237
Average	**0.366**	**0.492**	**0.355**	**0.260**

Table 7.7. Accuracy of within-upper limb comparisons by predictive probability type. The '~' denotes prediction and is read as y~x, where the bone on the right side of '~' predicts the bone to the left of '~'.

Comparison Type	Density	Equal	Size	Shape
Right Humerus~Right Radius	0.254	0.355	0.239	0.249
Right Radius~Right Humerus	0.299	0.356	0.280	0.153
Right Humerus~Right Ulna	0.245	0.339	0.237	0.217
Right Ulna~Right Humerus	0.242	0.352	0.224	0.191
Right Radius~Right Ulna	0.492	0.583	0.485	0.259
Right Ulna~Right Radius	0.501	0.620	0.494	0.268
Average	**0.339**	**0.434**	**0.327**	**0.223**

Table 7.8. Accuracy of between-lower limb comparisons by predictive probability type. The '~' denotes prediction and is read as y~x, where the bone on the right side of '~' predicts the bone to the left of '~'.

Comparison Type	Density	Equal	Size	Shape
Left Femur~Right Tibia	0.337	0.431	0.326	0.203
Right Femur~Left Tibia	0.380	0.479	0.367	0.274
Average	**0.359**	**0.455**	**0.347**	**0.239**

Table 7.9. Accuracy of between-upper limb comparisons by predictive probability type. The '~' denotes prediction and is read as y~x, where the bone on the right side of '~' predicts the bone to the left of '~'.

Comparison Type	Density	Equal	Size	Shape
Left Humerus~Right Radius	0.267	0.372	0.252	0.255
Left Humerus~Right Ulna	0.240	0.346	0.227	0.253
Right Humerus~Left Radius	0.290	0.360	0.277	0.261
Right Humerus~Left Ulna	0.277	0.299	0.216	0.195
Right Radius~Left Ulna	0.450	0.535	0.427	0.248
Left Radius~Right Ulna	0.403	0.562	0.391	0.237
Right Ulna~Left Radius	0.402	0.590	0.389	0.314
Left Ulna~Right Radius	0.427	0.532	0.410	0.233
Average	**0.338**	**0.450**	**0.324**	**0.250**

Table 7.10. Between upper limb and lower limb comparisons by predictive probability type. The '~' denotes prediction and is read as y~x, where the bone on the right side of '~' predicts the bone to the left of '~'.

Comparison Type	Density	Equal	Size	Shape
Right Femur~Right Radius	0.281	0.387	0.270	0.274
Right Radius~Right Femur	0.258	0.315	0.243	0.177
Right Femur~Right Ulna	0.236	0.336	0.225	0.168
Right Ulna~Right Femur	0.269	0.335	0.264	0.188
Right Humerus~Right Tibia	0.268	0.330	0.256	0.141
Right Tibia~Right Humerus	0.275	0.372	0.259	0.229
Right Radius~Right Tibia	0.304	0.422	0.279	0.211
Right Tibia~Right Radius	0.321	0.446	0.298	0.271
Average	**0.277**	**0.368**	**0.262**	**0.207**

A closer look at specific comparisons within these types demonstrates some interesting trends. For homologous comparisons, shape-only predictions are typically better than density-weighted predictions. For all other types of comparisons, however, density-weighted predictions perform better than shape-only predictions, with shape-only predictions performing close to size-only predictions. Distal element serially homologous comparisons outperform proximal comparisons by almost 10%. The similarity in overall upper limb and lower limb accuracy for within-and between-limb comparisons is the result of high accuracy of radius and ulna comparisons. Radius and ulna comparisons outperform humerus and radius/ulna comparisons by roughly 20% for both with-and between-upper limb comparisons. The high accuracy of radius and ulna comparisons combined with low accuracy of humerus and distal upper limb element comparisons bring the overall accuracy of upper limb comparisons close to the levels observed in the lower limb.

3. Comparisons details

This section presents descriptive statistics for predictive probabilities and typicality values for each comparison, separated by correct and incorrect classification. Additionally, the predictive probability ranks of correct matches are provided by predictive probability type. These details help to identify possible trends in these values and ranks for future application of this method. Each section provides correct match ranks and descriptive statistics for a comparison type. Correct match rank and descriptive statistics for specific comparisons are in the Appendix.

3.1. Homologous comparisons

Tables 7.11 and 7.12 give homologous comparison correct match ranks and descriptive statistics, respectively. While in general, predictive probability values are higher for correctly classified individuals, correct and incorrect classification ranges show extensive overlap. Typicality values show no obvious trends between classification and prediction types.

Like all comparisons, equal variable weight predictions provide the highest overall correct classification. Density predictions quickly "catch up" to equal weight performance, encompassing a similar percentage of the correct matches by the third largest predictive probability. Density predictions perform better than equal weight predictions by the fourth ranked predictive probability. This trend is interesting in light of the distributional properties of these predictive probabilities. For both correct and incorrect classifications, density weighted probabilities are roughly twice as large as their equal weight counterparts, with the maximum values for equal weight predictive probabilities lower than the mean value of density probabilities. Thus, while density probabilities are more certain of the best match, they are more often wrong than equal weight probabilities. There is a similar relationship between size and shape predictive probabilities. The best match is more often the correct match using shape probabilities compared to size probabilities. As stated above, shape information alone is more accurate than density probabilities, which use both shape and size information in estimation. However, size probabilities outperform shape probabilities by the second rank, encompassing 77.33% and 75.42% of correct matches, respectively. Mean values for size probabilities are more than twice that of shape probabilities. Again, like density and equal weight probabilities, the maximum values for shape probabilities are smaller than size probability mean values.

Table 7.11. Correct match predictive probability rank for homologous comparisons (n = 10000).

Density				Equal			
Rank	Frequency	Percent	Cumulative	Rank	Frequency	Percent	Cumulative
1	5676	56.76%	56.76%	1	7874	78.74%	78.74%
2	2251	22.51%	79.27%	2	962	9.62%	88.36%
3	1114	11.14%	90.41%	3	361	3.61%	91.97%
4	536	5.36%	95.77%	4	208	2.08%	94.05%
5	217	2.17%	97.94%	5	159	1.59%	95.64%
6	95	0.95%	98.89%	6	100	1.00%	96.64%
7	42	0.42%	99.31%	7	101	1.01%	97.65%
8	22	0.22%	99.53%	8	86	0.86%	98.51%
9	20	0.20%	99.73%	9	72	0.72%	99.23%
10	27	0.27%	100.00%	10	77	0.77%	100.00%
Size				Shape			
1	5173	51.73%	51.73%	1	6094	60.94%	60.94%
2	2560	25.60%	77.33%	2	1448	14.48%	75.42%
3	1257	12.57%	89.90%	3	747	7.47%	82.89%
4	576	5.76%	95.66%	4	454	4.54%	87.43%
5	237	2.37%	98.03%	5	314	3.14%	90.57%
6	105	1.05%	99.08%	6	269	2.69%	93.26%
7	50	0.50%	99.58%	7	206	2.06%	95.32%
8	22	0.22%	99.80%	8	157	1.57%	96.89%
9	13	0.13%	99.93%	9	150	1.50%	98.39%
10	7	0.07%	100.00%	10	161	1.61%	100.00%

Table 7.12. Descriptive statistics for predictive probability and typicality values for correctly and incorrectly classified homologous comparisons.

	Density			Equal			Size			Shape		
	Correct Classifications											
	Mean	Min	Max	Mean	Min	Max	Mean	Min	Max	Mean	Min	Max
Probability	0.421	0.163	0.828	0.207	0.132	0.399	0.503	0.169	1.000	0.195	0.136	0.412
Typicality	0.893	0.080	1.000	0.789	0.314	0.975	0.890	0.090	1.000	0.703	0.271	0.842
	Incorrect Classifications											
	Mean	Min	Max	Mean	Min	Max	Mean	Min	Max	Mean	Min	Max
Probability	0.315	0.161	0.735	0.171	0.128	0.283	0.354	0.165	0.965	0.169	0.132	0.323
Typicality	0.906	0.114	1.000	0.706	0.317	0.933	0.909	0.114	1.000	0.658	0.254	0.825

3.2. Serially homologous comparisons

Tables 7.13 and 7.14 give serially homologous comparison correct match ranks and descriptive statistics, respectively. Again, typicality values show no obvious trends and predictive probability values are higher for correctly classified individuals, with broad overlap. The difference between mean predictive probabilities for correctly and incorrectly classified individuals for serially homologous comparisons, however, is reduced compared to homologous comparison values. Additionally, serially homologous predictive probabilities distributional properties are similar across classification and prediction types, with mean values typically lower than homologous comparisons.

As shown in the accuracy section, serially homologous comparisons have much lower overall accuracy (0.409) compared to homologous comparisons (0.787). This uncertainty extends to the predictive probability rank of correct matches for serially homologous comparisons. For example, homologous comparisons have the correct match in the top three predictive probabilities over 90% of the time when all variables are considered. This amount of

correct match coverage is not attained until the sixth ranked predictive probability for serially homologous comparisons. Again, the trend for density weighted predictions to preform closer to the values observed in equally weighted predictions after the first rank holds true for serially homologous comparisons. Another interesting observation from serial homologous comparisons is the reduced performance of shape predictions. For homologous comparisons, shape predictions are second in performance after equal weight predictions. Shape predictions for serially homologous elements, however, perform poorly.

3.3. Within-limb comparisons

Tables 7.15 and 7.16 give within-limb comparison correct match ranks and descriptive statistics, respectively. The trend continues of larger predictive probability values with correct classifications, with large overlap in the distributions of these values. The relationship of mean values of predictive probability types, however, is different. With homologous and serially homologous comparisons, density-weighted and size probabilities are larger than equal-weight and shape probabilities (Tables 7.12 and 7.14). Within-limb comparisons, on the other hand, have predictive probability mean values that are much closer to each other.

Unlike predictive probability mean values, correct match predictive probability ranks for within-limb comparisons show a similar relationship between size and shape when compared to other comparison types. The addition of shape information improves model performance markedly, but only when shape variables are weighted equally when compared to size. When weighted by density, shape information provides only a very marginal improvement in model performance.

Table 7.13. Correct match predictive probability rank for serially homologous comparisons (n = 4000).

Density				Equal			
Rank	Frequency	Percent	Cumulative	Rank	Frequency	Percent	Cumulative
1	1177	29.43%	29.43%	1	1634	40.85%	40.85%
2	843	21.08%	50.50%	2	835	20.88%	61.73%
3	693	17.33%	67.83%	3	464	11.60%	73.33%
4	484	12.10%	79.93%	4	306	7.65%	80.98%
5	361	9.03%	88.95%	5	184	4.60%	85.58%
6	218	5.45%	94.40%	6	186	4.65%	90.23%
7	120	3.00%	97.40%	7	126	3.15%	93.38%
8	53	1.33%	98.73%	8	106	2.65%	96.03%
9	28	0.70%	99.43%	9	89	2.23%	98.25%
10	23	0.58%	100.00%	10	70	1.75%	100.00%
Size				Shape			
1	1113	27.83%	27.83%	1	1034	25.85%	25.85%
2	872	21.80%	49.63%	2	648	16.20%	42.05%
3	691	17.28%	66.90%	3	462	11.55%	53.60%
4	519	12.98%	79.88%	4	378	9.45%	63.05%
5	361	9.03%	88.90%	5	301	7.53%	70.58%
6	211	5.28%	94.18%	6	325	8.13%	78.70%
7	129	3.23%	97.40%	7	301	7.53%	86.23%
8	58	1.45%	98.85%	8	228	5.70%	91.93%
9	35	0.88%	99.73%	9	188	4.70%	96.63%
10	11	0.28%	100.00%	10	135	3.38%	100.00%

Table 7.14. Descriptive statistics for predictive probability and typicality values for correctly and incorrectly classified serially homologous comparisons.

	Density			Equal			Size			Shape		
	Correct Classifications											
	Mean	Min	Max	Mean	Min	Max	Mean	Min	Max	Mean	Min	Max
Probability	0.314	0.139	0.833	0.252	0.179	0.476	0.342	0.140	0.970	0.263	0.196	0.519
Typicality	0.917	0.142	1.000	0.820	0.392	0.984	0.914	0.142	1.000	0.690	0.323	0.790
	Incorrect Classifications											
	Mean	Min	Max	Mean	Min	Max	Mean	Min	Max	Mean	Min	Max
Probability	0.246	0.125	0.715	0.225	0.169	0.391	0.255	0.126	0.813	0.245	0.192	0.429
Typicality	0.938	0.216	1.000	0.799	0.371	0.986	0.939	0.216	1.000	0.687	0.314	0.792

3.4. Between-limb comparisons

Tables 7.17 and 7.18 give between-limb comparison correct match ranks and descriptive statistics, respectively. As with other comparisons, there is substantial overlap of correct and incorrect classified predictive probabilities and typicality values are of minimal importance for identifying classification error. Like within-limb comparisons, the mean values of predictive probability types are similar, although generally lower. In terms of correct match predictive probability ranks, between-limb comparisons follow a similar patterning to other comparisons types. Equal-weight predictions preform the best, followed by density-weighted, size, and lastly, shape. Again, shape information only improves equal-weight model performance, suggesting that size dominates density-weighted predictions.

6. Summary

The results support the proposed hypothetical structure of accuracy in osteometric reassociation. Homologous comparisons have the highest accuracy with a 78.7% correct

Table 7.15. Correct match predictive probability rank for within-limb comparisons (n = 8000).

Density				Equal			
Rank	Frequency	Percent	Cumulative	Rank	Frequency	Percent	Cumulative
1	2764	34.55%	34.55%	1	3589	44.86%	44.86%
2	1786	22.33%	56.88%	2	1661	20.76%	65.63%
3	1242	15.53%	72.40%	3	938	11.73%	77.35%
4	795	9.94%	82.34%	4	565	7.06%	84.41%
5	540	6.75%	89.09%	5	391	4.89%	89.30%
6	359	4.49%	93.58%	6	274	3.43%	92.73%
7	235	2.94%	96.51%	7	209	2.61%	95.34%
8	164	2.05%	98.56%	8	139	1.74%	97.08%
9	74	0.93%	99.49%	9	118	1.48%	98.55%
10	41	0.51%	100.00%	10	116	1.45%	100.00%
Size				Shape			
1	2669	33.36%	33.36%	1	1856	23.20%	23.20%
2	1833	22.91%	56.28%	2	1351	16.89%	40.09%
3	1259	15.74%	72.01%	3	1089	13.61%	53.70%
4	811	10.14%	82.15%	4	917	11.46%	65.16%
5	553	6.91%	89.06%	5	721	9.01%	74.18%
6	360	4.50%	93.56%	6	652	8.15%	82.33%
7	238	2.98%	96.54%	7	475	5.94%	88.26%
8	164	2.05%	98.59%	8	369	4.61%	92.88%
9	74	0.93%	99.51%	9	321	4.01%	96.89%
10	39	0.49%	100.00%	10	249	3.11%	100.00%

Table 7.16. Descriptive statistics for predictive probability and typicality values for correctly and incorrectly classified within-limb comparisons.

	Density			Equal			Size			Shape		
	Correct Classifications											
	Mean	Min	Max	Mean	Min	Max	Mean	Min	Max	Mean	Min	Max
Probability	0.365	0.148	0.847	0.361	0.230	0.647	0.386	0.149	0.926	0.383	0.271	0.723
Typicality	0.902	0.226	1.000	0.826	0.279	0.993	0.900	0.226	1.000	0.620	0.173	0.702
	Incorrect Classifications											
	Mean	Min	Max	Mean	Min	Max	Mean	Min	Max	Mean	Min	Max
Probability	0.284	0.140	0.781	0.316	0.219	0.608	0.291	0.141	0.838	0.344	0.258	0.706
Typicality	0.926	0.194	1.000	0.811	0.226	0.992	0.927	0.194	1.000	0.635	0.147	0.704

classification rate. Within-limb comparisons correctly classified matches in 44.9% of cases, followed by between-limb comparisons at 41.5% correctly classified. Serially homologous elements were last with 40.9% of cases correctly classified. For all comparisons basing predictions on equal variable weights provide the highest accuracy. Shape predictions are the second best predictor for homologous comparisons. For all other comparison types, density predictions are the second best predictor, with shape and size predictions vying for the third and fourth spots. Size and density predictions have the highest predictive probabilities compared to equal weight and shape probabilities. Despite the less certainty, however, equal weight probabilities are more often correct. Typicality values are of little use in identifying model error.

Table 7.17. Correct match predictive probability rank for between-limb comparisons (n = 18000).

Density				Equal			
Rank	Frequency	Percent	Cumulative	Rank	Frequency	Percent	Cumulative
1	5662	31.46%	31.46%	1	7475	41.53%	41.53%
2	4007	22.26%	53.72%	2	4021	22.34%	63.87%
3	2939	16.33%	70.04%	3	2362	13.12%	76.99%
4	2065	11.47%	81.52%	4	1318	7.32%	84.31%
5	1436	7.98%	89.49%	5	891	4.95%	89.26%
6	870	4.83%	94.33%	6	601	3.34%	92.60%
7	529	2.94%	97.27%	7	447	2.48%	95.08%
8	290	1.61%	98.88%	8	334	1.86%	96.94%
9	131	0.73%	99.61%	9	336	1.87%	98.81%
10	71	0.39%	100.00%	10	215	1.19%	100.00%
Size				Shape			
1	5401	30.01%	30.01%	1	4134	22.97%	22.97%
2	4131	22.95%	52.96%	2	2999	16.66%	39.63%
3	3009	16.72%	69.67%	3	2474	13.74%	53.37%
4	2110	11.72%	81.39%	4	1907	10.59%	63.97%
5	1437	7.98%	89.38%	5	1658	9.21%	73.18%
6	886	4.92%	94.30%	6	1341	7.45%	80.63%
7	542	3.01%	97.31%	7	1161	6.45%	87.08%
8	297	1.65%	98.96%	8	952	5.29%	92.37%
9	130	0.72%	99.68%	9	799	4.44%	96.81%
10	57	0.32%	100.00%	10	575	3.19%	100.00%

Table 7.18. Descriptive statistics for predictive probability and typicality values for correctly and incorrectly classified between limb comparisons.

	Density			Equal			Size			Shape		
	Correct Classifications											
	Mean	Min	Max	Mean	Min	Max	Mean	Min	Max	Mean	Min	Max
Probability	0.298	0.124	0.773	0.272	0.179	0.540	0.317	0.128	0.859	0.290	0.204	0.584
Typicality	0.814	0.261	0.889	0.735	0.360	0.881	0.813	0.262	0.889	0.558	0.221	0.629
	Incorrect Classifications											
	Mean	Min	Max	Mean	Min	Max	Mean	Min	Max	Mean	Min	Max
Probability	0.233	0.117	0.637	0.239	0.171	0.449	0.239	0.116	0.705	0.260	0.195	0.547
Typicality	0.831	0.189	0.889	0.727	0.253	0.882	0.832	0.189	0.889	0.567	0.226	0.630

Chapter 8

Discussion

This study tests a biologically informed hypothetical structure to accuracy in osteometric reassociation through simulating commingled assemblages. The experimentally determined structure of osteometric reassociation accuracy closely matches but is not identical to the hypothetical structure. An argument will be made for biological reasons that explain the experimentally determined structure with regards to the hypothetical structure. Other possible contributing factors are also woven into this discussion. Next, a classification example is provided showing the process of identifying the best match. This example highlights important aspects of knowledge building and evidence consideration when making a decision to reassociate commingled bones. Lastly, future avenues of research are discussed.

1. The experimentally determined structure of accuracy in osteometric reassociation

The hypothetical structure of accuracy proposed from ontogenetic and functional adaption theory is supported by the experimental results of this study, with a few significant caveats. Homologous comparisons (78.7%) are 33.8% more accurate than the second best comparison type, within-limb comparisons (44.9%). Only 4% difference in accuracy separates the second best comparison type from the least accurate comparison type, serially homologous comparisons (40.9%). Thus, the experimental structure could best be stated as "homologous comparisons and everything else". The reason for this difference in accuracy between homologous comparisons and all other types is likely not based wholly in biology, but also in research design. Limb bones are numerically represented as centroid size and PLS components

based on Procrustes coordinates. As the name implies, landmarks between homologous elements are the same landmarks taken on left and right sides. The shape covariance structure of homologous elements leads to PLS components with much better predictive ability compared to other comparison types. Accuracy in shape predictions strongly supports this statement, where the difference in accuracy between homologous comparisons (60.9%) and everything else (ranging from 23.0%-25.9%) is 35.0%-37.9% (Table 7.3).

Specific homologous comparisons also highlight some possible research design influences. Tibiae are correctly matched 89.2% of the time—the most accurate of any comparison. Radii, on the other hand, are correctly matched in 68.6% of cases. Given that homologous elements do not differ in ontogenetic programs, only in functional adaptation, one could reasonably assume that the differences between these comparisons are due to asymmetrical loading regimes. Ulnae and humeri comparisons (81.5% and 81.4%, respectively) both outperform femoral comparisons (75.7%), refuting the influence of functional adaption on accuracy in osteometric reassociation. However, given the nature of landmark data, most of the landmarks in this study tend to cluster at joints, with only midshaft and nutrient foramen landmarks representing diaphyseal morphology. As Chapter 4 showed, joints are canalized against gross morphological response to loading, instead accommodating loads through changes in trabecular structure. Hence, the form of long bone quantification used in this study may be "missing" much of the influence of functional adaptation.

Another interesting result is the high classification rates of tibiae comparisons. These comparisons outperformed other homologous comparisons by an average of 14% (range of

7.7%-20.6%). Limb bone variation studies provide support for higher accuracy in tibiae comparisons. Tibiae consistently show the highest amount of variation (Auerbach and Sylvester, 2011; Holliday and Ruff, 2001; Jantz and Jantz, 1999), suggesting that the high accuracy in matching the tibia is the result of consistency within an individual coupled with high variation on the population level. Another biological factor may also be influencing homologous comparison accuracy—nutrient foramen placement. As suggested in Chapter 3 and noticed by the researcher during data collection, the placement of the nutrient foramen on the tibia is consistent compared to other limb elements. This assertion is addressed by looking at the consistency of nutrient foramen placement along the diaphysis between left and right sides, as assessed through the location of the x-position of the anterior diaphysis at nutrient foramen landmark (Table 8.1). There is a moderate correlation between left and right side tibial nutrient foramen placement (r^2 = 0.589). As for the rest of the limb bones, these landmarks are essentially noise. This study inadvertently found a biologically relevant consideration for osteometric research. Outside of the tibia, measurements that use the nutrient foramen as a landmark are of little to no biological or comparative value.

Table 8.1. Correlation of proximal-distal nutrient foramen placement between left and right sides.

Bone	r-squared
Tibia	0.589
Radius	0.177
Femur	0.161
Humerus	0.016
Ulna	0.004

Other comparison types show some interesting trends. At first, the 5.8% difference between within-lower limb (49.2%) and within-upper limb (43.4%) seems less than expected given the functional integration of the lower limb and the wide range of motion allowed at the elbow. Looking at specific within-upper limb comparisons, however, an obvious trend stands out (Table 7.7). Within-upper limb and lower limb comparisons are similar to within-lower limb comparisons because of the high accuracy in ulna and radius comparisons (60.2%). Humerus and distal upper limb comparisons show a much lower accuracy (35.0%) than any other within-limb comparisons. These trends in specific within-limb comparisons make sense in the context of ontogenetic and functional adaptation. The radius and ulna are intimately linked during use and articulate at the proximal and distal ends. The humerus, on the other hand, is less integrated with distal elements during use. Furthermore, the humerus shows autonomy from the distal elements during ontogeny along the proximal/distal axis. Accurate reassociation of within-upper limb humerus/distal elements has several biological factors working against them, which is evident in the low accuracy of these comparisons. While within-lower limb comparisons are supported by functional integration, developmentally, they are not. The femur and tibia show some autonomy across both developmental axes. The developmental modularity of proximal and distal limb elements appears to lower accuracy in osteometric reassociation. This finding also supports previous research on the variability in human limb proportions and the autonomy between proximal and distal elements (Auerbach and Sylvester, 2011).

Given that the ulna and radius articulate at two locations and are functionally integrated, at least within an upper limb, these high levels of accuracy are expected. This relationship,

however, has a few unexpected consequences. First, between-upper limb distal element comparisons have higher accuracy than all within-or between-lower limb comparisons, a surprising finding given the functional modularity of the upper limb and integration of the lower limb. Furthermore, between-upper limb comparisons show slightly higher overall levels of accuracy than within-upper limb comparisons, likely due to the larger number of distal upper limb element comparisons for between-upper limbs (n=4) than within-upper limbs (n=2), compared to an equal number of proximal-distal upper limb element comparisons for between- and within-upper limbs (n=4) (Table 7.7 and 7.9). Regardless, this trend highlights the relative autonomy of the humerus compared to distal upper limb elements. Accuracy of within-and between-lower limb comparisons may also suggest autonomy between proximal and distal elements. Functionally these limbs are well integrated. Developmentally, the femur and tibia show modularity across both axes. Opposing functional and developmental signals could be why within-and between-lower limb comparisons have accuracies that fall between proximal-distal upper limb comparisons and distal upper limb comparisons.

Radius and tibia comparisons (43.4%)—two elements with no developmental or functional relationship—have accuracy rivaling within-lower limb comparisons (49.2%). However, the tibia is the serial homologue of the ulna. Thus, the high accuracy of radius and tibia comparisons could be explained by the high accuracy of radius and ulna comparisons. This relationship could be further examined by including the fibula in this study. For example, if ulna and fibula comparisons had accuracy levels comparable to those of the radius and tibia, the functional and developmental relationship interplay suggested as a cause for high accuracy

between the radius and tibia would have added credence. The fibula, however, has very few landmarks that could be easily and reliably identified. Additionally, compared to the other limb bones, the fibula is fragile. Given the lack of identifiable shape information on the fibula and the requisite of complete, undamaged limb elements, the fibula is excluded from the current study.

The patterning of accuracy discussed above speaks to a broader trend, distal elements are better for reassociation than proximal ones (Table 8.2). Proximal and distal homologous element comparisons are essentially the same. Distal elements significantly outperform proximal elements in every other comparison type. The most salient of these are serially homologous comparisons. Femur and humerus represents the proximal serially homologous comparison and ulna and tibia represent the distal serially homologous comparison. There is very little developmental or functional reasoning to expect an almost 10% difference in accuracy between these two comparisons. Limb variation research does point to one possible cause: increased variation in distal elements. Increased variation in distal elements provides the difference between individuals along with consistency within an individual to accurately reassociate these bones.

Table 8.2. A comparison of accuracy for proximal and distal elements by comparison type.

Comparison	Proximal	Distal
Homologous	0.783	0.798
Serially Homologous	0.359	0.451
Within-limb	0.351	0.602
Between-limb	0.344	0.555

2. Classification example

This section provides a step-by-step discussion of the methodology for resolving commingling used in this study, using femora matching as an example. Table 8.3 is the ten randomly sampled commingled individuals; the correct match (33-08D) is highlighted in bold. This should be a difficult assemblage to correctly reassociate, given that the correct match and seven other possible matches are female.

Possible matches are fit against posterior distribution for each variable to estimate the probability of a correct match. The 5% and 95% quantiles for each distribution are also provided. These quantiles can be interpreted as rejection thresholds for eliminating possible matches using a two-tailed test with $\alpha = 0.10$. These correct match probabilities build on each other to arrive at an overall correct match. Model descriptive statistics and diagnostic criteria are also provided for each variable to assess the validity of variable estimation.

Table 8.3. Simulated commingled assemblage.

Individual	Sex	Age	Ancestry
33-08D	**F**	**29**	**White**
113-10D	F	45	White
43-10D	F	41	White
57-09D	F	34	White
37-11D	F	57	White
101-06D	F	60	White
15-97D	F	35	White
38-09D	M	50	White
40-11D	F	58	White
05-08D	M	53	White

2.1. Diagnostic criteria

Diagnostic criteria for all variables strongly suggest that model parameter estimates are valid (see summary statistics table and diagnostics figure for each variable). Visual inspection of autocorrelation and chain mixture plots, R hat values between 1.0 and 1.1 and effective sample sizes that approach the 2000 post wupper limb-up iterations, show that the sampling algorithm efficiently explores parameter space. Additionally, despite assigning a uniform or uninformative prior to regression parameters, all parameter distributions approximate a normal distribution, conforming to the central limit theorem. This result suggests the likelihood of these data is driving estimation and the flexibility of an abstracted model that can be universally applied to all variables is justified.

2.2. Centroid size

The first variable assessed is centroid size. The low estimated sigma value (0.02) shows that this variable is very useful for predicting the best match (Table 8.3). Surprisingly, the correct match is the fifth best match considering only centroid size (Figure 8.1). Predictive probabilities drop to essentially zero after the fifth best match and all other possibilities are beyond the quantiles, showing that the left femur in question and right femora after the fifth best match are extremely unlikely to be the correct match and all plot beyond the quantiles. As expected, the two least likely matches are the two males in the assemblage.

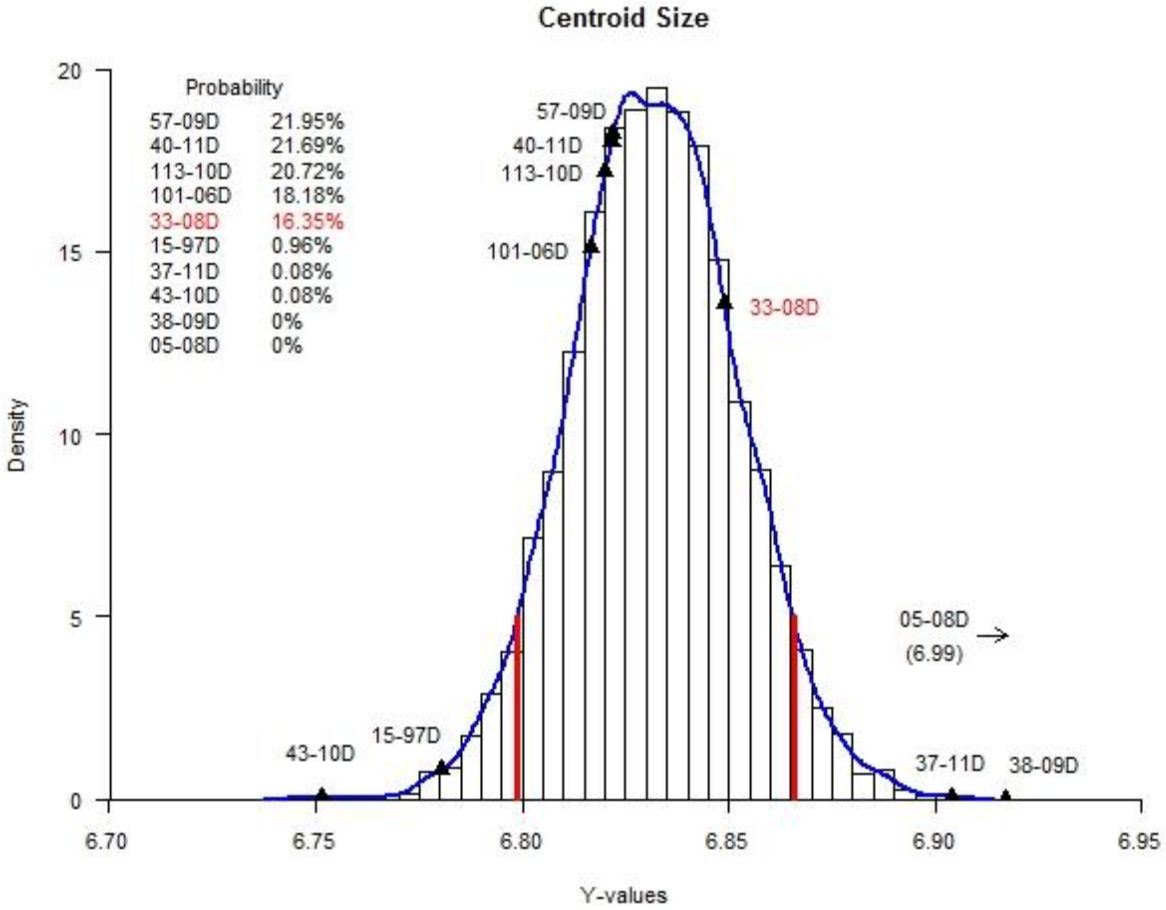

Figure 8.1. Histogram and kernel density estimate of y-values and match probabilities for centroid size. Red lines represent the 5% and 95% quantiles, respectively.

Table 8.4. Summary statistics for centroid size regression model.

Parameter	Mean	Std Error	SD	Effective n	R hat
alpha	0.35	0.01	0.16	1705	1.00
beta	0.95	0.00	0.02	1090	1.00
sigma	0.02	0.00	0.00	1576	1.00

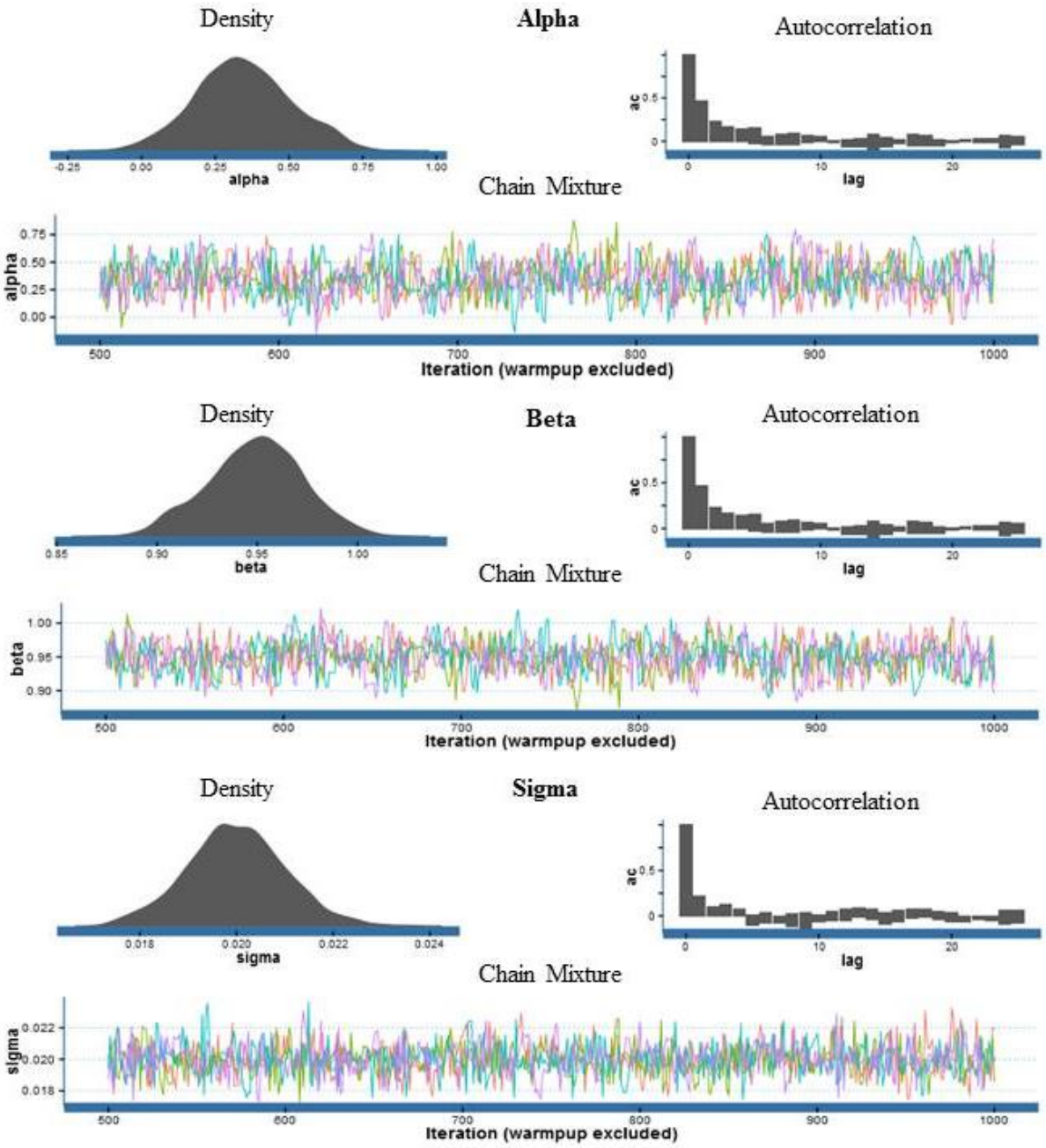

Figure 8.2. Summary and diagnostic visuals for centroid size regression model parameters. The density plot visualizes the posterior distribution of a parameter. The autocorrelation bar graph represents the correlation or dependency of MCMC draws. The chain mixture or trace plot measures how well the sampler is exploring parameter space.

2.3. First PLS component

Again, the correct match is the fifth best match based on the first PLS component (Figure 8.3). The large sigma value (8.86) for the first PLS component shows that there is a high degree of error associated with this variable, making it a relatively untrustworthy predictor (Table 8.3). Unlike centroid size, only one individual (38-09D) plots on an extreme tail of the distribution and can be confidently rejected as a possible match based on the first PLS component. Three of the four possible matches that rank higher than 33-08D for PLS 1 are also better matches based on centroid size. However, despite being the fifth best match for the first two variables, 33-08D is the fourth best match considering both variables. Three individuals, 15-97D, 101-06D, and 38-09D, plot beyond the quantiles.

2.4. Second PLS component

Like the first two variables, the correct match is the fifth best match (Figure 8.5). Additionally, most possible matches are fairly typical based on the second PLS component, suggesting that shape variables, in isolation, are poor for eliminating possible matches. This assertion is supported by only one individual, 05-08D, plotting beyond the quantiles. The correct match, 33-08D, remains the fourth best match after three variables.

2.5. Third PLS component

The correct individual is the second most likely match based on the third PLS component (Figure 8.7). Considering the first four variables, 33-08D is now the second best match. Interestingly, the two commingled males, 38-09D and 05-08D, are both ranked in the top five possible matches, suggesting size separates the sexes better than shape. Three individuals, 57-

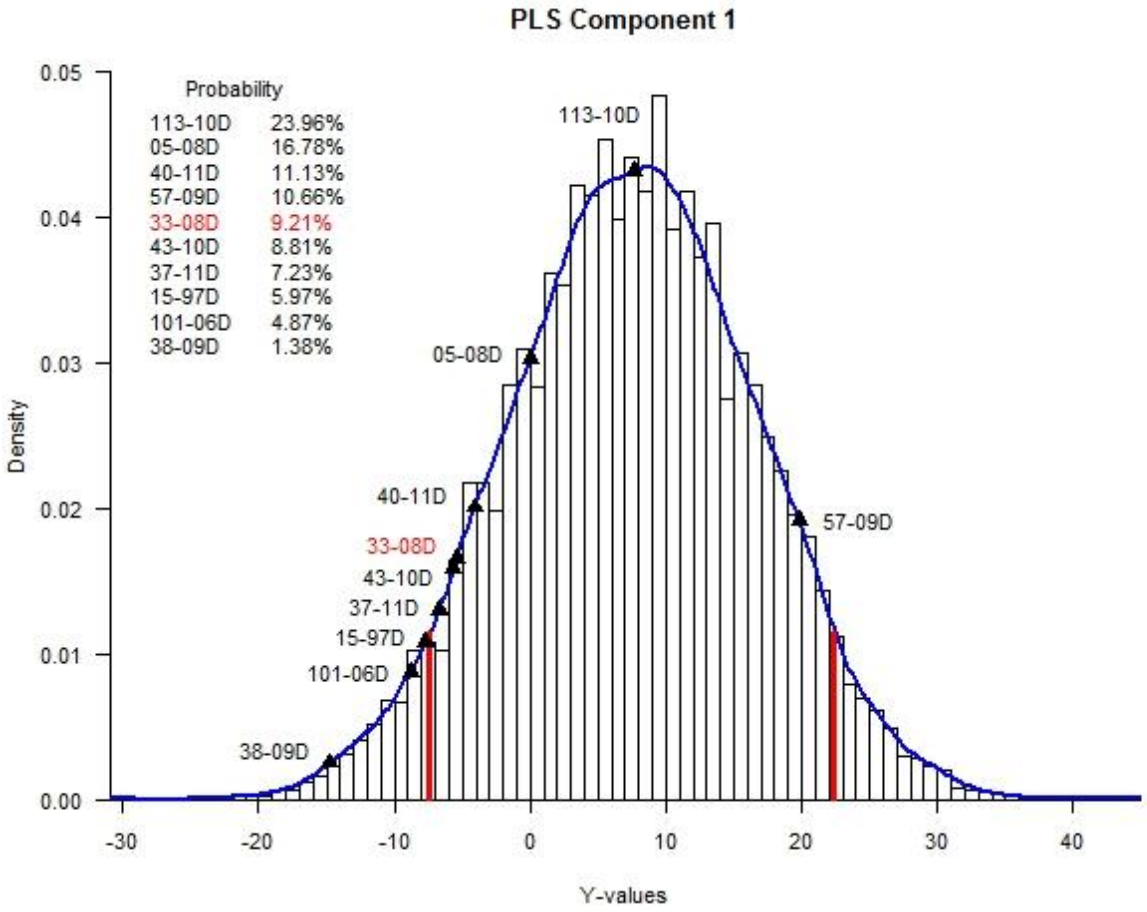

Figure 8.3. Histogram and kernel density estimate of y-values and match probabilities for PLS component 1. Red lines represent the 5% and 95% quantiles, respectively.

Table 8.5. Summary statistics for PLS component 1 regression model.

Parameter	Mean	Std Error	SD	Effective n	R hat
alpha	0.23	0.02	0.66	1662	1.00
beta	1.10	0.00	0.13	1467	1.00
sigma	8.86	0.01	0.47	1736	1.00

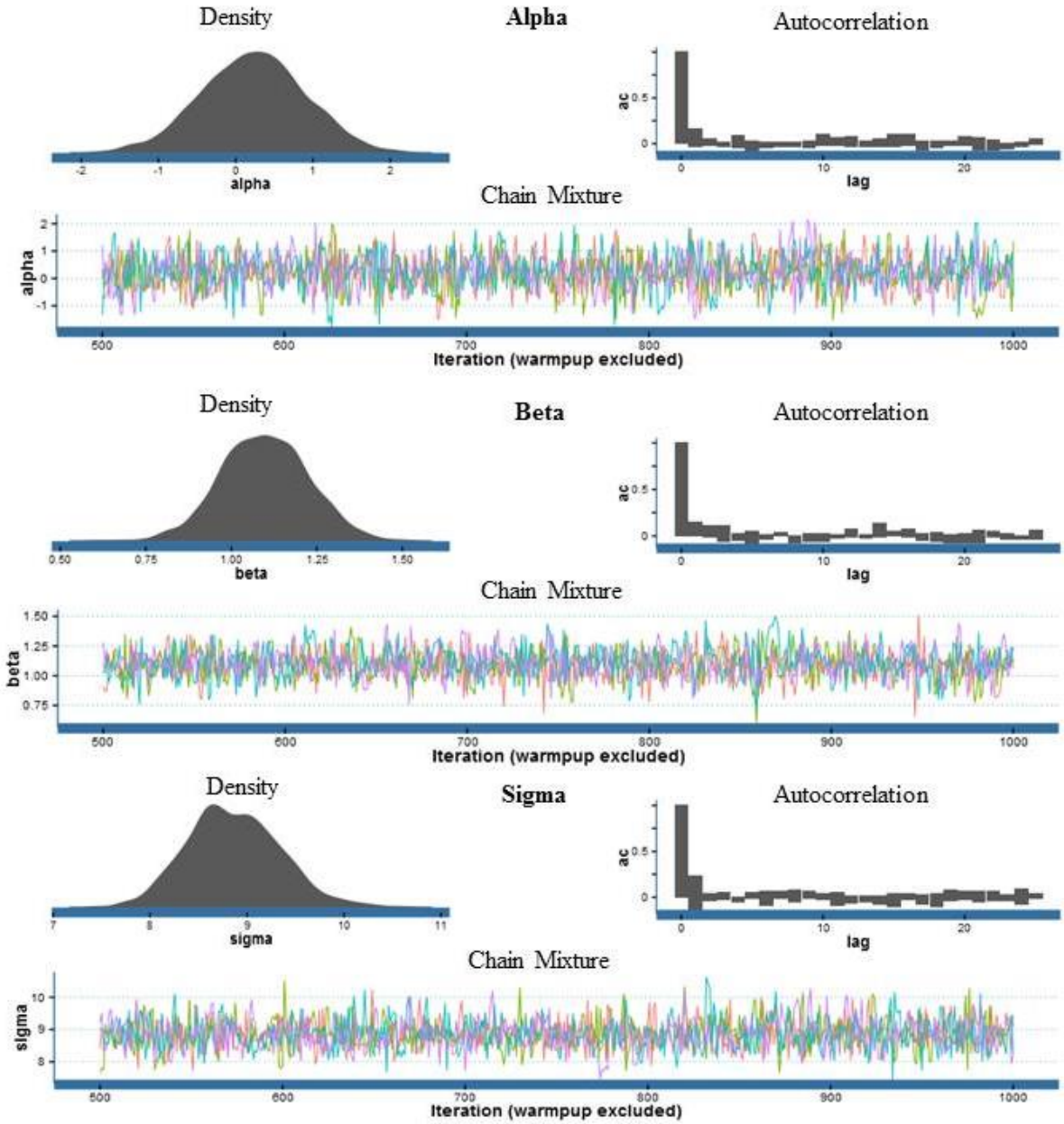

Figure 8.4. Summary and diagnostic visuals for PLS component 1 regression model parameters. The density plot visualizes the posterior distribution of a parameter. The autocorrelation bar graph represents the correlation or dependency of MCMC draws. The chain mixture or trace plot measures how well the sampler is exploring parameter space.

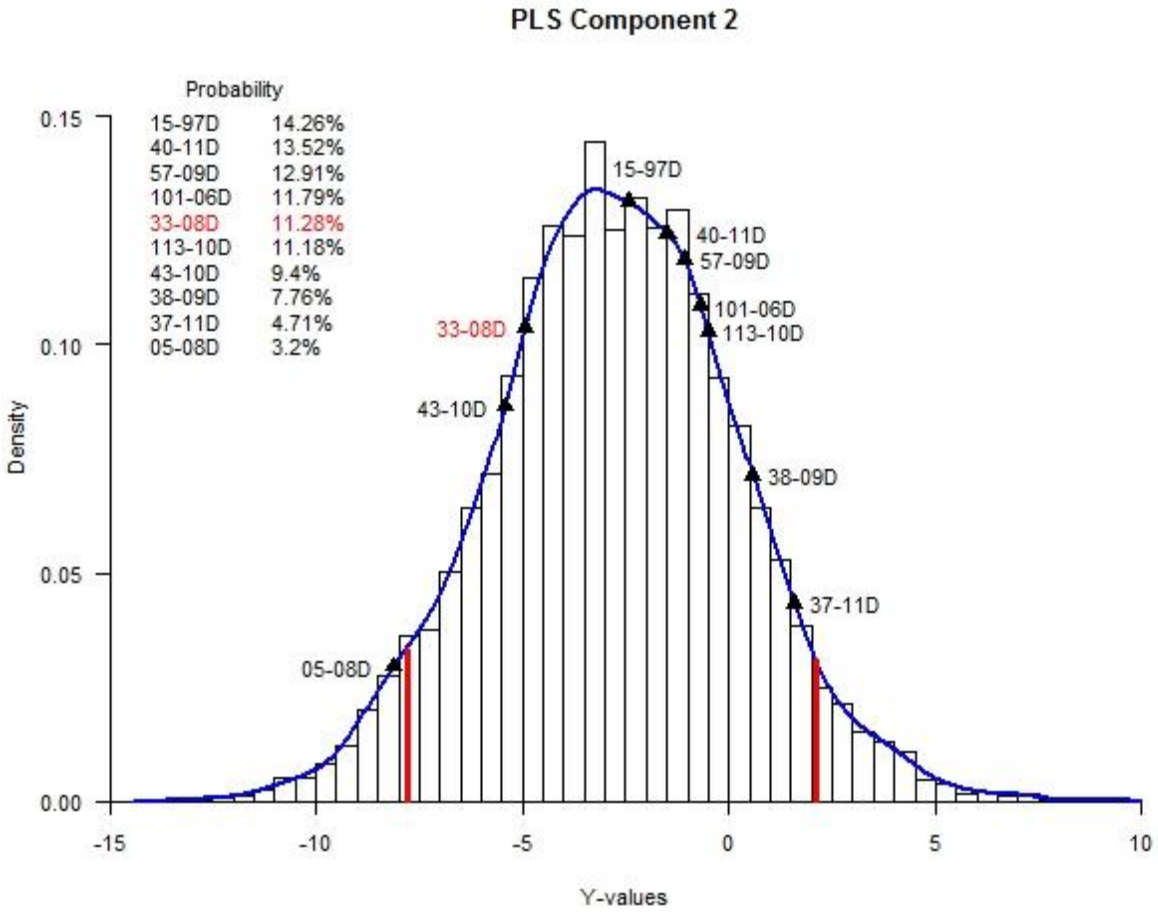

Figure 8.5. Histogram and kernel density estimate of y-values and match probabilities for PLS component 2. Red lines represent the 5% and 95% quantiles, respectively.

Table 8.6. Summary statistics for PLS component 2 regression model.

Parameter	Mean	Std Error	SD	Effective n	R hat
alpha	0.05	0.01	0.22	1605	1.00
beta	1.00	0.00	0.06	1800	1.00
sigma	2.98	0.00	0.15	1416	1.00

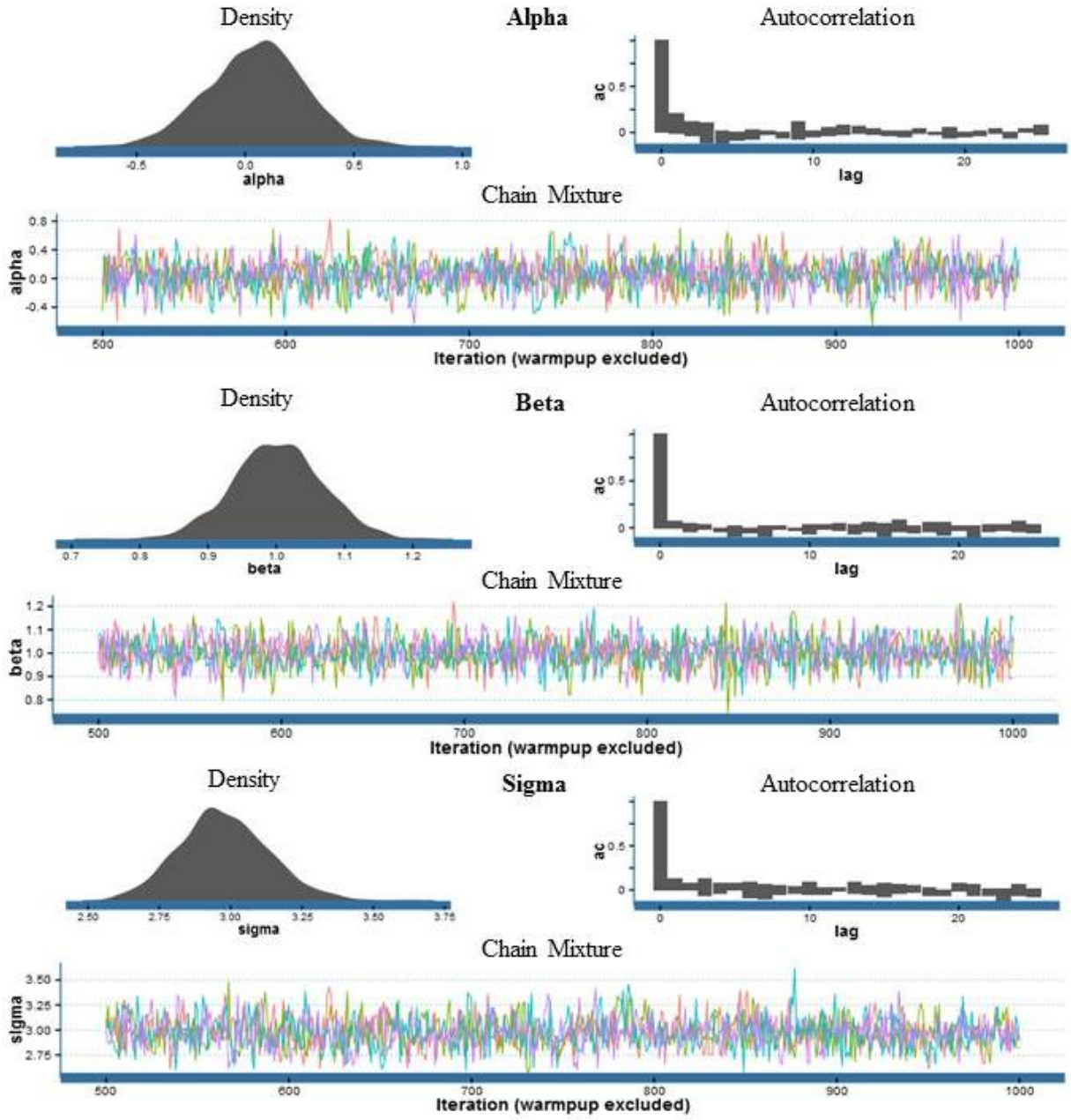

Figure 8.6. Summary and diagnostic visuals for PLS component 2 regression model parameters. The density plot visualizes the posterior distribution of a parameter. The autocorrelation bar graph represents the correlation or dependency of MCMC draws. The chain mixture or trace plot measures how well the sampler is exploring parameter space.

09D, 37-11D, and 40-11D, all fall beyond the quaniles.

2.6. Fourth PLS component

For the first time, 33-08D is the best match (Figure 8.9). Interestingly, unlike other PLS components, where most possible matches fall within a reasonable portion of the distribution, seven possible matches are on the extreme right tail of this variable, plotting beyond the 95% quantile. Because of this variable, 33-08D gains over 10% in its correct match probability, making it the best match.

Table 8.7. Cumulative predictive probabilities. The correct match and best match, 33-08D, is highlighted in bold.

Individual	Centroid	PLS 1	PLS 2	PLS 3	PLS 4	PLS 5	PLS 6	PLS 7	PLS 8
33-08D	**16.35**	**12.78**	**12.28**	**13.34**	**23.58**	**24.14**	**21.43**	**19.70**	**18.40%**
113-10D	20.72	22.34	18.62	15.45	13.45	11.41	11.68	12.05	11.99%
43-10D	0.08	4.45	6.10	10.13	8.10	10.02	10.55	11.07	11.76%
40-11D	21.69	16.41	15.45	11.59	9.27	8.49	9.39	9.69	10.59%
05-08D	0.00	8.39	6.66	8.91	7.13	10.75	9.92	9.89	9.50%
57-09D	21.95	16.31	15.17	12.01	15.22	13.01	11.15	9.77	8.72%
37-11D	0.08	3.66	4.02	3.21	2.95	4.69	5.62	6.71	7.78%
101-06D	18.18	11.53	11.61	12.53	10.03	9.03	8.52	8.39	7.63%
15-97D	0.96	3.42	7.03	7.54	6.04	5.16	6.66	7.17	7.29%
38-09D	0.00	0.69	3.04	5.29	4.23	3.63	5.34	5.81	6.56%

2.7. Fifth PLS component

For the fifth PLS component, 33-08D is the best match. Similar to the fourth PLS component, most possible matches are unlikely, falling near the tail of the distribution (Figure 8.11). Interestingly, other likely possible matches based on the fifth PLS component are much larger than 33-08D based on centroid size. Most of the comparably sized individuals are outside of the 5% quantile.

2.8. Sixth PLS component

Individual 33-08D is the seventh ranked match according to the sixth PLS component (Figure 8.13). Like the previous PLS component, many of the likely matches are poor matches for other variables. Only one individual, 57-09D, falls beyond the 95% quantile.

2.9. Seventh PLS component

Again, individual 33-08D is the seventh best match according to the seventh PLS component (Figure 8.15). However, unlike the previous two components, most possible matches are close to the mean predicted value. Only 57-09D falls outside of the 95% quantile.

2.10. Eighth PLS component

Like the previous two variables, 33-08D is the seventh best match according to PLS 8 (Figure 8.17). Two individuals, 57-09D and 101-06D are outside the quantiles. Despite being the seventh best match in the last three variables, 33-08D remains the best match when all variables are considered.

2.11. Model discussion

This example highlights the importance of including multiple lines of evidence in reassociating commingled remains. The correct match is the best match for only two of the nine variables. In fact, on average, 33-08D is the fourth best match. When all variables are considered together, however, 33-08D is the best match and over 1.5 more likely than the second best match. Additionally, 33-08D is the only individual with *no evidence against reassociation* (Table 8.14). All other individuals could be rejected as a possible match for at least two variables. Rejection criteria may be a useful metric for identifying model error, given that typicality values are generally not useful.

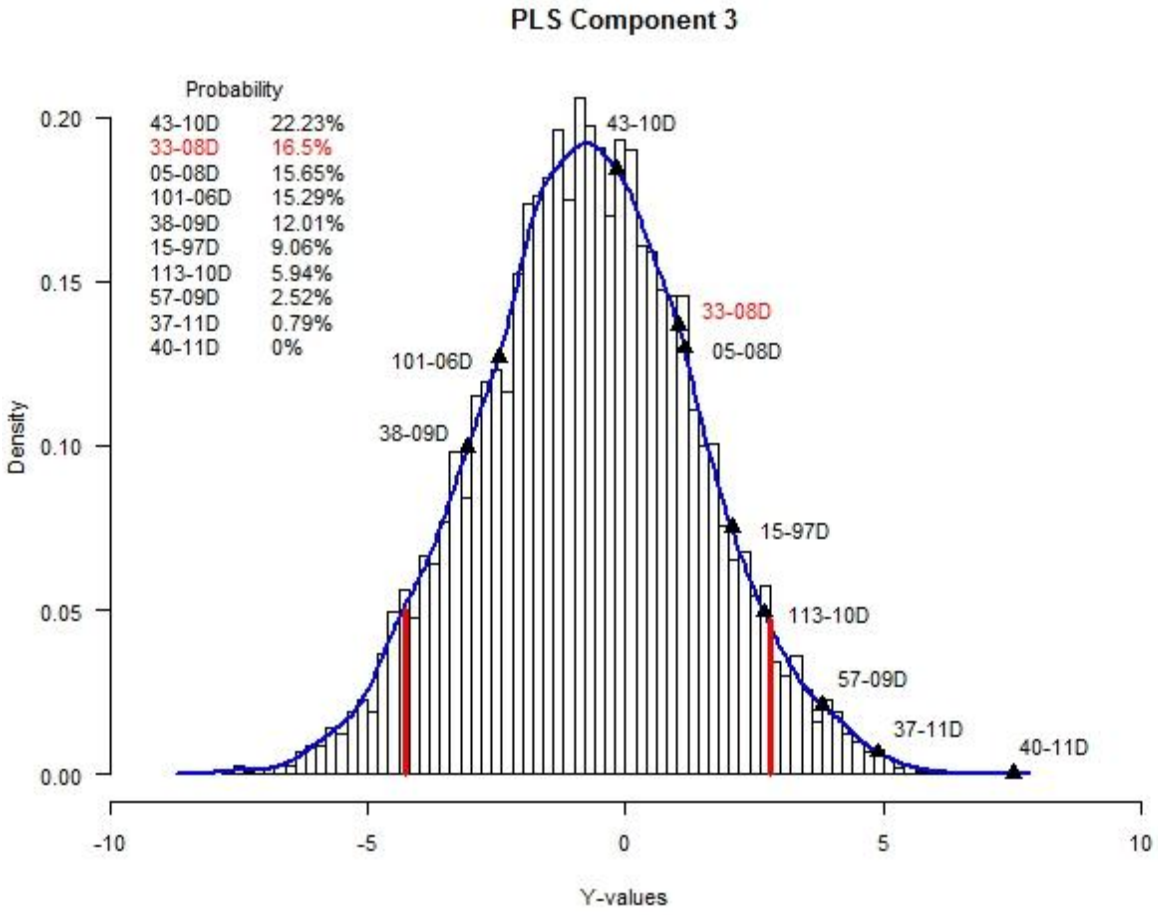

Figure 8.7. Histogram and kernel density estimate of y-values and match probabilities for PLS component 3. Red lines represent the 5% and 95% quantiles, respectively.

Table 8.8. Summary statistics for PLS component 3 regression model.

Parameter	Mean	Std Error	SD	Effective n	R hat
alpha	-0.03	0.00	0.15	1596	1.00
beta	1.00	0.00	0.05	1596	1.00
sigma	2.11	0.00	0.11	1414	1.00

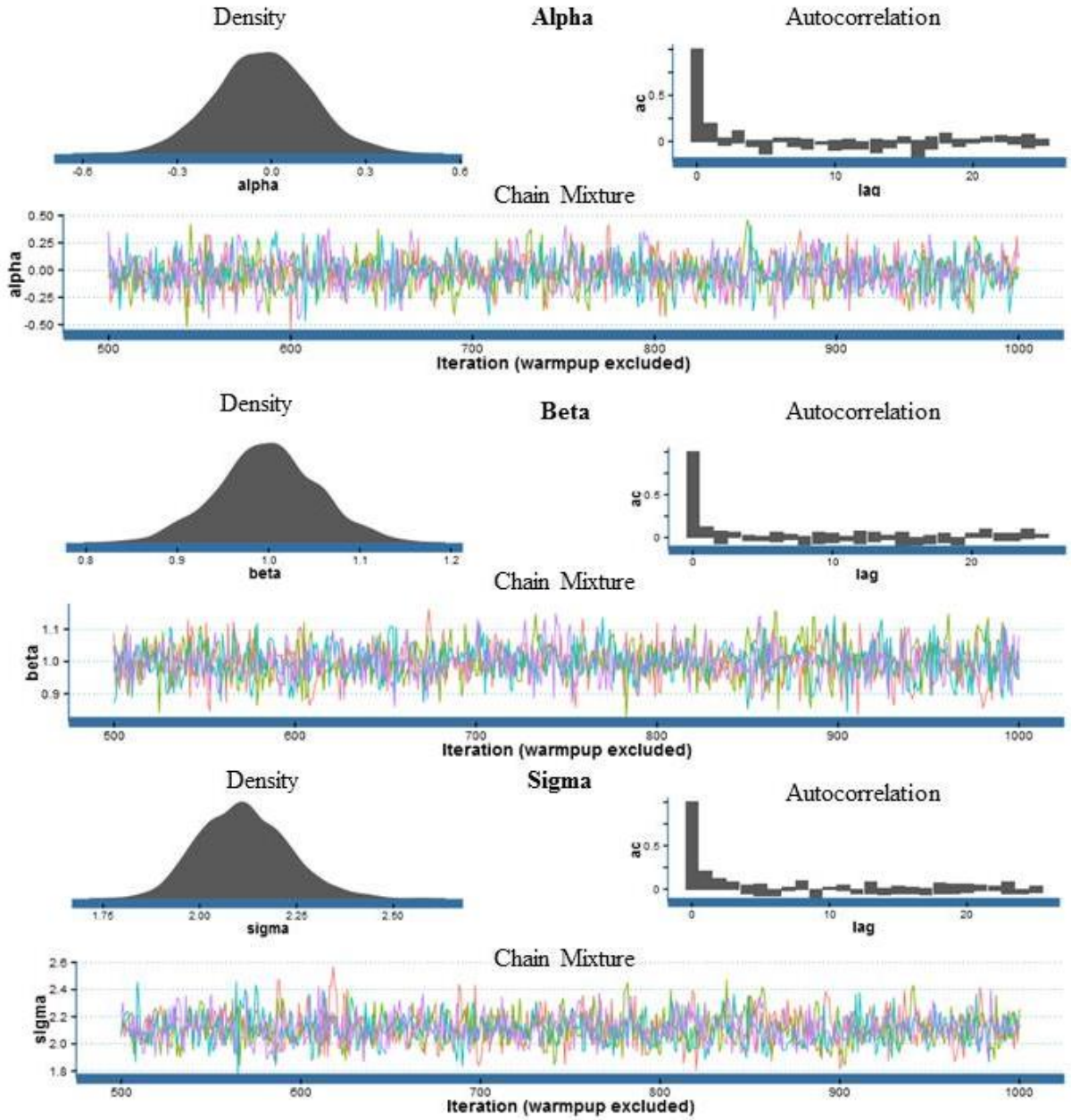

Figure 8.8. Summary and diagnostic visuals for PLS component 3 regression model parameters. The density plot visualizes the posterior distribution of a parameter. The autocorrelation bar graph represents the correlation or dependency of MCMC draws. The chain mixture or trace plot measures how well the sampler is exploring parameter space.

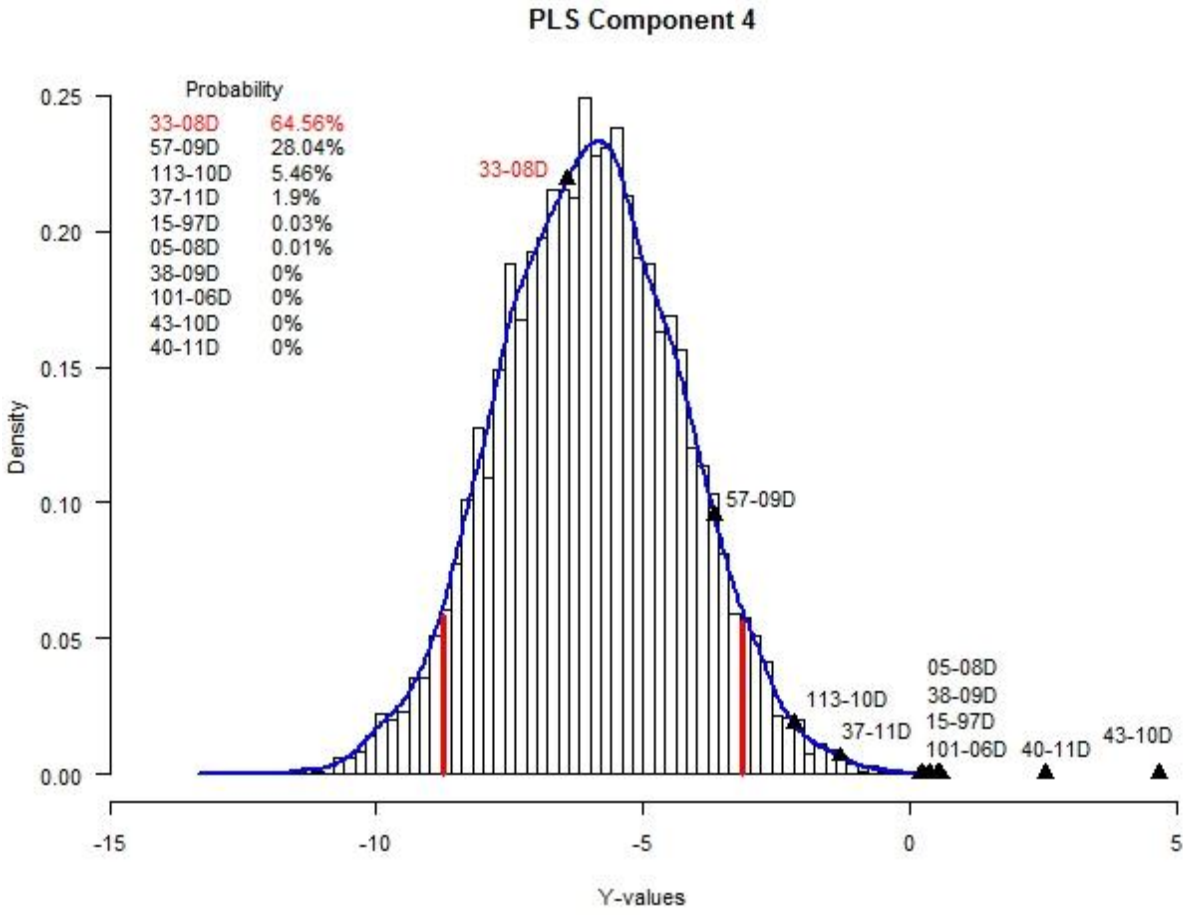

Figure 8.9. Histogram and kernel density estimate of y-values and match probabilities for PLS component 4. Red lines represent the 5% and 95% quantiles, respectively.

Table 8.9. Summary statistics for PLS component 4 regression model.

Parameter	Mean	Std Error	SD	Effective n	R hat
alpha	-0.01	0.00	0.12	1543	1.00
beta	1.00	0.00	0.05	1171	1.00
sigma	1.63	0.00	0.08	1357	1.00

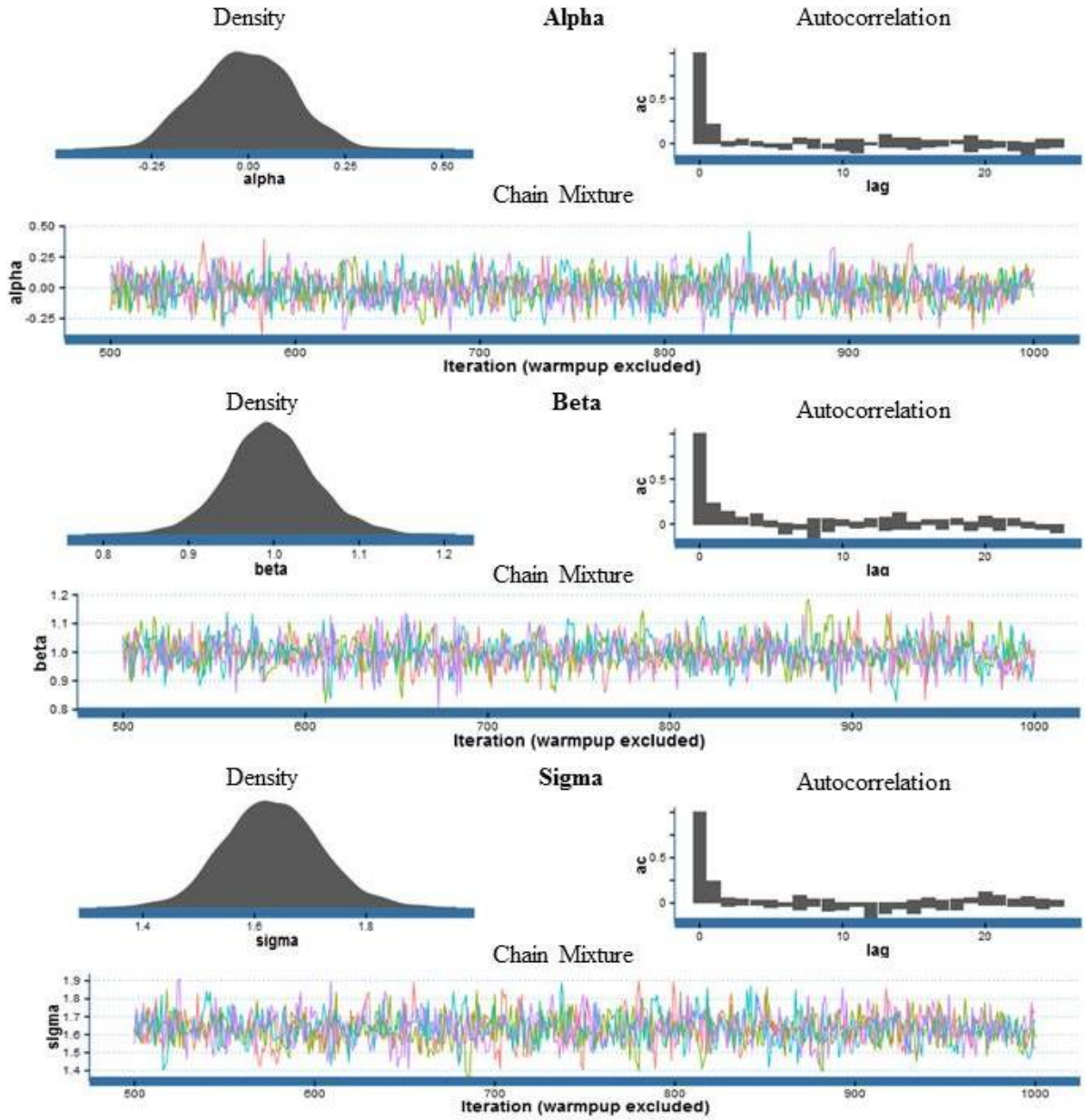

Figure 8.10. Summary and diagnostic visuals for PLS component 4 regression model parameters. The density plot visualizes the posterior distribution of a parameter. The autocorrelation bar graph represents the correlation or dependency of MCMC draws. The chain mixture or trace plot measures how well the sampler is exploring parameter space.

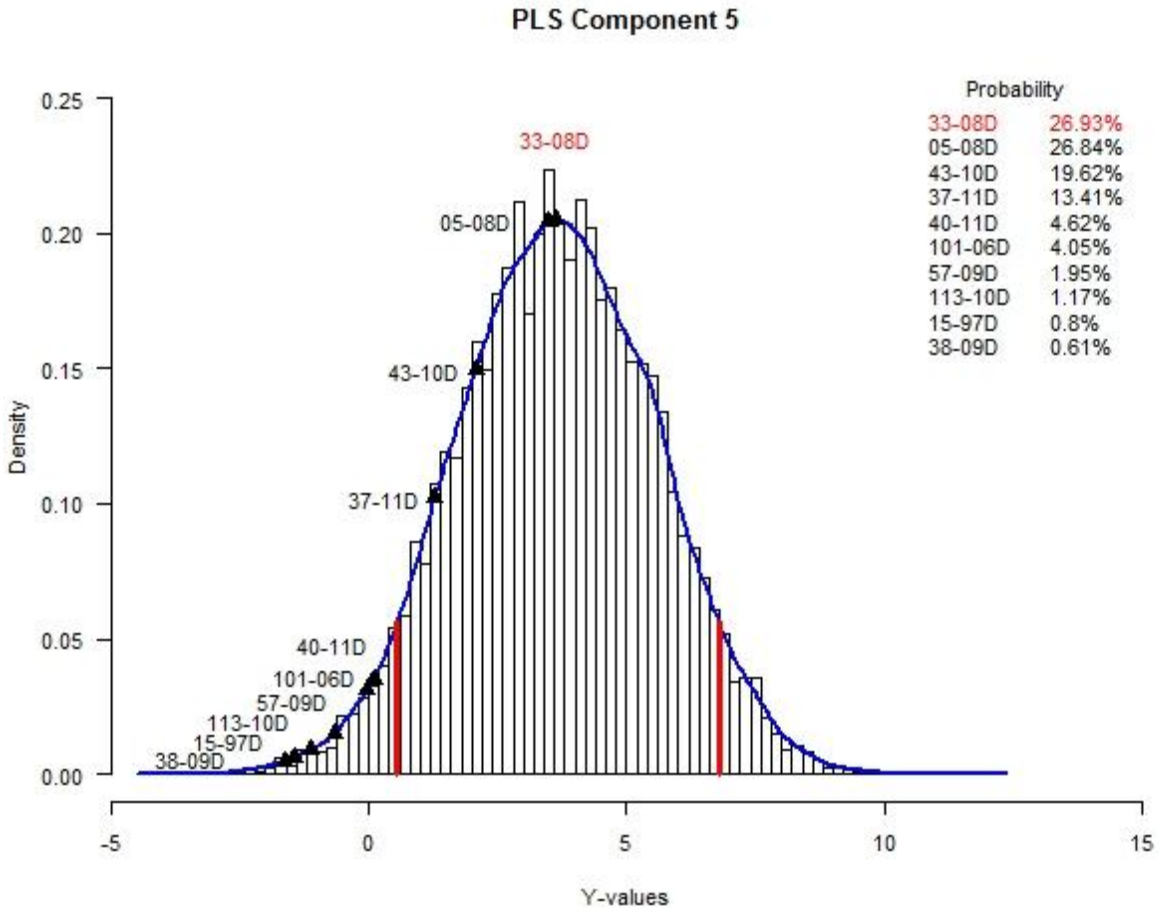

Figure 8.11. Histogram and kernel density estimate of y-values and match probabilities for PLS component 5. Red lines represent the 5% and 95% quantiles, respectively.

Table 8.10. Summary statistics for PLS component 5 regression model.

Parameter	Mean	Std Error	SD	Effective n	R hat
alpha	0.00	0.00	0.13	1571	1.00
beta	1.00	0.00	0.06	1361	1.00
sigma	1.83	0.00	0.10	1286	1.01

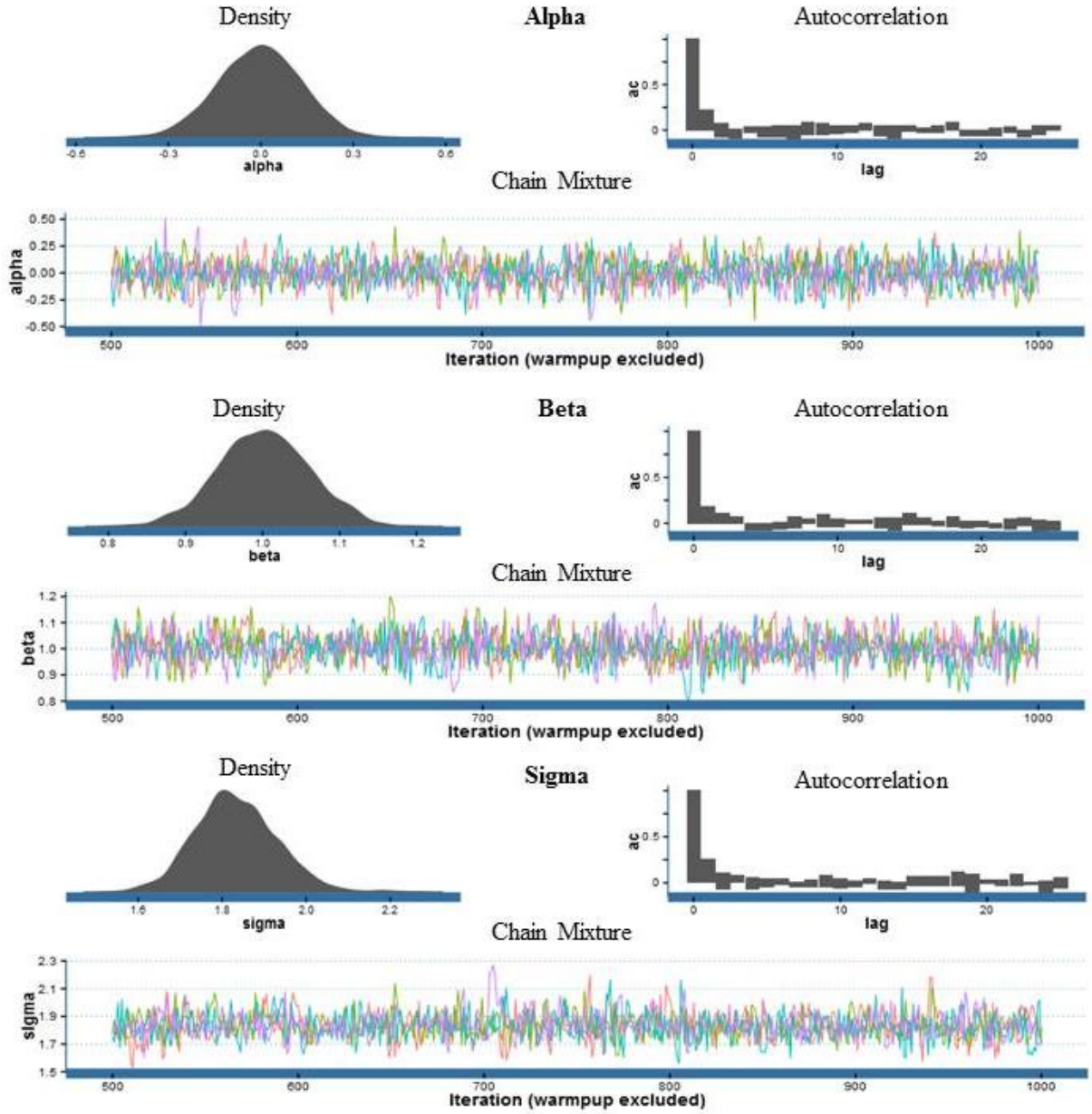

Figure 8.12. Summary and diagnostic visuals for PLS component 5 regression model parameters. The density plot visualizes the posterior distribution of a parameter. The autocorrelation bar graph represents the correlation or dependency of MCMC draws. The chain mixture or trace plot measures how well the sampler is exploring parameter space.

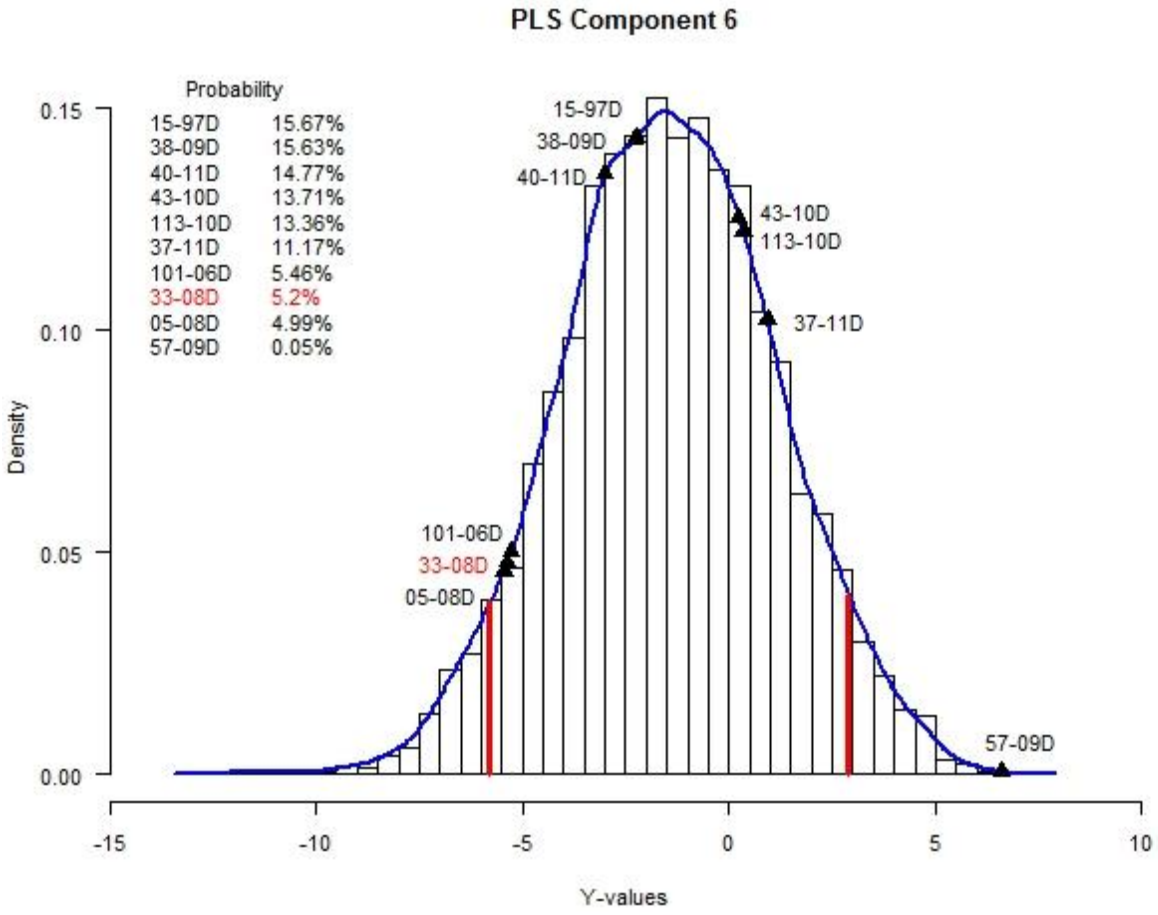

Figure 8.13. Histogram and kernel density estimate of y-values and match probabilities for PLS component 6. Red lines represent the 5% and 95% quantiles, respectively.

Table 8.11. Summary statistics for PLS component 6 regression model.

Parameter	Mean	Std Error	SD	Effective n	R hat
alpha	0.09	0.00	0.18	1526	1.00
beta	0.95	0.00	0.15	1708	1.00
sigma	2.25	0.00	0.13	1692	1.00

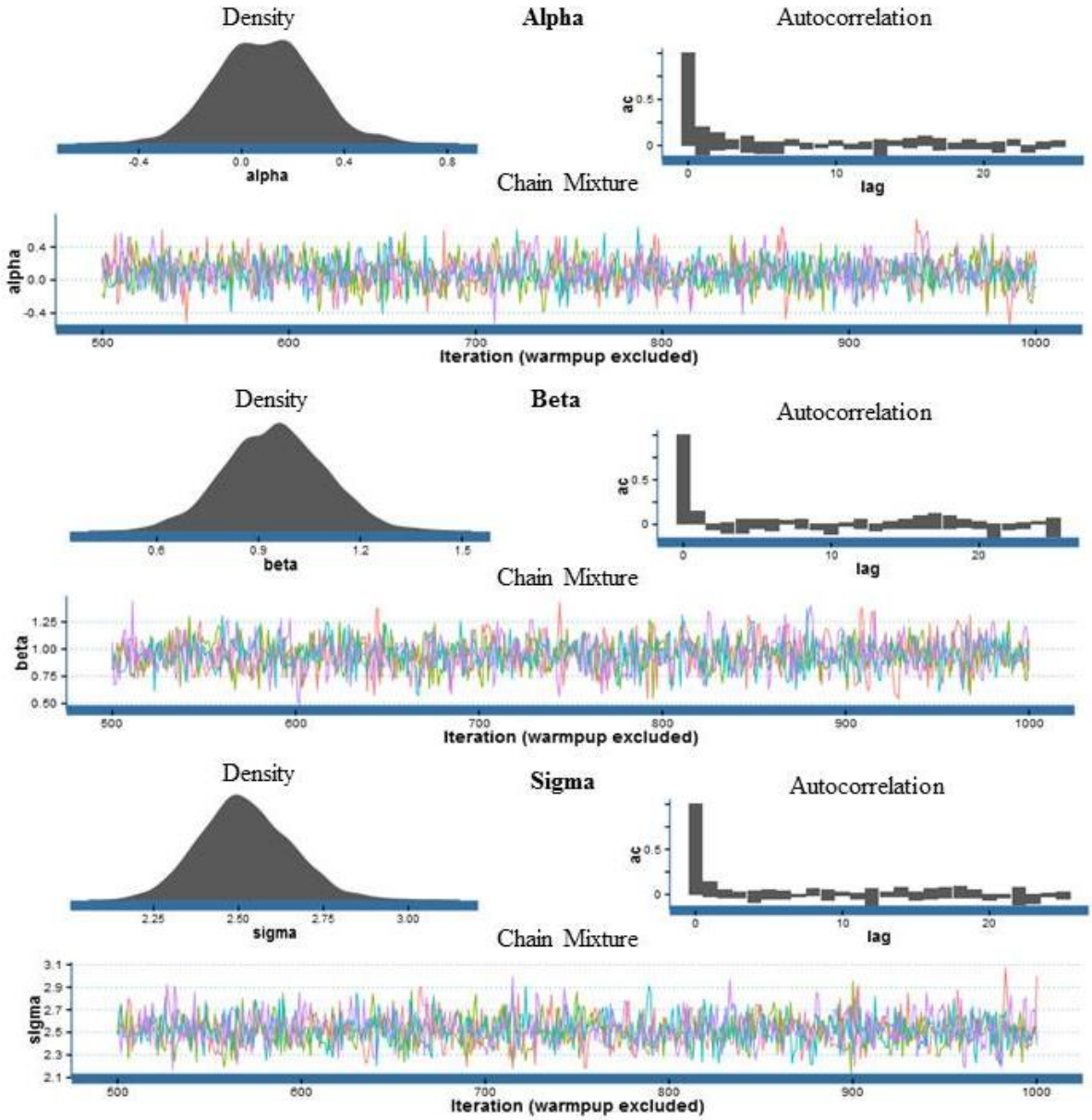

Figure 8.14. Summary and diagnostic visuals for PLS component 6 regression model parameters. The density plot visualizes the posterior distribution of a parameter. The autocorrelation bar graph represents the correlation or dependency of MCMC draws. The chain mixture or trace plot measures how well the sampler is exploring parameter space.

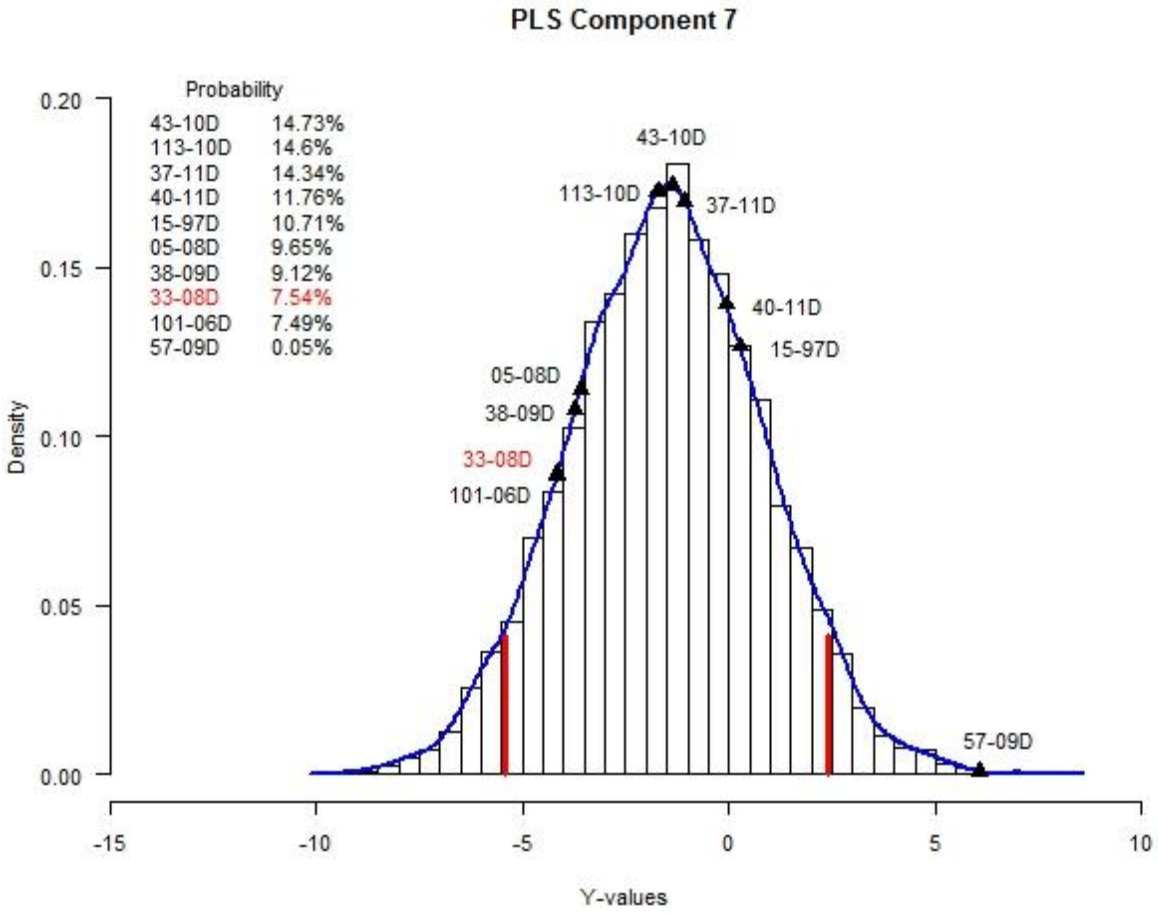

Figure 8.15. Histogram and kernel density estimate of y-values and match probabilities for PLS component 7. Red lines represent the 5% and 95% quantiles, respectively.

Table 8.12. Summary statistics for PLS component 7 regression model.

Parameter	Mean	Std Error	SD	Effective n	R hat
alpha	0.06	0.00	0.17	1582	1.00
beta	0.99	0.00	0.13	1669	1.00
sigma	2.32	0.00	0.12	1636	1.00

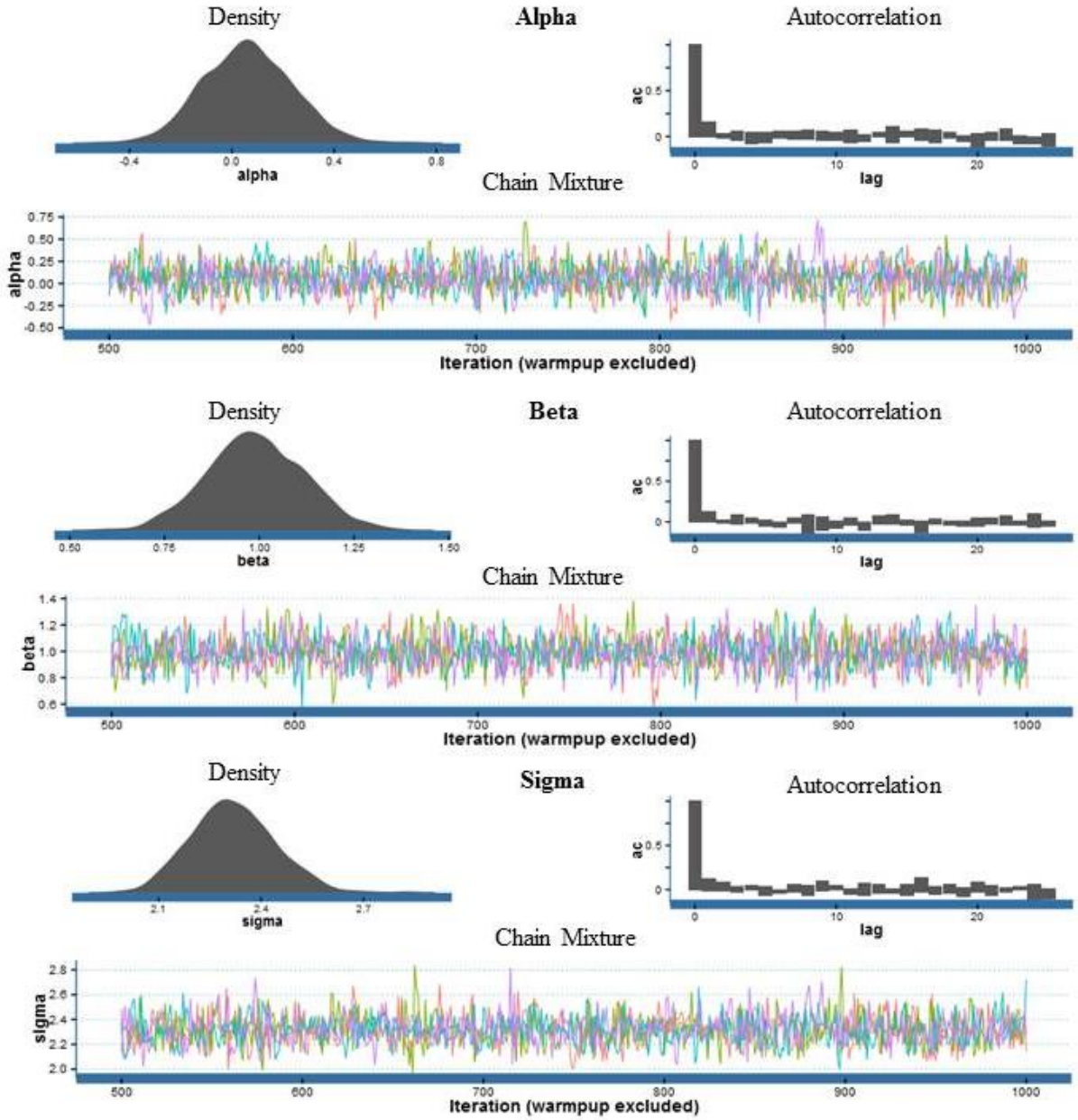

Figure 8.16. Summary and diagnostic visuals for PLS component 7 regression model parameters. The density plot visualizes the posterior distribution of a parameter. The autocorrelation bar graph represents the correlation or dependency of MCMC draws. The chain mixture or trace plot measures how well the sampler is exploring parameter space.

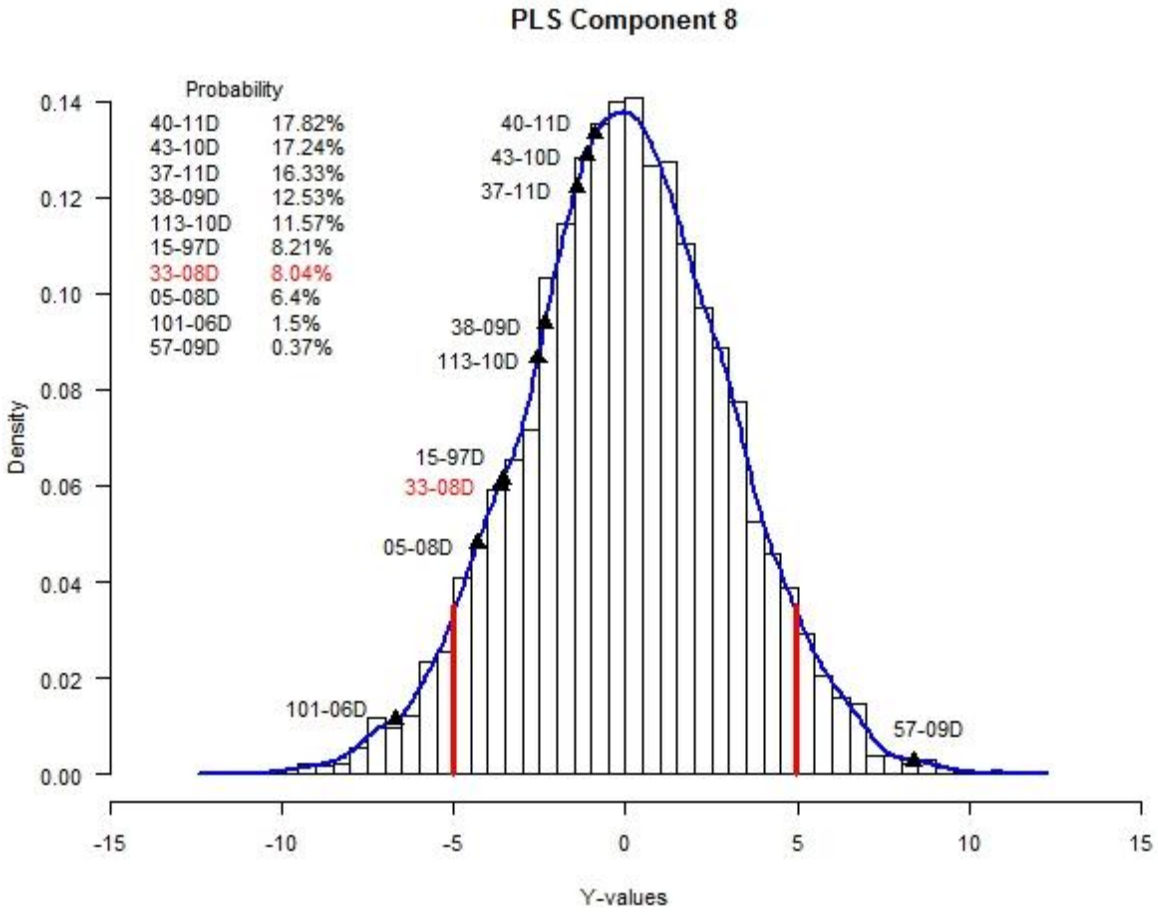

Figure 8.17. Histogram and kernel density estimate of y-values and match probabilities for PLS component 8. Red lines represent the 5% and 95% quantiles, respectively.

Table 8.13. Summary statistics for PLS component 8 regression model.

Parameter	Mean	Std Error	SD	Effective n	R hat
alpha	0.08	0.01	0.22	1705	1.00
beta	0.94	0.01	0.18	1090	1.00
sigma	2.98	0.00	0.16	1576	1.00

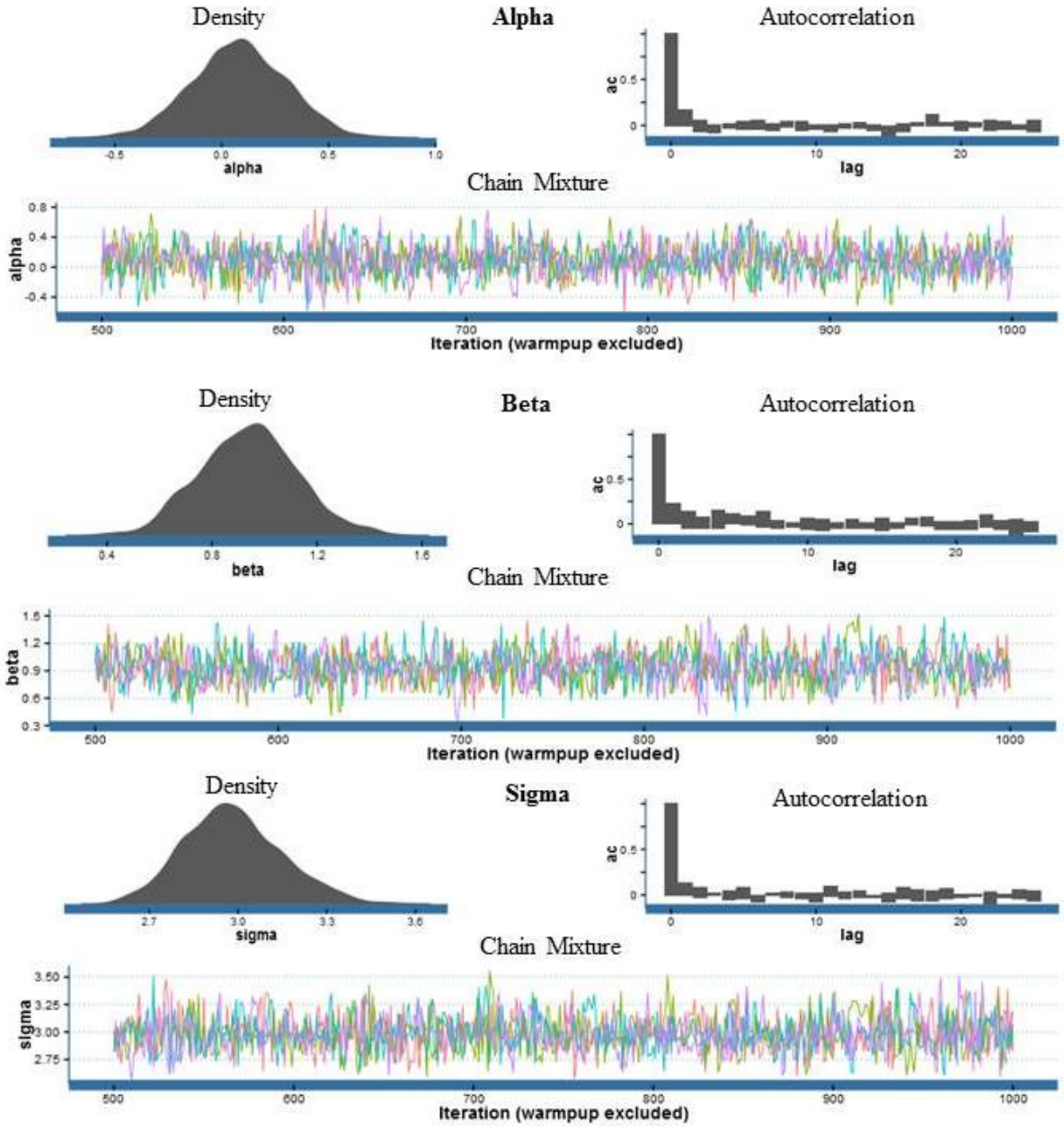

Figure 8.18. Summary and diagnostic visuals for PLS component 8 regression model parameters. The density plot visualizes the posterior distribution of a parameter. The autocorrelation bar graph represents the correlation or dependency of MCMC draws. The chain mixture or trace plot measures how well the sampler is exploring parameter space.

Table 8.14. The number of times an individual could be rejected as a possible match using the 5% and 95% quantiles as thresholds.

Individual	Rejections
33-08D	**0**
113-10D	2
43-10D	2
57-09D	5
37-11D	3
101-06D	4
15-97D	4
38-09D	4
40-11D	3
05-08D	3

Table 8.15. Density weighted predictive probabilities for the classification example.

Individual	Probability
40-11D	20.91%
57-09D	20.81%
113-10D	20.03%
101-06D	17.46%
33-08D	**16.25%**
15-97D	0.02%
43-10D	0.01%
37-11D	0.01%
05-08D	0.00%
38-09D	0.00%

Interestingly, 33-08D is the fifth best match based on centroid size, making her the least likely match of probable matches. This is a situation where density weighted probabilities misidentify the correct match (Table 8.15). Centroid size almost completely overwhelms shape information when density weights are used. The correct match, 33-08D, remained the fifth best match after considering all variables.

3. Summary

Because of biology and the nature of landmark data, homologous elements are by far the most accurate type of bone to reassociate. No evidence for a functional influence in structuring homologous accuracy is identified. Again, this finding is likely due to the landmarks used in this study, which cluster around joints. Given that joints are well represented by landmark data, functional integration should play a large role in structuring osteometric reassociation accuracy for other comparison types. This may be the case with radius and ulna comparisons and to a lesser extent femur and tibia comparisons. Development, however, appears to have a large influence on accuracy. This assertion is supported by low levels of accuracy for lower limb comparisons as well as proximal and distal comparisons. Perhaps the most intriguing finding is the low accuracy of proximal comparisons vis-a-vise distal comparisons. Previous research has shown that distal elements are more variable than proximal elements, allowing for the variation needed to accurately separate individuals while maintaining similarity within an individual.

The classification example shows the importance of building confidence in a decision based on multiple lines of evidence. It is unlikely that one variable can identify the correct match. However, identifying the correct match becomes very likely when all variables are considered. Additionally, the correct match in this example is the only individual with no evidence against reassociation, never falling outside of the 5^{th} and 95^{th} quantiles for any variable. While only examined for this example, the number of times an individual is rejected as a possible match may be a way to identify model error.

Chapter 9

Conclusion

The traditional osteometric sorting approach works within a frequentist framework to eliminate possible matches using a size variable calculated from SOM. Bones are reassociated if all other possible matches are eliminated. This study shows that many times bones cannot be reassociated using this approach because it is likely that even for a small scale commingled assemblage, such as the one used in this study, several possible matches will be close enough in size to not be eliminated.

An implicit assumption of the traditional approach is all comparison types are equally accurate as long as a certain threshold (alpha-level) is exceeded. Ignored in this assumption is the biological foundation for osteometric reassociation. The current study built a hypothetical structure to accuracy in osteometric reassociation based on developmental and functional adaptation research. The hypothetical structure to osteometric reassociation accuracy was tested by simulating commingled assemblages and estimating the correct match using geometric morphometric landmark data in a Bayesian framework. Overall, the experimentally determined structure closely matched the hypothetical structure of osteometric reassociation accuracy. Some salient points came from examining this structure in more detail.

1. Future implications and broader impact

1.1 Comparative biology

A vast majority of comparative biology studies using geometric landmark data and studies on vertebrate limb covariation structure rely on homologous landmarks and measurements. Homology is a requirement to make results comparable across taxa. This study

uses theory to inform inadequacies in practical application. The goal of this study is different than typical biological science, which seeks to build nomothetic theory from specific cases. Homology across all limb bones is sacrificed in this study to better capture bone morphology. Because of the lack of homology in limb bone quantification, the experimental structure identified here is in part due to research design. This point is obvious in homologous element comparisons, which by definition utilize homologous landmarks. Biological theory predicts that homologous elements should have the highest accuracy, but the stark contrast in accuracy between homologous comparisons and all other types is likely due to the nature of landmark data. That being said, it is certainly interesting that PLS components from non-homologous comparisons are still useful for estimating correct matches, as evident from equal weight probabilities always outperforming density weight probabilities.

Perhaps the most important findings are the modularity of proximal and distal elements suggested by low accuracy in proximal and distal comparisons and the overall higher levels of accuracy in distal elements compared to proximal elements. Both of these findings are suggested by previous ontogenetic and limb variation research. This study supports those previous findings. However, the support that this study provides for larger questions of limb variation, integration and modularity are purely circumstantial. This study does not directly address any of those topics—relevance is assumed based on reassociation accuracy. These data collected for this study do provided a potentially fruitful source of information for examining these topics, at least within humans. A detailed analytical methodology for addressing larger questions of human limb variation, integration and modularity is beyond the scope of this study. With that

said, some possible analytics include examining variance of eigenvalues of components for within and between elements and partial correlations between elements. Such analysis does not necessarily require all homologous landmarks (Young and Hallgrimsson, 2005). But reducing the total number of landmarks used in this study to a comparable (i.e. most proximal point of an element) and relevant number (i.e. removing nutrient foramen landmarks) would mitigate the influence of research design identified in this study. Additionally, scrutiny of landmark inclusion may reduce noise in the dataset and may increase accuracy beyond the levels found in the current study.

1.2 Applications in biological anthropology

The results of this study suggest that paired bones can be accurately reassociated without having to eliminate other possibilities. Other comparison types, however, are more often wrong than right in choosing the correct match. Practical applications of this method in forensic anthropology should employ a combination of estimating the correct match and eliminating possible matches to resolve commingling. Many times, over 95% of correct matches are in the top five ranked predictive probabilities. Using this logic, half of the possible matches can be eliminated with a high degree of confidence using a model that compares all possible matches. Such an approach has obvious strengths over traditional approaches, which require several independent tests to analyze an assemblage. Whether using a rejection-based or best match logic, the size of the commingled assemblage should have an inverse relationship with reassociation accuracy—as the size of the commingled assemblage increases, accuracy will decrease. In a similar vein, when element completeness decreases, so should accuracy due to

information loss. Both of these relationships can be addressed in the future by changing the size of the simulated commingled assemblage and by artificially eliminating landmarks and examining how these variables affect accuracy. Artificially eliminating landmarks, however, assumes that the landmarks that remain would be identifiable on elements too fragmentary to collect the missing landmarks. Care was taken to standardize the orientation of the element and perspective of the observer during data collection. This standardization, while mitigating intraobserver error, requires that elements are complete to collect these landmarks. Using linear measurements or employing other methods for creating a three-dimensional representation of long bones, such as CT scans, may be possible avenues for applying this method to fragmentary remains.

The main issue in accepting the best match as the correct match is identifying when the results could be wrong. In that regard, typicality values appear to be of little value. Examining how often, if at all, a possible match was rejected using the 5% and 95% quantiles of the y-value posterior distribution may be useful in identifying model error. This staunch focus on error mitigation, however, mostly applies to forensic contexts. In bioarchaeology the consequence for incorrectly reassociating limb elements is simply adding uncertainty to results; in forensic contexts an incorrect reassociation leads to a misidentification or missing an identification because two individuals were considered one. In this regard, reassociating commingled remains using this current methodology has obvious utility in bioarchaeological contexts, where the need to be correct is relaxed. More complete skeletons lead to better analysis and by extension, better inference about past individuals and populations.

Applying this method to bioarchaeological contexts also raises an interesting consideration: sample composition. The sample used in this study, while equally representative of males and females, is a rather homogenous group. Adding phenotypic, geographic, and temporal variability to the sample should increase accuracy, similar to how increased variability of distal elements likely increased their reassociation accuracy. This statement, however, assumes that intrapersonal relationships between elements would be similar across groups. Additionally, by gathering a more heterogenous sample, patterns of intrapersonal relationships between elements could be examined.

Theory is a powerful explanatory tool. The theory discussed in this study has been used in many fields of biology to improve our understanding of biological systems and the complex interactions that result in phenotypic variation. This study shows that theory also has a place in practice. Couching experimental results within a theoretical framework can give the practitioner a better understanding of how to interpret results, which leads to more informed decisions and an overall better science.

List of References

Adams BJ and Byrd JE 2014. *Commingled Human Remains: Methods in Recovery, Analysis, and Identification*. Academic Press.

Adams BJ and Byrd, JE 2008. *Recovery, analysis, and identification of commingled human remains*. Springer Science and Business Media.

Adams BJ and Byrd JE. 2006. Resolution of small-scale commingling: A case report from the Vietnam War. *Forensic Science International.* 156(1):63-69.

Adams BJ and Konigsberg LW. 2004. Estimation of the Most Likely Number of Individuals from Commingled Human Skeletal Remains. *American Journal of Physical Anthropology.* 125:138-151.

Adams BJ and Konigsberg LW 2008. How many people? Determining the number of individuals represented by commingled human remains. In: Byrd JE and Adams BJ. (eds.) *Recovery, Analysis, and Identification of Commingled Human Remains.* Humana Press. pgs. 241-255.

Adams DC, Rohlf FJ and Slice DE 2013. A field comes of age: geometric morphometrics in the 21st century. *Hystrix, the Italian journal of Mammalogy,* 24(1):7-14.

Allen J and Guy JBM. 1984. Optimal estimations of individuals in archaeological faunal assemblages: How minimal is the MNI? *Archaeology Oceania* 19:41-47.

Al-Qattan MM, Yingzi Y and Kozin SH. 2009. Embryology of the Upper Limb. *Journal of Hand Surgery* 34A:1340-1350.

Arnqvist G and Martensson T. 1998. Measurement error in geometric morphometrics: empirical strategies to assess and reduce its impact on measures of shape. *Acta Zoologica Academiae Scientiarum Hungaricae*, 44(1-2):73-96.

Auerbach BM. 2006. Limb bone bilateral asymmetry: variability and commonality among modern humans. *Journal of Human Evolution.* 50:203-218.

Auerbach BM and Sylvester AD. 2011. Allometry and apparent paradoxes in human limb proportions: implications for scaling factors. *American Journal of Physical Anthropology.* 144:382-391.

Bass SL, Saxon L, Daly RM, Turner CH, Robling AG, Seeman E and Stuckey S. 2002. The effect of mechanical loading on the size and shape of bone in pre-, peri-, and postpubertal girls: a study of tennis players. *Journal of Bone and Mineral Reserve.* 17:2274-2280.

Bayes T. 1764. An Essay Towards Solving a Problem in the Doctrine of Chances. *Philosophical Transactions of the Royal Society of London* 53:370-418.

Biewener AA. 1989. Scaling and Body Support in Mammals: Limb Posture and Muscle Mechanics. *Science.* 245(4913):45-48.

Bonewald L. 2011. The Amazing Osteocyte. *Journal of Bone and Mineral Research.* 26(2):229-238.

Bookstein FL. 1991. Morphometric Tools for Landmark Data: Geometry and Biology. Cambridge University Press.

Boulesteix AL and Strimmer K. 2007. Partial least squares: a versatile tool for the analysis of high-dimensional genomic data. *Briefings in Bioinformatics*. 8(1):32-44.

Bridges P, Blitz J and Solano M. 2000. Changes in long bone diaphyseal strength with horticultural intensification in west-central Illinois. *American Journal of Physical Anthropology.* 112:217–238.

Boyd C and Boyd DC. 2011. Theory and the Scientific Basis for Forensic Anthropology. *Journal of Forensic Sciences*. 56(6):1407-1415.

Buikstra JE, Gordon CC and St. Hoyme L. 1984. The case of the severed skull: individualization in forensic anthropology. In Rathburn TA and Buikstra JE. (eds.). *Human Identification: Case Studies in Forensic Anthropology*. Springfield, IL: C.C. Thomas. pgs. 90-98.

Byrd JE. 2008. Models and methods for osteometric sorting. In: Byrd JE and Adams BJ. (eds.) *Recovery, Analysis, and Identification of Commingled Human Remains.* Humana Press. pgs. 199-220.

Byrd JE and Adams BJ. 2003. Osteometric Sorting of Commingled Human Remains. *Journal of Forensic Science.* 48(4):1-8.

Byrd JE and Adams BJ. 2008. *Recovery, Analysis and Identification of Commingled Human Remains.* Totowa, NJ: Humana Press.

Byrd JE and Adams BJ. 2009. Analysis of Commingled Human Remains. In. Blau S and Ubelaker DH. (eds.) *Handbook of Forensic Anthropology and Archaeology*. pgs. 174-185.

Byrd JE and Adams BJ. 2014. *Commingled Human Remains: Methods in Recovery, Analysis and Identification.* Elsevier.

Byrd JE and LeGarde CB. 2014. Osteometric Sorting. In: Byrd JE and Adams BJ. (eds.) *Commingled Human Remains: Methods in Recovery, Analysis, and Identification*. pgs. 167-180.

Blau S and Briggs CA. 2011. The role of forensic anthropology in Disaster Victim Identification (DVI). *Forensic Science International.* 205:29-35.

Capdevila J and Belmonte JCI. 2001. Patterning mechanisms controlling vertebrate limb development. *Annual review of cell and developmental biology. 17*(1):87-132.

Chen Y and Hoo KA. 2011. Application of partial least square regression in uncertainty study area. *American Control Conference.* 2011:1958-1962

Cheverud JM. 1996. Developmental Integration and the Evolution of Pleiotropy. *American Zoology*. 36:44-50.

Cowgill LW. 2007. Humeral torsion revisited: a functional and ontogenetic model for populational variation. *American Journal of Physical Anthropology*. 134(4):472-480.

Curry JD. 2002. *Bones: Structure and Mechanics.* Princeton University Press.

Curtin AJ. 2008. Putting Together the Pieces: Reconstructing Mortuary Practices from Commingled Ossuary Cremains. In. Schmidt CW and Symes S (eds.). *The Analysis of Burned Human Remains.* pgs. 201-209.

Duong T. 2007. ks: Kernel density estimation and kernel discriminant analysis for multivariate data in R. *Journal of Statistical Software*. 21(7):1-16.

Egana S, Turner S, Doretti M, Bernardi P and Ginarte A. 2008. Commingled Remains and Human Rights Investigations. In: Adams BJ and Byrd JE (eds.). *Recovery, Analysis and Identification of Commingled Human Remains.* Humana Press. pgs. 210-221.

Fabry G, MacEwen GD, and Shands AR. 1973. Torsion of the femur. *Journal of Bone and Joint Surgery* 55A:1726-1738.

Feyerabend P. 1981. *Philosophical papers.* Princeton Press.

Frost HM. 1996. Bone development during childhood: insights from a new paradigm. In: Schoenau E. (ed.) *Paediatric osteology: new trends and developments in diagnostic and therapy.* Amersterdam: Elsevier Science. pgs. 3-39.

Frost HM. 2003. Bone's Mechanostat: A 2003 Update. *The Anatomical Record Part A.* 275A:1081-1101.

Galloway A, Willey P and Snyder L. 1997. Human bone mineral densities and survival of bone elements: a contemporary sample. In: Haglund WD, Sorg MH, editors. Forensic taphonomy: the postmortem fate of human remains. Boca Raton: CRC Press. pgs. 295–317

Garland AN and Janaway RC. 1989. The taphonomy of inhumation burials. *Burial archaeology: current research, methods and developments*. 2:15-37.

Giles E and Klepinger LL. 1988. Confidence intervals for estimates based on linear regression in forensic anthropology. *Journal of Forensic Sciences*. *33*(5):1218-1222.

Gray H. 1918. *Anatomy of the Human Body*. Lea and Febiger.

Grayson DK. 1978. Minimum numbers and sample size in vertebrate faunal analysis. *American Antiquity*. 53-65.

Grayson DK. 1981. The effects of sample size on some derived measures in vertebrate faunal analysis. *Journal of Archaeological Science*. 8(1):77-88.

Griffin NL, Gordon AD, Richmond BG and Anton SC. 2008. Cross-sectional geometric analysis of a foot bone assemblage from Mangaia, Cook Islands. *Homo-Journal of Comparative Human Biology*. 59:27-40.

Haenlein M and Kaplan AM. 2004. A beginner's guide to partial least squares analysis. *Understanding Statistics*. 3(4):283-297.

Hallgrímsson B. 1999. Ontogenetic patterning of skeletal fluctuating asymmetry in rhesus macaques and humans: evolutionary and developmental implications. *International Journal of Primatology*. 20(1):121-151.

Hallgrimsson B, Willmore K and Hall BK. 2002. Canalization, developmental stability, and morphological integration in primate limbs. *Yearbook of Physical Anthropology*. 45:131-158.

Herrmann NP and Devlin JB. 2008. Assessment of commingled human remains using a GIS-based approach. In: Adams BJ and Byrd JE (eds.) *Recovery, Analysis and Identification of Commingled Human Remains.* Humana Press. pgs. 257-269).

Hinkes MJ. 1989. The role of forensic anthropology in mass disaster resolution. *Aviation, space, and environmental medicine*. 60:A60-3.

Holliday TW and Ruff CB. 2001. Relative Variation in Human Proximal and Distal Limb Segment Lengths. *American Journal of Physical Anthropology.* 116:26-33.

Hsieh YF, Robling AG, Ambrosius WT, Burr DB and Turner CH. 2001. Mechanical loading of diaphyseal bone in vivo: the train threshold for an osteogenic response varies with location. *Journal of Bone Mineral Research.* 16:2291-2297.

Hutter CG and Scott W. 1949. Tibial torsion. *Journal of Bone and Joint Surgery.* 31A:511-518.

Immersion Corporation. 2002. MicroScribe G2 user's manual. San Jose, CA.

Jantz RL, Ousley SD. 2005. FORDISC 3.0. Computer Program. Knoxville, TN. University of Tennessee, Knoxville.

Jee WSS and Frost HM. 1992. Skeletal adaptions during growth. *Triangle.* 31:77-88.

Johnson RL and Tabin CJ. 1997. Molecular models for vertebrate review limb development. *Cell*. 90:979-990.

Junqueira LC and Carneiro J. 2005. *Basic histology text and atlas*. London: McGraw Hill.

Kate BR and Robert SL. 1965. Some observations on the upper end of the tibia in squatters. *Journal of Anatomy.* 99:137-141.

Karsenty G. 2003. The complexities of skeletal biology. *Nature*. 423(6937):316-318.

Kerr D, Morton A, Dick I and Prince R. 1996. Exercise effects on bone mass in postmenopausal women are site-specific and load-dependent. *Journal of Bone and Mineral Research*. 11(2):218-225.

Kéry M. 2010. *Introduction to WinBUGS for ecologists: Bayesian approach to regression, ANOVA, mixed models and related analyses*. Academic Press.

Klingenberg CP. 2011. MorphoJ: an integrated software package for geometric morphometrics. *Molecular ecology resources*. 11(2):353-357.

Klingenberg CP. 2009. Morphometric integration and modularity in configurations of landmarks: tools for evaluating a priori hypotheses. *Evolution and Development.* 11(4):405-421.

Klingenberg CP. 2008. Morphological integration and developmental modularity. *Annual review of ecology, evolution, and systematics*. 39:115-132.

Konigsberg LW and Adams BJ. 2014. Estimating the Number of Individuals Represented by Commingled Human Remains: A Critical Evaluation of Methods. In: Adams BJ and Byrd JE

(eds.) *Commingled Human Remains: Methods in Recovery, Analysis, and Identification*. pgs. 193-205.

Konigsberg LW and Frankenberg SR. 2013. Bayes in Biological Anthropology. *American Journal of Physical Anthropology.* 57:153-184.

Kontanis EJ and Sledzik PS. 2008. Resolving Commingling Issues During the Medicolegal Investigation of Mass Fatality Incidents. In: Adams BJ and Byrd JE (eds.) *Recovery, Analysis and Identification of Commingled Human Remains.* Humana Press. pgs. 105-118.

Lazenby RA, Cooper DM, Angus S and Hallgrímsson B. 2008. Articular constraint, handedness, and directional asymmetry in the human second metacarpal. *Journal of human evolution.,* 54(6):875-885.

Lew MJ. 2013. To P or not to P: on the evidential nature of P-values and their place in scientific inference stat.

Lieberman DE, Devlin MJ and Person OM. 2001. Articular area responses to mechanical loading: effects of exercise, age, and skeletal location. *American Journal of Physical Anthropology.* 116:266-277.

Lieberman DE, Polk JD and Demes B. 2004. Predicting Long Bone Loading From Cross-Sectional Geometry. *American Journal of Physical Anthropology.* 123:156-171.

Lynch SM. 2007. *Introduction to applied Bayesian statistics and estimation for social scientists*. Springer Science and Business Media.

Maitra S and Yan J. 2008. Principle component analysis and partial least squares: Two dimension reduction techniques for regression. *Applying Multivariate Statistical Models*. 79-91.

Martin RB, Burr DB and Sharkey NA. 1998. *Skeletal Tissue Mechanics*. NY: Springer Press.

Mariani FV and Martin GR. 2003. Deciphering skeletal patterning: clues from the limb. *Nature*. 423(6937):319-325.

Mayo DG and Spanos A. 2010. *Error and inference: Recent exchanges on experimental reasoning, reliability, and the objectivity and rationality of science*. Cambridge University Press.

McGowan C. 1999. *A Practical Guide to Vertebrate Mechanics.* Cambridge University Press.

Mercader N, Leonardo E, Piedra ME, Martinez AC, Ros MA and Torres M. 2000. Opposing RA and FGF signals control proximodistal vertebrate limb development through regulation of Meis genes. *Development*. 127(18):3961-3970.

Mitteroecker P, Gunz P, Windhager S and Schaefer K. 2013. A brief review of shape, form, and allometry in geometric morphometrics, with applications to human facial morphology. *Hystrix, the Italian Journal of Mammalogy*. 24(1):59-66.

Mitteroecker P and Gunz P. 2009. Advances in geometric morphometrics. *Evolutionary Biology*. 36(2):235-247.

Monteiro LR, Bordin B and dos Reis SF. 2000. Shape distances, shape spaces and the comparison of morphometric methods. *Trends in ecology & evolution*. 15(6):217-220.

Morgan JD and Somerville EW. 1960. Normal and abnormal growth at the upper end of the femur. *Journal of Bone and Joint Surgery.* 42B:264-272.

Mundorff AZ. 2008. Anthropologist-Directed Triage: Three Distinct Mass Fatality Events Involving Fragmentation of Human Remains. In: Adams BJ and Byrd JE (eds.). Recovery, Analysis and Identification of Commingled Human Remains. Humana Press. pgs. 30-42.

Mundorff AZ. 2012. Integrating forensic anthropology into disaster victim identification. *Forensic Science, Medicine, Pathology*. 8:131-139.

Noble SN. 2008. The osteocyte lineage. *Archives of Biochemistry and Biophysics*. 473:106-111.

Neal RM. 2011. MCMC using Hamiltonian dynamics. *Handbook of Markov Chain Monte Carlo*. 2-20.

O'Brien M and Storlie CB. 2011. An alternative bilateral refitting model for zooarchaeological assemblages. *Journal of Taphonomy.* 9:245–268.

Orchard TJ. 2005. The Use of Statistical Size Estimations in Minimum Number of Calculations. *International Journal of Osteoarchaeology.* 15:351-359.

Osborne D and Effmann EL. 1981. Disturbances of trabecular architecture in the upper end of the femur in childhood. *Skeletal Radiology.* 6:165-173.

Ousley SD. 2004. 3Skull Computer Program. Version2.1.111. Erie, PA: Mercyhurst University.

Ousley S and McKeown A. 2001. Three dimensional digitizing of human skulls as an archival procedure. *BAR INTERNATIONAL SERIES*. 934:173-186.

Owsley DW, Berryman HE and Bass WM. 1977. Demographic and osteological evidence for warfare at the Larson site, South Dakota. *Plains Anthropologist Memoir*. 13:119-131.

Pearson OM and Lieberman DE. 2004. The aging of Wolff's "law": ontogeny and responses to mechanical loading in cortical bone. *American Journal of Physical Anthropology.* 125(S39):63-99.

Penin X, Berge C and Baylac M. 2002. Ontogenetic Study of the Skull in Modern Humans and the Common Chimpanzees: Neotenic Hypothesis Reconsidered with a Tridimensional Procrustes Analysis. *American Journal of Physical Anthropology.* 118:50-62.

Plochocki JH. 2004. Bilateral Variation in Limb Articular Surface Dimensions. *American Journal of Human Biology.* 16:328-333.

Primorac D, Andelinovic S, Definis-Gojanovic M, Drmic I, Rezic B, Baden MM, Kennedy MA, Schanfield MS, Skakel SB and Lee HC. 1996. Identification of War Victims from Mass Graves in Croatia, Bosnia, and Herzegovina by the Use of Standard Forensic Methods and DNA Typing *Journal of Forensic Sciences.* 41(5):891-894.

R Core Team. 2015. R: A Language and Environment for Statistical Computing. Vienna, Austria: R Foundation for Statistical Computing. Available from: http://www.R-project.org/

Rabinowitz AH and Vokes SA. 2012. Integration of the transcriptional networks regulating limb morphogenesis. *Developmental Biology.* 368:165-180.

Reinecke GW and Hochrein MJ. 2008. Pieces of the Puzzle: FBI Evidence Response Team Approache to Scenes with Commingled Evidence. In: Adams BJ and Byrd JE (eds.). Recovery, Analysis and Identification of Commingled Human Remains. Humana Press. Totowa, NJ. pgs. 175-192.

Riggs CM, Vaughan LC, Evans GP, Lanyon LE and Boyde A. 1993. Mechanical implications of collagen fibre orientation in cortical bone of the equine radius. *Anatomy and Embryology.* 187:231-238.

Ringrose TJ. 1993. Bone counts and statistics: A critique. *Journal of Archaeological Science.* 20:121-157.

Ritter MA, DeRosa GP and Babcock JL. 1976. Tibial torsion? *Clinical Orthopaedics and Related Research.* 120:159-163.

Robling AG. 2009. Is Bone's Response to Mechanical Signals Dominated by Muscle Forces? *Medicine and Science in Sports and Exercise.* ??:2044-2049.

Robling AG, Castillo AB and Turner CH. 2006. Biomechanical and Molecular Regulation of Bone Remodeling. *Annual Review of Biomedical Engineering.* 8:455-498.

Robling AG and Turner CH. 2009. Mechanical Signaling for Bone Modeling and Remodeling. *Eukaryotic Gene Expression* 19. (4):319-338.

Rohlf FJ. 1999. Shape statistics: Procrustes superimpositions and tangent spaces. *Journal of Classification*. 16(2):197-223.

Rosas A and Bastir M. 2002. Thin-plate spline analysis of allometry and sexual dimorphism in the human craniofacial complex. *American Journal of Physical Anthropology*. 117(3):236-245.

Rosing FW and Pischtschan E. 1995. Re-individualisation of commingled skeletal remains. In: Jacob B and Bonte W. (eds.). *Advances in Forensic Sciences.* Berlin: Verlag. pgs. 1-9.

Rosipal R and Krämer N. 2006. Overview and recent advances in partial least squares. In *Subspace, latent structure and feature selection*. Springer Berlin Heidelberg. pgs. 34-51.

Roux W. 1894. The problems, methods, and scope of developmental mechanics. In: *Biological lectures at the Marine Biology Laboratory*. Woods Hole, Ginn: Boston. pgs. 149-190.

Royall R. 2000. On the probability of observing misleading statistical evidence. *Journal of the American Statistical Association*. *95*(451):760-768.

Royall R. 1997. *Statistical evidence: a likelihood paradigm* (Vol. 71). CRC press.

Ruff CB. 1987. Sexual dimorphism in human lower limb bone structure: relationship to subsistence strategy and sexual division of labor. *Journal of Human Evolution.* 16:391-416.

Ruff CB. 2000. Body size, body shape, and long bone strength in modern humans. *Journal of Human Evolution.* 38:269-290.

Ruff CB and Hayes W. 1983a. Cross-Sectional Geometry of Pecos Pueblo Femora and Tibaie—a Biomechanical Investigation: 1. Method and General Patterns of Variation. *American Journal of Physical Anthropology.* 60:359-381.

Ruff CB and Hayes W. 1983b. Cross-Sectional Geometry of Pecos Pueblo Femora and tiabiae—a Biomechanical Investigation: II. Sex, Age, and Side Differences. *American Journal of Physical Anthropology*. 60:383-400.

Ruff CB, Holt B and Trinkaus E. 2006. Who's afraid of the big bad Wolff?:"Wolff's law" and bone functional adaptation. *American Journal of Physical Anthropology.* 129*:*4 (2006): 484-498.

Ruff CB, Trinkaus E, Walker A and Spencer Larsen C. 1993. Postcranial Robusticity in *Homo* I: Temporal Trends and Mechanical Interpretation. *American Journal of Physical Anthropology.* 91:21-53.

Sanchez G. (2015). plsdepot: Partial Least Squares (PLS) Data Analysis Methods. *R package version 0.1, 17*.

Schachar JS, Charubhumi D and Marquez S. 2009. Femoral neck anteversion: an orthopaedic evaluation between multi-regional populations. *The Journal of the Federation of American Societies for Experimental Biology*. 23:822.6 (Meeting Abstract Supplement).

Schaefer M. 2008. Patterns of Epiphyseal Union and Their Use in the Detection and Sorting of Commingled Remains. In: Adams BJ and Byrd JE (eds.). Recovery, Analysis and Identification of Commingled Human Remains. Humana Press. Totowa, NJ. pgs. 53-60.

Scheuer L and Black S. 2004. *The Juvenile Skeleton*. Elsevier Academic Press, London, UK.

Schoenau E, Neu CM, Mokov E, Wassmer G and Manz F. 2000. Influence of Puberty on Muscle Area and Cortical Bone Area of the Foreupper limb in Boys and Girls. *The Journal of Clinical Endocrinology and Metabolism.* 85(3):1095-1098.

Shubin N, Tabin C and Carroll S. 1997. Fossils, genes and the evolution of animal limbs. *Nature.* 388:639-648.

Skawina A and Wyczolkowski M. 1987. Nutrient foramina in femoral, tibial and fibular bone in human fetuses. *Folia Morphologica (Warszawa).* 41:469-481.

Snow CC. 1948. The identification of the unknown war dead. *American Journal of Physical Anthropology*. 6:323-326.

Sledzik PS and Rodriguez WC. 2002. Damnum fatale: the taphonomic fate of human remains in mass disasters. *Advances in Forensic Taphonomy: Method, Theory, and Archaeological Perspectives*. pgs. 321-330.

Snow CC and Folk ED. 1970. Statistical assessment of commingled skeletal remains. *American Journal of Physical Anthropology.* 32:423-427.

Steadman DW, Sperry K, Snow F, Fulginiti L and Craig E. 2008. Anthropological Investigations of the Tri-State Crematorium Incident. In: Adams BJ and Byrd JE (eds.). Recovery, Analysis and Identification of Commingled Human Remains. Humana Press. Totowa, NJ. pgs. 111-121.

SWGANTH 2013. Resolving Commingled Human Remains (Revision 2). Retrieved from http://www.swganth.org

Tardieu C. 1998. Short adolescence in early Homininids: infantile and adolescent growth of the human femur. *American Journal of Physical Anthropology.* 107:163-178.

Tardieu C and Trinkaus E. 1994. Early ontogeny of the human femoral bicondylar angle. *American Journal of Physical Anthropology.* 95:183-195.

Tickle C. 1991. Retinonic acid and chick limb bud development. *Development Supplemental*. 1:113-121.

Trinkaus E. 1997. Appendicular Robusticity and the Paleobiology of Modern Human Emergence. *Proceedings of the National Academy of Science.* 94:13367-13373.

Turner CH and Forwood MR. 1995. What role does the osteocyte network play in bone adaptation? *Bone.* 16(3): 283-285.

Tuller H, Hofmeister U and Daley S. 2008. Spatial Analysis of Mass Grave Mapping Data to Assist in the Reassociation of Disarticulated Commingled Human Remains. In: Adams BJ and Byrd JE (eds.) *Recovery, Analysis and Identification of Commingled Human Remains.* Humana Press. pgs. 267-280.

Tzchori L, Day TF, Carolan PJ, Zhao Y, Wassif CA, Li L, Lewandoski M, Gorivodsky M, Love PE, Porter FD, Westphal H and Yang Y. 2009. LIM homeobox transcription factors integrate signaling events that control three-dimensional limb patterning and growth. *Development.* 136:1375-1385.

Ubelaker DH. 1974. Reconstruction of Demographic Profiles from Ossuary Skeletal Samples: A Case Study from the Tidewater Potomac, Smithsonian Contributions to Anthropology 18.

Ubelaker, DH. 2002. Approaches to the Study of Commingling in Human Skeletal Biology. In Haglund and Sorg (eds.). *Advances in Forensic Taphonomy: Method, Theory, and Archaeological Perspectives.* New York, NY: CRC Press. pgs. 10-18.

Ubelaker DH and Rife JL. 2008. Approaches to Commingling Issues in Archeological Samples: A Case Study from Roman Era Tombs in Greece. In: Adams BJ and Byrd JE (eds.). *Recovery, Analysis and Identification of Commingled Human Remains.* Humana Press. pgs. 22-34.

Vaananen HK, Zhao M, Mulari M and Halleen JM. 2000. The cell biology of osteoclast function. *Journal of Cell Science.* 113:377-381.

Varas CG and Leiva MI. 2012. Managing commingled remains from mass graves: Considerations, implications and recommendations from a human rights case in Chile. *Croatian Medical Journal.* 44(3):251-258.

Vidoli GM and Mundorff AZ. 2012. Victim Fragmentation Patterns and Seat Location Supplements Crash Data: American Airlines Flight 587. *Aviation, Space, and Environmental Medicine.* 83(4):412-417.

Wantanabe RS. 1974. Embryology of the Human Hip. *Clinical Orthopedics.* 98:8-26.

Wagner GP, Pavlicev M and Cheverud JM. 2007. The road to modularity. *Nature.* 8:921-931.

Wegelin JA. 2000. A Survey of Partia1 Least Squares (PLS) Methods, with Emphasis on the Two-Block Case.

Williams ED and Crews JD. 2003. From Dust to Dust: Ethical and Practical Issues Involved in the Location, Exhumation, and Identification of Bodies from Mass Graves. *Croatian Medical Journal.* 44(3):251-258.

Willey PS. 1990. *Prehistoric warfare on the Great Plains: skeletal analysis of the Crow Creek massacre victims*. Garland Publication.

Willey P and Emerson TE. 1993. The osteology and archaeology of the Crow Creek massacre. *The Plains Anthropologist*. 227-269.

Willey P, Galloway A and Snyder L. 1997. Bone mineral density and survival of elements and element portions in the bones of the Crow Creek massacre victims. *American Journal of Physical Anthropology*. *104*(4):513-528.

Young NM and Hallgrimsson B. 2005. Serial homology and the evolution of mammalian limb covariation structure. *Evolution*. 59(12):2691-2704.

Young NM, Wagner GP and Hallgrimsson B. 2010. Development and the evolvability of human limbs. *PNAS.* 107(8):3400-3405.

Zelditch ML, Lundrigan BL and Garland T. 2004. Developmental regulation of skull morphology. I. Ontogenetic dynamics of variance. *Evolution and Development*. *6*(3):194-206.

Zeller R, Lopez-Rios J and Zuniga A. 2009. Vertebrate limb bud development: moving towards integrative analysis of organogenesis. *Nature Reviews.* 10:845-858.

Appendix

A.1 Homologous comparisons

A.1.1. Correct match ranks

Table 9.1. Correct match predictive probability ranks for right femur predicting left femur.

Density				Equal			
Rank	Frequency	Percent	Cumulative	Rank	Frequency	Percent	Cumulative
1	535	53.50%	53.50%	1	782	78.20%	78.20%
2	258	25.80%	79.30%	2	88	8.80%	87.00%
3	110	11.00%	90.30%	3	34	3.40%	90.40%
4	59	5.90%	96.20%	4	28	2.80%	93.20%
5	20	2.00%	98.20%	5	17	1.70%	94.90%
6	11	1.10%	99.30%	6	14	1.40%	96.30%
7	0	0.00%	99.30%	7	14	1.40%	97.70%
8	4	0.40%	99.70%	8	15	1.50%	99.20%
9	2	0.20%	99.90%	9	3	0.30%	99.50%
10	1	0.10%	100.00%	10	5	0.50%	100.00%
Size				Shape			
1	488	48.80%	48.80%	1	615	61.50%	61.50%
2	285	28.50%	77.30%	2	142	14.20%	75.70%
3	127	12.70%	90.00%	3	68	6.80%	82.50%
4	62	6.20%	96.20%	4	54	5.40%	87.90%
5	19	1.90%	98.10%	5	26	2.60%	90.50%
6	10	1.00%	99.10%	6	27	2.70%	93.20%
7	1	0.10%	99.20%	7	13	1.30%	94.50%
8	3	0.30%	99.50%	8	16	1.60%	96.10%
9	2	0.20%	99.70%	9	17	1.70%	97.80%
10	3	0.30%	100.00%	10	22	2.20%	100.00%

Table 9.2. Correct match predictive probability ranks for left femur predicting right femur.

Density				Equal			
Rank	Frequency	Percent	Cumulative	Rank	Frequency	Percent	Cumulative
1	550	55.00%	55.00%	1	722	72.20%	72.20%
2	206	20.60%	75.60%	2	127	12.70%	84.90%
3	119	11.90%	87.50%	3	34	3.40%	88.30%
4	65	6.50%	94.00%	4	19	1.90%	90.20%
5	30	3.00%	97.00%	5	25	2.50%	92.70%
6	19	1.90%	98.90%	6	19	1.90%	94.60%
7	5	0.50%	99.40%	7	14	1.40%	96.00%
8	4	0.40%	99.80%	8	11	1.10%	97.10%
9	1	0.10%	99.90%	9	19	1.90%	99.00%
10	1	0.10%	100.00%	10	10	1.00%	100.00%
Size				Shape			
1	487	48.70%	48.70%	1	577	57.70%	57.70%
2	247	24.70%	73.40%	2	149	14.90%	72.60%
3	133	13.30%	86.70%	3	69	6.90%	79.50%
4	67	6.70%	93.40%	4	49	4.90%	84.40%
5	33	3.30%	96.70%	5	27	2.70%	87.10%
6	20	2.00%	98.70%	6	45	4.50%	91.60%
7	6	0.60%	99.30%	7	25	2.50%	94.10%
8	4	0.40%	99.70%	8	14	1.40%	95.50%
9	1	0.10%	99.80%	9	31	3.10%	98.60%
10	2	0.20%	100.00%	10	14	1.40%	100.00%

Table 9.3. Correct match predictive probability ranks for left radius predicting right radius.

Density				Equal			
Rank	Frequency	Percent	Cumulative	Rank	Frequency	Percent	Cumulative
1	478	47.80%	47.80%	1	704	70.40%	70.40%
2	236	23.60%	71.40%	2	115	11.50%	81.90%
3	143	14.30%	85.70%	3	43	4.30%	86.20%
4	75	7.50%	93.20%	4	30	3.00%	89.20%
5	43	4.30%	97.50%	5	23	2.30%	91.50%
6	12	1.20%	98.70%	6	20	2.00%	93.50%
7	9	0.90%	99.60%	7	14	1.40%	94.90%
8	0	0.00%	99.60%	8	22	2.20%	97.10%
9	1	0.10%	99.70%	9	13	1.30%	98.40%
10	3	0.30%	100.00%	10	16	1.60%	100.00%
Size				Shape			
1	453	45.30%	45.30%	1	552	55.20%	55.20%
2	246	24.60%	69.90%	2	135	13.50%	68.70%
3	151	15.10%	85.00%	3	87	8.70%	77.40%
4	81	8.10%	93.10%	4	46	4.60%	82.00%
5	47	4.70%	97.80%	5	37	3.70%	85.70%
6	13	1.30%	99.10%	6	29	2.90%	88.60%
7	9	0.90%	100.00%	7	35	3.50%	92.10%
8	0	0.00%	100.00%	8	28	2.80%	94.90%
9	0	0.00%	100.00%	9	20	2.00%	96.90%
10	0	0.00%	100.00%	10	31	3.10%	100.00%

Table 9.4. Correct match predictive probability ranks for right radius predicting left radius.

Density				Equal			
Rank	Frequency	Percent	Cumulative	Rank	Frequency	Percent	Cumulative
1	452	45.20%	45.20%	1	668	66.80%	66.80%
2	260	26.00%	71.20%	2	123	12.30%	79.10%
3	142	14.20%	85.40%	3	52	5.20%	84.30%
4	82	8.20%	93.60%	4	40	4.00%	88.30%
5	39	3.90%	97.50%	5	31	3.10%	91.40%
6	17	1.70%	99.20%	6	19	1.90%	93.30%
7	7	0.70%	99.90%	7	23	2.30%	95.60%
8	1	0.10%	100.00%	8	17	1.70%	97.30%
9	0	0.00%	100.00%	9	16	1.60%	98.90%
10	0	0.00%	100.00%	10	11	1.10%	100.00%
Size				Shape			
1	412	41.20%	41.20%	1	480	48.00%	48.00%
2	286	28.60%	69.80%	2	136	13.60%	61.60%
3	154	15.40%	85.20%	3	85	8.50%	70.10%
4	81	8.10%	93.30%	4	57	5.70%	75.80%
5	40	4.00%	97.30%	5	44	4.40%	80.20%
6	20	2.00%	99.30%	6	45	4.50%	84.70%
7	5	0.50%	99.80%	7	46	4.60%	89.30%
8	2	0.20%	100.00%	8	43	4.30%	93.60%
9	0	0.00%	100.00%	9	33	3.30%	96.90%
10	0	0.00%	100.00%	10	31	3.10%	100.00%

Table 9.5. Correct match predictive probability ranks for left tibia predicting right tibia.

Density				Equal			
Rank	Frequency	Percent	Cumulative	Rank	Frequency	Percent	Cumulative
1	694	69.40%	69.40%	1	900	90.00%	90.00%
2	199	19.90%	89.30%	2	56	5.60%	95.60%
3	65	6.50%	95.80%	3	14	1.40%	97.00%
4	24	2.40%	98.20%	4	9	0.90%	97.90%
5	8	0.80%	99.00%	5	6	0.60%	98.50%
6	4	0.40%	99.40%	6	3	0.30%	98.80%
7	2	0.20%	99.60%	7	0	0.00%	98.80%
8	0	0.00%	99.60%	8	1	0.10%	98.90%
9	3	0.30%	99.90%	9	0	0.00%	98.90%
10	1	0.10%	100.00%	10	11	1.10%	100.00%
Size				Shape			
1	652	65.20%	65.20%	1	726	72.60%	72.60%
2	234	23.40%	88.60%	2	117	11.70%	84.30%
3	70	7.00%	95.60%	3	60	6.00%	90.30%
4	30	3.00%	98.60%	4	36	3.60%	93.90%
5	7	0.70%	99.30%	5	19	1.90%	95.80%
6	5	0.50%	99.80%	6	15	1.50%	97.30%
7	2	0.20%	100.00%	7	8	0.80%	98.10%
8	0	0.00%	100.00%	8	5	0.50%	98.60%
9	0	0.00%	100.00%	9	2	0.20%	98.80%
10	0	0.00%	100.00%	10	12	1.20%	100.00%

Table 9.6. Correct match predictive probability ranks for right tibia predicting left tibia.

Density				Equal			
Rank	Frequency	Percent	Cumulative	Rank	Frequency	Percent	Cumulative
1	669	66.90%	66.90%	1	884	88.40%	88.40%
2	223	22.30%	89.20%	2	71	7.10%	95.50%
3	68	6.80%	96.00%	3	10	1.00%	96.50%
4	20	2.00%	98.00%	4	8	0.80%	97.30%
5	4	0.40%	98.40%	5	3	0.30%	97.60%
6	1	0.10%	98.50%	6	1	0.10%	97.70%
7	1	0.10%	98.60%	7	5	0.50%	98.20%
8	0	0.00%	98.60%	8	3	0.30%	98.50%
9	2	0.20%	98.80%	9	4	0.40%	98.90%
10	12	1.20%	100.00%	10	11	1.10%	100.00%
Size				Shape			
1	633	63.30%	63.30%	1	711	71.10%	71.10%
2	251	25.10%	88.40%	2	132	13.20%	84.30%
3	67	6.70%	95.10%	3	58	5.80%	90.10%
4	31	3.10%	98.20%	4	31	3.10%	93.20%
5	6	0.60%	98.80%	5	20	2.00%	95.20%
6	4	0.40%	99.20%	6	9	0.90%	96.10%
7	2	0.20%	99.40%	7	9	0.90%	97.00%
8	2	0.20%	99.60%	8	8	0.80%	97.80%
9	3	0.30%	99.90%	9	7	0.70%	98.50%
10	1	0.10%	100.00%	10	15	1.50%	100.00%

Table 9.7. Correct match predictive probability ranks for left ulna predicting right ulna.

Density				Equal			
Rank	Frequency	Percent	Cumulative	Rank	Frequency	Percent	Cumulative
1	662	66.20%	66.20%	1	812	81.20%	81.20%
2	202	20.20%	86.40%	2	90	9.00%	90.20%
3	68	6.80%	93.20%	3	43	4.30%	94.50%
4	41	4.10%	97.30%	4	12	1.20%	95.70%
5	9	0.90%	98.20%	5	10	1.00%	96.70%
6	1	0.10%	98.30%	6	6	0.60%	97.30%
7	4	0.40%	98.70%	7	10	1.00%	98.30%
8	1	0.10%	98.80%	8	6	0.60%	98.90%
9	6	0.60%	99.40%	9	7	0.70%	99.60%
10	6	0.60%	100.00%	10	4	0.40%	100.00%
Size				Shape			
1	559	55.90%	55.90%	1	654	65.40%	65.40%
2	264	26.40%	82.30%	2	137	13.70%	79.10%
3	105	10.50%	92.80%	3	62	6.20%	85.30%
4	44	4.40%	97.20%	4	47	4.70%	90.00%
5	11	1.10%	98.30%	5	28	2.80%	92.80%
6	3	0.30%	98.60%	6	25	2.50%	95.30%
7	5	0.50%	99.10%	7	18	1.80%	97.10%
8	4	0.40%	99.50%	8	7	0.70%	97.80%
9	4	0.40%	99.90%	9	10	1.00%	98.80%
10	1	0.10%	100.00%	10	12	1.20%	100.00%

Table 9.8. Correct match predictive probability ranks for right ulna predicting left ulna.

Density				Equal			
Rank	Frequency	Percent	Cumulative	Rank	Frequency	Percent	Cumulative
1	650	65.00%	65.00%	1	818	81.80%	81.80%
2	197	19.70%	84.70%	2	100	10.00%	91.80%
3	85	8.50%	93.20%	3	35	3.50%	95.30%
4	32	3.20%	96.40%	4	16	1.60%	96.90%
5	14	1.40%	97.80%	5	12	1.20%	98.10%
6	12	1.20%	99.00%	6	2	0.20%	98.30%
7	4	0.40%	99.40%	7	5	0.50%	98.80%
8	2	0.20%	99.60%	8	5	0.50%	99.30%
9	1	0.10%	99.70%	9	4	0.40%	99.70%
10	3	0.30%	100.00%	10	3	0.30%	100.00%
Size				Shape			
1	553	55.30%	55.30%	1	633	63.30%	63.30%
2	253	25.30%	80.60%	2	162	16.20%	79.50%
3	122	12.20%	92.80%	3	80	8.00%	87.50%
4	40	4.00%	96.80%	4	38	3.80%	91.30%
5	14	1.40%	98.20%	5	27	2.70%	94.00%
6	10	1.00%	99.20%	6	16	1.60%	95.60%
7	4	0.40%	99.60%	7	14	1.40%	97.00%
8	3	0.30%	99.90%	8	10	1.00%	98.00%
9	1	0.10%	100.00%	9	12	1.20%	99.20%
10	0	0.00%	100.00%	10	8	0.80%	100.00%

A.1.2. Descriptive statistics

Table 9.9. Predictive probability and typicality descriptive statistics for correct and incorrect left femur predicting right femur.

	Density			Equal			Size			Shape		
	Correct Classifications											
	Mean	Min	Max	Mean	Min	Max	Mean	Min	Max	Mean	Min	Max
Probability	0.389	0.147	0.816	0.189	0.129	0.337	0.465	0.148	1.000	0.181	0.132	0.334
Typicality	0.909	0.049	1.000	0.795	0.325	0.984	0.906	0.049	1.000	0.729	0.319	0.877
	Incorrect Classifications											
	Mean	Min	Max	Mean	Min	Max	Mean	Min	Max	Mean	Min	Max
Probability	0.313	0.157	0.682	0.163	0.125	0.342	0.339	0.160	0.969	0.162	0.127	0.314
Typicality	0.918	0.188	1.000	0.702	0.342	0.922	0.921	0.188	1.000	0.665	0.316	0.822

Table 9.10. Predictive probability and typicality descriptive statistics for correct and incorrect right femur predicting left femur.

	Density			Equal			Size			Shape		
	Correct Classifications											
	Mean	Min	Max	Mean	Min	Max	Mean	Min	Max	Mean	Min	Max
Probability	0.373	0.160	0.740	0.173	0.119	0.283	0.471	0.161	1.000	0.157	0.112	0.265
Typicality	0.910	0.156	1.000	0.802	0.343	0.970	0.907	0.156	1.000	0.747	0.399	0.880
	Incorrect Classifications											
	Mean	Min	Max	Mean	Min	Max	Mean	Min	Max	Mean	Min	Max
Probability	0.292	0.144	0.690	0.146	0.115	0.196	0.330	0.147	0.999	0.141	0.112	0.206
Typicality	0.918	0.184	1.000	0.716	0.367	0.941	0.921	0.184	1.000	0.690	0.367	0.874

Table 9.11. Predictive probability and typicality descriptive statistics for correct and incorrect left radius predicting right radius.

	Density			Equal			Size			Shape		
	Correct Classifications											
	Mean	Min	Max	Mean	Min	Max	Mean	Min	Max	Mean	Min	Max
Probability	0.401	0.176	0.786	0.187	0.127	0.319	0.508	0.182	1.000	0.173	0.125	0.303
Typicality	0.882	0.135	1.000	0.796	0.311	0.962	0.881	0.135	1.000	0.726	0.189	0.866
	Incorrect Classifications											
	Mean	Min	Max	Mean	Min	Max	Mean	Min	Max	Mean	Min	Max
Probability	0.312	0.153	0.647	0.158	0.120	0.259	0.362	0.158	0.888	0.155	0.127	0.225
Typicality	0.879	0.072	1.000	0.718	0.317	0.926	0.881	0.072	1.000	0.695	0.249	0.874

Table 9.12. Predictive probability and typicality descriptive statistics for correct and incorrect right radius predicting left radius.

	Density			Equal			Size			Shape		
	Correct Classifications											
	Mean	Min	Max	Mean	Min	Max	Mean	Min	Max	Mean	Min	Max
Probability	0.398	0.169	0.790	0.198	0.128	0.402	0.481	0.171	1.000	0.192	0.145	0.489
Typicality	0.882	0.106	1.000	0.792	0.272	0.964	0.877	0.106	1.000	0.723	0.164	0.848
	Incorrect Classifications											
	Mean	Min	Max	Mean	Min	Max	Mean	Min	Max	Mean	Min	Max
Probability	0.326	0.168	0.709	0.170	0.128	0.262	0.361	0.172	0.909	0.172	0.132	0.281
Typicality	0.897	0.063	1.000	0.734	0.458	0.935	0.900	0.063	1.000	0.703	0.247	0.850

Table 9.13. Predictive probability and typicality descriptive statistics for correct and incorrect left tibia predicting right tibia.

	Density			Equal			Size			Shape		
	Correct Classifications											
	Mean	Min	Max	Mean	Min	Max	Mean	Min	Max	Mean	Min	Max
Probability	0.519	0.172	0.861	0.220	0.122	0.465	0.635	0.172	1.000	0.197	0.131	0.479
Typicality	0.870	0.028	1.000	0.781	0.267	0.978	0.865	0.028	1.000	0.714	0.359	0.867
	Incorrect Classifications											
	Mean	Min	Max	Mean	Min	Max	Mean	Min	Max	Mean	Min	Max
Probability	0.377	0.183	0.803	0.168	0.132	0.239	0.420	0.190	1.000	0.165	0.129	0.305
Typicality	0.885	0.006	1.000	0.678	0.238	0.909	0.893	0.010	1.000	0.653	0.402	0.826

Table 9.14. Predictive probability and typicality descriptive statistics for correct and incorrect right tibia predicting left tibia.

	Density			Equal			Size			Shape		
	Correct Classifications											
	Mean	Min	Max	Mean	Min	Max	Mean	Min	Max	Mean	Min	Max
Probability	0.509	0.221	0.863	0.200	0.129	0.328	0.623	0.227	1.000	0.182	0.121	0.319
Typicality	0.890	0.185	1.000	0.785	0.388	0.954	0.888	0.185	1.000	0.727	0.362	0.868
	Incorrect Classifications											
	Mean	Min	Max	Mean	Min	Max	Mean	Min	Max	Mean	Min	Max
Probability	0.373	0.187	0.723	0.154	0.112	0.224	0.425	0.193	0.999	0.152	0.118	0.261
Typicality	0.880	0.047	1.000	0.656	0.245	0.883	0.885	0.047	1.000	0.657	0.245	0.832

Table 9.15. Predictive probability and typicality descriptive statistics for correct and incorrect left ulna predicting right ulna.

	Density			Equal			Size			Shape		
	Correct Classifications											
	Mean	Min	Max	Mean	Min	Max	Mean	Min	Max	Mean	Min	Max
Probability	0.366	0.140	0.900	0.222	0.126	0.484	0.388	0.155	0.995	0.203	0.120	0.625
Typicality	0.920	0.113	1.000	0.830	0.496	0.999	0.921	0.113	1.000	0.584	0.310	0.666
	Incorrect Classifications											
	Mean	Min	Max	Mean	Min	Max	Mean	Min	Max	Mean	Min	Max
Probability	0.271	0.138	0.898	0.186	0.129	0.386	0.277	0.138	0.977	0.168	0.119	0.505
Typicality	0.937	0.221	1.000	0.800	0.285	0.998	0.936	0.221	1.000	0.599	0.200	0.666

Table 9.16.Predictive probability and typicality descriptive statistics for correct and incorrect right ulna predicting left ulna.

	Density			Equal			Size			Shape		
	Correct Classifications											
	Mean	Min	Max	Mean	Min	Max	Mean	Min	Max	Mean	Min	Max
Probability	0.338	0.149	0.757	0.213	0.139	0.458	0.409	0.150	1.000	0.217	0.148	0.516
Typicality	0.936	0.001	1.000	0.784	0.403	0.972	0.935	0.107	1.000	0.703	0.280	0.863
	Incorrect Classifications											
	Mean	Min	Max	Mean	Min	Max	Mean	Min	Max	Mean	Min	Max
Probability	0.290	0.157	0.698	0.177	0.132	0.273	0.317	0.160	0.982	0.183	0.141	0.325
Typicality	0.945	0.000	1.000	0.704	0.417	0.929	0.948	0.001	1.000	0.649	0.165	0.843

A.2. Serially homologous comparisons

A.2.1. Correct match rank

Table 9.17. Correct match predictive probability ranks for right ulna predicting right tibia.

Density				Equal			
Rank	Frequency	Percent	Cumulative	Rank	Frequency	Percent	Cumulative
1	310	31.00%	31.00%	1	451	45.10%	45.10%
2	241	24.10%	55.10%	2	208	20.80%	65.90%
3	165	16.50%	71.60%	3	136	13.60%	79.50%
4	115	11.50%	83.10%	4	75	7.50%	87.00%
5	85	8.50%	91.60%	5	34	3.40%	90.40%
6	42	4.20%	95.80%	6	24	2.40%	92.80%
7	22	2.20%	98.00%	7	14	1.40%	94.20%
8	16	1.60%	99.60%	8	19	1.90%	96.10%
9	3	0.30%	99.90%	9	17	1.70%	97.80%
10	1	0.10%	100.00%	10	22	2.20%	100.00%
Size				Shape			
1	283	28.30%	28.30%	1	299	29.90%	29.90%
2	259	25.90%	54.20%	2	170	17.00%	46.90%
3	163	16.30%	70.50%	3	114	11.40%	58.30%
4	125	12.50%	83.00%	4	86	8.60%	66.90%
5	82	8.20%	91.20%	5	87	8.70%	75.60%
6	46	4.60%	95.80%	6	63	6.30%	81.90%
7	22	2.20%	98.00%	7	70	7.00%	88.90%
8	15	1.50%	99.50%	8	40	4.00%	92.90%
9	4	0.40%	99.90%	9	48	4.80%	97.70%
10	1	0.10%	100.00%	10	23	2.30%	100.00%

Table 9.18. Correct match predictive probability ranks for right tibia predicting right ulna.

Density				Equal			
Rank	Frequency	Percent	Cumulative	Rank	Frequency	Percent	Cumulative
1	309	30.90%	30.90%	1	451	45.10%	45.10%
2	212	21.20%	52.10%	2	237	23.70%	68.80%
3	180	18.00%	70.10%	3	104	10.40%	79.20%
4	123	12.30%	82.40%	4	47	4.70%	83.90%
5	88	8.80%	91.20%	5	44	4.40%	88.30%
6	52	5.20%	96.40%	6	46	4.60%	92.90%
7	26	2.60%	99.00%	7	32	3.20%	96.10%
8	9	0.90%	99.90%	8	11	1.10%	97.20%
9	1	0.10%	100.00%	9	20	2.00%	99.20%
10	0	0.00%	100.00%	10	8	0.80%	100.00%
Size				Shape			
1	292	29.20%	29.20%	1	271	27.10%	27.10%
2	215	21.50%	50.70%	2	188	18.80%	45.90%
3	190	19.00%	69.70%	3	132	13.20%	59.10%
4	122	12.20%	81.90%	4	90	9.00%	68.10%
5	93	9.30%	91.20%	5	68	6.80%	74.90%
6	51	5.10%	96.30%	6	68	6.80%	81.70%
7	29	2.90%	99.20%	7	61	6.10%	87.80%
8	7	0.70%	99.90%	8	58	5.80%	93.60%
9	1	0.10%	100.00%	9	40	4.00%	97.60%
10	0	0.00%	100.00%	10	24	2.40%	100.00%

Table 9.19. Correct match predictive probability ranks for right femur predicting right humerus.

Density				Equal			
Rank	Frequency	Percent	Cumulative	Rank	Frequency	Percent	Cumulative
1	279	27.90%	27.90%	1	366	36.60%	36.60%
2	195	19.50%	47.40%	2	195	19.50%	56.10%
3	174	17.40%	64.80%	3	112	11.20%	67.30%
4	123	12.30%	77.10%	4	92	9.20%	76.50%
5	94	9.40%	86.50%	5	53	5.30%	81.80%
6	62	6.20%	92.70%	6	58	5.80%	87.60%
7	36	3.60%	96.30%	7	40	4.00%	91.60%
8	14	1.40%	97.70%	8	38	3.80%	95.40%
9	12	1.20%	98.90%	9	26	2.60%	98.00%
10	11	1.10%	100.00%	10	20	2.00%	100.00%
Size				Shape			
1	269	26.90%	26.90%	1	232	23.20%	23.20%
2	199	19.90%	46.80%	2	145	14.50%	37.70%
3	169	16.90%	63.70%	3	108	10.80%	48.50%
4	136	13.60%	77.30%	4	101	10.10%	58.60%
5	93	9.30%	86.60%	5	73	7.30%	65.90%
6	57	5.70%	92.30%	6	97	9.70%	75.60%
7	39	3.90%	96.20%	7	85	8.50%	84.10%
8	18	1.80%	98.00%	8	65	6.50%	90.60%
9	15	1.50%	99.50%	9	50	5.00%	95.60%
10	5	0.50%	100.00%	10	44	4.40%	100.00%

Table 9.20. Correct match predictive probability ranks for right humerus predicting right femur.

Density				Equal			
Rank	Frequency	Percent	Cumulative	Rank	Frequency	Percent	Cumulative
1	279	27.90%	27.90%	1	366	36.60%	36.60%
2	195	19.50%	47.40%	2	195	19.50%	56.10%
3	174	17.40%	64.80%	3	112	11.20%	67.30%
4	123	12.30%	77.10%	4	92	9.20%	76.50%
5	94	9.40%	86.50%	5	53	5.30%	81.80%
6	62	6.20%	92.70%	6	58	5.80%	87.60%
7	36	3.60%	96.30%	7	40	4.00%	91.60%
8	14	1.40%	97.70%	8	38	3.80%	95.40%
9	12	1.20%	98.90%	9	26	2.60%	98.00%
10	11	1.10%	100.00%	10	20	2.00%	100.00%
Size				Shape			
1	269	26.90%	26.90%	1	232	23.20%	23.20%
2	199	19.90%	46.80%	2	145	14.50%	37.70%
3	169	16.90%	63.70%	3	108	10.80%	48.50%
4	136	13.60%	77.30%	4	101	10.10%	58.60%
5	93	9.30%	86.60%	5	73	7.30%	65.90%
6	57	5.70%	92.30%	6	97	9.70%	75.60%
7	39	3.90%	96.20%	7	85	8.50%	84.10%
8	18	1.80%	98.00%	8	65	6.50%	90.60%
9	15	1.50%	99.50%	9	50	5.00%	95.60%
10	5	0.50%	100.00%	10	44	4.40%	100.00%

A.2.2. Descriptive Statistics

Table 9.21. Predictive probability and typicality descriptive statistics for correct and incorrect right ulna predicting right tibia.

	Density			Equal			Size			Shape		
	Correct Classifications											
	Mean	Min	Max	Mean	Min	Max	Mean	Min	Max	Mean	Min	Max
Probability	0.337	0.145	0.867	0.319	0.216	0.634	0.371	0.146	1.000	0.337	0.231	0.769
Typicality	0.910	0.096	1.000	0.838	0.317	0.996	0.906	0.096	1.000	0.662	0.249	0.748
	Incorrect Classifications											
	Mean	Min	Max	Mean	Min	Max	Mean	Min	Max	Mean	Min	Max
Probability	0.260	0.133	0.722	0.271	0.197	0.485	0.269	0.133	0.868	0.300	0.227	0.622
Typicality	0.927	0.259	1.000	0.801	0.300	0.989	0.929	0.259	1.000	0.660	0.269	0.749

Table 9.22. Predictive probability and typicality descriptive statistics for correct and incorrect right tibia predicting right ulna.

	Density			Equal			Size			Shape		
	Correct Classifications											
	Mean	Min	Max	Mean	Min	Max	Mean	Min	Max	Mean	Min	Max
Probability	0.332	0.153	0.812	0.218	0.155	0.388	0.374	0.153	0.987	0.230	0.172	0.482
Typicality	0.890	0.194	1.000	0.786	0.327	0.977	0.889	0.194	1.000	0.690	0.185	0.825
	Incorrect Classifications											
	Mean	Min	Max	Mean	Min	Max	Mean	Min	Max	Mean	Min	Max
Probability	0.259	0.130	0.574	0.195	0.152	0.297	0.274	0.130	0.662	0.206	0.165	0.376
Typicality	0.928	0.344	1.000	0.779	0.349	0.966	0.928	0.344	1.000	0.700	0.280	0.819

Table 9.23. Predictive probability and typicality descriptive statistics for correct and incorrect right femur predicting right humerus.

	Density			Equal			Size			Shape		
	Correct Classifications											
	Mean	Min	Max	Mean	Min	Max	Mean	Min	Max	Mean	Min	Max
Probability	0.301	0.132	0.881	0.239	0.170	0.468	0.317	0.132	0.995	0.245	0.189	0.475
Typicality	0.938	0.041	1.000	0.824	0.511	0.987	0.936	0.041	1.000	0.699	0.436	0.790
	Incorrect Classifications											
	Mean	Min	Max	Mean	Min	Max	Mean	Min	Max	Mean	Min	Max
Probability	0.233	0.121	0.851	0.217	0.164	0.413	0.240	0.122	0.934	0.238	0.186	0.377
Typicality	0.950	0.082	1.000	0.811	0.449	0.999	0.950	0.082	1.000	0.694	0.415	0.799

Table 9.24. Predictive probability and typicality descriptive statistics for correct and incorrect right humerus predicting right femur.

	Density			Equal			Size			Shape		
	Correct Classifications											
	Mean	Min	Max	Mean	Min	Max	Mean	Min	Max	Mean	Min	Max
Probability	0.286	0.127	0.773	0.233	0.174	0.412	0.304	0.127	0.897	0.241	0.192	0.351
Typicality	0.928	0.237	1.000	0.830	0.413	0.974	0.925	0.237	1.000	0.710	0.420	0.795
	Incorrect Classifications											
	Mean	Min	Max	Mean	Min	Max	Mean	Min	Max	Mean	Min	Max
Probability	0.232	0.116	0.711	0.215	0.163	0.369	0.238	0.117	0.787	0.237	0.191	0.340
Typicality	0.946	0.179	1.000	0.805	0.384	0.991	0.947	0.179	1.000	0.694	0.293	0.799

A.3. Within-limb comparisons

A.3.1. Correct match rank

Table 9.25. Correct match predictive probability ranks for right ulna predicting right radius.

Density				Equal			
Rank	Frequency	Percent	Cumulative	Rank	Frequency	Percent	Cumulative
1	501	50.10%	50.10%	1	620	62.00%	62.00%
2	250	25.00%	75.10%	2	193	19.30%	81.30%
3	134	13.40%	88.50%	3	91	9.10%	90.40%
4	73	7.30%	95.80%	4	25	2.50%	92.90%
5	31	3.10%	98.90%	5	27	2.70%	95.60%
6	9	0.90%	99.80%	6	16	1.60%	97.20%
7	2	0.20%	100.00%	7	14	1.40%	98.60%
8	0	0.00%	100.00%	8	9	0.90%	99.50%
9	0	0.00%	100.00%	9	5	0.50%	100.00%
10	0	0.00%	100.00%	10	0	0.00%	100.00%
Size				Shape			
1	494	49.40%	49.40%	1	268	26.80%	26.80%
2	254	25.40%	74.80%	2	172	17.20%	44.00%
3	136	13.60%	88.40%	3	162	16.20%	60.20%
4	74	7.40%	95.80%	4	118	11.80%	72.00%
5	31	3.10%	98.90%	5	82	8.20%	80.20%
6	9	0.90%	99.80%	6	86	8.60%	88.80%
7	2	0.20%	100.00%	7	39	3.90%	92.70%
8	0	0.00%	100.00%	8	21	2.10%	94.80%
9	0	0.00%	100.00%	9	34	3.40%	98.20%
10	0	0.00%	100.00%	10	18	1.80%	100.00%

Table 9.26. Correct match predictive probability ranks for right ulna predicting right humerus.

Density				Equal			
Rank	Frequency	Percent	Cumulative	Rank	Frequency	Percent	Cumulative
1	242	24.20%	24.20%	1	352	35.20%	35.20%
2	193	19.30%	43.50%	2	208	20.80%	56.00%
3	189	18.90%	62.40%	3	128	12.80%	68.80%
4	118	11.80%	74.20%	4	77	7.70%	76.50%
5	76	7.60%	81.80%	5	63	6.30%	82.80%
6	67	6.70%	88.50%	6	57	5.70%	88.50%
7	47	4.70%	93.20%	7	39	3.90%	92.40%
8	45	4.50%	97.70%	8	17	1.70%	94.10%
9	16	1.60%	99.30%	9	21	2.10%	96.20%
10	7	0.70%	100.00%	10	38	3.80%	100.00%
Size				Shape			
1	224	22.40%	22.40%	1	191	19.10%	19.10%
2	197	19.70%	42.10%	2	164	16.40%	35.50%
3	196	19.60%	61.70%	3	130	13.00%	48.50%
4	123	12.30%	74.00%	4	114	11.40%	59.90%
5	78	7.80%	81.80%	5	109	10.90%	70.80%
6	66	6.60%	88.40%	6	88	8.80%	79.60%
7	47	4.70%	93.10%	7	58	5.80%	85.40%
8	46	4.60%	97.70%	8	58	5.80%	91.20%
9	16	1.60%	99.30%	9	44	4.40%	95.60%
10	7	0.70%	100.00%	10	44	4.40%	100.00%

Table 9.27. Correct match predictive probability ranks for right tibia predicting right femur.

Density				Equal			
Rank	Frequency	Percent	Cumulative	Rank	Frequency	Percent	Cumulative
1	368	36.80%	36.80%	1	492	49.20%	49.20%
2	278	27.80%	64.60%	2	219	21.90%	71.10%
3	148	14.80%	79.40%	3	110	11.00%	82.10%
4	93	9.30%	88.70%	4	56	5.60%	87.70%
5	58	5.80%	94.50%	5	52	5.20%	92.90%
6	30	3.00%	97.50%	6	23	2.30%	95.20%
7	14	1.40%	98.90%	7	13	1.30%	96.50%
8	8	0.80%	99.70%	8	16	1.60%	98.10%
9	1	0.10%	99.80%	9	11	1.10%	99.20%
10	2	0.20%	100.00%	10	8	0.80%	100.00%
Size				Shape			
1	357	35.70%	35.70%	1	237	23.70%	23.70%
2	286	28.60%	64.30%	2	186	18.60%	42.30%
3	153	15.30%	79.60%	3	142	14.20%	56.50%
4	90	9.00%	88.60%	4	103	10.30%	66.80%
5	60	6.00%	94.60%	5	77	7.70%	74.50%
6	29	2.90%	97.50%	6	74	7.40%	81.90%
7	14	1.40%	98.90%	7	68	6.80%	88.70%
8	8	0.80%	99.70%	8	52	5.20%	93.90%
9	1	0.10%	99.80%	9	35	3.50%	97.40%
10	2	0.20%	100.00%	10	26	2.60%	100.00%

Table 9.28. Correct match predictive probability ranks for right radius predicting right ulna.

Density				Equal			
Rank	Frequency	Percent	Cumulative	Rank	Frequency	Percent	Cumulative
1	492	49.20%	49.20%	1	583	58.30%	58.30%
2	245	24.50%	73.70%	2	217	21.70%	80.00%
3	149	14.90%	88.60%	3	102	10.20%	90.20%
4	69	6.90%	95.50%	4	44	4.40%	94.60%
5	30	3.00%	98.50%	5	23	2.30%	96.90%
6	10	1.00%	99.50%	6	13	1.30%	98.20%
7	5	0.50%	100.00%	7	13	1.30%	99.50%
8	0	0.00%	100.00%	8	3	0.30%	99.80%
9	0	0.00%	100.00%	9	1	0.10%	99.90%
10	0	0.00%	100.00%	10	1	0.10%	100.00%
Size				Shape			
1	485	48.50%	48.50%	1	259	25.90%	25.90%
2	251	25.10%	73.60%	2	196	19.60%	45.50%
3	150	15.00%	88.60%	3	168	16.80%	62.30%
4	68	6.80%	95.40%	4	111	11.10%	73.40%
5	31	3.10%	98.50%	5	93	9.30%	82.70%
6	10	1.00%	99.50%	6	59	5.90%	88.60%
7	5	0.50%	100.00%	7	35	3.50%	92.10%
8	0	0.00%	100.00%	8	28	2.80%	94.90%
9	0	0.00%	100.00%	9	29	2.90%	97.80%
10	0	0.00%	100.00%	10	22	2.20%	100.00%

Table 9.29. Correct match predictive probability ranks for right radius predicting right humerus.

Density				Equal			
Rank	Frequency	Percent	Cumulative	Rank	Frequency	Percent	Cumulative
1	299	29.90%	29.90%	1	356	35.60%	35.60%
2	172	17.20%	47.10%	2	190	19.00%	54.60%
3	156	15.60%	62.70%	3	142	14.20%	68.80%
4	107	10.70%	73.40%	4	101	10.10%	78.90%
5	91	9.10%	82.50%	5	63	6.30%	85.20%
6	69	6.90%	89.40%	6	41	4.10%	89.30%
7	46	4.60%	94.00%	7	42	4.20%	93.50%
8	31	3.10%	97.10%	8	26	2.60%	96.10%
9	16	1.60%	98.70%	9	22	2.20%	98.30%
10	13	1.30%	100.00%	10	17	1.70%	100.00%
Size				Shape			
1	280	28.00%	28.00%	1	153	15.30%	15.30%
2	185	18.50%	46.50%	2	141	14.10%	29.40%
3	161	16.10%	62.60%	3	135	13.50%	42.90%
4	105	10.50%	73.10%	4	143	14.30%	57.20%
5	93	9.30%	82.40%	5	115	11.50%	68.70%
6	70	7.00%	89.40%	6	111	11.10%	79.80%
7	47	4.70%	94.10%	7	86	8.60%	88.40%
8	30	3.00%	97.10%	8	57	5.70%	94.10%
9	15	1.50%	98.60%	9	34	3.40%	97.50%
10	14	1.40%	100.00%	10	25	2.50%	100.00%

Table 9.30. Correct match predictive probability ranks for right humerus predicting right ulna.

Density				Equal			
Rank	Frequency	Percent	Cumulative	Rank	Frequency	Percent	Cumulative
1	245	24.50%	24.50%	1	339	33.90%	33.90%
2	204	20.40%	44.90%	2	231	23.10%	57.00%
3	150	15.00%	59.90%	3	138	13.80%	70.80%
4	116	11.60%	71.50%	4	115	11.50%	82.30%
5	102	10.20%	81.70%	5	54	5.40%	87.70%
6	69	6.90%	88.60%	6	35	3.50%	91.20%
7	49	4.90%	93.50%	7	30	3.00%	94.20%
8	39	3.90%	97.40%	8	23	2.30%	96.50%
9	21	2.10%	99.50%	9	15	1.50%	98.00%
10	5	0.50%	100.00%	10	20	2.00%	100.00%
Size				Shape			
1	237	23.70%	23.70%	1	217	21.70%	21.70%
2	205	20.50%	44.20%	2	143	14.30%	36.00%
3	151	15.10%	59.30%	3	138	13.80%	49.80%
4	114	11.40%	70.70%	4	121	12.10%	61.90%
5	109	10.90%	81.60%	5	102	10.20%	72.10%
6	68	6.80%	88.40%	6	98	9.80%	81.90%
7	52	5.20%	93.60%	7	63	6.30%	88.20%
8	40	4.00%	97.60%	8	55	5.50%	93.70%
9	20	2.00%	99.60%	9	32	3.20%	96.90%
10	4	0.40%	100.00%	10	31	3.10%	100.00%

Table 9.31. Correct match predictive probability ranks for right femur predicting right tibia.

Density				Equal			
Rank	Frequency	Percent	Cumulative	Rank	Frequency	Percent	Cumulative
1	363	36.30%	36.30%	1	492	49.20%	49.20%
2	249	24.90%	61.20%	2	197	19.70%	68.90%
3	153	15.30%	76.50%	3	112	11.20%	80.10%
4	98	9.80%	86.30%	4	55	5.50%	85.60%
5	63	6.30%	92.60%	5	48	4.80%	90.40%
6	38	3.80%	96.40%	6	37	3.70%	94.10%
7	24	2.40%	98.80%	7	25	2.50%	96.60%
8	8	0.80%	99.60%	8	15	1.50%	98.10%
9	4	0.40%	100.00%	9	12	1.20%	99.30%
10	0	0.00%	100.00%	10	7	0.70%	100.00%
Size				Shape			
1	353	35.30%	35.30%	1	282	28.20%	28.20%
2	255	25.50%	60.80%	2	185	18.50%	46.70%
3	149	14.90%	75.70%	3	115	11.50%	58.20%
4	106	10.60%	86.30%	4	120	12.00%	70.20%
5	62	6.20%	92.50%	5	69	6.90%	77.10%
6	39	3.90%	96.40%	6	62	6.20%	83.30%
7	24	2.40%	98.80%	7	53	5.30%	88.60%
8	8	0.80%	99.60%	8	39	3.90%	92.50%
9	4	0.40%	100.00%	9	43	4.30%	96.80%
10	0	0.00%	100.00%	10	32	3.20%	100.00%

Table 9.32. Correct match predictive probability ranks for right humerus predicting right radius.

Density				Equal			
Rank	Frequency	Percent	Cumulative	Rank	Frequency	Percent	Cumulative
1	254	25.40%	25.40%	1	355	35.50%	35.50%
2	195	19.50%	44.90%	2	206	20.60%	56.10%
3	163	16.30%	61.20%	3	115	11.50%	67.60%
4	121	12.10%	73.30%	4	92	9.20%	76.80%
5	89	8.90%	82.20%	5	61	6.10%	82.90%
6	67	6.70%	88.90%	6	52	5.20%	88.10%
7	48	4.80%	93.70%	7	33	3.30%	91.40%
8	33	3.30%	97.00%	8	30	3.00%	94.40%
9	16	1.60%	98.60%	9	31	3.10%	97.50%
10	14	1.40%	100.00%	10	25	2.50%	100.00%
Size				Shape			
1	239	23.90%	23.90%	1	249	24.90%	24.90%
2	200	20.00%	43.90%	2	164	16.40%	41.30%
3	163	16.30%	60.20%	3	99	9.90%	51.20%
4	131	13.10%	73.30%	4	87	8.70%	59.90%
5	89	8.90%	82.20%	5	74	7.40%	67.30%
6	69	6.90%	89.10%	6	74	7.40%	74.70%
7	47	4.70%	93.80%	7	73	7.30%	82.00%
8	32	3.20%	97.00%	8	59	5.90%	87.90%
9	18	1.80%	98.80%	9	70	7.00%	94.90%
10	12	1.20%	100.00%	10	51	5.10%	100.00%

A.3.2. Descriptive statistics

Table 9.33. Predictive probability and typicality descriptive statistics for correct and incorrect right ulna predicting right radius.

	Density			Equal			Size			Shape		
	Correct Classifications											
	Mean	Min	Max	Mean	Min	Max	Mean	Min	Max	Mean	Min	Max
Probability	0.546	0.203	0.988	0.494	0.272	0.822	0.578	0.204	1.000	0.474	0.313	0.867
Typicality	0.829	0.067	1.000	0.792	0.233	0.994	0.826	0.067	1.000	0.589	0.263	0.666
	Incorrect Classifications											
	Mean	Min	Max	Mean	Min	Max	Mean	Min	Max	Mean	Min	Max
Probability	0.391	0.173	0.895	0.404	0.258	0.652	0.399	0.174	0.959	0.402	0.299	0.797
Typicality	0.896	0.192	1.000	0.767	0.219	0.990	0.897	0.192	1.000	0.605	0.196	0.667

Table 9.34. Predictive probability and typicality descriptive statistics for correct and incorrect right ulna predicting right humerus.

	Density			Equal			Size			Shape		
	Correct Classifications											
	Mean	Min	Max	Mean	Min	Max	Mean	Min	Max	Mean	Min	Max
Probability	0.260	0.124	0.748	0.350	0.242	0.668	0.271	0.137	0.838	0.427	0.306	0.839
Typicality	0.926	0.363	1.000	0.852	0.086	0.998	0.922	0.363	1.000	0.591	0.085	0.667
	Incorrect Classifications											
	Mean	Min	Max	Mean	Min	Max	Mean	Min	Max	Mean	Min	Max
Probability	0.222	0.124	0.589	0.316	0.225	0.603	0.225	0.124	0.630	0.375	0.286	0.777
Typicality	0.956	0.431	1.000	0.853	0.313	0.999	0.957	0.431	1.000	0.619	0.146	0.667

Table 9.35. Predictive probability and typicality descriptive statistics for correct and incorrect right tibia predicting right femur.

	Density			Equal			Size			Shape		
	Correct Classifications											
	Mean	Min	Max	Mean	Min	Max	Mean	Min	Max	Mean	Min	Max
Probability	0.398	0.154	0.921	0.321	0.206	0.563	0.422	0.154	1.000	0.311	0.245	0.587
Typicality	0.897	0.180	1.000	0.814	0.421	0.985	0.896	0.180	1.000	0.654	0.240	0.747
	Incorrect Classifications											
	Mean	Min	Max	Mean	Min	Max	Mean	Min	Max	Mean	Min	Max
Probability	0.307	0.152	0.838	0.286	0.202	0.524	0.316	0.153	0.915	0.297	0.223	0.552
Typicality	0.918	0.174	1.000	0.788	0.371	0.990	0.918	0.174	1.000	0.660	0.235	0.749

Table 9.36. Predictive probability and typicality descriptive statistics for correct and incorrect right radius predicting right ulna.

	Density			Equal			Size			Shape		
	Correct Classifications											
	Mean	Min	Max	Mean	Min	Max	Mean	Min	Max	Mean	Min	Max
Probability	0.537	0.192	0.974	0.501	0.269	0.855	0.564	0.193	1.000	0.484	0.317	0.855
Typicality	0.853	0.043	1.000	0.770	0.088	0.991	0.851	0.043	1.000	0.557	0.072	0.666
	Incorrect Classifications											
	Mean	Min	Max	Mean	Min	Max	Mean	Min	Max	Mean	Min	Max
Probability	0.385	0.160	0.811	0.408	0.250	0.812	0.394	0.162	0.846	0.412	0.294	0.839
Typicality	0.871	0.084	1.000	0.760	0.085	0.996	0.872	0.084	1.000	0.599	0.076	0.666

Table 9.37. Predictive probability and typicality descriptive statistics for correct and incorrect right radius predicting right humerus.

	Density			Equal			Size			Shape		
	Correct Classifications											
	Mean	Min	Max	Mean	Min	Max	Mean	Min	Max	Mean	Min	Max
Probability	0.256	0.126	0.694	0.334	0.229	0.583	0.267	0.117	0.786	0.385	0.282	0.747
Typicality	0.947	0.518	1.000	0.873	0.553	0.999	0.945	0.518	1.000	0.610	0.301	0.666
	Incorrect Classifications											
	Mean	Min	Max	Mean	Min	Max	Mean	Min	Max	Mean	Min	Max
Probability	0.217	0.117	0.578	0.306	0.231	0.602	0.222	0.120	0.630	0.355	0.273	0.801
Typicality	0.953	0.223	1.000	0.867	0.224	1.000	0.954	0.223	1.000	0.621	0.016	0.667

Table 9.38. Predictive probability and typicality descriptive statistics for correct and incorrect right humerus predicting right ulna.

	Density			Equal			Size			Shape		
	Correct Classifications											
	Mean	Min	Max	Mean	Min	Max	Mean	Min	Max	Mean	Min	Max
Probability	0.260	0.125	0.744	0.345	0.248	0.682	0.269	0.125	0.810	0.422	0.295	0.783
Typicality	0.941	0.382	1.000	0.840	0.183	0.992	0.939	0.382	1.000	0.601	0.024	0.666
	Incorrect Classifications											
	Mean	Min	Max	Mean	Min	Max	Mean	Min	Max	Mean	Min	Max
Probability	0.223	0.117	0.770	0.320	0.228	0.667	0.226	0.117	0.808	0.384	0.288	0.827
Typicality	0.948	0.129	1.000	0.843	0.110	0.997	0.949	0.129	1.000	0.611	0.081	0.667

Table 9.39. Predictive probability and typicality descriptive statistics for correct and incorrect right humerus predicting right radius.

	Density			Equal			Size			Shape		
	Correct Classifications											
	Mean	Min	Max	Mean	Min	Max	Mean	Min	Max	Mean	Min	Max
Probability	0.264	0.132	0.821	0.273	0.198	0.505	0.283	0.132	0.975	0.300	0.222	0.610
Typicality	0.938	0.227	1.000	0.861	0.291	0.989	0.937	0.227	1.000	0.674	0.041	0.746
	Incorrect Classifications											
	Mean	Min	Max	Mean	Min	Max	Mean	Min	Max	Mean	Min	Max
Probability	0.225	0.130	0.928	0.252	0.191	0.624	0.231	0.130	0.945	0.282	0.220	0.635
Typicality	0.945	0.175	1.000	0.834	0.187	0.993	0.946	0.175	1.000	0.677	0.143	0.749

Table 9.40. Predictive probability and typicality descriptive statistics for correct and incorrect right femur predicting right tibia.

	Density			Equal			Size			Shape		
	Correct Classifications											
	Mean	Min	Max	Mean	Min	Max	Mean	Min	Max	Mean	Min	Max
Probability	0.399	0.126	0.887	0.268	0.174	0.501	0.435	0.126	1.000	0.259	0.190	0.498
Typicality	0.883	0.025	1.000	0.803	0.378	0.994	0.880	0.025	1.000	0.685	0.359	0.794
	Incorrect Classifications											
	Mean	Min	Max	Mean	Min	Max	Mean	Min	Max	Mean	Min	Max
Probability	0.304	0.144	0.840	0.234	0.165	0.378	0.316	0.144	0.972	0.244	0.181	0.418
Typicality	0.921	0.143	1.000	0.777	0.295	0.973	0.922	0.143	1.000	0.685	0.284	0.797

A.4. Between-limb

A.4.1. Correct match rank

Table 9.41. Correct match predictive probability ranks for right humerus predicting left ulna.

Density				Equal			
Rank	Frequency	Percent	Cumulative	Rank	Frequency	Percent	Cumulative
1	227	22.70%	22.70%	1	299	29.90%	29.90%
2	182	18.20%	40.90%	2	225	22.50%	52.40%
3	194	19.40%	60.30%	3	160	16.00%	68.40%
4	130	13.00%	73.30%	4	98	9.80%	78.20%
5	97	9.70%	83.00%	5	73	7.30%	85.50%
6	72	7.20%	90.20%	6	53	5.30%	90.80%
7	42	4.20%	94.40%	7	35	3.50%	94.30%
8	28	2.80%	97.20%	8	18	1.80%	96.10%
9	20	2.00%	99.20%	9	25	2.50%	98.60%
10	8	0.80%	100.00%	10	14	1.40%	100.00%
Size				Shape			
1	216	21.60%	21.60%	1	195	19.50%	19.50%
2	190	19.00%	40.60%	2	161	16.10%	35.60%
3	193	19.30%	59.90%	3	143	14.30%	49.90%
4	137	13.70%	73.60%	4	116	11.60%	61.50%
5	93	9.30%	82.90%	5	79	7.90%	69.40%
6	69	6.90%	89.80%	6	86	8.60%	78.00%
7	44	4.40%	94.20%	7	73	7.30%	85.30%
8	31	3.10%	97.30%	8	56	5.60%	90.90%
9	19	1.90%	99.20%	9	52	5.20%	96.10%
10	8	0.80%	100.00%	10	39	3.90%	100.00%

Table 9.42. Correct match predictive probability ranks for right humerus predicting left radius.

Density				Equal			
Rank	Frequency	Percent	Cumulative	Rank	Frequency	Percent	Cumulative
1	290	29.00%	29.00%	1	360	36.00%	36.00%
2	210	21.00%	50.00%	2	238	23.80%	59.80%
3	140	14.00%	64.00%	3	140	14.00%	73.80%
4	127	12.70%	76.70%	4	87	8.70%	82.50%
5	87	8.70%	85.40%	5	54	5.40%	87.90%
6	64	6.40%	91.80%	6	27	2.70%	90.60%
7	40	4.00%	95.80%	7	40	4.00%	94.60%
8	25	2.50%	98.30%	8	18	1.80%	96.40%
9	11	1.10%	99.40%	9	19	1.90%	98.30%
10	6	0.60%	100.00%	10	17	1.70%	100.00%
Size				Shape			
1	277	27.70%	27.70%	1	261	26.10%	26.10%
2	214	21.40%	49.10%	2	157	15.70%	41.80%
3	147	14.70%	63.80%	3	127	12.70%	54.50%
4	126	12.60%	76.40%	4	90	9.00%	63.50%
5	87	8.70%	85.10%	5	83	8.30%	71.80%
6	68	6.80%	91.90%	6	74	7.40%	79.20%
7	39	3.90%	95.80%	7	60	6.00%	85.20%
8	25	2.50%	98.30%	8	62	6.20%	91.40%
9	9	0.90%	99.20%	9	42	4.20%	95.60%
10	8	0.80%	100.00%	10	44	4.40%	100.00%

Table 9.43. Correct match predictive probability ranks for right femur predicting right ulna.

Density				Equal			
Rank	Frequency	Percent	Cumulative	Rank	Frequency	Percent	Cumulative
1	236	23.60%	23.60%	1	336	33.60%	33.60%
2	224	22.40%	46.00%	2	234	23.40%	57.00%
3	185	18.50%	64.50%	3	140	14.00%	71.00%
4	115	11.50%	76.00%	4	82	8.20%	79.20%
5	94	9.40%	85.40%	5	84	8.40%	87.60%
6	71	7.10%	92.50%	6	44	4.40%	92.00%
7	40	4.00%	96.50%	7	38	3.80%	95.80%
8	23	2.30%	98.80%	8	16	1.60%	97.40%
9	8	0.80%	99.60%	9	19	1.90%	99.30%
10	4	0.40%	100.00%	10	7	0.70%	100.00%
Size				Shape			
1	225	22.50%	22.50%	1	168	16.80%	16.80%
2	230	23.00%	45.50%	2	162	16.20%	33.00%
3	185	18.50%	64.00%	3	153	15.30%	48.30%
4	116	11.60%	75.60%	4	111	11.10%	59.40%
5	94	9.40%	85.00%	5	113	11.30%	70.70%
6	75	7.50%	92.50%	6	92	9.20%	79.90%
7	40	4.00%	96.50%	7	63	6.30%	86.20%
8	22	2.20%	98.70%	8	63	6.30%	92.50%
9	9	0.90%	99.60%	9	47	4.70%	97.20%
10	4	0.40%	100.00%	10	28	2.80%	100.00%

Table 9.44. Correct match predictive probability ranks for right femur predicting right radius.

Density				Equal			
Rank	Frequency	Percent	Cumulative	Rank	Frequency	Percent	Cumulative
1	281	28.10%	28.10%	1	387	38.70%	38.70%
2	204	20.40%	48.50%	2	183	18.30%	57.00%
3	181	18.10%	66.60%	3	143	14.30%	71.30%
4	109	10.90%	77.50%	4	86	8.60%	79.90%
5	89	8.90%	86.40%	5	54	5.40%	85.30%
6	61	6.10%	92.50%	6	36	3.60%	88.90%
7	43	4.30%	96.80%	7	21	2.10%	91.00%
8	21	2.10%	98.90%	8	29	2.90%	93.90%
9	10	1.00%	99.90%	9	37	3.70%	97.60%
10	1	0.10%	100.00%	10	24	2.40%	100.00%
Size				Shape			
1	270	27.00%	27.00%	1	274	27.40%	27.40%
2	208	20.80%	47.80%	2	153	15.30%	42.70%
3	181	18.10%	65.90%	3	109	10.90%	53.60%
4	115	11.50%	77.40%	4	68	6.80%	60.40%
5	88	8.80%	86.20%	5	83	8.30%	68.70%
6	63	6.30%	92.50%	6	85	8.50%	77.20%
7	45	4.50%	97.00%	7	71	7.10%	84.30%
8	19	1.90%	98.90%	8	60	6.00%	90.30%
9	10	1.00%	99.90%	9	51	5.10%	95.40%
10	1	0.10%	100.00%	10	46	4.60%	100.00%

Table 9.45. Correct match predictive probability ranks for right femur predicting left tibia.

Density				Equal			
Rank	Frequency	Percent	Cumulative	Rank	Frequency	Percent	Cumulative
1	380	38.00%	38.00%	1	479	47.90%	47.90%
2	246	24.60%	62.60%	2	227	22.70%	70.60%
3	155	15.50%	78.10%	3	104	10.40%	81.00%
4	115	11.50%	89.60%	4	60	6.00%	87.00%
5	51	5.10%	94.70%	5	44	4.40%	91.40%
6	29	2.90%	97.60%	6	33	3.30%	94.70%
7	21	2.10%	99.70%	7	16	1.60%	96.30%
8	3	0.30%	100.00%	8	14	1.40%	97.70%
9	0	0.00%	100.00%	9	10	1.00%	98.70%
10	0	0.00%	100.00%	10	13	1.30%	100.00%
Size				Shape			
1	367	36.70%	36.70%	1	274	27.40%	27.40%
2	252	25.20%	61.90%	2	176	17.60%	45.00%
3	157	15.70%	77.60%	3	125	12.50%	57.50%
4	119	11.90%	89.50%	4	103	10.30%	67.80%
5	51	5.10%	94.60%	5	72	7.20%	75.00%
6	30	3.00%	97.60%	6	46	4.60%	79.60%
7	21	2.10%	99.70%	7	64	6.40%	86.00%
8	3	0.30%	100.00%	8	54	5.40%	91.40%
9	0	0.00%	100.00%	9	47	4.70%	96.10%
10	0	0.00%	100.00%	10	39	3.90%	100.00%

Table 9.46. Correct match predictive probability ranks for left ulna predicting right radius.

Density				Equal			
Rank	Frequency	Percent	Cumulative	Rank	Frequency	Percent	Cumulative
1	427	42.70%	42.70%	1	532	53.20%	53.20%
2	255	25.50%	68.20%	2	229	22.90%	76.10%
3	154	15.40%	83.60%	3	117	11.70%	87.80%
4	92	9.20%	92.80%	4	53	5.30%	93.10%
5	47	4.70%	97.50%	5	30	3.00%	96.10%
6	10	1.00%	98.50%	6	20	2.00%	98.10%
7	4	0.40%	98.90%	7	6	0.60%	98.70%
8	0	0.00%	98.90%	8	4	0.40%	99.10%
9	3	0.30%	99.20%	9	6	0.60%	99.70%
10	8	0.80%	100.00%	10	3	0.30%	100.00%
Size				Shape			
1	410	41.00%	41.00%	1	233	23.30%	23.30%
2	262	26.20%	67.20%	2	177	17.70%	41.00%
3	163	16.30%	83.50%	3	150	15.00%	56.00%
4	93	9.30%	92.80%	4	105	10.50%	66.50%
5	45	4.50%	97.30%	5	115	11.50%	78.00%
6	14	1.40%	98.70%	6	71	7.10%	85.10%
7	6	0.60%	99.30%	7	72	7.20%	92.30%
8	3	0.30%	99.60%	8	40	4.00%	96.30%
9	2	0.20%	99.80%	9	22	2.20%	98.50%
10	2	0.20%	100.00%	10	15	1.50%	100.00%

Table 9.47. Correct match predictive probability ranks for left radius predicting right ulna.

Density				Equal			
Rank	Frequency	Percent	Cumulative	Rank	Frequency	Percent	Cumulative
1	403	40.30%	40.30%	1	562	56.20%	56.20%
2	270	27.00%	67.30%	2	226	22.60%	78.80%
3	174	17.40%	84.70%	3	110	11.00%	89.80%
4	90	9.00%	93.70%	4	40	4.00%	93.80%
5	39	3.90%	97.60%	5	28	2.80%	96.60%
6	20	2.00%	99.60%	6	12	1.20%	97.80%
7	4	0.40%	100.00%	7	10	1.00%	98.80%
8	0	0.00%	100.00%	8	8	0.80%	99.60%
9	0	0.00%	100.00%	9	3	0.30%	99.90%
10	0	0.00%	100.00%	10	1	0.10%	100.00%
Size				Shape			
1	391	39.10%	39.10%	1	237	23.70%	23.70%
2	277	27.70%	66.80%	2	185	18.50%	42.20%
3	179	17.90%	84.70%	3	174	17.40%	59.60%
4	86	8.60%	93.30%	4	121	12.10%	71.70%
5	42	4.20%	97.50%	5	82	8.20%	79.90%
6	21	2.10%	99.60%	6	66	6.60%	86.50%
7	4	0.40%	100.00%	7	54	5.40%	91.90%
8	0	0.00%	100.00%	8	35	3.50%	95.40%
9	0	0.00%	100.00%	9	30	3.00%	98.40%
10	0	0.00%	100.00%	10	16	1.60%	100.00%

Table 9.48. Correct match predictive probability ranks for left humerus predicting right ulna.

Density				Equal			
Rank	Frequency	Percent	Cumulative	Rank	Frequency	Percent	Cumulative
1	267	26.70%	26.70%	1	372	37.20%	37.20%
2	204	20.40%	47.10%	2	221	22.10%	59.30%
3	151	15.10%	62.20%	3	137	13.70%	73.00%
4	129	12.90%	75.10%	4	71	7.10%	80.10%
5	112	11.20%	86.30%	5	57	5.70%	85.80%
6	54	5.40%	91.70%	6	40	4.00%	89.80%
7	35	3.50%	95.20%	7	32	3.20%	93.00%
8	31	3.10%	98.30%	8	27	2.70%	95.70%
9	10	1.00%	99.30%	9	28	2.80%	98.50%
10	7	0.70%	100.00%	10	15	1.50%	100.00%
Size				Shape			
1	252	25.20%	25.20%	1	255	25.50%	25.50%
2	203	20.30%	45.50%	2	176	17.60%	43.10%
3	160	16.00%	61.50%	3	119	11.90%	55.00%
4	133	13.30%	74.80%	4	95	9.50%	64.50%
5	113	11.30%	86.10%	5	97	9.70%	74.20%
6	53	5.30%	91.40%	6	72	7.20%	81.40%
7	38	3.80%	95.20%	7	45	4.50%	85.90%
8	32	3.20%	98.40%	8	51	5.10%	91.00%
9	10	1.00%	99.40%	9	55	5.50%	96.50%
10	6	0.60%	100.00%	10	35	3.50%	100.00%

Table 9.49. Correct match predictive probability ranks for left humerus predicting right radius.

Density				Equal			
Rank	Frequency	Percent	Cumulative	Rank	Frequency	Percent	Cumulative
1	267	26.70%	26.70%	1	372	37.20%	37.20%
2	204	20.40%	47.10%	2	221	22.10%	59.30%
3	151	15.10%	62.20%	3	137	13.70%	73.00%
4	129	12.90%	75.10%	4	71	7.10%	80.10%
5	112	11.20%	86.30%	5	57	5.70%	85.80%
6	54	5.40%	91.70%	6	40	4.00%	89.80%
7	35	3.50%	95.20%	7	32	3.20%	93.00%
8	31	3.10%	98.30%	8	27	2.70%	95.70%
9	10	1.00%	99.30%	9	28	2.80%	98.50%
10	7	0.70%	100.00%	10	15	1.50%	100.00%
Size				Shape			
1	252	25.20%	25.20%	1	255	25.50%	25.50%
2	203	20.30%	45.50%	2	176	17.60%	43.10%
3	160	16.00%	61.50%	3	119	11.90%	55.00%
4	133	13.30%	74.80%	4	95	9.50%	64.50%
5	113	11.30%	86.10%	5	97	9.70%	74.20%
6	53	5.30%	91.40%	6	72	7.20%	81.40%
7	38	3.80%	95.20%	7	45	4.50%	85.90%
8	32	3.20%	98.40%	8	51	5.10%	91.00%
9	10	1.00%	99.40%	9	55	5.50%	96.50%
10	6	0.60%	100.00%	10	35	3.50%	100.00%

Table 9.50. Correct match predictive probability ranks for left femur predicting right tibia.

Density				Equal			
Rank	Frequency	Percent	Cumulative	Rank	Frequency	Percent	Cumulative
1	337	33.70%	33.70%	1	431	43.10%	43.10%
2	232	23.20%	56.90%	2	219	21.90%	65.00%
3	173	17.30%	74.20%	3	132	13.20%	78.20%
4	114	11.40%	85.60%	4	71	7.10%	85.30%
5	66	6.60%	92.20%	5	40	4.00%	89.30%
6	42	4.20%	96.40%	6	27	2.70%	92.00%
7	28	2.80%	99.20%	7	16	1.60%	93.60%
8	7	0.70%	99.90%	8	29	2.90%	96.50%
9	1	0.10%	100.00%	9	24	2.40%	98.90%
10	0	0.00%	100.00%	10	11	1.10%	100.00%
Size				Shape			
1	326	32.60%	32.60%	1	203	20.30%	20.30%
2	239	23.90%	56.50%	2	167	16.70%	37.00%
3	176	17.60%	74.10%	3	159	15.90%	52.90%
4	115	11.50%	85.60%	4	107	10.70%	63.60%
5	65	6.50%	92.10%	5	97	9.70%	73.30%
6	39	3.90%	96.00%	6	69	6.90%	80.20%
7	28	2.80%	98.80%	7	61	6.10%	86.30%
8	9	0.90%	99.70%	8	58	5.80%	92.10%
9	3	0.30%	100.00%	9	39	3.90%	96.00%
10	0	0.00%	100.00%	10	40	4.00%	100.00%

Table 9.51. Correct match predictive probability ranks for right ulna predicting right femur.

Density				Equal			
Rank	Frequency	Percent	Cumulative	Rank	Frequency	Percent	Cumulative
1	269	26.90%	26.90%	1	335	33.50%	33.50%
2	195	19.50%	46.40%	2	197	19.70%	53.20%
3	158	15.80%	62.20%	3	145	14.50%	67.70%
4	128	12.80%	75.00%	4	106	10.60%	78.30%
5	100	10.00%	85.00%	5	68	6.80%	85.10%
6	77	7.70%	92.70%	6	46	4.60%	89.70%
7	47	4.70%	97.40%	7	34	3.40%	93.10%
8	15	1.50%	98.90%	8	28	2.80%	95.90%
9	9	0.90%	99.80%	9	23	2.30%	98.20%
10	2	0.20%	100.00%	10	18	1.80%	100.00%
Size				Shape			
1	264	26.40%	26.40%	1	188	18.80%	18.80%
2	205	20.50%	46.90%	2	132	13.20%	32.00%
3	150	15.00%	61.90%	3	139	13.90%	45.90%
4	129	12.90%	74.80%	4	101	10.10%	56.00%
5	104	10.40%	85.20%	5	93	9.30%	65.30%
6	75	7.50%	92.70%	6	88	8.80%	74.10%
7	46	4.60%	97.30%	7	82	8.20%	82.30%
8	16	1.60%	98.90%	8	67	6.70%	89.00%
9	11	1.10%	100.00%	9	60	6.00%	95.00%
10	0	0.00%	100.00%	10	50	5.00%	100.00%

Table 9.52. Correct match predictive probability ranks for right ulna predicting left radius.

Density				Equal			
Rank	Frequency	Percent	Cumulative	Rank	Frequency	Percent	Cumulative
1	402	40.20%	40.20%	1	590	59.00%	59.00%
2	287	28.70%	68.90%	2	203	20.30%	79.30%
3	150	15.00%	83.90%	3	82	8.20%	87.50%
4	83	8.30%	92.20%	4	44	4.40%	91.90%
5	46	4.60%	96.80%	5	21	2.10%	94.00%
6	20	2.00%	98.80%	6	26	2.60%	96.60%
7	7	0.70%	99.50%	7	13	1.30%	97.90%
8	5	0.50%	100.00%	8	10	1.00%	98.90%
9	0	0.00%	100.00%	9	6	0.60%	99.50%
10	0	0.00%	100.00%	10	5	0.50%	100.00%
Size				Shape			
1	389	38.90%	38.90%	1	314	31.40%	31.40%
2	292	29.20%	68.10%	2	175	17.50%	48.90%
3	156	15.60%	83.70%	3	139	13.90%	62.80%
4	84	8.40%	92.10%	4	104	10.40%	73.20%
5	46	4.60%	96.70%	5	75	7.50%	80.70%
6	21	2.10%	98.80%	6	56	5.60%	86.30%
7	7	0.70%	99.50%	7	60	6.00%	92.30%
8	5	0.50%	100.00%	8	39	3.90%	96.20%
9	0	0.00%	100.00%	9	32	3.20%	99.40%
10	0	0.00%	100.00%	10	6	0.60%	100.00%

Table 9.53. Correct match predictive probability ranks for right tibia predicting right radius.

Density				Equal			
Rank	Frequency	Percent	Cumulative	Rank	Frequency	Percent	Cumulative
1	321	32.10%	32.10%	1	446	44.60%	44.60%
2	227	22.70%	54.80%	2	254	25.40%	70.00%
3	159	15.90%	70.70%	3	121	12.10%	82.10%
4	107	10.70%	81.40%	4	58	5.80%	87.90%
5	89	8.90%	90.30%	5	40	4.00%	91.90%
6	43	4.30%	94.60%	6	22	2.20%	94.10%
7	32	3.20%	97.80%	7	25	2.50%	96.60%
8	15	1.50%	99.30%	8	12	1.20%	97.80%
9	4	0.40%	99.70%	9	16	1.60%	99.40%
10	3	0.30%	100.00%	10	6	0.60%	100.00%
Size				Shape			
1	298	29.80%	29.80%	1	271	27.10%	27.10%
2	233	23.30%	53.10%	2	181	18.10%	45.20%
3	168	16.80%	69.90%	3	137	13.70%	58.90%
4	113	11.30%	81.20%	4	95	9.50%	68.40%
5	90	9.00%	90.20%	5	88	8.80%	77.20%
6	44	4.40%	94.60%	6	60	6.00%	83.20%
7	31	3.10%	97.70%	7	67	6.70%	89.90%
8	17	1.70%	99.40%	8	53	5.30%	95.20%
9	3	0.30%	99.70%	9	27	2.70%	97.90%
10	3	0.30%	100.00%	10	21	2.10%	100.00%

Table 9.54. Correct match predictive probability ranks for right tibia predicting right humerus.

Density				Equal			
Rank	Frequency	Percent	Cumulative	Rank	Frequency	Percent	Cumulative
1	275	27.50%	27.50%	1	372	37.20%	37.20%
2	194	19.40%	46.90%	2	235	23.50%	60.70%
3	142	14.20%	61.10%	3	138	13.80%	74.50%
4	125	12.50%	73.60%	4	83	8.30%	82.80%
5	112	11.20%	84.80%	5	37	3.70%	86.50%
6	60	6.00%	90.80%	6	31	3.10%	89.60%
7	49	4.90%	95.70%	7	35	3.50%	93.10%
8	26	2.60%	98.30%	8	28	2.80%	95.90%
9	14	1.40%	99.70%	9	20	2.00%	97.90%
10	3	0.30%	100.00%	10	21	2.10%	100.00%
Size				Shape			
1	259	25.90%	25.90%	1	229	22.90%	22.90%
2	206	20.60%	46.50%	2	168	16.80%	39.70%
3	139	13.90%	60.40%	3	140	14.00%	53.70%
4	132	13.20%	73.60%	4	106	10.60%	64.30%
5	112	11.20%	84.80%	5	77	7.70%	72.00%
6	61	6.10%	90.90%	6	91	9.10%	81.10%
7	47	4.70%	95.60%	7	61	6.10%	87.20%
8	24	2.40%	98.00%	8	47	4.70%	91.90%
9	17	1.70%	99.70%	9	50	5.00%	96.90%
10	3	0.30%	100.00%	10	31	3.10%	100.00%

Table 9.55. Correct match predictive probability ranks for right radius predicting right tibia.

Density				Equal			
Rank	Frequency	Percent	Cumulative	Rank	Frequency	Percent	Cumulative
1	304	30.40%	30.40%	1	422	42.20%	42.20%
2	212	21.20%	51.60%	2	220	22.00%	64.20%
3	177	17.70%	69.30%	3	143	14.30%	78.50%
4	133	13.30%	82.60%	4	75	7.50%	86.00%
5	78	7.80%	90.40%	5	49	4.90%	90.90%
6	54	5.40%	95.80%	6	30	3.00%	93.90%
7	24	2.40%	98.20%	7	22	2.20%	96.10%
8	10	1.00%	99.20%	8	11	1.10%	97.20%
9	5	0.50%	99.70%	9	18	1.80%	99.00%
10	3	0.30%	100.00%	10	10	1.00%	100.00%
Size				Shape			
1	279	27.90%	27.90%	1	211	21.10%	21.10%
2	224	22.40%	50.30%	2	167	16.70%	37.80%
3	194	19.40%	69.70%	3	150	15.00%	52.80%
4	127	12.70%	82.40%	4	119	11.90%	64.70%
5	78	7.80%	90.20%	5	104	10.40%	75.10%
6	56	5.60%	95.80%	6	80	8.00%	83.10%
7	23	2.30%	98.10%	7	62	6.20%	89.30%
8	12	1.20%	99.30%	8	47	4.70%	94.00%
9	4	0.40%	99.70%	9	34	3.40%	97.40%
10	3	0.30%	100.00%	10	26	2.60%	100.00%

Table 9.56. Correct match predictive probability ranks for right radius predicting right femur.

Density				Equal			
Rank	Frequency	Percent	Cumulative	Rank	Frequency	Percent	Cumulative
1	258	25.80%	25.80%	1	315	31.50%	31.50%
2	204	20.40%	46.20%	2	238	23.80%	55.30%
3	170	17.00%	63.20%	3	152	15.20%	70.50%
4	135	13.50%	76.70%	4	83	8.30%	78.80%
5	91	9.10%	85.80%	5	58	5.80%	84.60%
6	74	7.40%	93.20%	6	49	4.90%	89.50%
7	25	2.50%	95.70%	7	28	2.80%	92.30%
8	30	3.00%	98.70%	8	30	3.00%	95.30%
9	10	1.00%	99.70%	9	31	3.10%	98.40%
10	3	0.30%	100.00%	10	16	1.60%	100.00%
Size				Shape			
1	243	24.30%	24.30%	1	177	17.70%	17.70%
2	210	21.00%	45.30%	2	138	13.80%	31.50%
3	176	17.60%	62.90%	3	131	13.10%	44.60%
4	138	13.80%	76.70%	4	127	12.70%	57.30%
5	88	8.80%	85.50%	5	87	8.70%	66.00%
6	73	7.30%	92.80%	6	72	7.20%	73.20%
7	30	3.00%	95.80%	7	89	8.90%	82.10%
8	30	3.00%	98.80%	8	71	7.10%	89.20%
9	9	0.90%	99.70%	9	72	7.20%	96.40%
10	3	0.30%	100.00%	10	36	3.60%	100.00%

Table 9.57. Correct match predictive probability ranks for right radius predicting left ulna.

Density				Equal			
Rank	Frequency	Percent	Cumulative	Rank	Frequency	Percent	Cumulative
1	450	45.00%	45.00%	1	535	53.50%	53.50%
2	242	24.20%	69.20%	2	216	21.60%	75.10%
3	153	15.30%	84.50%	3	98	9.80%	84.90%
4	59	5.90%	90.40%	4	48	4.80%	89.70%
5	47	4.70%	95.10%	5	32	3.20%	92.90%
6	13	1.30%	96.40%	6	28	2.80%	95.70%
7	10	1.00%	97.40%	7	12	1.20%	96.90%
8	7	0.70%	98.10%	8	8	0.80%	97.70%
9	6	0.60%	98.70%	9	9	0.90%	98.60%
10	13	1.30%	100.00%	10	14	1.40%	100.00%
Size				Shape			
1	427	42.70%	42.70%	1	248	24.80%	24.80%
2	262	26.20%	68.90%	2	194	19.40%	44.20%
3	152	15.20%	84.10%	3	124	12.40%	56.60%
4	66	6.60%	90.70%	4	102	10.20%	66.80%
5	48	4.80%	95.50%	5	91	9.10%	75.90%
6	17	1.70%	97.20%	6	62	6.20%	82.10%
7	13	1.30%	98.50%	7	65	6.50%	88.60%
8	4	0.40%	98.90%	8	35	3.50%	92.10%
9	3	0.30%	99.20%	9	37	3.70%	95.80%
10	8	0.80%	100.00%	10	42	4.20%	100.00%

Table 9.58. Correct match predictive probability ranks for right humerus predicting right tibia.

Density				Equal			
Rank	Frequency	Percent	Cumulative	Rank	Frequency	Percent	Cumulative
1	268	26.80%	26.80%	1	330	33.00%	33.00%
2	215	21.50%	48.30%	2	235	23.50%	56.50%
3	172	17.20%	65.50%	3	163	16.30%	72.80%
4	145	14.50%	80.00%	4	102	10.20%	83.00%
5	79	7.90%	87.90%	5	65	6.50%	89.50%
6	52	5.20%	93.10%	6	37	3.70%	93.20%
7	43	4.30%	97.40%	7	32	3.20%	96.40%
8	13	1.30%	98.70%	8	17	1.70%	98.10%
9	10	1.00%	99.70%	9	14	1.40%	99.50%
10	3	0.30%	100.00%	10	5	0.50%	100.00%
Size				Shape			
1	256	25.60%	25.60%	1	141	14.10%	14.10%
2	221	22.10%	47.70%	2	154	15.40%	29.50%
3	173	17.30%	65.00%	3	136	13.60%	43.10%
4	148	14.80%	79.80%	4	142	14.20%	57.30%
5	80	8.00%	87.80%	5	125	12.50%	69.80%
6	54	5.40%	93.20%	6	99	9.90%	79.70%
7	42	4.20%	97.40%	7	67	6.70%	86.40%
8	13	1.30%	98.70%	8	63	6.30%	92.70%
9	11	1.10%	99.80%	9	47	4.70%	97.40%
10	2	0.20%	100.00%	10	26	2.60%	100.00%

A.4.2. Descriptive statistics

Table 9.59. Predictive probability and typicality descriptive statistics for correct and incorrect right femur predicting right radius.

	Density			Equal			Size			Shape		
	Correct Classifications											
	Mean	Min	Max	Mean	Min	Max	Mean	Min	Max	Mean	Min	Max
Probability	0.299	0.127	0.840	0.239	0.171	0.433	0.323	0.127	0.977	0.245	0.189	0.416
Typicality	0.929	0.447	1.000	0.827	0.583	0.978	0.928	0.447	1.000	0.697	0.339	0.797
	Incorrect Classifications											
	Mean	Min	Max	Mean	Min	Max	Mean	Min	Max	Mean	Min	Max
Probability	0.238	0.132	0.721	0.217	0.166	0.442	0.247	0.132	0.847	0.234	0.188	0.434
Typicality	0.947	0.162	1.000	0.812	0.382	0.978	0.947	0.162	1.000	0.693	0.388	0.794

Table 9.60. Predictive probability and typicality descriptive statistics for correct and incorrect right femur predicting left tibia.

	Density			Equal			Size			Shape		
	Correct Classifications											
	Mean	Min	Max	Mean	Min	Max	Mean	Min	Max	Mean	Min	Max
Probability	0.390	0.152	0.874	0.265	0.174	0.487	0.426	0.152	1.000	0.249	0.196	0.468
Typicality	0.892	0.063	1.000	0.814	0.343	0.987	0.889	0.063	1.000	0.691	0.419	0.788
	Incorrect Classifications											
	Mean	Min	Max	Mean	Min	Max	Mean	Min	Max	Mean	Min	Max
Probability	0.296	0.144	0.767	0.233	0.171	0.381	0.306	0.144	0.862	0.237	0.186	0.420
Typicality	0.917	0.261	1.000	0.791	0.315	0.976	0.919	0.261	1.000	0.693	0.286	0.794

Table 9.61. Predictive probability and typicality descriptive statistics for correct and incorrect left ulna predicting right radius.

	Density			Equal			Size			Shape		
	Correct Classifications											
	Mean	Min	Max	Mean	Min	Max	Mean	Min	Max	Mean	Min	Max
Probability	0.366	0.140	0.900	0.222	0.126	0.484	0.388	0.155	0.995	0.203	0.120	0.625
Typicality	0.920	0.113	1.000	0.830	0.496	0.999	0.921	0.113	1.000	0.584	0.310	0.666
	Incorrect Classifications											
	Mean	Min	Max	Mean	Min	Max	Mean	Min	Max	Mean	Min	Max
Probability	0.271	0.138	0.898	0.186	0.129	0.386	0.277	0.138	0.977	0.168	0.119	0.505
Typicality	0.937	0.221	1.000	0.800	0.285	0.998	0.936	0.221	1.000	0.599	0.200	0.666

Table 9.62. Predictive probability and typicality descriptive statistics for correct and incorrect left radius predicting right ulna.

	Density			Equal			Size			Shape		
	Correct Classifications											
	Mean	Min	Max	Mean	Min	Max	Mean	Min	Max	Mean	Min	Max
Probability	0.464	0.163	0.982	0.256	0.140	0.681	0.492	0.163	1.000	0.236	0.122	0.565
Typicality	0.860	0.131	1.000	0.778	0.153	0.999	0.856	0.131	1.000	0.551	0.113	0.666
	Incorrect Classifications											
	Mean	Min	Max	Mean	Min	Max	Mean	Min	Max	Mean	Min	Max
Probability	0.343	0.134	0.823	0.208	0.137	0.411	0.352	0.135	0.881	0.174	0.116	0.466
Typicality	0.898	0.081	1.000	0.775	0.154	0.997	0.900	0.081	1.000	0.601	0.038	0.667

Table 9.63. Predictive probability and typicality descriptive statistics for correct and incorrect left humerus predicting right ulna.

	Density			Equal			Size			Shape		
	Correct Classifications											
	Mean	Min	Max	Mean	Min	Max	Mean	Min	Max	Mean	Min	Max
Probability	0.295	0.123	0.849	0.279	0.203	0.524	0.313	0.144	0.932	0.299	0.229	0.519
Typicality	0.925	0.426	1.000	0.822	0.353	0.979	0.926	0.426	1.000	0.667	0.383	0.749
	Incorrect Classifications											
	Mean	Min	Max	Mean	Min	Max	Mean	Min	Max	Mean	Min	Max
Probability	0.232	0.134	0.688	0.256	0.193	0.526	0.238	0.123	0.842	0.290	0.224	0.625
Typicality	0.946	0.385	1.000	0.820	0.346	0.983	0.946	0.385	1.000	0.661	0.198	0.748

Table 9.64. Predictive probability and typicality descriptive statistics for correct and incorrect left humerus predicting right radius.

	Density			Equal			Size			Shape		
	Correct Classifications											
	Mean	Min	Max	Mean	Min	Max	Mean	Min	Max	Mean	Min	Max
Probability	0.282	0.145	0.793	0.234	0.168	0.441	0.303	0.146	0.916	0.249	0.179	0.504
Typicality	0.939	0.362	1.000	0.821	0.501	0.983	0.938	0.362	1.000	0.700	0.178	0.793
	Incorrect Classifications											
	Mean	Min	Max	Mean	Min	Max	Mean	Min	Max	Mean	Min	Max
Probability	0.234	0.126	0.562	0.214	0.166	0.369	0.241	0.126	0.632	0.234	0.186	0.405
Typicality	0.943	0.365	1.000	0.808	0.342	0.995	0.944	0.365	1.000	0.694	0.338	0.798

Table 9.65. Predictive probability and typicality descriptive statistics for correct and incorrect left femur predicting right tibia.

	Density			Equal			Size			Shape		
	Correct Classifications											
	Mean	Min	Max	Mean	Min	Max	Mean	Min	Max	Mean	Min	Max
Probability	0.340	0.132	0.906	0.248	0.176	0.490	0.365	0.133	0.995	0.243	0.197	0.394
Typicality	0.914	0.111	1.000	0.818	0.413	0.984	0.911	0.111	1.000	0.690	0.467	0.786
	Incorrect Classifications											
	Mean	Min	Max	Mean	Min	Max	Mean	Min	Max	Mean	Min	Max
Probability	0.268	0.137	0.794	0.223	0.169	0.404	0.276	0.137	0.877	0.234	0.188	0.350
Typicality	0.934	0.147	1.000	0.808	0.473	0.988	0.935	0.147	1.000	0.699	0.489	0.794

Table 9.66. Predictive probability and typicality descriptive statistics for correct and incorrect right humerus predicting right tibia.

	Density			Equal			Size			Shape		
	Correct Classifications											
	Mean	Min	Max	Mean	Min	Max	Mean	Min	Max	Mean	Min	Max
Probability	0.286	0.129	0.767	0.341	0.242	0.674	0.299	0.131	0.831	0.375	0.299	0.823
Typicality	0.936	0.331	1.000	0.853	0.357	0.997	0.934	0.331	1.000	0.612	0.024	0.666
	Incorrect Classifications											
	Mean	Min	Max	Mean	Min	Max	Mean	Min	Max	Mean	Min	Max
Probability	0.245	0.127	0.920	0.321	0.236	0.633	0.249	0.127	0.922	0.361	0.277	0.831
Typicality	0.942	0.173	1.000	0.849	0.053	0.996	0.943	0.173	1.000	0.621	0.045	0.667

Table 9.67. Predictive probability and typicality descriptive statistics for correct and incorrect right humerus predicting left ulna.

	Density			Equal			Size			Shape		
	Correct Classifications											
	Mean	Min	Max	Mean	Min	Max	Mean	Min	Max	Mean	Min	Max
Probability	0.246	0.120	0.765	0.339	0.234	0.677	0.255	0.119	0.842	0.406	0.305	0.867
Typicality	0.938	0.616	1.000	0.847	0.312	0.991	0.937	0.616	1.000	0.602	0.070	0.666
	Incorrect Classifications											
	Mean	Min	Max	Mean	Min	Max	Mean	Min	Max	Mean	Min	Max
Probability	0.210	0.119	0.540	0.313	0.227	0.616	0.213	0.118	0.631	0.387	0.294	0.788
Typicality	0.954	0.371	1.000	0.857	0.384	0.999	0.954	0.371	1.000	0.617	0.262	0.667

Table 9.68. Predictive probability and typicality descriptive statistics for correct and incorrect right ulna predicting right femur.

	Density			Equal			Size			Shape		
	Correct Classifications											
	Mean	Min	Max	Mean	Min	Max	Mean	Min	Max	Mean	Min	Max
Probability	0.308	0.131	0.875	0.366	0.245	0.684	0.320	0.145	0.991	0.417	0.291	0.777
Typicality	0.934	0.342	1.000	0.830	0.480	0.999	0.932	0.342	1.000	0.599	0.303	0.666
	Incorrect Classifications											
	Mean	Min	Max	Mean	Min	Max	Mean	Min	Max	Mean	Min	Max
Probability	0.238	0.119	0.622	0.321	0.233	0.601	0.241	0.118	0.672	0.371	0.280	0.832
Typicality	0.945	0.243	1.000	0.844	0.341	0.997	0.945	0.251	1.000	0.611	0.218	0.666

Table 9.69. Predictive probability and typicality descriptive statistics for correct and incorrect right ulna predicting left radius.

	Density			Equal			Size			Shape		
	Correct Classifications											
	Mean	Min	Max	Mean	Min	Max	Mean	Min	Max	Mean	Min	Max
Probability	0.475	0.184	0.948	0.265	0.146	0.698	0.507	0.184	1.000	0.238	0.118	0.588
Typicality	0.851	0.060	1.000	0.792	0.256	0.998	0.849	0.060	1.000	0.565	0.073	0.666
	Incorrect Classifications											
	Mean	Min	Max	Mean	Min	Max	Mean	Min	Max	Mean	Min	Max
Probability	0.339	0.159	0.856	0.203	0.128	0.420	0.348	0.160	0.919	0.174	0.115	0.538
Typicality	0.918	0.074	1.000	0.773	0.113	0.996	0.918	0.074	1.000	0.595	0.060	0.667

Table 9.70. Predictive probability and typicality descriptive statistics for correct and incorrect right tibia predicting right radius.

	Density			Equal			Size			Shape		
	Correct Classifications											
	Mean	Min	Max	Mean	Min	Max	Mean	Min	Max	Mean	Min	Max
Probability	0.314	0.136	0.827	0.297	0.205	0.537	0.342	0.137	1.000	0.323	0.226	0.619
Typicality	0.921	0.290	1.000	0.823	0.505	0.986	0.919	0.290	1.000	0.653	0.306	0.745
	Incorrect Classifications											
	Mean	Min	Max	Mean	Min	Max	Mean	Min	Max	Mean	Min	Max
Probability	0.254	0.118	0.617	0.266	0.191	0.431	0.264	0.118	0.701	0.286	0.209	0.599
Typicality	0.932	0.169	1.000	0.813	0.221	0.987	0.933	0.170	1.000	0.667	0.221	0.748

Table 9.71. Predictive probability and typicality descriptive statistics for correct and incorrect right tibia predicting right humerus.

	Density			Equal			Size			Shape		
	Correct Classifications											
	Mean	Min	Max	Mean	Min	Max	Mean	Min	Max	Mean	Min	Max
Probability	0.300	0.136	0.873	0.365	0.235	0.766	0.318	0.136	0.992	0.417	0.296	0.881
Typicality	0.935	0.505	1.000	0.855	0.440	0.993	0.934	0.517	1.000	0.609	0.313	0.666
	Incorrect Classifications											
	Mean	Min	Max	Mean	Min	Max	Mean	Min	Max	Mean	Min	Max
Probability	0.242	0.114	0.609	0.324	0.229	0.524	0.247	0.113	0.658	0.367	0.275	0.686
Typicality	0.944	0.201	1.000	0.847	0.352	0.998	0.944	0.201	1.000	0.622	0.351	0.667

Table 9.72. Predictive probability and typicality descriptive statistics for correct and incorrect right radius predicting right tibia.

	Density			Equal			Size			Shape		
	Correct Classifications											
	Mean	Min	Max	Mean	Min	Max	Mean	Min	Max	Mean	Min	Max
Probability	0.336	0.146	0.888	0.387	0.245	0.693	0.364	0.148	0.999	0.438	0.324	0.766
Typicality	0.906	0.251	1.000	0.840	0.429	0.988	0.903	0.251	1.000	0.612	0.123	0.667
	Incorrect Classifications											
	Mean	Min	Max	Mean	Min	Max	Mean	Min	Max	Mean	Min	Max
Probability	0.257	0.136	0.530	0.338	0.228	0.588	0.264	0.135	0.572	0.390	0.284	0.750
Typicality	0.936	0.279	1.000	0.822	0.335	0.996	0.937	0.279	1.000	0.613	0.290	0.667

Table 9.73. Predictive probability and typicality descriptive statistics for correct and incorrect right radius predicting right femur.

	Density			Equal			Size			Shape		
	Correct Classifications											
	Mean	Min	Max	Mean	Min	Max	Mean	Min	Max	Mean	Min	Max
Probability	0.297	0.148	0.907	0.365	0.252	0.691	0.310	0.148	0.993	0.416	0.291	0.841
Typicality	0.934	0.288	1.000	0.846	0.493	0.993	0.930	0.288	1.000	0.611	0.316	0.666
	Incorrect Classifications											
	Mean	Min	Max	Mean	Min	Max	Mean	Min	Max	Mean	Min	Max
Probability	0.246	0.130	0.685	0.323	0.237	0.663	0.249	0.130	0.705	0.370	0.282	0.780
Typicality	0.936	0.244	1.000	0.840	0.248	0.998	0.937	0.244	1.000	0.617	0.411	0.667

Table 9.74. Predictive probability and typicality descriptive statistics for correct and incorrect right radius predicting left ulna.

	Density			Equal			Size			Shape		
	Correct Classifications											
	Mean	Min	Max	Mean	Min	Max	Mean	Min	Max	Mean	Min	Max
Probability	0.367	0.128	0.917	0.420	0.256	0.767	0.388	0.128	1.000	0.462	0.295	0.862
Typicality	0.924	0.367	1.000	0.829	0.366	0.996	0.923	0.375	1.000	0.597	0.246	0.666
	Incorrect Classifications											
	Mean	Min	Max	Mean	Min	Max	Mean	Min	Max	Mean	Min	Max
Probability	0.281	0.136	0.831	0.354	0.244	0.679	0.286	0.136	1.000	0.402	0.292	0.833
Typicality	0.937	0.025	1.000	0.823	0.216	0.997	0.937	0.025	1.000	0.609	0.271	0.667

Vita

Kyle Aidan McCormick was born in Orland Park, Illinois. He received his Bachelors of Arts degree in Anthropology from Michigan State University in 2004. In 2009 he received his Masters of Arts degree in Anthropology from California State University, Chico. In January of 2013 he transferred to the University of Tennessee, Knoxville. Five months prior to transferring he was a fellow at the Forensic Science Academy in Honolulu, Hawaii. He is now a Forensic Anthropologist with the Defense POW/MIA Accounting Agency in Honolulu, Hawaii and is finishing his Ph.D. degree in Anthropology.